

VESICLES IN SIMPLE BINARY
WATER – NON-IONIC SURFACTANT SYSTEMS

Inaugural Dissertation

zur

Erlangung des Doktorgrades
der Mathematisch-Naturwissenschaftlichen Fakultät
der Universität zu Köln

vorgelegt von

Ivana Fehr
(geb. Savić)

geboren in Belgrad

Köln 2009

Berichterstatter:

Prof. Dr. Reinhard Strey, Universität zu Köln

Prof. Dr. Gerhard Gompper, FZ Jülich, IFF – Institute

Vorsitz der Prüfungskommission:

Prof. Dr. Axel G. Griesbeck, Universität zu Köln

Tag der mündlichen Prüfung:

04. Februar 2010

*Meiner Mama,
Marcel und Lennox*

ABSTRACT

This work aims at improving our understanding of the equilibrium structure of the vesicular L_{α}^+ phase in the model system water – non-ionic surfactant $C_{12}E_4$. The results may help the theoretical description of vesicles formed in more complicated, biologically relevant systems. We investigated the mean size and bilayer thickness of the vesicles formed. In order to shed light on the thermodynamic stability of the vesicular phase negative and positive temperature jump experiments from the adjacent single phases were performed. The idea is, should the structures obtained following opposite temperature jumps be in agreement, the vesicular phase should be a thermodynamically stable phase. Dynamic Light Scattering (DLS), Small Angle Neutron Scattering (SANS) and Deuterium Nuclear Magnetic Resonance (2H - NMR) experiments were used as experimental tools. Mutually supporting each other these techniques facilitate the characterization of the equilibrium structure of the L_{α}^+ phase for a wide range of surfactant concentrations and sample preparation procedures. In some cases in addition Freeze Fracture Electron Microscopy (FFEM) was performed. The results show that regions in the phase diagram denoted by L_{α}^+ represent a wealth of structural aggregates among which vesicular objects are present. However, in most cases lamellar phase fragments and overlapping network supra-structures are found. Even when vesicles were the dominant feature, they were far from being well-defined in size and number of lamellae. Often uni- and multilamellar vesicles were coexisting having a diameters of order 30nm, 100nm and 1 μ m, respectively. Thus, a thermodynamic stability of the L_{α}^+ phase is not supported by this work.

KURZZUSAMMENFASSUNG

Das Ziel dieser Arbeit ist es die Gleichgewichtsstruktur der Vesikelphase L_{α}^+ im binären System Wasser – nichtionisches Tensid $C_{12}E_4$ zu untersuchen und zu vervollständigen, um unter anderem die theoretischen Beschreibungen von Vesikeln in komplizierteren, biologisch relevanten Systemen zu verbessern. Die Vesikel wurden auf mittlere Größe und Dicke der Doppelschicht hin untersucht. Um Aufschluss über die thermodynamische Stabilität der Vesikelphase zu geben, wurden aus den Phasen, die sich im Phasendiagramm über bzw. unter der Vesikelphase befinden, negative sowie positive Temperatursprungexperimente durchgeführt. Die Idee ist, wenn eine Übereinstimmung der Strukturen für beide Arten von Temperatursprüngen gefunden würde, wäre dies ein Indiz für eine stabile Vesikelphase, da eine thermodynamisch stabile Phase sich spontan und wegunabhängig ausbildet. Als Untersuchungsmethoden wurden Dynamische Lichtstreuung (DLS), Kleinwinkelneutronenstreuung (SANS) und Deuterium-Kernspinresonanz (NMR) gewählt. Die gegenseitige Ergänzung der einzelnen Methoden ermöglicht die Charakterisierung der Gleichgewichtsstruktur der L_{α}^+ Phase für einen breiten Konzentrationsbereich und verschiedene Präparationsmethoden. Ausgewählte Proben wurden zusätzlich mit Gefrierbruchelektronenmikroskopie (FFEM) untersucht. Aus den Ergebnissen geht hervor, dass in der als L_{α}^+ bezeichneten Region eine Fülle an Aggregaten vorliegt. Neben Vesikeln findet man Fragmente der lamellaren Phase, sowie Netzwerkstrukturen. Die Vesikel zeigen jedoch keine wohldefinierte Form, Größe und Anzahl der Lamellen (in multischaligen Vesikeln). Uni- und multilamellare Vesikel kommen gleichermaßen vor und weisen Größenordnungen von 30nm, 100nm und $1\mu\text{m}$ vor. Somit kann diese Arbeit die thermodynamische Stabilität der L_{α}^+ Phase nicht bestätigen.

ACKNOWLEDGMENTS/ DANKSAGUNG

Die vorliegende Arbeit entstand im Zeitraum von November 2006 bis Dezember 2009 am Institut für physikalische Chemie der Universität zu Köln unter der wissenschaftlichen Anleitung von Herrn Prof. Dr. Reinhard Strey. Ihm danke ich zum einen dafür, dass er stets Vertrauen in mich gesetzt hat. Außerdem danke für die wissenschaftliche Unterstützung jederzeit und für die freundschaftlich-väterlichen Ratschläge.

Herrn Prof. Dr. Gerhard Gompper möchte ich für die Übernahme des Co-Referats danken.

Dr. Thomas Sottmann möchte ich zum einen für die wissenschaftliche Anleitung und für hilfreiche Diskussionen danken. Zum anderen hat er immer freundschaftliches Interesse gehabt und mir in schwierigen Zeiten sehr zur Seite gestanden. Seine Hilfe war schließlich ausschlaggebend für das Gelingen dieser Arbeit.

Dr. Magdalena Baciú – Gotter danke ich für die Betreuung und fachliche Unterstützung und das besondere Engagement bei den SANS Messungen und Auswertungen.

Prof. Dr. Ulf Olsson danke ich, dass er mich so nett in Lund empfangen und betreut hat. Die vielen Diskussionen an der kleinen Tafel waren sehr interessant und aufschlussreich. Die Zeit in Lund hat mir sowohl wissenschaftlich als auch persönlich sehr viel gegeben.

Zudem möchte ich mich bei Prof. Dr. Claudia Schmidt für die Einarbeitung in das Gebiet der NMR Technik und für Ihre Diskussionsbereitschaft in Lund bedanken.

Dr. Lhoussaine Belkoura sei gedankt für die sorgfältige Einarbeitung in die Dynamische Lichtstreuung, außerdem für die Anfertigung der Gefrierbruchmikroskopie-Aufnahmen und für die Unterstützung bei den Auswertungen. Des Weiteren möchte ich Herrn Belkoura auch für sein Interesse an dieser Arbeit und der Diskussionsbereitschaft danken.

Verena Posselt danke ich für intensive und ganz besondere Teamarbeit zuerst während des ganzen Studiums und während der anschließenden Doktorarbeit. Aus der zunächst kleinen Lerngemeinschaft hat sich eine tolle Freundschaft entwickelt.

Dr. Renate Tessendorf hat die Korrektur der Arbeit liebenswerter Weise übernommen und viel Zeit investiert. Danke dafür und für die freundschaftliche und kollegiale Hundeunterstützung.

Sabine Schetzberg danke ich für die abwechslungsreiche Zusammenarbeit im gemeinsamen Labor. Die Fahrten nach Jülich und zu den Konferenzen werde ich nie vergessen.

Sascha Datta und Michael Klostermann danke ich dafür, dass sie mich in München bei den SANS Messungen kräftig unterstützt haben, außerdem hatten beide stets ein offenes Ohr und immer Zeit für SANS-Angelegenheiten.

Dem gesamten AK Strey danke ich für ein sehr gutes kollegiales und freundschaftliches Klima. Ganz besonders möchte ich hier Dr. Judith Wölk, Dr. Michael Schwan, Dr. Jan Wedekind, Dr. Tobias Foster, Dr. Thomas Wielpütz, Guram Chkonia, Alexandra Manka und Michael Meyer erwähnen.

Aus dem Arbeitskreis in Lund danke ich Ingrid Åslund für ihre Unterstützung bei den NMR Auswertungen, Bruno Medronho für die wissenschaftliche Hilfe und sportliche Unterstützung. Außerdem danke ich meinen Labornachbarn Irem Nasir, Stephane Douzane, und ganz besonders möchte ich Bruno Silva, Sanja Bulut, Agnieszka Nowacka, Nina Reichelt, Ana Sverino, Laura Mazzaferro, Gabriel Rata hervorheben...

Ganz besonders danke ich meiner Mama für die grenzenlose Unterstützung in jeder Hinsicht und Ihrem Mann Saša. Mamas sind die einzigartigste, beste Erfindung dieser Welt!!

Hanne und Peter möchte ich besonders dafür danken, dass sie so tolle Omi und Opi sind! Durch die Hilfe von beiden ist es erst möglich gewesen diese Arbeit zeitnah fertig zu stellen.

Omi und Opi danke ich für die viele Unterstützung durch Verständnis und Liebe.

Meinem Mann und allerbesten Freund, Marcel, der mit mir seit 13 Jahren durch dick und dünn geht und immer für mich da ist. Mit großer Vorfreude auf unsere gemeinsame Zukunft und Familie mit Lennox!

Diese Arbeit würde von der *International Helmholtz Research School of Biophysics and Soft Matter* (IHRS BioSoft) finanziert. Der Auslandsaufenthalt wurde vom *Deutschen Akademischen Austausch Dienst* (DAAD) finanziert.

TABLE OF CONTENTS

1	INTRODUCTION.....	1
1.1	<i>Complex Fluids & Self-Assembly in Binary Systems.....</i>	1
1.2	<i>Task Description.....</i>	7
2	BASIC THEORIES.....	9
2.1	<i>Surfactants and Self-Assembly.....</i>	9
2.2	<i>Aggregation</i>	11
2.3	<i>Binary Systems.....</i>	15
2.4	<i>Pseudo Binary Systems</i>	19
2.5	<i>Curvature of Amphiphilic Film</i>	22
2.6	<i>Bending Rigidity of Amphiphilic Film</i>	25
2.7	<i>Temperature Jumps (T – Jumps).....</i>	29
3	EXPERIMENTAL TECHNIQUES	31
3.1	<i>Phase Behavior.....</i>	31
3.2	<i>Dynamic Light Scattering.....</i>	33
3.3	<i>Small Angle Neutron Scattering.....</i>	39
3.4	<i>Freeze Fracture Electron Microscopy.....</i>	44
3.5	<i>Nuclear Magnetic Resonance.....</i>	49
4	PHASE BEHAVIOR AND MICROSTRUCTURE.....	59
4.1	<i>Phase Diagrams.....</i>	59
4.2	<i>Structure Determination with Dynamic Light Scattering</i>	68
4.3	<i>Small Angle Neutron Scattering.....</i>	78
4.4	<i>Imaging of Lamellar-, Sponge- and Vesicle Phase</i>	100
4.5	<i>Nuclear Magnetic Resonance Experiments</i>	114
5	DISCUSSION.....	131
6	SUMMARY & CONCLUSION.....	143
7	APPENDIX.....	147
8	TABLES.....	161

1 INTRODUCTION

1.1 COMPLEX FLUIDS & SELF-ASSEMBLY IN BINARY SYSTEMS

Complex fluids are liquids that contain mesoscopic structures with length scales of several nanometers to a few micrometers. For decades, physicists have been studying complex fluids such as polymers, liquid crystals and colloids¹. Colloids are small solid particles, typically with a diameter in the micrometer range. In a colloid one substance is finely divided and distributed evenly (relatively speaking) throughout another substance². Both the dispersed and the continuous phase can be a solid, a liquid, or a gas. Commonly encountered examples of colloids are smoke (solid particles dispersed in air), fog (small liquid droplets dispersed in air), paints (small solid particles dispersed in liquid), gels (polymer molecules which, when dissolved in solvent, confer a semisolid structure to the solution), bones (small particles of calcium phosphate dispersed in a solid matrix of collagen) and emulsions, as *e.g.* milk (liquid fat dispersed in an aqueous phase) or butter, (water dispersed in a continuous fat phase)³. Emulsions are, in general, thermodynamically unstable and thus do not form spontaneously. Energy input through shaking or stirring are needed to form an emulsion. With time emulsions phase separate via coalescence and Ostwald ripening processes. In order to increase the kinetic stability of an emulsion emulsifiers which decrease the interfacial tension between the two immiscible liquids are often added to the formulation.

¹ G. Gompper, J. K. G. Dhont, D. Richter, *Physik in unserer Zeit*, **Januar**, 12 (2003).

² G. Gompper, U. B. Kaupp, J. K. G. Dhont, D. Richter, R. G. Winkler, *Physics meets Biology; From Soft Matter to Cell Biology*, eds., Jülich (2004).

³ D. Myers, *Surfaces, Interfaces, and Colloids: Principles and Applications*, 2nd ed.. Wiley: NY (1999).

Contrary to the emulsions, microemulsions are thermodynamically stable, macroscopic homogeneous and nanostructured mixtures of at least the three components: water, oil and surfactant^{4,5,6}. The thermodynamic stability of microemulsions derives from the adsorption of surfactant molecules at the water/oil – interface, which causes a dramatic decrease of interfacial tension to effectively zero^{7,8,9}. Therewith thermal energy “ $k_B T$ ” is sufficient to disperse the incompatible solvents into each other^{10,11}. The resulting nanostructure of microemulsions has been investigated since 1980’s. Besides spherical micelles also bicontinuous structures were proposed¹² and finally proven by *Strey et al.*^{13,14} with freeze fracture electron microscopy and by *Lindman et al.*¹⁵ by diffusion-NMR. These nanostructures with typical length scales of 1 to 100nm are formed by the surfactant molecules building up an extended amphiphilic film. *Strey et al.*^{16,17} and others¹⁸ were able to describe the main properties of microemulsions considering the bending energy of these amphiphilic monolayers. However, the bending energy concept was already proposed in the 1970’s by *Helfrich*¹⁹, who used the model to predict the shape of vesicles and, perhaps, red blood cells. Due to their special properties microemulsions are nowadays used in several applications, *e.g.* cosmetics and pharmacology (microcapsules, liposomes, vesicles), but also in oil production industry, varnishes, as detergent. In general but also for technical applications it is essential to understand the complex phase behavior of microemulsions.

*Kahlweit and Strey*²⁰ could show that a general insight into the phase behavior of an unknown system is facilitated by considering the phase behavior of the systems representing the faces of the appropriate phase space^{6,20}. In the case of a ternary system one has to consider the diagrams of three binary systems forming the faces of the prism. Because of its great variety of *self-assembled* structures^{21,22,23} formed on the nano-scale the binary

⁴ J. H. Schulman, W. Stoeckenius, L. M. Prince, *J. Chem. Phys.* **63**, 1677 (1959).

⁵ M. Kahlweit, R. Strey, *Angewandte Chemie. International Edition in English* **24**, 654 (1985).

⁶ T. Sottmann, R. Strey, in *Fundamentals of Interface and Colloid Science*, edited by J. Lyklema (Elsevier Academic Press, Heidelberg, 2005).

⁷ J. Hao, Z. Yuan, W. Liu, H. Hoffmann, *J. Phys. Chem. B.* **108**, 5105 – 5112 (2004).

⁸ T. Sottmann, R. Strey, *J. Chem. Phys.* **106**, 8606 (1997).

⁹ T. Sottmann, R. Strey, *Tenside Surfactants Detergents* **35**, 34 (1998).

¹⁰ M. Volmer, *Z. Phys. Chem.* **125**, 151 (1927).

¹¹ M. Volmer, *Z. Phys. Chem.* **206**, 181 (1927).

¹² L. E. Scriven, *Nature* **263**, 123–125 (1976).

¹³ W. Jahn, R. Strey, in *Physics of Amphiphilic Layers*, Ed. J. Meunier, D. Langevin, N. Boccardo, *Proceedings in Physics*, vol. 21, Springer, Berlin Heidelberg, 353 (1987).

¹⁴ W. Jahn, R. Strey, *J. Phys. Chem.* **92**, 2294 (1988).

¹⁵ P. G. Nilsson, *J. Phys. Chem.* **88**, 4764-69 (1988).

¹⁶ R. Strey, *Colloid and Polymer Science* **272**, 1005 (1994).

¹⁷ T. Sottmann, R. Strey, S. H. Chen, *J. Chem. Phys.* **106**(15), 6483 (1993).

¹⁸ R. Wagner, R. Strey, *Langmuir* **15** (4), 902 (1999).

¹⁹ W. Helfrich, *Z. Naturforsch.* **28 C**, 693 (1973).

²⁰ M. Kahlweit and R. Strey, *Angew. Chem.* **97**, 655-669 (1985).

²¹ G. G. Chernik, *Curr. Opin. Colloid Interface Sci.* **4**, 381 (2000).

²² B. Jönsson, B. Lindman, K. Holmberg, B. Kronberg, *Surfactants and Polymers in Aqueous Solution*, 2nd ed.; John Wiley & Sons: NY (2003).

²³ D. J. Mitchell, G. J. T. Tiddy, L. Warning, T. Bostock, M. P. Mc Donald, *J. Chem. Soc., Faraday Trans.* **79**, 975 (1983).

water - surfactant system is the most interesting. Starting with *McBain et al.*²⁴ who investigated the phase behavior of water - potassium oleate in 1926, numerous studies dealt with water - soap systems. To mention some of the groups: *Ekwall*²⁵, *Tiddy*²⁶, *Lang* and *Morgan*²⁷ and *Laughlin*²⁸.

The first investigations of binary water - non-ionic surfactant systems were performed in 1967 by *Clunie et al.*²⁹ and a systematic overview of binary water - non-ionic surfactant systems was given in 1983 by *Mitchell et al.*³⁰. Especially appropriate surfactants to study these binary systems systematically are *n*-alkylpolyglycoethers (C_iE_j). It turned out that the properties of these systems can easily be controlled tuning the number *i* of carbon atoms in the hydrocarbon chain and the number *j* of ethylene oxide units in the head group. $H_2O - C_iE_j$ systems show an upper miscibility gap and above the *cmc* the surfactant molecules self-assemble into micelles. Furthermore at high surfactant concentrations often liquid crystalline phases^{26,27,30}, such as the hexagonal phases H_1 and H_2 , cubic phases, having different topologies (I_1, V_1, V_2), and the lamellar phase L_α occur.

With increasing amphiphilicity, *e.g.* increasing both the length of the hydrocarbon chain and the size of the headgroup of the non-ionic surfactant, dilute lamellar phases, as well as dilute sponge phase L_3 , are stabilized^{31,32,33}. A systematic study of these diluted bilayer phases is performed in 1990's by *Strey*¹⁸. By increasing the length *i* of the hydrocarbon chain further an additional bilayer structure, the vesicular phase appears in form of an island within the region of the lamellar phase L_α . Contrary to L_3 , that shows birefringence under shear, colored streaks can be observed between crossed polarizer's, if a vesicular phase is sheared. The vesicular phase, denoted L_α^+ , appears bluish in scattered and brownish in transmitted light. This L_α^+ phase was found by *Jonströmer and Strey*³⁴ in the water - $C_{12}E_4$ and water - $C_{12}E_3$ systems but also in non-ionic multi-component mixtures ($H_2O/NaCl + C_{12}E_5$, $H_2O - C_{12}E_5/ C_6E_0$, $H_2O - C_{12}E_5/ C_{12}E_3$ and $H_2O - C_{12}E_5/ C_{14}E_5$). In 1996 the L_α^+ phase of the $H_2O - C_{12}E_4$ system was pictured with freeze fracture electron microscopy³⁵. In the same year, normal vesicles in the $H_2O - C_{12}E_4$ system, having radii in the order of 100nm, and reverse vesicles in the $H_2O - n$ -decane - $C_{16}E_6/ DKE$ system, with radii of 20 -

²⁴ J. W. McBain, J. W. Elford, *J. Chem. Soc.* **421** (1926).

²⁵ P. Ekwall, in *Advances in Liquid Crystals*, edited by G. H. Brown, Academic Press, London (1975).

²⁶ G. J. T. Tiddy, *Physics Reports* **57**, 1 (1980).

²⁷ J. C. Lang, J. C. Morgan, *J. Chem. Phys.* **73**, 5849 (1980).

²⁸ R. G. Laughlin, *The Aqueous Phase Behavior of Surfactants*, Academic Press, New York (1994).

²⁹ J. S. Clunie, J. M. Corkill, J. F. Goodman, P. C. Symons, J. R. Tate, *Trans. Faraday Society* **63** (359P), 2839 (1967).

³⁰ D. J. Mitchell, *J. Chem. Soc. Faraday Trans. 1* **79**, 975-1000 (1983).

³¹ R. Strey, R. Schomäcker, D. Roux, F. Nallet, and U. Olsson, *J. Chem. Soc. Faraday T.* **86** (12), 2253 (1990).

³² R. Strey, W. Jahn, G. Porte, and P. Bassereau, *Langmuir* **6** (11), 1635 (1990).

³³ C. Stubenrauch, S. Burauer, R. Strey, C. Schmidt, *Liq. Cryst.* **31** (1), 39 (2004).

³⁴ M. Jonstromer, R. Strey, *J. Phys. Chem.* **96** (14), 5993 (1992).

³⁵ R. Strey, *Berichte Der Bunsen-Gesellschaft-Physical Chemistry Chemical Physics* **100** (3), 182 (1996).

30nm, were investigated using the ^1H – NMR self-diffusion technique³⁶. In the case of normal vesicles, the water solvent is found to exchange rapidly between the inside and outside of the vesicles, while in the reverse vesicle case either a fast or a slow exchange, depending, on the oil and the bilayer composition was observed. Furthermore, a number of publications study the formation of multi lamellar vesicles (MLV's) by shearing the lamellar phase of water – non-ionic surfactant systems^{37,38,39,40}. *Richtering and co-workers*⁴¹ investigated in 2001 the effect of shear on the lamellar phase in water - C_{10}E_3 system. They determined the microstructure by means of dynamic light and small angle neutron scattering (DLS and SANS) experiments and presented a so-called dynamic phase diagram of the water - C_{10}E_3 system. Moreover in the same year *Richtering and co-workers*⁴² examined the influence of ionic surfactant SDS on the water - C_{10}E_3 system with SANS and found out that firstly the long range orientational order and secondly the shear viscosity are increased when SDS is added.

The research on vesicles made of non-ionic surfactants currently concentrates on membranes decorated with polymers. In 2008 *T. dos Santos et al.*⁴³, studied the influence of the hydrophobically modified telechelic polymer HM-PEG on vesicles formed in the water - C_{12}E_4 surfactant system. They showed via NMR self diffusion measurements that gel-like mixtures of polymer and vesicles are found to associate in network domains. 2009 *Fujii et al.*⁴⁴ investigated the influence of the triblock copolymer poly(ethylene oxide)₂₀-b-poly(propylene oxide)₇₀-b-poly(ethylene oxide)₂₀ (Pluronic P123) on shear-induced vesicle formation from the lamellar phase in H_2O – C_{10}E_3 system by means of rheology, SANS and microscopy. They found that the MLV's formed are less stable than the ones induced by shearing the polymer-free system⁴⁴.

In general, vesicles are known since many years. In the 1920's, the colloidal behavior of lipid dispersions which consist mainly of lipid double layer structures were studied by *Gordel et al.*⁴⁵. In the 1950's, *Saunders et al.*⁴⁶ reported on vesicles formation by sonication of a lecithin sol, but they called them "micelles". Later, *A. D. Bangham*⁴⁷ named vesicles which are formed by lipid double layers, liposomes. During the 1970's, the packing potential of

³⁶ U. Olsson, K. Nakamura, H. Kuniieda, and R. Strey, *Langmuir* **12** (12), 3045 (1996).

³⁷ B. Medronho, S. Fujii, W. Richtering, M. G. Miguel, U. Olsson, *Colloid Polym Sci* **284**(3):317–321 (2005).

³⁸ B. Medronho, M. G. Miguel, U. Olsson, *Langmuir* **23**(10),5270–5274 (2007).

³⁹ B. Medronho, S. Shafaei, R. Szopko, M. G. Miguel, U. Olsson, C. Schmidt, *Langmuir* **24**, 6480–6486 (2008).

⁴⁰ K. Miyazaki, Y. Kosaka, Y. Kawabata, S. Komura, T. Kato *J. Appl. Cryst.* **40**, 332–334. (2007).

⁴¹ T. D. Le, U. Olsson, K. Mortensen, J. Zipfel, W. Richtering, *Langmuir* **17**, 999–1008 (2001).

⁴² F. Nettesheim, J. Zipfel, P. Lindner, W. Richtering, *Colloids and Surfaces A: Physicochem. Eng. Aspects* **183-185**, 563-574 (2001).

⁴³ T. dos Santos, B. Medronho, F. E. Antunes, B. Lindman, M. Miguel, *Colloids and Surfaces A: Physicochem. Eng. Aspects* **319**, 173-179 (2008).

⁴⁴ S. Fujii, S. Koschoreck, P. Lindner, W. Richtering, *Langmuir* **25**(10), 5476-83 (2009).

⁴⁵ E. Gordel, F. Grendel, *J. Exp. Med.* **41** (1925).

⁴⁶ L. Saunders, J. Perrin, D. Gammack, *J. Pharm. Pharmacol* **14** (1962).

⁴⁷ A. D. Bangham, R. W. Horne, *J. Mol. Biol.* **8**, 660 (1961).

these liposomes was recognized by Gebicki *et al.*^{48,49}. Embedding drugs into the inner part of vesicles^{50,51}, a controlled release of drugs could be established. Another step was made in the 1980's, where investigations were focused on applications requiring the injection of liposomes into the blood circulation, and the delivery of drugs directly to the specific location⁵² in the human body, *e.g.* for the treatment of tumors.

The systematic study of vesicles formed by surfactant bilayers started in the 1980's. With regard to the molecular structure, several main classes of surfactant molecules forming vesicles can be distinguished⁵³: first, vesicles made of ionic surfactants, in most cases double-chain^{54,55,56} dialkyldimethylammonium surfactants with bromide, chloride hydroxide, acetate, or halide counterions^{57,58}. Second, vesicles formed within aqueous mixtures of oppositely charged surfactants, the so-called catanionic vesicles^{59,60,61} and third, vesicles formed in multi component systems including non-ionic surfactant/co-surfactant/water, and sometimes with a small quantity of an ionic co-surfactant^{62,63,64} or a polymer added aiming at a monodisperse population of vesicles^{65,66,67}. In most cases vesicles^{68,69} are discussed as metastable structures of a high kinetic stability⁷⁰ (but not thermodynamic stability), because their formation usually requires some energy input. They can be formed by common preparation methods, *e.g.*, sonication, electroformation, or extrusion from diluted lamellar dispersions^{71,72,73} constitute the group of surfactant vesicles with incorporated polymers

The search for thermodynamically stable vesicles was in the focus of many studies in the 1990's. However, the problem of spontaneous formation and thus thermodynamic equilibrium can be a difficult issue to reveal experimentally⁷⁴. The coarsening mechanism of

⁴⁸ J. M. Gebicki, M. Hicks, *Chem. Phys. Lipids* **16** (1976).

⁴⁹ M. Hicks, J. M. Gebicki, *Chem. Phys. Lipids* **20** (1977).

⁵⁰ K. Hammond, I. G. Lyle, M. N. Jones, *Colloids Surf. A* **23** (1997).

⁵¹ U. Seifert, K. Berndt, R. Lipowski, *Phys. Rev. A* **44** (1991).

⁵² B. E. Cohen, *Biochim. Biophys. Acta* **857** (1986).

⁵³ E. F. Marques, *Langmuir* **16** (2000).

⁵⁴ A. Martino, E. W. Kaler, *Colloids Surf. A* **99** (1995).

⁵⁵ E. W. Kaler, A. H. Falls, H. T. Davis, L. E. Scriven, W. G. Miller, *J. Colloid. Interface Sci.* **90** (1982).

⁵⁶ R. T. Hamilton, E. W. Kaler, *J. Colloid. Interface Sci.* **116** (1987).

⁵⁷ Y. Talmon, D. F. Evens, B. W. Ninham, *Science* **211** (1983).

⁵⁸ E. F. Marques, A. Khan, M. G. Miguel, B. Lindman, *J. Phys.Chem.* **97**, 4729–36 (1993).

⁵⁹ C. Vautrin, T. Zemb, M. Schneider, M. Tanaka, *J. Phys.Chem. B* **108** (2004).

⁶⁰ D. J. Iampietro, L. L. Brasher, E. W. Kaler, A. Stradner, O. Glatter, *J. Phys.Chem. B* **102** (1998).

⁶¹ L. L. Brasher, K. L. Herrington, E. W. Kaler, *Langmuir* **11** (1995).

⁶² M. T. Yacilla, K. L. Herrington, L. L. Brasher, E. W. Kaler, S. Chiruvolu, J. A. Zasadzinski, *J. Phys.Chem.* **100** (1996).

⁶³ J. Oberdisse, O. Regev, G. Porte, *J. Phys.Chem. B* **102** (1998).

⁶⁴ H. Hoffmann, T. Thunig, D. Miller, *Colloids. Surf. A* **210** (2002).

⁶⁵ M. Gradzielski, M. Bergmeier, H. Hoffmann, M. Mueller, I. Grillo, *J. Phys.Chem. B* **104** (2000).

⁶⁶ D. Robertson, T. Hellweg, B. Tiersch, J. Koetz, *J. Colloid. Interface Sci.* **270** (2004).

⁶⁷ E. F. Marques, *Langmuir* **16**, 4798 (2000).

⁶⁸ O. Regev, F. Guillemet, *Langmuir* **15** (1999).

⁶⁹ L. Rydhag, P. Stenius, L. Oedberg, *J. Colloid. Interface Sci.* **86** (1982).

⁷⁰ M. Gradzielski, *Curr. Opin. Colloid. Interface Sci.* **8** (2003).

⁷¹ R. M. Watwe, J. R. Bellare, *Curr. Sci.* **68** (1995).

⁷² W. Wang, L. Tetley, I. F. Uchegbu, *J. Colloid. Interface. Sci.* **237** (2001).

⁷³ K. Edwards, M. Almgreen, J. Bellare, W. Brown, *Langmuir* **5** (1989).

⁷⁴ S. Šegota, D. Težak, *Advances in Colloid and Interface Science* **121**, 51 (2006).

Ostwald ripening is expected to be very slow in vesicle systems and may even lead to a kinetically trapped size distribution⁷⁵. Still there is a vast number of systems reported in the literature in which vesiculation occurs spontaneously^{74,76}. Such spontaneously formed vesicles may or may not be the equilibrium state⁷⁷. In principle, thermodynamically stable vesicles should⁷⁸: (i) be generated spontaneously, *i.e.* with minimal shearing forces (*e.g.* gentle mixing of components in solution), and in a controlled, reversible way; (ii) be stable in time with respect to size and shape; (iii) have size distributions and be stable independent of the formation path; (iv) be found in equilibrium with other phases, such as solids and lamellar phases, in appropriate multiphase regions. Not all of these criteria are always easily accessed experimentally, but if vesicles form spontaneous and reversibly, attain an invariant size distribution and remain stable, they have essentially the features of equilibrium vesicles.

In the special case of vesicles in binary water – non-ionic surfactant mixtures theoretical descriptions predict instability of vesicles due to the surfactant geometry^{79,80}. But, as already discussed above experiments using freeze fracture electron microscopy (FFEM)³⁵, nuclear magnetic resonance technique (NMR)³⁶ and scattering techniques⁸¹ have confirmed the existence of vesicles in water – C₁₂E₄ system. Even though this system has been extensively studied over the years^{82,83,84,85} there is still no common understanding regarding the equilibrium structure of the vesicular L_α⁺-phase.

⁷⁵ U. Olsson, H. Wennerström, *J. Phys. Chem. B* **106**, 5135 (2002).

⁷⁶ E. W. Kaler, A. K. Murthy, B. E. Rodrigues, J. A. N. Zasadzinski, *Science* **245** (1989).

⁷⁷ D. D. Lasic, R. Joannic, B. C. Keller, P. M. Frederik, L. Auvray, *Adv. Colloid Interface Sci.* **89** (2001).

⁷⁸ E. W. Kaler, K. L. Herrington, A. K. Murthy, J. A. N. Zasadzinski, *J Phys Chem.* **96**, 6698 (1992).

⁷⁹ D. C. Morse, *Phys. Rev. E* **50**, R2423 (1994).

⁸⁰ L. Golubovic, T. C. Lubensky, *Phys. Rev. A* **41**, 4343 (1990).

⁸¹ S. Müller, C. Börschig, W. Gronshi, C. Schmidt, *Langmuir* **15**, 7558 (1999).

⁸² R. Strey, *Habilitation* (1992).

⁸³ R. Strey, *Ber. Bunsenges. Phys. Chem.* **100**, 182 – 189 (1996).

⁸⁴ U. Olsson, K. Nakamura, H. Kunieda, R. Strey, *Langmuir* **12**, 3045 – 3054 (1996).

⁸⁵ K. Bryskhe, S. Bulut, U. Olsson, *J. Phys. Chem. B* **109**, 9265 – 9274 (2005).

1.2 TASK DESCRIPTION

The present work is motivated by the two fundamental questions: (i) can vesicles be thermodynamically stable structures in binary water – non-ionic surfactant systems? And (ii) which conditions can lead to spontaneous formation? These topics should be traced studying the binary system $\text{H}_2\text{O} - \text{C}_{12}\text{E}_4$. However, this system was not chosen arbitrarily. It derives from unpublished intriguing observations of *Olsson* and *Strey* made by performing temperature jumps from the L_α to the L_{α^+} phase. They found that without stirring the phase stays anisotropic. After slight and short stirring the anisotropy vanishes and the sample appears brownish in transmitted light, which is typical for the L_{α^+} phase. However a few hours later the phase becomes more reddish in transmitted and bluish in scattered light. Furthermore the size of the formed vesicles seems to be correlated with the bilayer repeat distance within the lamellar phase, since the samples become increasingly bluish with decreasing surfactant concentration.

In order to elucidate these intriguing observations the phase behavior of the respective binary system $\text{H}_2\text{O} - \text{C}_{12}\text{E}_4$ was to be revisited as a first step. Because the additives NaCl and glycerol (which also increases the viscosity and therefore allows better characterization of L_{α^+} phase by FFEM) are known to increase the vesicle stability also the phase behavior of the systems $\text{H}_2\text{O}/\text{NaCl} - \text{C}_{12}\text{E}_5$ and $\text{H}_2\text{O}/\text{glycerol} - \text{C}_{12}\text{E}_4$ should be investigated. On the basis of the achieved knowledge about phase behavior, in a next step a detailed characterization of the microstructures occurring in the L_{α^+} -phase was planned by using three complementary methods, *i.e.* Dynamic Light Scattering (DLS), Small Angle Neutron Scattering (SANS) and Freeze Fracture Electron Microscopy (FFEM). Such experiments were expected to allow the determination of both the size and shape of structures existing in the L_{α^+} phase as function of the surfactant concentration and temperature. In order to study the thermodynamic stability of the L_{α^+} phase the vesicles should be prepared by positive (L_1 to L_{α^+}) and negative (L_3 and L_α to L_{α^+}) temperature-jumps as well as by other preparation methods (gently stirring, shearing and vortexing the L_{α^+} phase). Furthermore, deuterium Nuclear Magnetic Resonance (^2H -NMR) were to be applied to yield additional information concerning the structure of the lamellar phase and vesicles at higher surfactant concentrations.

This thesis is organized as follows: in chapter 2 the basics of the phase behavior of binary water – non-ionic surfactant systems including bilayer structures will be described. In chapter 3 a short description of the experimental techniques used in this work is given.

The results will be presented in chapter 4 followed by the discussion in chapter 5. A summary of the obtained results in chapter 6 brings this work to an end.

2 BASIC THEORIES

For the understanding of this work a series of basic principles is indispensable. Starting with the explanation of surfactants, self-assembly processes and aggregation, phase behavior in binary and pseudo-binary systems will be explained. This chapter ends with the theoretical approach of mono- and bilayers, with emphasis on curvature and bending rigidity of amphiphilic films.

2.1 SURFACTANTS AND SELF-ASSEMBLY

The common feature of complex fluids is the presence of a mesoscopic length scale which necessarily plays a key role in determining the properties of a system, including colloidal suspensions, micellar solutions, surfactant monolayers and microemulsions, vesicles and model cell membranes, and new “soft condensed” materials⁸⁶.

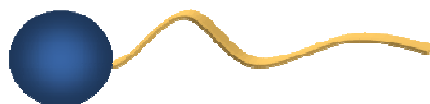


Figure 1: Sketch of a single surfactant molecule, showing the hydrophilic head group (blue) and the hydrophobic tail (yellow).

⁸⁶ W. M. Gelbart, A. Ben-Shaul, *J. Phys. Chem.* **100**, 13169, (1996).

In mixture with solvent of some kind (*e.g.* water) amphiphilic molecules, substances whose molecule consists of two distinctly different moieties one which is water-loving (hydrophilic) part and the other one which is water-hating (hydrophobic) part (Figure 1), spontaneously self-organize into a variety of structures.

The forces that hold amphiphilic molecules in self-assembled structures together are not due to strong covalent or ionic bonds but arise from weaker *Van der Waals*, hydrophobic, hydrogen-bonding, and screened electrostatic interactions. Thus if the solution conditions, such as electrolyte concentration or simply the temperature are changed they will have an effect on the structures built. Those will not only affect the interactions between the aggregates but they will also affect the forces between the molecules within each aggregate, thereby modifying the size and shape of the structures themselves. It is therefore necessary to begin by considering the factors that determine how and why certain molecules associate into various well-defined structures. Surfactants (surface active agents) are a class of amphiphilic compounds⁸⁷. A surfactant can be classified by the presence of formally charged groups in its head group. A *non-ionic* surfactant has no charge groups in its head. The head of an ionic surfactant carries a net charge. If the charge is negative, the surfactant is more specifically called *anionic*; if the charge is positive, it is called *cationic*. If a surfactant contains a head with two oppositely charged groups, it is termed *zwitterionic*. In ionic surfactants the presence of the counterions provides the neutrality of the surfactant molecule. The hydrophobic chain can be single or double chain of various length and can be branched, saturated or unsaturated^{88,89}.

For all further discussions only non-ionic surfactants of type *n*-alkylpolyoxyethylene ether (C_iE_j) will be considered, because of relevance for this thesis.

⁸⁷ J. Goodby, G. W. Gray, H. W. Spiess, V. Vill, D. Demus, *Handbook of Liquid Crystals* **3**: 341 – 392, Wiley-VCH (1998).

⁸⁸ A. M. Figueiredo Neto, P. Tolédano, *Phase Transitions in Complex Fluids*, World Scientific (1998).

⁸⁹ M. C. Holmes, *Current Opinion in Coll. And Interf. Sci.* **3** (1998).

2.2 AGGREGATION

Amphiphilic self-assembly processes are: spontaneous, characterised by start-stop features and they produce aggregates with well-defined properties. To characterize the amphiphilic aggregation process, we can begin by considering how adding surfactant to water leads to the formation of this typical structures^{90,91}. By adding a few surfactant molecules to water they disperse and are present as monomers up to a concentration where they start to aggregate. This concentration is specific for each surfactant and is called critical micelle concentration (*cmc*), because micelles are the first aggregates that form in a water/amphiphile mixture. In order to form micelles, the chains must be flexible and this only occurs above a certain temperature (when the solubility of the surfactant is equal to *cmc*) called *Krafft temperature* (T_K). Thus, the formation of micelles occurs when both conditions are met: the temperature is above the *Krafft temperature* and the concentration of surfactant in solvent is above the *cmc*. At *cmc* the fraction of surfactant building monomers is the same as the fraction of surfactants building aggregates. The number of monomers will stay the same during further increase of surfactant concentration. Adding more surfactant to the binary mixture, elongated or wormlike micelles start to form until the aggregates pack into networks. With even further increase of surfactant concentration lamellae (and other lyotropic mesophases) are built. Thus, the second parameter that influences aggregation due to the surfactant concentration is the temperature⁹⁰. At low temperatures water hydrates the hydrophilic head groups of the surfactant (non-ionic, C_iE_j) and therefore this head groups seem virtually bigger and occupy more space at the interfacial film while hydrophobic tails size remains the same. This is why we have micelles not only at low surfactant concentrations but at low temperatures as well. At higher temperatures the hydrophilic head groups are less hydrated due to *Brownian* motion of water molecules. The interfacial film is now curved the other way around. The higher the temperature is water becomes a less good solvent.

⁹⁰ D. Fennell Evans, H. Wennerström, *The colloidal Domain - Where Physics, Chemistry, Biology and Technology meet*- 2nd, VCH Publishers, Inc.: NY (1994).

⁹¹ J. N. Israelachvili, *Intermolecular and Surface Forces*, Academic Press (1985).

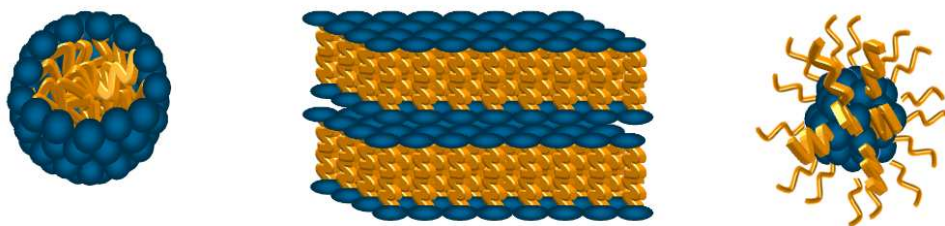


Figure 2: Schematic drawing of surfactant aggregates (micelle, lamellar structure and inverse micelle) forming in water with increasing surfactant concentration and temperature from left to the right.

The number of perturbing (“bound”) water molecules per head group of a non-ionic surfactant molecule depends due to temperature also on surfactant concentration. For total surfactant concentration of 1 mole, w_b and w_f , the numbers of moles of bound and free water per molecule surfactant, are related by

$$w_f = \frac{w_b}{K_A(q - w_b) - w_b} \quad [1]$$

and

$$w_b = \frac{rK_B w_f^r}{K_B w_f^r + (w_f + 1)^r} \quad [2]$$

where q is the number of binding sites per surfactant molecule, r is the number of involved water molecules, K_A and K_B are the equilibrium constants (mole fractions)⁹².

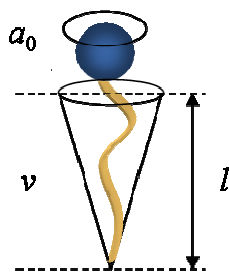
The driving force of surfactant self-assembly is the minimization of energy⁹³. Apart from the requirement of the hydrophobic tail to minimize contact with water, there are two more contributions to the free energy of self-assembly, which is made up of three terms: a *hydrophobic contribution*, a *surface term* (of the hydrocarbons, which on the one hand want

⁹² K. Rendall, J. T. Tiddy, *J. Chem. Soc., Faraday Trans. 1* **80**, 3339 – 3357 (1984).

⁹³ D. F. Evans, H. Wennerström, *The Colloidal Domain: Where Physics, Chemistry, Biology and Technology Meet*; VCH Publishers, Inc.: NY (1994).

to stack closer together in order to minimize water contact and on the other hand the electrostatic repulsion) and a *packing term*, which considers the geometry of the amphiphile. While the first mentioned term, minimization of *hydrophobic interactions* (thermodynamic driving force) is responsible for the *spontaneously* forming of aggregates to form a variety of microstructures, the last two terms (repulsion force) is the limiting force that minimizes the number of molecules that can be packed in an aggregate.

For dilute solutions, where the interaggregate interactions can be neglected, a number called *SURFACTANT PACKING PARAMETER* can be defined as⁹¹:



$$N_s = \frac{v}{la_0} \quad [3]$$

Figure 3: Schematic drawing visualizing the calculation of the surfactant packing parameter N_s , where a_0 is the effective area per head group, v the volume of the hydrophobic part of the surfactant molecule and l the length of the hydrocarbon chain⁹¹.

The presented parameters stand for: the volume v of the hydrophobic part of the surfactant molecule, l is the length of the hydrocarbon chains and a_0 the effective area per head group.

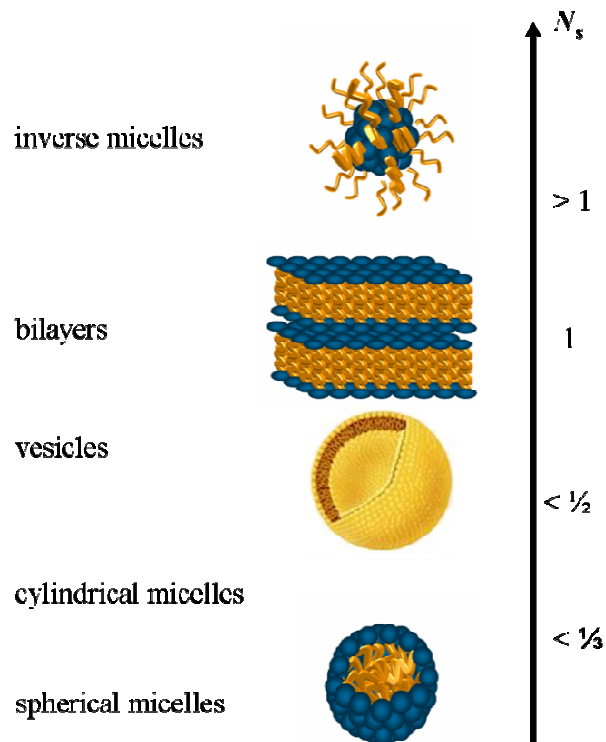


Figure 4: Left: Schematic drawing of some common aggregates, like spherical micelles, vesicles, bilayer sheet and inverse micelles. The packing parameters are: for micelles: $N_s \approx \frac{1}{3}$ for rods $N_s \approx \frac{1}{2}$, for lamellae and big vesicles $N_s \approx 1$, inverse micelles $N_s > 1$.

The surfactant packing parameter relates the properties of a molecule to a preferred curvature of the aggregate formed. Surfactants with big head groups tend to have a lower value of N_s and therefore the aggregates prefer a more curved geometry (micelles: $N_s \approx \frac{1}{3}$, rods: $N_s \approx \frac{1}{2}$, lamellae, vesicles: $N_s \approx 1$).

2.3 BINARY SYSTEMS

Investigation of binary water – surfactant systems already took place in the 1930`s. *McBain*²⁴ determined water – potassium oleate system. In this thesis, the model system used for investigations of surfactant assembly is a non-ionic surfactant system based on *n*-alkylpolyoxyethylene ether. An extensive presentation of basic principles of phase behavior, the interference between molecular structure and phase behavior and aggregates built in binary systems (including liquid crystalline phases) have been given by *Laughlin*²⁸ and *Tiddy*²⁶. Non-ionic surfactant systems with water have been investigated first by *Clunie et al.*²⁹ A systematic overview of phase diagrams of several C_iE_j surfactants varying the hydrophobic and the hydrophilic surfactant characteristics was given by *Mitchell et al.*³⁰.

2.3.1 BINARY SYSTEM $H_2O - C_iE_j$

Generally a phase diagram represents the equilibrium structures of a binary mixture. The phase behavior of a binary system of a non-ionic surfactant in water crucially depends on the surfactant concentration and temperature.

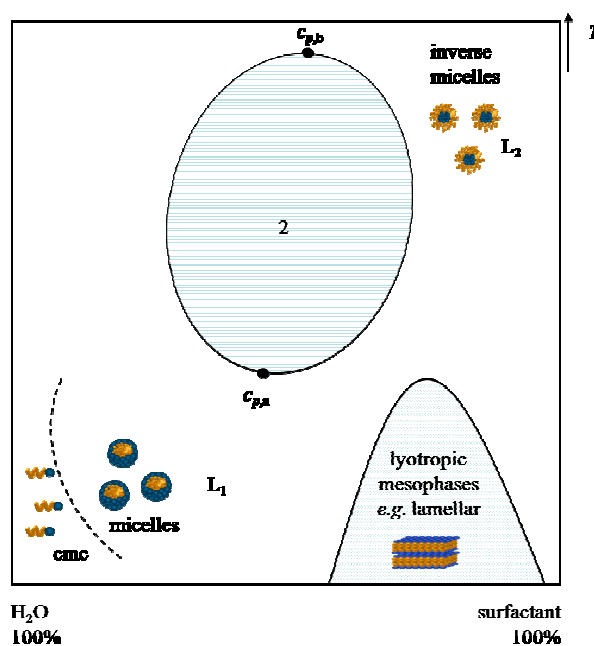


Figure 5: Schematic picture of the temperature dependent phase behavior of the binary system H_2O – non-ionic surfactant. $c_{p,a}$ denotes the lower critical point and $c_{p,b}$ denotes the upper critical point of the upper miscibility gap^{35,94}.

⁹⁴ K. Selber, S. Muller, H. Gieren, J. Thommes, T. Sottmann, R. Strey, R. M. Kula, *Bioseparation* **10**(4-5), 243 (2001).

Generally one finds an upper miscibility gap with a lower critical point at high temperatures. At ambient pressure the critical temperature is mostly below the melting point of the mixture. At ambient temperatures the surfactant solubility in water decreases with increasing temperature. In Figure 5a schematic binary system H_2O – non-ionic surfactant is shown. At low surfactant concentrations the surfactant is monomerically dissolved in water. With increasing surfactant concentration, higher than the *cmc* (critical micelle concentration), micelles form. Then larger aggregates start forming, like cylindrical micelles, until at sufficient high surfactant concentrations networks and then lyotropic mesophases such as lamellar phase occur^{95,96}.

When long chain surfactants are used the phase behavior becomes more complex. Figure 6 shows the schematic phase diagram for such a binary system. At higher surfactant concentrations liquid crystalline phases are built *e.g.* hexagonale phase H_1 and H_2 , cubic phases I_1 , V_1 and V_2 or the lamellar phase L_α ^{26,27,30}.

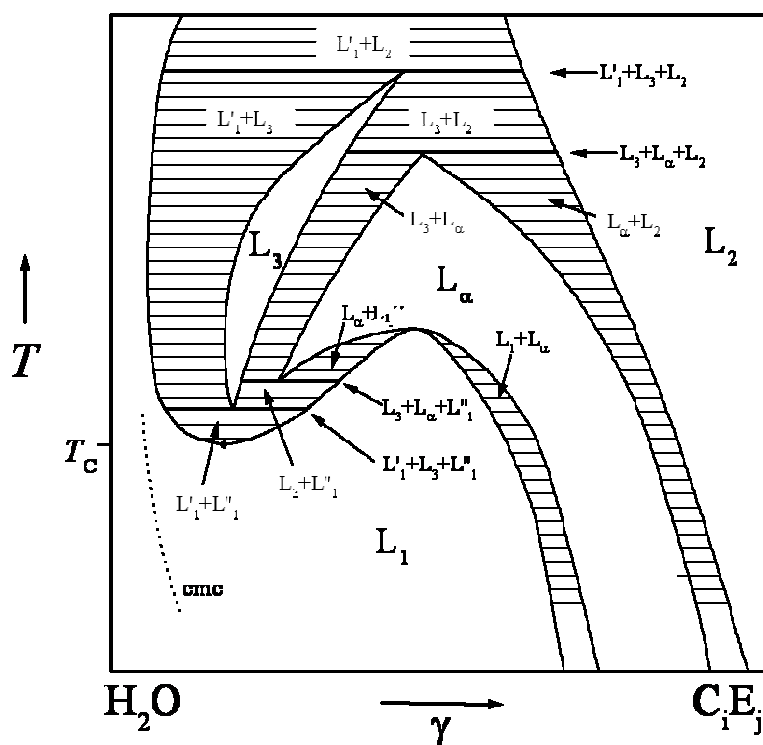


Figure 6: Schematic phase diagram of a binary system of the type $\text{H}_2\text{O} - \text{C}_j\text{E}_j$. The mesophases which appear are the micellar and the inverse micellar phases L_1 and L_2 , the sponge phase L_3 and the lamellar phase L_α . The hatched areas show the coexisting phases within two-phase regions and the bold lines stand for the coexistence of three phases⁹⁷.

⁹⁵A. Bernheim-Groswasser, E. Wachtel, Y. Talmon, *Langmuir* **16**, 4131(2000).

⁹⁶O. Glatter, G. Fritz, H. Lindner, J. Brunner-Popela, R. Mittelbach, R. Strey, S. U. Egelhaaf, *Langmuir* **16**, 8692 (2000).

⁹⁷G. Porte, J. Appell, P. Bassereau, M. Marignan, M. Skouri, I. Billard, M. Delsanti, S. J. Candau, R. Strey, W. Jahn, P. Snabre, *Trends in Colloid and Interface Science V* **84**, 264 (1991).

The grade of extension of lyotropic mesophases strongly depends on the structure of the surfactant. Lamellar phase in systems with long chained, highly structured surfactants tend to overlap with the upper miscibility and can also become stable in the dilute region of the phase diagram. Moreover a number of two-phase regions as well as three phase lines (according to *Gibbs's* phase rule) are built.

Because of their importance for the present work sponge- L_3 , lamellar- L_α and vesicle phase L_α^+ will be described in the following. The L_α phase is, as already mentioned, a liquid crystalline phase being highly viscous at high surfactant concentrations and less viscous at lower surfactant concentrations. Furthermore L_α has a highly ordered smectic structure formed of layers and is therefore anisotropic (Figure 7). In a binary system the water domains are separated by surfactant bilayers. The mean curvature H as well as the *Gauss* curvature K is zero⁹⁸.

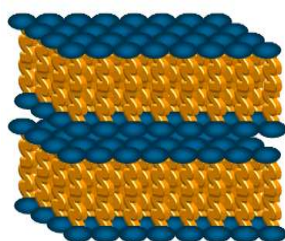


Figure 7: Schematic drawing of a lamellar phase, containing two layers. Between the polar head groups (blue) there is water whereas the tails form the lipophilic region.

The L_3 phase⁹⁹ can be found at very high dilutions. The structure reminds of a sponge or foam consisting of bilayers surrounding water domains. L_3 is optically an isotropic phase, contrary to L_α . Looking through two cross polarizers the L_3 phase can show streaming birefringence. The higher the dilution is the bigger the domains are and L_3 looks opalescent bluish.

⁹⁸ T. Nylander, *Proteins at liquid Interfaces*, Elsevier, 385 (1998).

⁹⁹ P. Ekwall, *Advances in Liquid Crystals*, ed. G. H. Brown, Academic Press: NY, 1, 1 (1975).



Figure 8: Schematic representation of an L_3 sponge phase. The zoomed area shows the bilayer nature of the sponge phase³².

The mean curvature is zero due to the saddle point structure, but Gaussian curvature is slightly negative¹⁰⁰.

In some binary systems, when the surfactant is hydrophobic, as $C_{12}E_4$, bilayer structures in form of vesicles can be found. Vesicles are closed bilayers enclosing a pool of solvent, denoted L_{α}^+ . One can find water domains enclosed in the vesicle respectively surrounding them. Unilamellar vesicles (ULV) consist of only one bilayer, having the mean curvature of zero and being isotropic while multilamellar vesicles (MLV) can consist of many bilayers and at high *cmc* cannot be separated from the lamellar phase L_{α} . Depending on size the L_{α}^+ solutions are less viscous than L_{α} phase and they appear to be reddish⁹⁰.



Figure 9: Schematic representation of a single vesicle. Left: unilamellar vesicle (ULV). Right: multilamellar vesicle (MLV). The number of layers can vary.

2.3.2 BIREFRINGENCE

Birefringence, or double reflection, is the phenomenon by which a ray of light decomposes into two rays (the ordinary and the extraordinary ray) when it passes through optically anisotropic materials¹⁰¹. Additionally, the vibration plane of light is altered. If the

¹⁰⁰ D. Anderson, H. Wennerström, U. Olsson, *J. Phys. Chem.* **93**, 4243 (1989).

¹⁰¹ <http://scienceworld.wolfram.com/physics/Birefringence.html>

material has a single axis of anisotropy, the birefringence phenomenon can be quantified according to:

$$\Delta n = n_o - n_e \quad [4]$$

where n_o and n_e are the refractive indices of the polarization planes perpendicular (n_o) and parallel (n_e) to the major axis of anisotropy. Birefringence is easily seen when an optically anisotropic sample is placed between crossed polarizers. The polarized light coming from the first polarizer will not pass through the second polarizer unless the vibration plane is changed by the sample. This happens if the sample is birefringent and under these conditions it will appear bright against a dark background.

Liquid crystalline phases that occur in binary water – non-ionic systems investigated in the present work, have different refractive indices along different space directions and thus are also optically anisotropic and birefringent. Placing a sample between crossed polarizers provides thus a straightforward way of checking for optically anisotropic liquid crystalline phases. Lamellar (or hexagonal) phases display static birefringence, while sponge and vesicular phases display birefringence under shear.

2.4 PSEUDO BINARY SYSTEMS

When an additive soluble in one of the two components of a binary system is added, we call it a pseudo binary system. Additives like salt or glycerol do have an effect on the phase behavior and this effect will be described in the following paragraph on the exemplary system H₂O/additive – C₁₂E₅.

2.4.1 SALT

Generally one distinguishes between lyotropic and hydrotropic salts. By adding a lyotropic¹⁰² salt to the solution the head group of the surfactant is less hydrolyzed, that is to say the hydrophilicity of the non-ionic surfactant decreases. As a result the phase boundaries shift to lower temperatures. The addition of hydrotropic salts has the opposite

¹⁰² M. Kahlweit, R. Strey, P. Firman, D. Haase, J. Jen, R. Schomäcker, *Langmuir* 4 (3), 499 (1988).

effect^{103,104}, which will not be discussed in this thesis because it is not relevant for the present work. The most conventional lyotropic salt in use is sodium chloride, NaCl. We can quantify the amount of salt in a binary system by using the parameter ϵ

$$\epsilon = \frac{m_{\text{salt}}}{m_{\text{salt}} + m_{\text{water}}} \quad [5]$$

The impact of the lyotropic salt on the phase behavior is shown below.

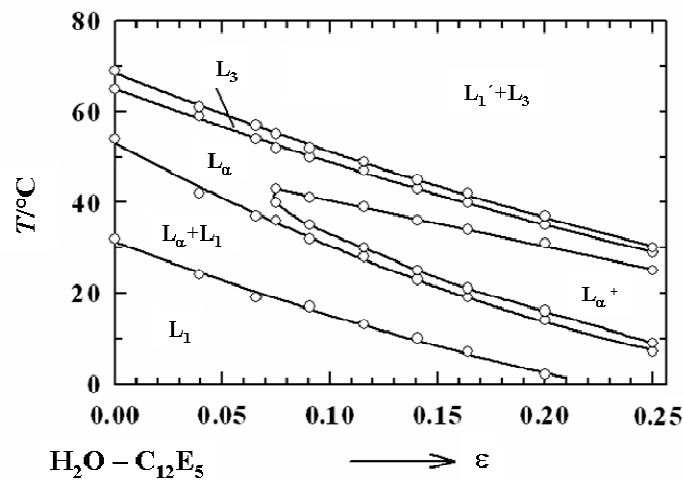


Figure 10: Effect of NaCl on the phase behavior of the binary system $\text{H}_2\text{O} - \text{C}_{12}\text{E}_5$ with $\gamma = 0.02$. With increasing amount of salt the phase transition lines shift to lower temperature⁸³. Moreover, a new phase occurs at $\epsilon = 0.075$, the so called vesicular phase L_{α}^+ .

In Figure 10 the surfactant concentration is kept constant at $\gamma = 0.02$ and only the amount of salt, ϵ , was varied. In the beginning one observes the phase sequence $L_1 \rightarrow L_{\alpha}+L_1 \rightarrow L_{\alpha} \rightarrow L_{\alpha}+L_3$ (not shown in the diagram) $\rightarrow L_3 \rightarrow L_1'+L_3$. Adding NaCl to the system leads to a decrease of temperature in which the initial phase boundaries exist with increasing amount of salt. Furthermore the vesicular phase L_{α}^+ which consists of single- and multilamellar vesicles appears.

¹⁰³ M. Kahlweit, E. Lessner, R. Strey, *J Phys. Chem.* **88** (10), 1937 (1984).

¹⁰⁴ K. V. Schubert, G. Busse, R. Strey, M. Kahlweit, *J Phys. Chem.* **97**, 248 (1984).

2.4.2 GLYCEROL

Glycerol as a hydrophilic component is water soluble and therefore we call it co-solvent. Its addition to the binary system H₂O – surfactant affects the phase behavior due to the competition of both glycerol and surfactant head groups for the water. Figure 11 shows the effect of glycerol on the binary system H₂O – C₁₂E₄. By gradually replacing water by glycerol the phase transition boundaries shift to lower temperatures. ψ stands for the amount of glycerol in the water phase

$$\psi = \frac{m_{\text{glycerol}}}{m_{\text{glycerol}} + m_{\text{water}}} \quad [6]$$

At a $\psi = 0.40$ the L_{α}^{+} phase can be found to exist down to zero degrees. This is, however, a possibility to tune the phase behavior for example in order to use techniques at room temperature.

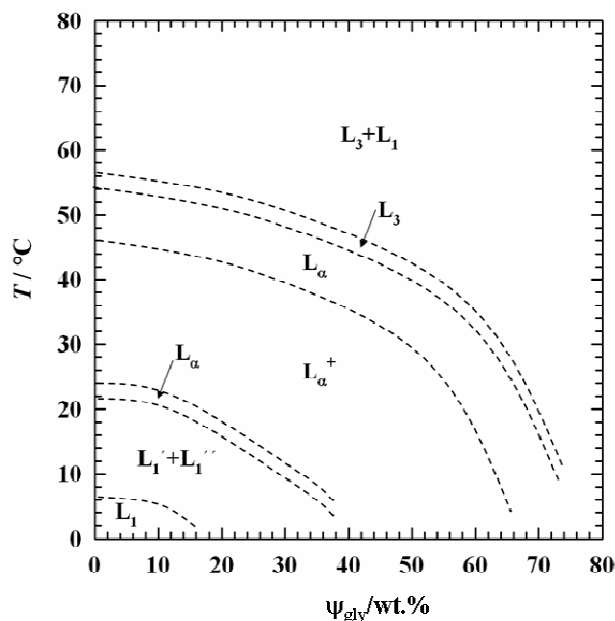


Figure 11: The diagram shows the effect of glycerol on the binary system H₂O – C₁₂E₄ for a constant surfactant concentration $\gamma = 0.02$. Temperature is plotted against ψ (in wt. %), which is the fraction of glycerol in the water/glycerol mixture⁸³.

Furthermore, with increasing amount of glycerol the viscosity ($\eta_{\text{water}}^{20} = 1 \text{ Pa s}$, $\eta_{\text{glycerol}}^{20} = 1480 \text{ Pa s}^{105}$) of the system increases. This leads to slower kinetics.

2.5 CURVATURE OF AMPHIPHILIC FILM

The great variety of structures formed in self-assembled systems like spherical and cylindrical micelles (L_1), lamellar phase (L_α) and sponge phase (L_3), is believed to be a consequence of the variation of the curvature of the amphiphilic interfacial films due to the minimization of the interfacial energy. In order to understand the stability of micelles (L_1) the properties of the surfactant monolayers, for vesicles (here: L_α^+) and lamellar phase (L_α), the properties of the surfactant bilayers (which are presented here in the experiments) must be described for the respective topologies. Helfrich¹⁰⁶ developed the so called *flexible surface model* which gives a theoretical description for both mono- and bilayers in terms of their curvatures and bending energies. This model will briefly be presented here.

The curvature at any point of a two dimensional surface can be described via the principal curvatures c_1 and c_2 , which are reciprocals of the principle curvature radii

$$r_1 = \frac{1}{c_1} \text{ and } r_2 = \frac{1}{c_2}. \quad [7]$$

By convention, a curvature towards a hydrophilic domain is defined as negative and curvature towards a hydrophobic domain accordingly positive. Thus on average, for micelles of surfactant in water and spherical membranes (vesicles) $c_1 = c_2 < 0$, while for the lamellar phase $c_1 = c_2 = 0$ and for saddle-like structures of a sponge phase $c_1 = -c_2$.

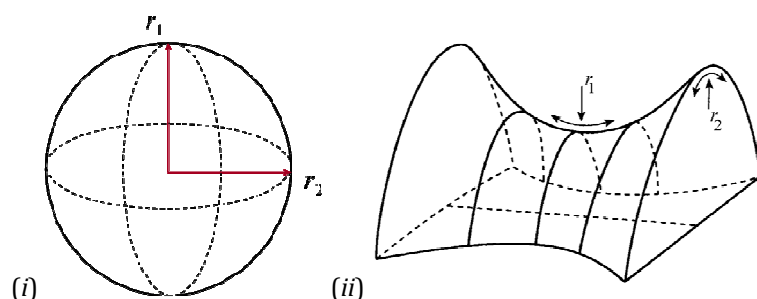


Figure 12: Definition of the principal curvature radii r_i for (i) a sphere, like a micelle or a spherical membrane and sponge-like structure, which can be regarded as an ensemble of saddle-like elements. For a sphere both principal radii have the same sign. For saddle-like element the principal radii have an opposite sign.

¹⁰⁶ W. Helfrich, *Z. Naturforsch.* **28C**, 693 (1973).

The mean curvature H of an arbitrary point on the surface is defined by

$$H = \frac{1}{2} \left(\frac{1}{r_1} + \frac{1}{r_2} \right) = \frac{1}{2} (c_1 + c_2) \quad [8]$$

while the Gaussian curvature K is given by

$$K = \frac{1}{r_1} \cdot \frac{1}{r_2} = c_1 \cdot c_2. \quad [9]$$

The temperature dependence of many properties of self-assembled surfactant systems can be explained by a variation of the mean curvature H of Figure 13. This temperature dependence stems mainly from the interaction of water molecules with ethylene oxide (EO) groups of non-ionic surfactant¹⁰⁷, *i.e.* the hydration of EO-groups decreases with increasing temperature¹⁰⁸. This in turn affects the preferred curvature of the surfactant film, which leads accordingly to different topologies. It could be shown by *Strey et al.*¹⁷, that the mean curvature H of systems of type water - n -alkane - non-ionic surfactant can be described linearly over a large temperature interval according to

$$H = c(\bar{T} - T). \quad [10]$$

where c is the temperature coefficient of curvature and \bar{T} the phase inversion temperature, *i.e.* the mean temperature of the three phase body. Similarly, the development of the principal curvatures is given by

$$c_1 = c(T_u - T) \text{ and } c_2 = c(T_l - T) \quad [11]$$

¹⁰⁷ P. G. Nilsson, B. Lindman, *J. Phys. Chem.* **87**, 4756 (1983).

¹⁰⁸ G. J. T. Tiddy, *Phys. Rep.* **57**, 1 (1980).

with T_u and T_l being the upper and lower temperatures of the three phase body respectively.

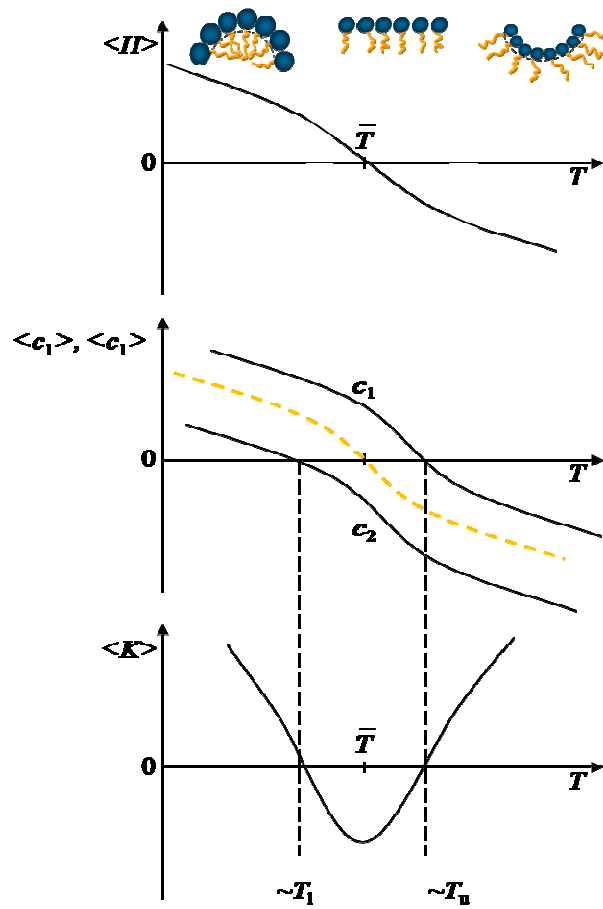


Figure 13: Schematic representation of mean curvature H (top), mean curvature decomposed into the two principal curvatures c_i (center) and Gaussian curvature K (bottom)¹⁷.

2.6 BENDING RIGIDITY OF AMPHIPHILIC FILM

Which curvature is energetically favorable at given temperature is determined by the Helfrich bending energy of the flexible surface model that was originally developed for vesicular lipid membrane structures¹⁹. The general expression of the bending energy E of an area element A is given by

$$dE = \left[\frac{\kappa}{2} (c_1 + c_2 - 2c_0)^2 + \bar{\kappa} c_1 c_2 \right] dA \quad [12]$$

or

$$dE = \left[2\kappa(H - c_0)^2 + \bar{\kappa}K \right] dA \quad [13]$$

with dA being an area element. Therefore three quantities are required to describe the elasticity of the amphiphilic film: c_0 , κ and $\bar{\kappa}$, where c_0 is the spontaneous curvature of the film (a theoretical quantity that signifies a film's minimum energy configuration in the absence of restrictions), κ and $\bar{\kappa}$ are the elastic bending moduli. κ is the rigidity modulus, which quantifies a film's resistance to deformation, and $\bar{\kappa}$ is the saddle splay modulus, which defines its preferred topology of curved surface. Theoretical predictions claim that variation of both moduli κ and $\bar{\kappa}$ can be varied in the borders of $-2 < \bar{\kappa} / \kappa < 0$ ^{79,109}, whereas the values for surfactant monolayers are in the range of $k_B T$. Sottmann *et al.*¹¹⁰ have characterized κ for various non-ionic surfactant systems.

The spontaneous curvature for a monolayer cannot be experimentally determined, but should have a similar dependence on temperature as mean curvature

$$c_{0, \text{mono}} = c(\bar{T} - T). \quad [14]$$

¹⁰⁹ T. Sottmann, R. Strey, *J. Chem. Phys.* **106**, 8606 (1997).

¹¹⁰ T. Sottmann, R. Strey, H.-S. Chen, *J. Chem. Phys.* **106**, 6483 (1997).

All the arguments above ignore the thermal fluctuations of the membranes. The role of membrane fluctuations⁸⁰ can be emphasized by using the scale-dependent reduction of the elastic moduli¹¹¹

$$\kappa_{\text{mono}}(\xi) = \kappa_{\text{mono}} - \frac{\alpha_{\kappa} k_B T}{4\pi} \ln \frac{\xi}{a} \quad [15]$$

and

$$\bar{\kappa}_{\text{mono}}(\xi) = \bar{\kappa}_{\text{mono}} + \frac{\alpha_{\bar{\kappa}} k_B T}{4\pi} \ln \frac{\xi}{a} \quad [16]$$

with the macroscopic length scale $a = v_c/a_c$ that can be related to the effective length of the surfactant molecule in the interface, and $\alpha_{\kappa} = 3$ and $\alpha_{\bar{\kappa}} = 10/3$ ^{112,113,114}. The characteristic structural length ξ is inversely proportional to the surfactant volume fraction ϕ by $\phi \sim a/\xi$. Taking into account, the two “topological persistence length” ξ_{κ} ¹¹⁵ and $\xi_{\bar{\kappa}}$ ¹¹⁶, that were introduced by *De Gennes* and *Taupin*, are defined as the length scales for which $\kappa(\xi_{\kappa}) = 0$ or $\bar{\kappa}(\xi_{\bar{\kappa}}) = 0$, *i.e.*,

$$\xi_{\kappa} = a \exp\left(\frac{4\pi\kappa}{\alpha_{\kappa} k_B T}\right) \quad [17]$$

and

$$\xi_{\bar{\kappa}} = a \exp\left(-\frac{4\pi\bar{\kappa}}{\alpha_{\bar{\kappa}} k_B T}\right) \quad [18]$$

Up to this point surfactant monolayers were considered. In view of the L_3 , L_{α} and L_{α}^+ phases in the binary system water – non-ionic surfactant, the structural properties of bilayers structures have to be extended.

¹¹¹ D. Andelman, M. E. Cates, D. Roux, S. A. Safran, *J. Phys. Chem.* **87**, 7229(1987).

¹¹² L. Peliti, S. Leibler, *Phys. Rev. Lett.* **54** (15), 1690 (1985).

¹¹³ F. David, in *Statistical Mechanics of Membranes and Surfaces*, edited by D. Nelson, T. Piran, S. Weinberg, World Scientific, Singapore (1989).

¹¹⁴ W. Cai, T. C. Lubensky, N. P., T. Powers, *J. Phys II (France)* **4**, 931 (1994).

¹¹⁵ P. G. De Gennes, C. Taupin, *J. Phys. Chem.* **86**, 2294 (1982).

¹¹⁶ G. Porte, J. Appel, P. Bassereau, J. Marignan, *J. Physique* **50**, 1335 (1989).

SURFACTANT BILAYERS

The static picture of a bilayer or membrane structure is that of two identical monolayers fixed opposite to each other. As these two monolayers have an identical solvent on either side the resulting bilayer are locally symmetrical with respect to their midsurface¹¹⁶. If both individual monolayers of such a bilayer have a mean curvature of zero ($H_{mono} = 0$), a planar bilayer is formed. At a level of the midsurface for the bilayer of these lamellar structures, both principal curvatures are zero ($c_1 \approx c_2 \approx 0$) and therefore the mean curvature of the bilayer $H_{bil} = 0$ and the Gaussian curvature of the bilayer $K_{bil} = 0$. For vesicles $c_1 \approx c_2 \neq 0$ is valid. However, the individual monolayers forming the L_3 phase bilayer have a mean curvature towards water with $H_{bil} < 0$. This is a consequence of the smaller area of the bilayer surface at the surfactant head group position compared to the bilayer midplane. When fixed to each other in a planar bilayer each monolayer will feel frustrated¹¹⁷. The frustration of the monolayers can be partially relieved by forming the distorted three-dimensional saddle-shaped structure that has been established for the L_3 phase³². For the bilayers in a dilute L_3 phase the principle curvatures at the midsurface are then small but non-zero and have opposite signs with $c_1 \approx -c_2$. Consequently they still add up to a mean curvature $H_{bil} = 0$, but in contrast to L_α phase, have Gaussian curvature $K_{bil} < 0$.

L_3 as well as L_α and L_α^+ bilayers are locally symmetrical with respect to their midsurface³².

$$\kappa_{bil} = 2 \cdot \kappa_{mono} \quad [19]$$

$$\bar{\kappa}_{bil} = 2 \cdot \bar{\kappa}_{mono} - 8 \cdot \varepsilon \cdot c_{0,mono} \cdot \kappa_{mono} \quad [20]$$

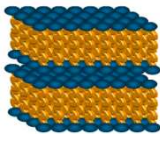
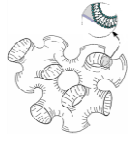

The bilayer thickness $d_{bil} = 2\varepsilon$. The energy spend for bending must therefore be invariant upon changing the signs of both principal curvatures c_1 and c_2 , *i.e.* the spontaneous curvature of the bilayer has a value $c_{0,bil} = 0$. Eq. [13] reduces to

$$dE = \left[\frac{\kappa_{bil}}{2} (c_1 + c_2)^2 + \bar{\kappa}_{bil} K \right] dA \quad [21]$$

¹¹⁷ J. F. Sadoc, J. Charvolin, *J. Phys.* **47**, 683 (1986).

resulting in the elastic bending energy of symmetric bilayers. The lamellar phase is energetically stable only for $\kappa > 0$. For $\kappa < 0$, the flat phase is unstable to the formation of infinite minimal surfaces, *i.e.* sponge phases, with $c_1 \approx -c_2$. While in the other hand for $\kappa < 0$, there is instability towards creating a vesicle phase, with $c_1 \approx c_2$, since vesicle form an almost perfect sphere¹¹⁸. Theoretical approach of vesicle formation in various systems is given by *Morse*¹¹⁶ and *Golubović*¹¹⁹. In Table 1 Mean curvature H , Gaussian curvature K , curvature free energy E and stability of the bilayer morphologies: lamellar-, sponge- and vesicle phase are summarized.

Table 1: Mean curvature H , Gaussian curvature K , curvature free energy E and stability of the bilayer morphologies: lamellar-, sponge- and vesicle phase.

<i>morphology</i>			
H	0	0	$\frac{1}{r}$
K	0	$-\frac{1}{r^2}$	$\frac{1}{r^2}$
E	0	$-\frac{\bar{\kappa}}{r^2}$	$-\frac{1}{r^2}(2\kappa + \bar{\kappa})$
stability	most stable bilayer morphology; $\bar{\kappa} < 0$ and $\bar{\kappa} > -2\kappa$	$\bar{\kappa} > 0$	$\bar{\kappa} < 0$ and $\bar{\kappa} < -2\kappa$

¹¹⁸ C. H. Lee, W. C. Lin, J. Wang, *Phys. Rev. E* **64**, (2001).

¹¹⁹ L. Golubovic, *Phys. Rev. E* **50**, R2419 (1994).

2.7 TEMPERATURE JUMPS (T - JUMPS)

The main focus of this work was the study of the equilibrium structure of the L_{α}^+ phase and therefore temperature jumps (T - jump) from the phases adjacent, (L_{α} phase (below L_{α}^+) and L_1 phase, (L_{α} phase (above L_{α}^+) and L_3 phase) were used as a method to trigger the formation of the L_{α}^+ phase. By doing T - jumps from a maximal stable region of a single, well equilibrated phase like L_{α} , L_1 or L_3 , it is expected to reach the equilibrium structure in an optimal way. ΔT is the driving force of the transition, since temperature determines the monolayer spontaneous curvature c_0 , and thus saddle splay modulus of the bilayers $\bar{\kappa}_{bil}$, which in interaction with bilayer Gaussian curvature K_{bil} , gives the bilayer bending Energy E . Should the structures obtained following complementary opposite temperature jumps be in agreement, this will be an indication for the fact that the vesicular phase is thermodynamically stable.

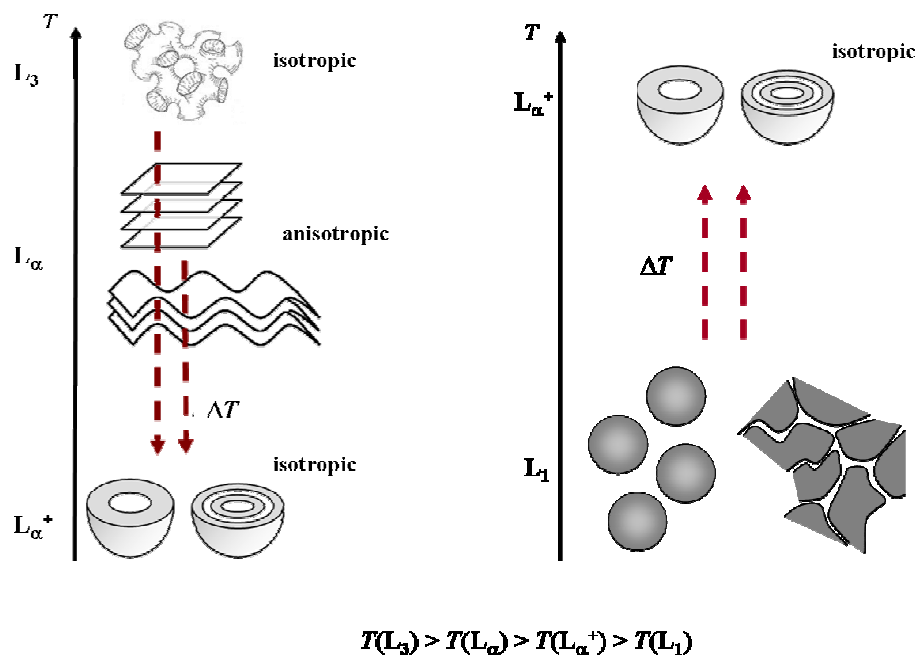


Figure 14: Temperature jump experiments. A schematic overview is given of the temperature jumps that have been performed in the present work. The left picture shows a negative temperature jump from higher temperatures, where the L_3 phase is present, to lower temperatures, where one can find the lamellar phase L_{α} . Jumping to even lower temperatures one reaches a region where vesicles L_{α}^+ exist. Right: The figure on the right side shows the opposite the positive temperature jump where the micellar phase (low surfactant concentrations) and micellar networks (high surfactant concentrations) is shown.

3 EXPERIMENTAL TECHNIQUES

In the following chapter, the basics of experimental techniques employed in this work will be presented. The emphasis is on the information that can be extracted from the technique and on data evaluation, rather than on the comprehensive physical process behind it. The experimental techniques used in this work are phase behavior measurements, dynamic light scattering (DLS), small angle neutron scattering (SANS), viscosity measurements in order to support DLS results, freeze fracture electron microscopy (FFEM) and last but not least deuterium nuclear magnetic resonance ($^2\text{H-NMR}$). The order of the techniques in this chapter is geared to the chronology of the experiments in the lab.

3.1 PHASE BEHAVIOR

In order to characterize the temperature dependent phase behavior of complex fluids phase behavior measurements are used. For sample preparation the substances are weighted in a flat bottom test tube ($V = 17\text{mL}$) with a precision of $\Delta m = \pm 0.001\text{g}$. The order of the weighted components is dependent on the stability and amount of the components. Moreover a stirring bar is added to ensure subsequent sample mixing and homogenization, finally the test tube is closed with a polyethylene stopper. For an adequate protection of light sensitive components *e.g.* D_2O , amber colored test tubes are used. Before the investigation of the phase behavior begins the samples have to be homogenized and the

thermodynamically balance has to be warranted. Since the kinetics of the system to be determined is known stirring and heating for 5 minutes is sufficient.

The determination of phase transitions in a conventional water bath (capacity ~ 10L) is an optical method. For temperature control thermostats (*Haake Company*) are used, for low temperatures below $T = 14^{\circ}\text{C}$ cryostats (*Lauda Company*) are used. Furthermore, the setup consists of a magnetic stirrer (*Heidolph Company*) to ensure an adequate mixing of the sample. As light source special microscopy lamps (*Gerhardt Optik*) are placed behind the setup. The experiment is carried out at atmospheric pressure.

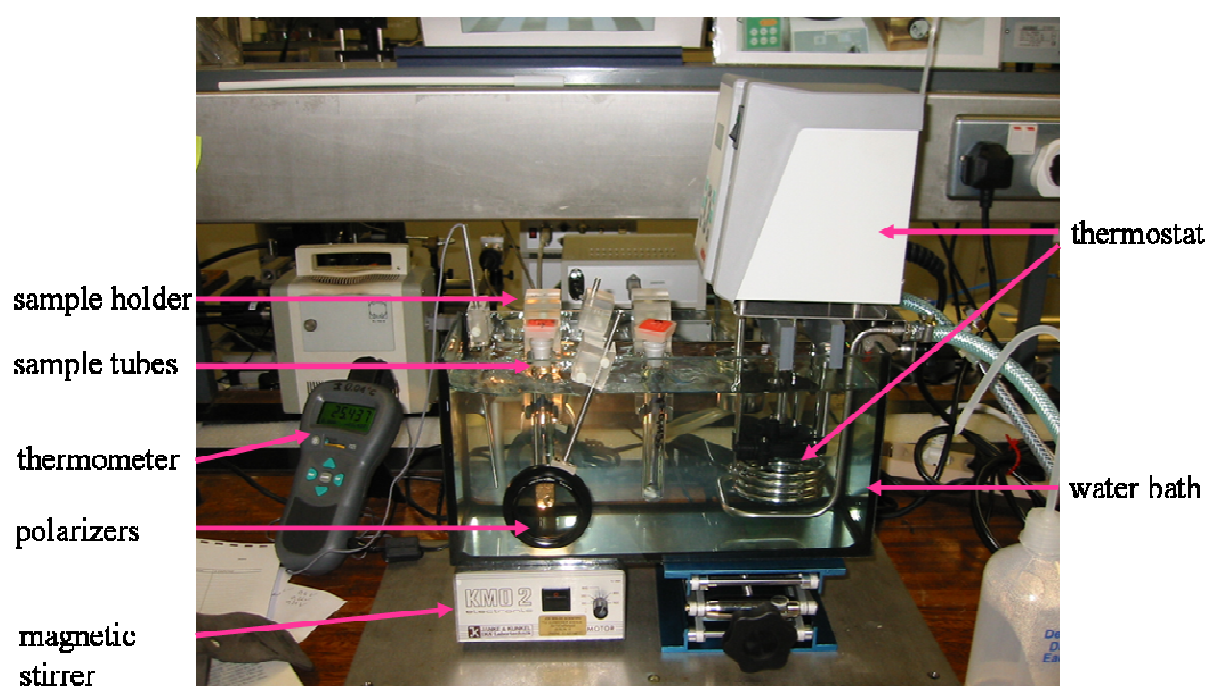


Figure 15: Experimental setup for phase behavior measurements, showing a water bath, thermostat, magnetic stirrer, thermometer, sample holder and sample tubes with a polarizer.

First the test tube with sample inside is placed in the transparent, thermostated water bath (Figure 15) with a temperature control up to $\Delta T = \pm 0.01^{\circ}\text{C}$. While the temperature is varied the sample is stirred until equilibration is reached within the entire sample. Depending on the sample kinetics some minutes up to an hour pass until thermodynamic equilibrium of sample in the water bath is reached. At higher temperatures equilibration time is faster than at low temperatures. The equilibration time also depends strongly on the surfactant concentration. To identify the phases, the sample tube is observed carefully with both transmitted and scattered light, cross polarizers to recognize anisotropic phases were used.

3.2 DYNAMIC LIGHT SCATTERING

Already in the 1960s it had been recognized that the innocent seeming assumption of a *Brownian* process as the underlying process for a solution of scattering particles can be used to estimate the size of the scattering particles to an impressively high degree of accuracy. By analyzing time dependent fluctuations of scattering intensity information of association-, dispersion- and molecular colloids can be obtained. This technique is one of the most popular methods used to determine the size of particles covering structure size range of few nanometers to few microns. The main advantage of dynamic light scattering (DLS) over rival particle sizing techniques is that size information can be obtained on the order of minutes. Furthermore, it is almost completely automated so that routine measurements can be easily reproduced. DLS allows a quantitative coverage of *Brownian* molecular motion in diluted solutions. The interaction of an oscillating electric field like *e.g.* light source, induces an electric dipole momentum at scattering center of particles. The oscillating dipoles emit then electromagnetic radiation independent of directions in the form of scattered light. If no energy transfer takes place one speaks of elastic light scattering.

3.2.1 EXPERIMENTAL SETUP

DLS is also known as Photon Correlation Spectroscopy. Shining a monochromatic light beam, such as a laser, onto a solution with spherical particles in *Brownian* motion causes a *Doppler* shift when the light hits the moving particle, changing the wavelength of the incoming light. This change is related to the size of the particle. It is possible to compute the sphere size distribution and give a description of the particle's motion in the medium, measuring the diffusion coefficient of the particle and using the autocorrelation function. This method has several advantages: first of all the experiment duration is short and it is almost all automatized so that for routine measurements an extensive experience is not required. Moreover, this method has modest development costs.

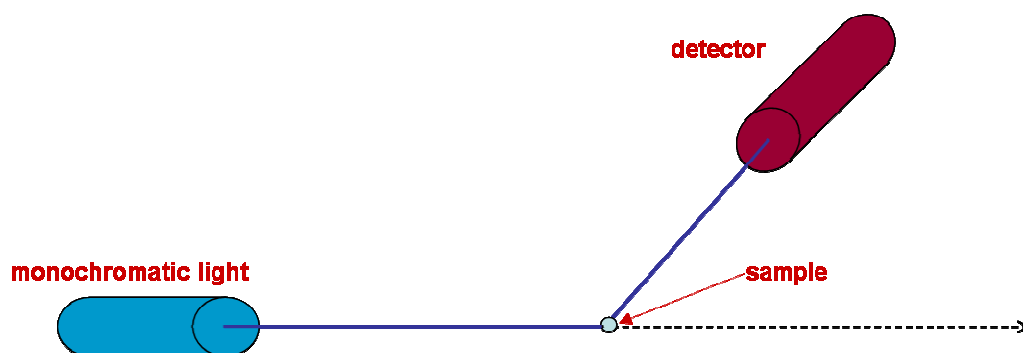


Figure 16: Schematic picture of a DLS setup. A monochromatic light source is sent through the sample and finally the scattered light is detected by a detector.

When a beam of light passes through a colloidal dispersion, the particles or droplets or aggregates in general scatter some of the light in all directions. When the particles are very small compared with the wavelength of the light, the intensity of the scattered light is uniform in all directions (*Rayleigh* scattering); for larger particles (above approximately 250nm diameter), the intensity is angle dependent (*Mie* scattering). If the light is coherent and monochromatic, as from a laser for example, it is possible to observe time-dependent fluctuations in the scattered intensity using a suitable detector such as a photomultiplier capable of operating in photon counting mode. These fluctuations arise from the fact that the particles are small enough to undergo random thermal (*Brownian*) motion and the distance between them is therefore constantly varying. Constructive and destructive interference of light scattered by neighboring particles within the illuminated zone gives rise to the intensity fluctuation at the detector plane which, as it arises from particle motion, contains information about this motion. Particles, emulsions and molecules in suspension undergo Brownian motion. This is the motion induced by the bombardment by solvent molecules that themselves are moving due to their thermal energy. Analysis of the time dependence of the intensity fluctuation - therefore yield the diffusion coefficient of the particles from which, via the Stokes Einstein equation, knowing the viscosity of the medium, the hydrodynamic radius or diameter of the particles can be calculated via Eq. [28].

Typical applications of DLS are the measurement of the size and size distribution of particles and molecules dispersed or dissolved in a liquid. *e.g.*: proteins, polymers, micelles, carbohydrates, nanoparticles, colloidal dispersions, emulsions and microemulsions. The diameter calculated following Dynamic Light Scattering measurements is called the hydrodynamic diameter. The diameter obtained by this technique is that of a sphere that has the same translational diffusion coefficient as the particle being measured. The translational

diffusion coefficient will depend not only on the size of the particle “core”, but also on any surface structure, as well as the concentration and type of ions in the medium. This means that the size can be larger than measured by electron microscopy, for example.

3.2.2 EVALUATION OF DLS DATA

Fluctuations of light intensity gained by *Brownian* molecular motion of particles within the solution are transfused to the digital correlator as photon counting rate.

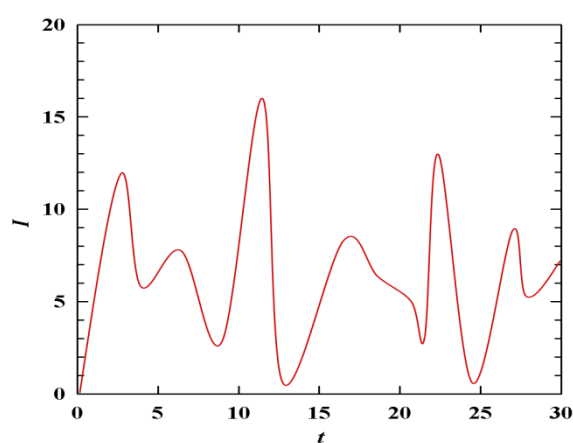


Figure 17: Recorded intensity fluctuation with time (noise diagram). Time is plotted as function of intensity of the signal. The values fluctuate around the mean value.

The digital correlator calculates the basis corrected normed intensity-intensity-autocorrelation function $g^{(2)}(t)$, the so called *Siegert*-correlation

$$g^{(2)}(t) = 1 + Ae^{(-2\Gamma t)} \quad [22]$$

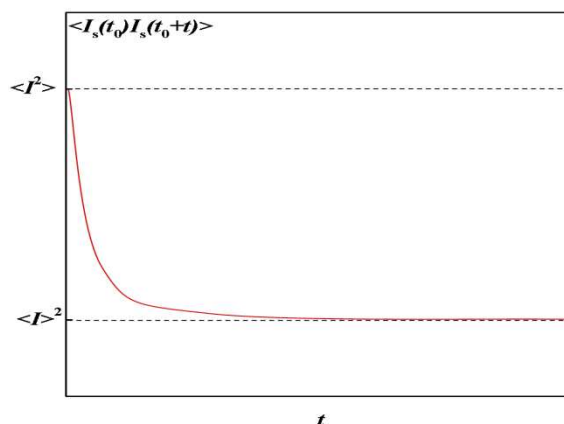


Figure 18: $\langle I \rangle$ and $\langle I^2 \rangle$ plotted against the time. The values of $\langle I \rangle$ and $\langle I^2 \rangle$ can be maximum 2 and minimum 1 (see the Siegert – correlation).

The analysis of exponential relaxation time τ with *Batcon 3* from *Topp* and *Contin* from *Provencher* gives distributions of several reciprocal times. Those are also denoted as line width $\Gamma \sim \tau^{-1}$.

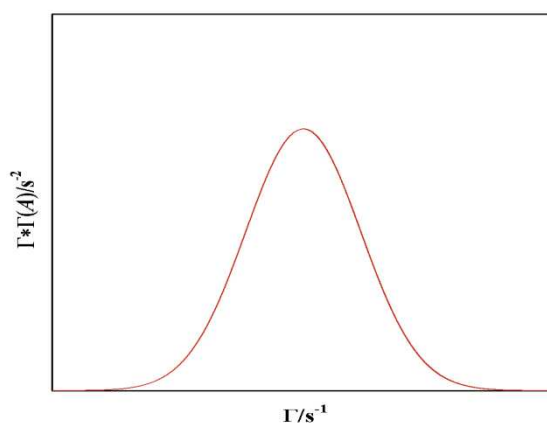


Figure 19: Distributions of several reciprocal times. The line width Γ (measured at half height) is a rate for polydispersity of a solution.

The narrower this distribution is the more monodisperse the particles are. *Landau – Placzek* describes the maximum of line widths Γ

$$\Gamma = Dq^2$$

[23]

whereas q is the absolute value of the scattering vector,

$$q = 4\pi \frac{n_\lambda}{\lambda_0} \sin\left(\frac{\theta}{2}\right) \quad [24]$$

and λ_0 is being the wave length of the incoming beam in vacuum, n_λ being the refractive index of the solvent at each wavelength λ and θ being the scattering angle. The refractive index n_λ of water is dependent on wavelength and temperature.

Assuming that the observed particles are spherical, the diffusion coefficient D can be calculated from *Stokes – Einstein* equation

$$D = \frac{k_B T}{6\pi\eta_{(T)} R_{\text{hydr}}} \quad [25]$$

where k_B is called *Boltzmann* constant, $\eta_{(T)}$ the viscosity of the solvent as function of temperature T . The viscosity of the measured samples was measured with a falling ball viscometer for each concentration and temperature.

Moreover *Contin* calculates half - width distribution, which is the standard deviation of the mean values (σ/μ). The squared value of this term gives the polydispersity index PD.

$$PD = \left(\frac{\sigma}{\mu}\right)^2 \quad [26]$$

When PD is smaller than 0.02 one speaks of a monodisperse sample. A narrow distribution is given when $0.02 \leq PD \leq 0.08$, when $PD > 0.08$ the sample is polydisperse.

The hydrodynamic radius R_{hydr} can be calculated in two ways:

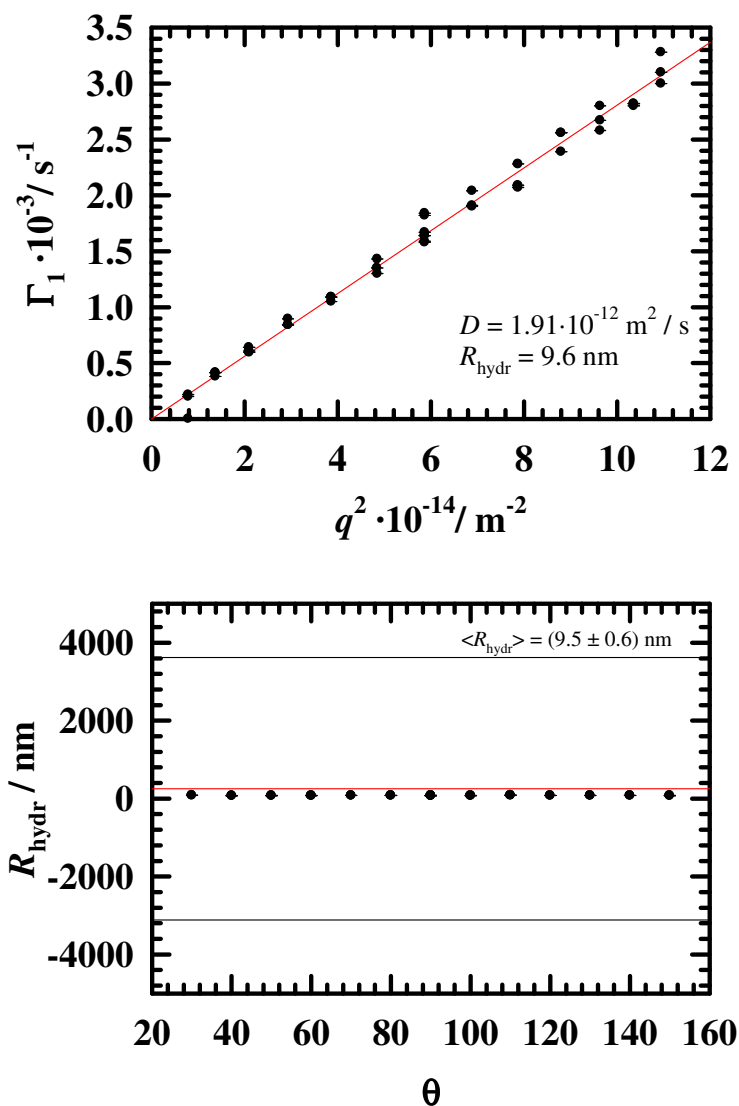


Figure 20: DLS data obtained from an exemplary latex sample with particle size of 9.5nm. The graph above shows the diffusion coefficient $D = 9.97 \cdot 10^{-12} \text{ m}^2 / \text{s}$, the graph beneath shows the hydrodynamic radius $R_{\text{hydr}} = 9.5 \text{ nm}$ plotted against the squared value of wave vector q^2 .

1. The slope of the plot of Γ against q^2 gives the diffusion coefficient D . From *Stokes – Einstein* correlation follows the hydrodynamic radius R_{hydr} . This method is applied to see whether q^2 is linearly dependent on Γ and whether the straight line goes through the origin.
2. A more concrete method is to calculate the diffusion coefficient of each Γ/q^2 – pair of values. Averaged individual values of the hydrodynamic radius can be obtained by Eq. [28].

3.3 SMALL ANGLE NEUTRON SCATTERING

Light-, X-ray- and neutron scattering are applied to determine the structure of binary systems since a long time^{120,121,122,123,124}. In order to determine the structures of colloidal dimensions small angle neutron scattering (SANS) is often the method of choice, because of characteristic length scales. Slow neutrons with a wave length between $\lambda = 1\text{\AA}$ and $\lambda = 40\text{\AA}$ which is in the same range as the internuclear distance in molecules can probe the matter deeply and investigate its volume characteristics as they are not charged. Typical q -range is between $0.001 < q < 1\text{\AA}^{-1}$ and following *Bragg's* law ($q = 2\pi/d$) therefore correspond to a length of 6000\AA to 6\AA . If deuterated substances are used the contrast in binary systems is high and advantageous for SANS measurements. The advantage of neutron to X-ray scattering experiments is that the scattering cross section depends on the characteristics of the atomic nuclei and can be increased specifically by isotope exchange. The large difference in the scattering strength of hydrogen and deuterium allows for contrast matching by selective deuteration (bulk and film contrast). Small angle neutron scattering experiments assume a scattering angle $\theta < 10^\circ$. The experiments in this work were carried out at the Forschungsneutronenquelle *Heinz-Maier-Leibnitz* FRM II in Garching using the instrument KWS-2.

3.3.1 BASIC THEORY

An incident neutron beam can be described via the characteristics of waves and wave functions. Waves are approximately scattered elastic on inhomogeneous matter. It is advantageous to use the small wave length of $3 - 30\text{\AA}$ which is excited from controlled uranium fission



The uranium fission provides cold neutrons of $0.1 - \text{MeV}$. The neutrons produced in a nuclear reaction are slowed down in helium at temperatures around $T = 25 \text{ K}$ to achieve a

¹²⁰ S. H. Chen, *Annu. Rev. Phys. Chem.* **37**, 351 (1986).

¹²¹ O. Glatter, R. Strey, K. V. Schubert, and E. W. Kaler, *Phys. Chem. Chem. Phys.* **100** (3), 323 (1996).

¹²² P. Lindner, in *Neutrons, X-rays and Light: Scattering Methods Applied to Soft Condensed Matter*, edited by P. Lindner and T. Zemb (Elsevier, Amsterdam, 2002).

¹²³ Y. B. Melnichenko and G. D. Wignall, *J. Appl. Phys.* **102** (2007).

¹²⁴ P. N. Pusey, in *Neutrons, X-rays and Light: Scattering Methods Applied to Soft Condensed matter*, edited by P. Lindner and T. Zemb, Elsevier, Amsterdam (2002).

smaller velocity range. The subsequent neutron conductor sends thermal neutrons by total reflectance to the selector. The neutron flux per area and second $\phi(v)dv$ can be described by *Maxwell* correlation function and it is furthermore dependent on the moderator temperature T and the initial speed v of the neutrons

$$\phi(v) \propto v^3 \exp\left(\frac{1/2 mv^2}{k_B T}\right). \quad [27]$$

The maximal speed of neutrons can be obtained from the first derivative of the *Maxwell* correlation function, which is

$$v_{\max} = v^3 \exp\left(\frac{3k_B T}{m}\right)^{1/2}. \quad [28]$$

Furthermore the thermal energy of neutrons can be defined via *de Broglie* expression which states the relation of wave length λ and speed v

$$\lambda = \frac{h}{mv}. \quad [29]$$

Practically, only neutrons that are scattered in forward direction (parallel beam) are detected

$$q = \frac{4\pi}{\lambda} \sin \frac{\theta}{2} \quad [30]$$

where as q is defined through the scattering angle θ and λ the wave length.

A two dimensional detector as well as the variation of sample to detector distance allow the q - range of $1 \text{ \AA}^{-1} < q < 0.001 \text{ \AA}^{-1}$. Thus microstructures of 6 \AA up to 2000 \AA can be detected. The scattering intensity I_{SANS} is also dependent on the difference of scattering length density $\Delta\rho$

$$I_{\text{SANS}} \propto (\Delta\rho)^2 \quad [31]$$

where as the scattering length density is defined as

$$\rho = \sum_i b_i \frac{\rho^0 N_A}{M_w} \quad [32]$$

ρ^0 is the macroscopic density, M_w molecular weight of the component and the *Avogadro* constant N_A .

3.3.2 EXPERIMENTAL SETUP

In a SANS experiment, a parallel beam of neutrons ($\lambda = 0.1\text{-}2\text{nm}$), of intensity I_0 incident on a flat sample cell containing the sample, and then scattered in a small cone around the forward direction. The measurement of the scattered neutron intensity I_s at an angle θ is carried out with a detector at a distance l away from the sample. Afterwards, the raw data are reduced and made absolute by measuring the scattering of the standard. This quantity is referred to as the scattering cross section per unit volume $d\Sigma/d\Omega(q)$ or, alternatively, as the absolute intensity $I(q)$.

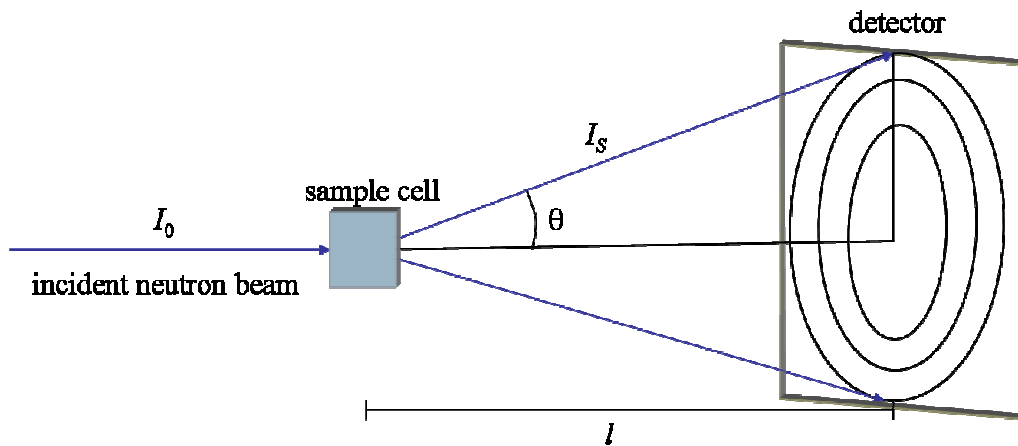


Figure 21: Schematic picture of the SANS experiment. An incident neutron beam is sent through the sample cell including the sample solution where the neutrons are scattered and finally detected on a detector.

The neutron beam with the required velocity ($4.5 < \lambda / \text{\AA} < 40$) is adjusted to the distance of the sample to the detector (between 1.9m and 8m) via a collimator before hitting the sample. The sample holder can be thermo stated and quartz cells of various thicknesses can be used. The neutron beam is detected in scattering direction with a 64cm x 64cm BF_3 detector. A beam stop protects the detector against overloading by the primary beam. Damaged cells and the borders of the detector are masked before the measurement. To produce radially averaged scattering spectra corrections for dark background, pixel efficiency and spatial inhomogeneities are made. The scattering curve is corrected using the scattering of the empty cell and the callibrant and brought to absolute intensity due to the variable sample to detector distances.

3.3.3 DATA ANALYSIS

The measurement of the scattered neutron intensity I_s at an angle θ is carried out with a detector distance l away from the sample. Afterwards, the raw data are reduced and the intensity is brought to absolute values in order to be able to directly compare the obtained results with those of other experiments. The absolute scattering intensity $I(q)$ is given by

$$I(q) = \frac{I_{\text{sample}} - I_{\text{background}} - \frac{T_{\text{sample}}}{T_{\text{emptycell}}} (I_{\text{emptycell}} - I_{\text{background}})}{I_{\text{H}_2\text{O}} - I_{\text{background}} - \frac{T_{\text{H}_2\text{O}}}{T_{\text{emptycell}}} (I_{\text{emptycell}} - I_{\text{background}})} \frac{T_{\text{H}_2\text{O}} d_{\text{H}_2\text{O}}}{T_{\text{sample}} d_{\text{sample}}} \frac{d\Sigma}{d\Omega}(\text{H}_2\text{O}) \quad [33]$$

Here T is transmittance ($T = I/I_0$), where I_0 is the intensity of the incident neutron beam. The subscripts of transmission and intensity denote the values for the sample, water, empty cell and the background. The chosen background for the present measurements was boron carbide (B_4C , background). B_4C is an extremely hard ceramic (9.3 hardness on mohs scale) and its ability to absorb neutrons without forming long lived radionuclides makes the material very attractive as an absorbent for neutron radiation. The last term in the equation, $d\Sigma/d\Omega(\text{water})$ is the differential total scattering cross section of water over the differential of solid angle Ω . The scattering cross section of a molecule is closely related to the scattering length values of its atoms.

3.4 FREEZE FRACTURE ELECTRON MICROSCOPY

Since scattering techniques like DLS or SANS provide the *Fourier* transform of the spatial autocorrelation function, a quantitative interpretation of the scattering data requires knowledge of the shapes of the microstructure. Hence, scattering techniques and microscopy complement each other. Three different EM techniques, namely FFEM, Cryo-Direct Imaging (Cryo-DI)¹²⁵ and freeze fracture direct imaging (FFDI)¹²⁶, can be used to visualize the structure. In this thesis FFEM is the method of choice and therefore presented in the following chapter. FFEM is a useful technique to visualize structures that occur *e.g.* in binary systems but also in many other systems. In biology FFEM is very important for ultra-structure research and therefore very often used¹²⁷.

3.4.1 SAMPLE PREPARATION

In FFEM samples are prepared in a protected fashion in a sandwich¹²⁸. They are then rapidly frozen, fractured, shadowed with metal, replicated with a thin carbon film and finally observed in the microscope. *Jahn et al.*¹²⁹ have improved the method of *Costello et al.*^{130,131}, in which the preparation was directly on the grid that is needed for the electron microscopy. Figure 22 shows the grid between a sandblasted and roughen copper layer and another copper layer with a hole in the center. Hold with tweezers we call the 3 layers “sandwich”. The tweezers is fastened to a pivot arm with a transfer mechanics driven by a spring. With this one is able to transfer the sample sandwich within 10ms from a thermostated water bath to the liquid cryogen¹³², *e.g.* liquid ethane.

¹²⁵ J. F. Bodet, J. R. Bellare, H. T. Davis, L. E. Scriven, W. G. Miller, *J. Phys. Chem.*, **92**, 1898-1902 (1988).

¹²⁶ L. Belkoura, C. Stubenrauch, R. Strey, *Langmuir*, **20**, 4391-4399 (2004).

¹²⁷ R. Strey, *Habilitation* (1992).

¹²⁸ C. Stubenrauch, *Microemulsions: Background, New Concepts, Applications, Perspectives*, Wiley (2009).

¹²⁹ W. Jahn, R. Strey, *J. Phys. Chem.* **92**, 2294 (1988).

¹³⁰ T. Gulik, Krzywicki, M. J. Costallo, *J Microscopy*, **112**, 103 (1978).

¹³¹ M. J. Costello, R. Fetter, J. M. Corless, *Science of Biological specimen Preparation* (1984).

¹³² S. Burauer, *Dissertation* (2001).

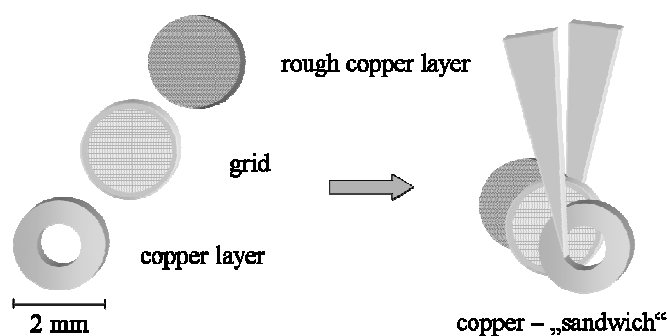


Figure 22: Schematic drawing of a so called sandwich which consists of two thin copper layers amplifying the grid. On the right side, the sandwich is hold by a tweezers¹²⁷.

The sample preparation consists can be split into four main steps: (i) grid preparation, (ii) jump, (iii) fracture and (iv) aftertreatment. Those will be explained briefly in the following.

(i) GRID PREPARATION

Firstly, the sandwich is pre-tempered at room temperature, before dipping it into the sample solution, while the sample solution has equilibrated at constant temperature already. The solution can penetrate through the hole in the first copper layer. The sandwich is kept in solution for at least 30 minutes.

(ii) TEMPERATURE - JUMP

After the temperature equilibrium is achieved, the sandwich is transferred into the cryogen (liquid ethane) within 10 ms through the spring-mechanism. It has been found out that ethane is the most appropriate cryogen for this technique¹³³. It has a freezing point of 90 K and has a very high thermic conductivity ($0.24 \text{ Jm}^{-1}\text{s}^{-1}\text{K}^{-1}$) as well as a very high heat capacity ($2.27 \text{ Jg}^{-1}\text{K}^{-1}$)^{134,135,136}, Propane could also be an alternative, but not nitrogen^{137,138}. Nitrogen has the disadvantage that it builds a gas layer around the sample and therefore leads to slower freezing process. The most important, advantageous characteristic of the above described freezing process is the freezing mechanics. The sandwich can equilibrate,

¹³³ S. M. Bailey, J. A. N. Zasadzinski, *J. Microscopy*, **163**, 307 (1991).

¹³⁴ P. Echlin, Plenum Press, NY (1992).

¹³⁵ K. P. Ryan, D. H. Purse, S. G. Robinson, J. W. Wood, *J. Microscopy*, **145**, 89 (1987).

¹³⁶ A. W. Robards, U. B. Sleyts, *Practical methods in Electron Microscopy*, Ed. A. M. Glauert, North Holland Publishing Company, Amsterdam (1985).

¹³⁷ N. R. Sylvester, S. Marches-Ragona, D. N. Johnzone, *J. Microscopy*, **128**, 175 (1982).

¹³⁸ W. B. Bald, *J. Microscopy*, **134**, 261 (1984).

and be cryofixed within milliseconds. There is evidence that the structure is not changed due to temperature gradients.

(iii) CRYOFIXATION

After cryofixing the sandwich, which now contains the sample, is put into liquid nitrogen where it is fractured *e.g.* the copper layers are removed from the grid. Further the net is fixed in a transfer box with a closure head, which are both filled with liquid nitrogen up to the top.

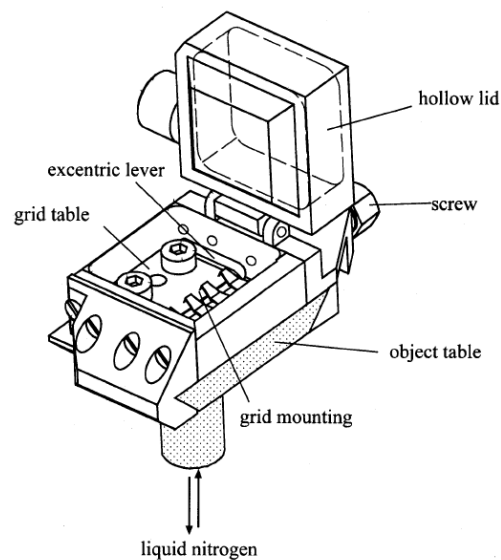


Figure 23: Schematic drawing of a transfer unit for the freeze fracture apparatus. The grids are placed in liquid nitrogen under the tip of the grid mounting and fixed by the excentric lever. The grid table is mounted with two socket screws on the transfer table, which in turn is mounted on the nitrogen-cooled object table inside the bell jar. During transfer the hollow lid works as an anticontaminator as it is filled with liquid nitrogen.

The closure box is used as anti - contaminator. In a next step the transfer unit is transferred into the vaporization machine at normal pressure and locked on the sample desk. After evacuating the machine all the nitrogen is solid and the coldest point is in the closure cap. Thus it is functioning as anti-contaminator. The grid is shadowed with a 2nm thin layer of Ta/W in a 45° angle after opening the closure cap. The perpendicular evaporation with a 20nm thin carbon film stabilizes the heavy metal layer and therefore prevents oxidation. The layer thickness of the carbon film is controlled by a quartz

oscillating analyzer. Figure 24 shows the schematic picture of the principle of angular evaporation. Just behind the shoulders or peaks there is no shadowing, as well as behind the valleys.

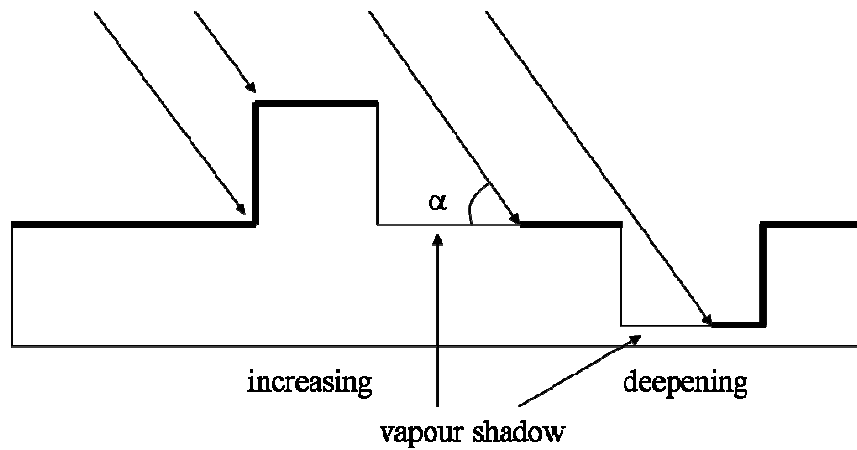


Figure 24: Schematic picture of the geometrical ratios of the angular shadowing. α is the evaporation angle. The metal coating from the area behind the peaks is not possible.

(iv) AFTERTREATMENT

As soon as the evaporation is finished, the transfer box is get out of the evaporation machine. The remained solution is removed from the grid with acetone. The advantage of this method is that the replica of the fracture area and the imaging metal layer are both bound directly to the grid.

3.4.2 SURFACE FRACTIONS

A frozen sandwich can be broken in different ways. Ideally the fraction of the frozen solution goes through the water- and oil domains. Fractions at the metal surface are not wanted, because the structure is not representative anymore. Those can lead to contradictory results.

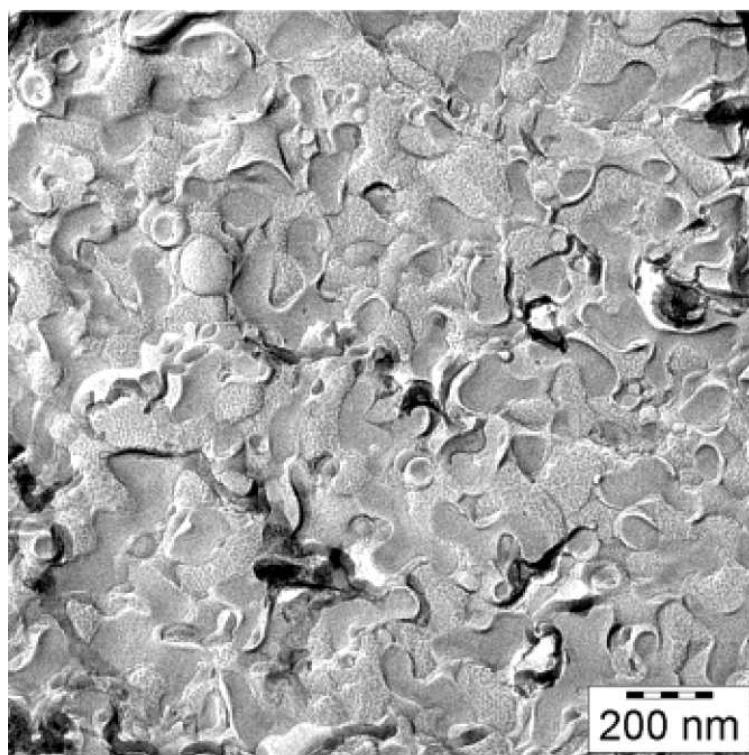


Figure 25: FFEM picture: surface fraction through a bicontinuous microemulsion of an exemplary system¹³⁹.

Figure 25 shows the structure, which represent the pattern for bicontinuous microemulsions¹³⁹. One can easily distinguish between the oil rich phase and the water rich phase because of the texture of the oil domains, which stems from the above described shadowing of the fractured surface with Ta/W. Also the domain size of the bicontinuous structure can be determined. As can be seen, the fracture through the water domains is in most cases planar, whereas for the oil domains the fracture follows the amphiphilic film. This difference leads to a three dimensional impression of the oil domains. Furthermore, one sees water rich and oil rich domains are mutually intertwined in a sponge-like fashion showing many saddle-shape structures.

¹³⁹ S. Burauer, L. Belkoura, C. Stubenrauch, R. Strey, *Colloid Surface A* **228** (1-3), 159 (2003).

3.5 NUCLEAR MAGNETIC RESONANCE

Though it was a scientific curiosity initially, the phenomenon of Nuclear Magnetic Resonance (NMR) has now evolved to a powerful analytical tool used in physics, chemistry, biology and medicine. Discovered initially by *Purcell* and *Bloch* shortly after Second World War^{140,141}, nuclear magnetic resonance studies the absorption of electromagnetic energy by inducement of transitions between spin states from lower to upper energy. Since the frequency of the emitted electromagnetic signals is determined by the energy difference of the states of the nuclei and the decay of the signal in time depends on the molecular environment of the nuclei, the NMR signals received by an radio frequency (rf) probe (simple test device to detect radio frequency oscillation in an electronic circuit) can be analyzed to study the properties of the nuclei and their environment. In lyotropic liquid crystal systems (such as H₂O – C₁₂E₄) NMR is used to determine *e.g.* phase boundaries between isotropic and anisotropic structures (that will be presented in this thesis), to elucidate dynamics of structure changes and to find out more about present structures.

3.5.1 FUNDAMENTALS AND THEORY

In this chapter a brief overview of the physical principles of NMR and the phenomenological treatment of an NMR experiment will be presented. One defines NMR as the interaction between electromagnetic radiation in the rf range and the atomic nuclei when placed in a magnetic field.

SPIN ANGULAR MOMENTUM AND SPIN QUANTIZATION

Magnetic nuclei possess an intrinsic angular momentum, known as spin. The nucleus spin is a function of the number of protons and neutrons in the nucleus. An even number of protons and neutrons gives no spin, with an odd number of protons and neutrons the nucleus possesses a half integer spin (*i.e.* 1/2, 3/2...), if number of protons and neutrons is even the atom has an integer spin (*i.e.* 1, 2, 3...).

¹⁴⁰ E. M Purcell, H. C. Torrey, R. V. Pound, Resonance Absorption by Nuclear Magnetic Moments in a Solid, *Phys. Rev.* **69**, 37 – 8 (1946).

¹⁴¹ F. Bloch, W. W. Hansen, M. Packard, Nuclear Induction, *Phys. Rev.* **69**, 127 (1946).

The total spin angular momentum I , is a vector and its magnitude and orientation in space are quantized in an external magnetic field. The magnitude of the spin angular momentum is given by

$$|\mathbf{I}| = [I(I+1)]^{1/2} \hbar, \quad [34]$$

$$I = 0, \frac{1}{2}, 1, \frac{3}{2}, \dots$$

where I is the spin quantum number and is either integral or a half-integral and is determined by the number of unpaired protons and neutrons. For example the isotope ^{12}C has an even number of protons and neutrons, giving a net spin angular momentum of zero. A nucleus with odd numbers of protons and neutrons *e.g.* ^{13}C possesses a spin angular momentum, $I > 0$. The *Dirac* constant \hbar is $h/2\pi$, where *Planck's* constant is known as $h = 6.6262 \cdot 10^{-34} \text{Js}$. Since the spin angular momentum is a vector property a full description requires specification of the direction. Another quantum number m_I is used to specify the direction of the spin angular momentum, I . The number of projections of the spin angular momentum onto an arbitrary chosen axis is $2I+1$. The z component if I is called I_z .

$$I_z = \hbar m_I, \quad [35]$$

$$m_I = -I, -I+1, \dots, I-1, I.$$

The space quantization is illustrated in Figure 26. In the absence of a magnetic field the spin angular momentum has no preferred directions.

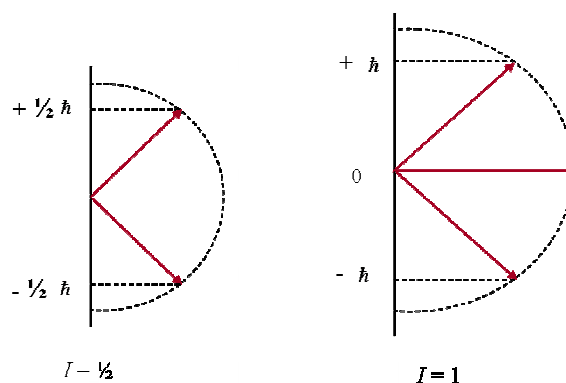


Figure 26: Space quantization for nuclei with spin $1/2$ (left) and spin-1 (right).

THE MAGNETIC MOMENT

Any motion of a charged body causes a magnetic field. Therefore nuclei with $I > 0$ have an associated magnetic moment, $\boldsymbol{\mu}$, which is a vector property. The magnitude and orientation are both quantized. The magnetic moment and the nuclear spin angular momentum are closely related by the proportionality constant, γ , called the gyromagnetic ratio (unit: $\text{T}^{-1}\text{s}^{-1}$) the value of which is nucleus specific. The magnitude of $\boldsymbol{\mu}$ is given by

$$|\boldsymbol{\mu}| = \gamma |\mathbf{I}|, \quad [36]$$

$$\mu_z = \gamma I_z$$

Where μ_z is the z component of $\boldsymbol{\mu}$ and I_z is the z component of I .

NUCLEI IN A MAGNETIC FIELD

For example, the nucleus of a hydrogen atom (proton) has just two permitted orientations, as shown in Figure 27. Roughly speaking, the magnetic moment can point in the *same* direction as the field or in the *opposite* direction¹⁴². These two states are separated by an energy ΔE , which depends on the strength of the interaction between the nucleus and the field. ΔE may be measured by applying electromagnetic radiation of frequency ν , which

¹⁴² P. J. Hore. *Nuclear Magnetic Resonance*, Oxford University Press (2004).

causes nuclei to “flip” from the lower energy level to the upper one, provided the resonance condition $\Delta E = h\nu$ (h is *Planck’s constant*) is satisfied. This is nuclear magnetic resonance (or NMR) spectroscopy.

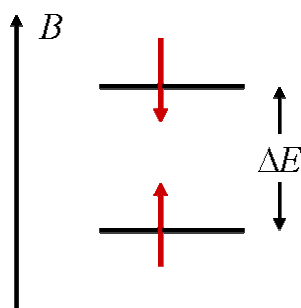


Figure 27: Energy levels of a spin $\frac{1}{2}$ nucleus (^1H or ^{13}C) in a magnetic field. The two permitted orientations of the nuclear magnetic moment relative to the magnetic field direction have energies differing by ΔE .

In the absence of an external magnetic field the orientation of the isolated spin is random, and is independent of the spin quantum number m_l . The energy levels are degenerate in the absence of an external magnetic field. In a magnetic field, B , the energy levels of the spin split up.

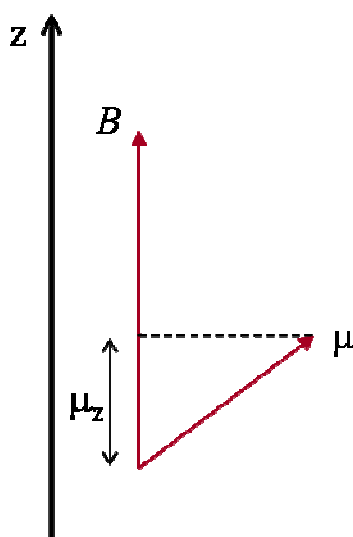


Figure 28: The interaction of the static magnetic field with the magnetic moment, and the projection on the magnetic moments z component onto B .

The quantization of the total spin angular momentum implies that only certain energy levels of the spin are allowed. The energy E in a magnetic field is given by the magnetic moment

$$E = -\boldsymbol{\mu} \cdot \mathbf{B} ,$$

$$E = -\mu_z \cdot B$$
[37]

where B is the magnetic field parallel to z (a vector property) and B is its magnetic strength, μ_z is the z component of $\boldsymbol{\mu}$ (the projections of m onto B). Figure 29 illustrates the relationship between the magnetic field B (along z -direction) and the nuclear magnetic moment, $\boldsymbol{\mu}$.

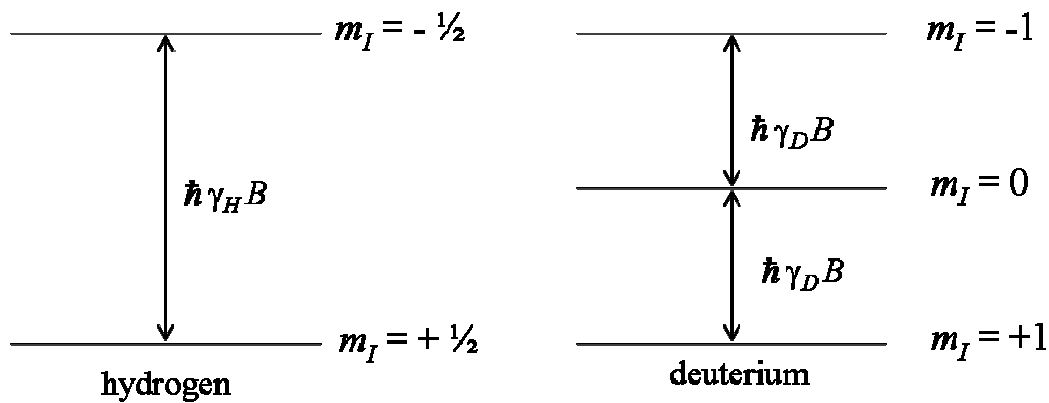


Figure 29: Zeeman energy levels of hydrogen and deuterium nuclei in a magnetic field B .

There are $(2I+1)$ non-degenerated energy levels for the spins. The transitions between the levels can be induced by electromagnetic radiation of frequency, ν , with a value obtained from $\hbar\gamma B = \nu h$.

The selection rule for NMR is $\Delta m_I = \pm 1$; the allowed transitions are therefore between the adjacent energy levels. The resonance condition $\Delta E = h\nu = \hbar\gamma B_0$ is thus

$$\nu_0 = \frac{\gamma B_0}{2\pi} .$$
[38]

where ν_0 is the electromagnetic radiation frequency or the *Larmor* frequency (in some literature referred to as ν_L). All $2I$ allowed transitions for a spin- I nucleus have the same energy. The magnetic field experienced by a nucleus in a molecule differs slightly from the external field such that the exact resonance frequency is characteristic of the chemical environment of the nucleus. This interaction is called the chemical shift.

QUADRUPOLEAR SPLITTING

Nuclei with $I > \frac{1}{2}$, as ^2H -nuclei, possess in addition to their magnetic dipole moment, an electric quadrupole moment that can interact with local electric field gradients (efg). Quadrupole moments are intrinsic properties of a given nucleus type and they are usually expressed as eQ , where e is the elementary charge and Q a quantity which is normally referred to as the electric quadrupole moment of a nucleus. When a quadrupolar nucleus is placed in a magnetic field, there are two energy terms that have to be considered: firstly, the energy from quadrupolar interaction and secondly, the energy from the Zeeman interaction.

The three *Zeeman* energy levels ($m_I = -1, 0$ and 1) of ^2H -nuclei ($I = 1$) can be calculated using:

$$E_{m_I} = -\gamma m_I \hbar \cdot \|\vec{B}\| + \frac{3}{8} \chi h \cdot (3m_I^2 - 2) \cdot (3\cos^2 \theta - 1) \quad [39]$$

where $\chi = \frac{e^2 q Q}{h}$ and is known as the nuclear quadrupole coupling constant. In isotropic conditions the quadrupolar interactions are averaged to zero and the non-perturbed *Zeeman* energy levels are present. These levels are equidistant. When we apply the selection rule, which is $m_I = \pm 1$ and only one spin can be transformed per transition (single quantum transition), the $m_I = +1$ and $m_I = -1$ transition both contribute to a signal detected at *Larmor* frequency ν_0 . In anisotropic conditions, where q between the principal component of the efg tensor q and the magnetic field B is constant, the singlet is split into a doublet due to the quadrupolar interactions and the two signals of the previous intensity now appear at ν^+ and ν^- centered around ν_L .

DEUTERIUM NMR IN LYOTROPIC LIQUID CRYSTALLINE SYSTEMS

Deuterium has nuclear spin $I = 1$ and therefore possesses a quadrupole moment that defines the non spherical distribution of nuclear charges. The Hamiltonian H for the deuterium nucleus in a magnetic field is given by

$$H = H_0 + H_Q, \quad [40]$$

where H_0 is the *Zeeman Hamiltonian* and H_Q is the *quadrupole Hamiltonian*, which is dependent on orientation. The quadrupole interaction is a weak perturbation of the *Zeeman* interaction so that the corresponding energy levels can be easily estimated by perturbation theory. The basic features of deuterium NMR exploited for our investigation reside in the fact that ^2H NMR can easily detect anisotropic motions in the system. For a rapid isotropic motion, the deuterium NMR spectrum consist of one single line, while for an anisotropic motion each deuteron contributes a doublet due to the quadrupole moment of the deuterium nucleus. The doublet spacing $\Delta\nu_Q$ defined by Eq. 24, depends on the degree of anisotropy and the reorientation of the deuteron with respect to the molecular symmetry axis. In oriented samples, the quadrupole splitting depends further on the angle between the magnetic field and the axis of motional averaging (director axis), Figure 30. In fact, D_2O can participate in the anisotropic motion of the solute molecule^{143,144}. There exist two types of water molecules: firstly, the free water that is free to move and secondly, the temporarily perturbed water that is in contact with the polar group of the surfactant molecule. Because of the fast exchange between both types of water, only an average motion is detected. Therefore a splitting is an indication that the average motion of the D_2O molecules is anisotropic^{145,146}. It is then possible to determine region of phase coexistence of the lamellar phase with an isotropic phase. The splitting of the ^2H NMR signal is a measure of the degree of order in the L_α , which helps in discussing the structural change.

¹⁴³ C. Stubenrauch, S. Burauer, R. Strey, C. Schmidt, *Liq. Cryst.* **31**, 39 – 53 (2004).

¹⁴⁴ G. Briganti, A. L. Segre, D. Capitani, C. Casieri, C. La Mesa, *J. Phys. Chem. B*, **103**, 825 – 830 (1999).

¹⁴⁵ M. Gotter, PhD Thesis (2008).

¹⁴⁶ B. Medronho, S. Shafaei, R. Szopko, M. G. Miguel, U. Olsson, C. Schmidt, *Langmuir*, **24**, 6480 – 6486 (2008).

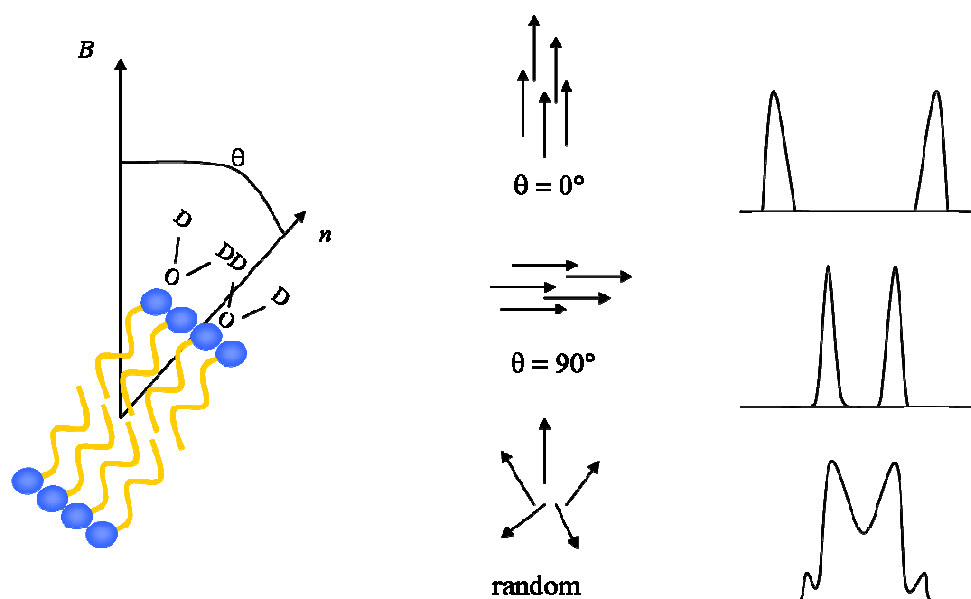


Figure 30: The orientation of a bilayer in the magnetic field and the possible NMR spectra that can be obtained. n is the director of the bilayer. The perturbed water sits around the head groups.

The ^2H NMR technique probes the motionally averaged electric quadrupole couplings between the deuterium nuclei (spin $I=1$) and the electric field gradients at the sites of the observed nuclei¹⁴⁷. The residual couplings arise from the anisotropy of the rotational motions of the water molecules and thus depend on the curvature of the hydrophobic/hydrophilic interface^{148,149}. When D_2O molecules experience a macroscopically anisotropic environment, the quadrupolar interaction has a nonzero average, leading to a splitting of the resonance. In the case of uniaxial symmetry, as for the L_α phase, the ^2H spectrum consists of a doublet with a frequency separation $\Delta\nu$ given by

$$\Delta\nu = \frac{3}{4}\delta(\cos^2\theta - 1) \quad [41]$$

where θ is the angle between the director (the symmetry axis of the phase) and the magnetic field and $\delta = e^2qQ/h$ (with e the elementary charge, h Planck's constant, eq the anisotropy of the averaged electric field gradient, and eQ the nuclear quadrupole moment) is the motionally averaged quadrupole coupling constant. According to the equation above, the deuterium NMR line shape depends on the distribution of director orientations. A simple doublet is observed only if the lamellar phase has been well aligned, for example, by the

¹⁴⁷ A. Abragam, *Principles of nuclear magnetism*; Clarendon: Oxford, 1961.

¹⁴⁸ M. Baciú, U. Olsson, M. Leaver, M. J. Holmes, *J. Phys. Chem. B* **110**, 46 (2006).

¹⁴⁹ M. Gotter, R. Strey, U. Olsson, H. Wennerström, *Faraday Discuss.* **129**, 327 (2005).

action of the magnetic field or by the application of shear. A disordered lamellar phase consisting of many domains of extended flat layers whose orientations are isotropically distributed in space gives rise to the characteristic line shape of a polycrystalline sample also known as powder or *Pake* powder pattern^{150,151}.

¹⁵⁰ G. E. Pake, *J. Chem. Phys.*, **16**, 4 (1948).

¹⁵¹ J. H. Davis, *Biochim. Biophys. Acta*, **737**, 117 (1983).

4 PHASE BEHAVIOR AND MICROSTRUCTURE

This chapter starts with the investigation of the phase behavior of the binary systems H₂O – C₁₂E₄, D₂O – C₁₂E₄, H₂O/glycerol – C₁₂E₄ and H₂O/NaCl – C₁₂E₄ focusing particularly on the determination of the phase boundaries between the lamellar to vesicular phase. Having characterized the phase behavior the structural nature of the vesicular phase is studied over a wide range of surfactant concentrations. Therefore different complementary techniques were used. Dynamic Light Scattering (DLS) and Small Angle Neutron Scattering (SANS) were applied for surfactant mass fractions between $\gamma = 0.01$ and $\gamma = 0.11$. To support the findings, selected samples were studied by freeze fracture electron microscopy (FFEM). Samples with higher surfactant mass fractions are studied by the Nuclear Magnetic Resonance (NMR) technique. The results will be presented in the chronological order.

4.1 PHASE DIAGRAMS

In this chapter the phase behavior of binary and pseudo-binary water - surfactant mixtures were measured as function of temperature and surfactant mass fraction. All phase boundaries were determined visually by keeping the samples in a thermostated water bath and varying the temperature. The lamellar- (L_α) and vesicular (L_α^+) phase were identified using crossed polarizers. While the L_α phase is clearly anisotropic, the L_α^+ phase is birefringent only under shear. The properties of the binary system H₂O – C₁₂E₄ are at the core of this work. Its phase behavior is presented in Figure 31. Furthermore it will be shown how the addition of a third component like salt (Figure 33) on the one hand and glycerol

(Figure 34) on the other hand influences the phase behavior of the binary system. Bearing in mind that experiments, like SANS and NMR were planned to study the structural nature of the vesicular phase, also the phase behavior of the system, where H₂O is replaced with D₂O (Figure 32) will be presented and discussed.

4.1.1 H₂O – C₁₂E₄

The phase diagram of the binary system H₂O – C₁₂E₄ which was initially characterized by Strey *et al.*³⁵ and revisited in this work is shown in Figure 31. Temperature is plotted against surfactant mass fraction γ using a log-scale for the γ -axis. As can be seen the H₂O – C₁₂E₄ system exhibits a rich phase behavior. At low surfactant concentrations and the surfactant is dissolved monomerically in water. Above $\gamma = 0.000015$ almost spherical micelles are formed which grow to cylindrical micelles and micellar networks at higher surfactant mass fractions γ ^{35,152}. This entire one phase micellar-region comprising spherical, cylindrical and network-like structures is denoted L₁.

Increasing the temperature in the dilute region of the phase diagram one finds the following sequence of phases (omitting the triple lines, which were not within the scope of this work): L₁ → L₁' + L₁'' → L_α → L_α⁺ → L_α⁺ → L_α + L₃ → L₃ → L₁ + L₃ → L₁ + L₂. In the two phase region L₁' + L₁'' a dilute (L₁') micellar phase coexists with a concentrated (L₁'') micellar phase. The vesicular L_α⁺-phase is located between two branches of the lamellar phase, one at high and one at low temperature. These separate branches connect, though, at higher surfactant mass fraction γ . At higher temperatures the L_α phase coexists with the sponge phase denoted L₃. Increasing the temperature further one finds the pure L₃ phase and the two phase regions L₁ + L₃ and L₁ + L₂ (where L₂ is the inverse micellar phase). At high surfactant concentrations the lamellar phase becomes more and more stable. Thus, one can find L_α almost over the whole experimentally accessible temperature range for surfactant mass fraction between $\gamma = 0.40$ and $\gamma = 0.90$. However, at such high surfactant concentrations the samples look turbid, (a possible reason might be that patches of bilayer stacks with slightly different compositions cause a high grade of scattering). Finally at surfactant mass fractions above $\gamma = 0.90$ (90% surfactant, 10% water) the surfactant prefers to form inverse micelles, *i.e.* L₂.

¹⁵²A. Zilman, S. A. Safran, T. Sottmann, and R. Strey, *Langmuir*, **20** (6), 2199 (2004).

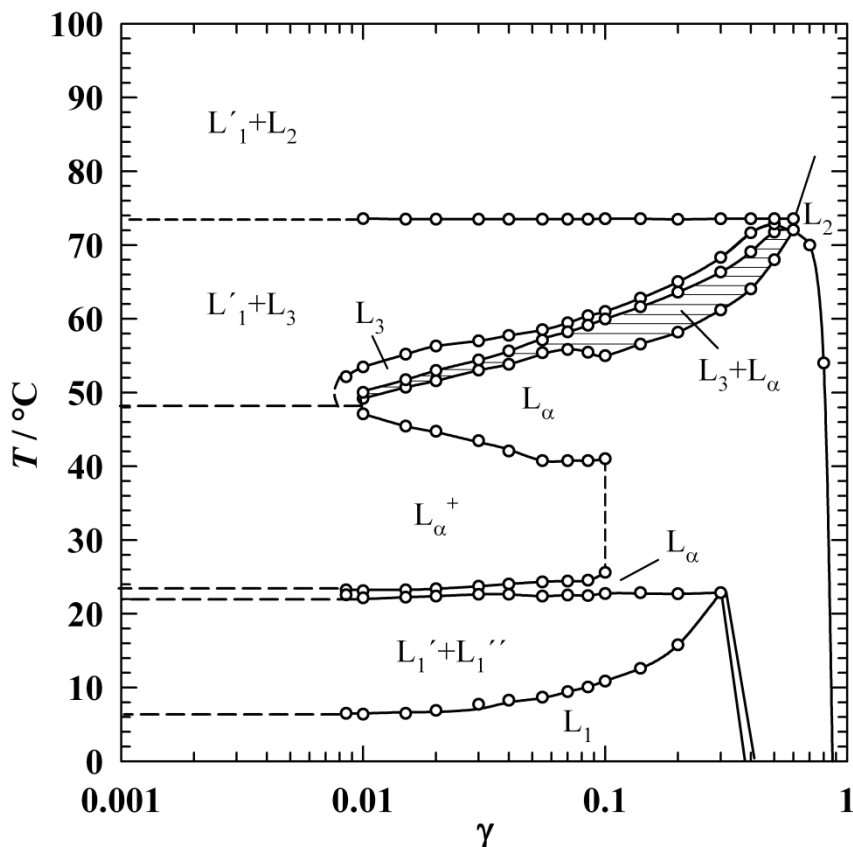


Figure 31: Phase behavior of the binary system $\text{H}_2\text{O} - \text{C}_{12}\text{E}_4$.

The phases of interest are L_α , L_{α^+} , but also L_1 and L_3 , namely their equilibrium structure, but also the transitions between them. As the work at hand aims at improving the understanding of the equilibrium nature of the vesicular L_{α^+} phase, the main focus, however, was to study the microstructure of the L_{α^+} phase. Temperature - jumps from adjacent phases to the L_{α^+} phase were used to trigger the formation of the L_{α^+} phase. The transitions studied are the ones between the lower and upper branch of the lamellar phase L_α and the vesicular phase L_{α^+} , as well as transition from the micellar phase L_1 to vesicular phase L_{α^+} .

4.1.2 D₂O – C₁₂E₄

One outstanding feature of Small Angle Neutron Scattering (SANS) is the opportunity to generate contrasts by using deuterated instead of protonated substances. Here H₂O was replaced with D₂O (²H₂O). Figure 32 shows the phase diagram of the D₂O – C₁₂E₄ system. As one can see the phase behavior does not change qualitatively by replacing H₂O with D₂O, *i.e.* we observe the same number and sequences of phases.

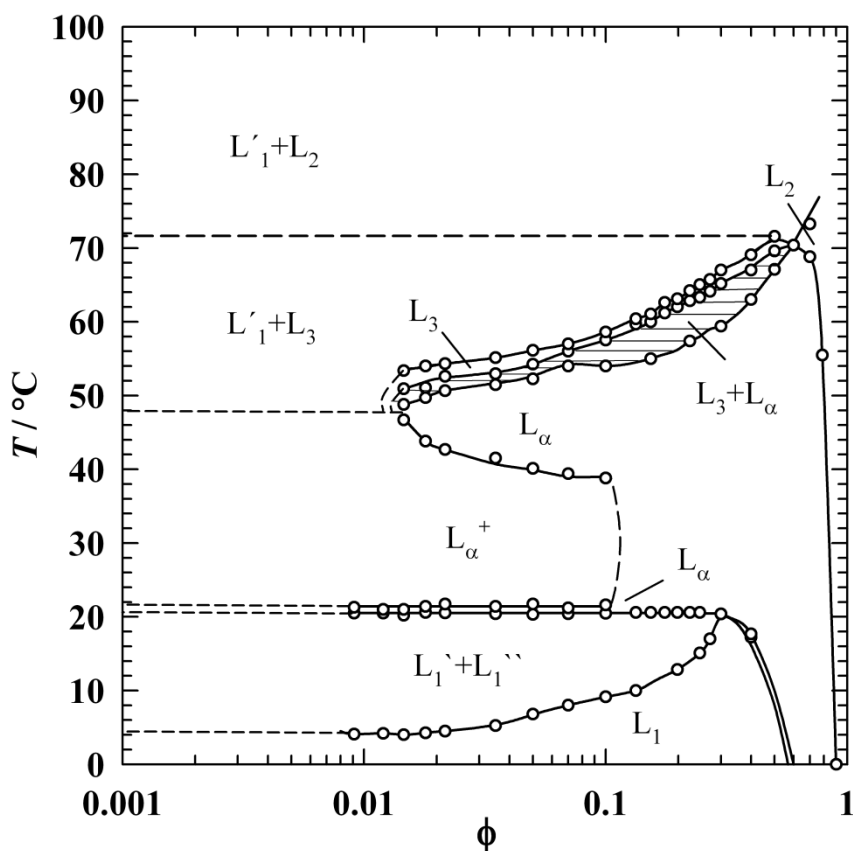


Figure 32: Phase behavior of the binary system D₂O – C₁₂E₄. Note, that the volume fraction ϕ of C₁₂E₄ is used in this case while in Figure 31 the temperature was plotted versus the surfactant mass fractions γ .

However, due to the use of heavy water, the phase boundaries suffer, as it is known from literature¹⁵³, a temperature change. Thus all phase boundaries are shifted to lower temperatures ($\Delta T \sim 2^\circ\text{C}$) (Figure 32). Additionally one can notice a slight change in the extension of the lamellar phase.

¹⁵³ R. Strey, O. Glatter, K. V. Schubert, E. W. Kaler, *J. Chem. Phys.* **105**, 1175 (1996).

4.1.3 H₂O/GLYCEROL – C₁₂E₄

As mentioned above, freeze fracture electron microscopy will be used as a complementary method to study the microstructure of water – non-ionic surfactant systems. However, one main problem of this method is that the samples pass – during the cryofixation - a wide 2 phase region ($L_1' + L_1''$). Therefore, if the freezing of the specimen is not done fast enough, phase separation may occur. This is known to be the main reason why many previous attempts to picture the L_{α}^+ phase but also the L_{α} and L_3 phase have been unsuccessful. However, replacing water partially with glycerol all phase boundaries are shifted to lower temperatures and the kinetics of the system is slowed down. This approach has been successfully used in the past to tune the phase behavior³⁵.

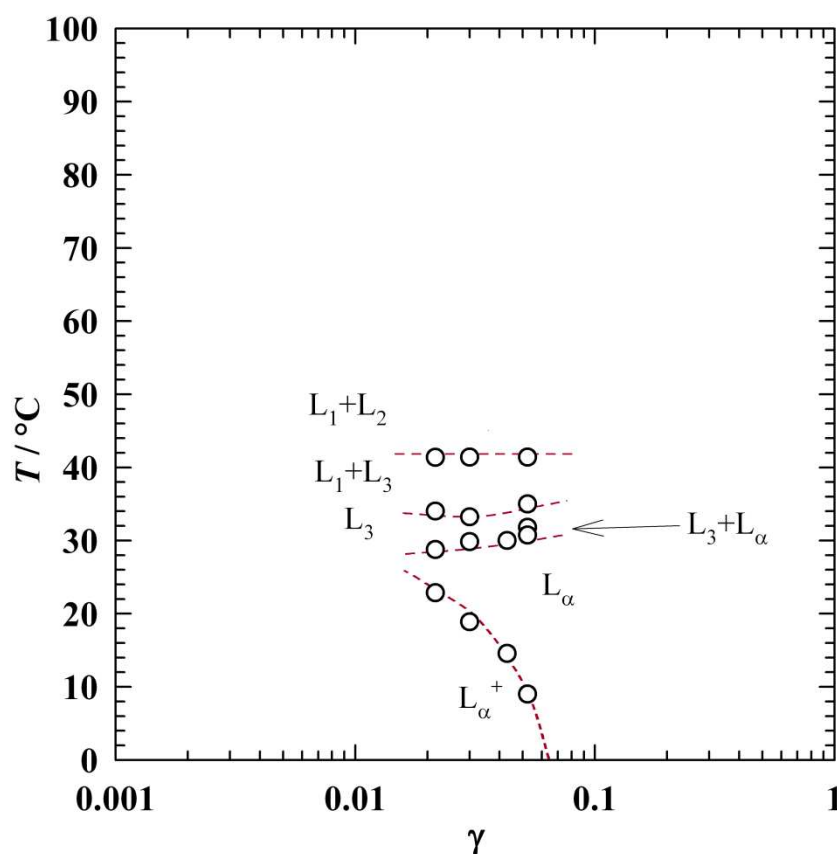


Figure 33: Phase behavior of the pseudo binary system H₂O/glycerol – C₁₂E₄ at a mass fraction of glycerol in the water/glycerol mixture of $\psi=0.50$ for four concentrations $\gamma = 0.02, 0.03, 0.04$ and 0.05 .

The lowering of the phase boundaries by replacing water gradually with glycerol is shown exemplary in chapter 2 by means of the binary system H₂O – C₁₂E₄ (Figure 11). In the work at hand 50 wt.% of water are replaced by glycerol ($\psi = 0.50$). Figure 33 shows the

phase behavior of the pseudo-binary system H₂O/glycerol – C₁₂E₄ for four concentrations in the range of $\gamma = 0.02 - 0.05$. Comparing the phase diagram of the glycerol-free and glycerol containing system one can see that the phase boundaries are shifted to lower temperatures by approximately 20°C. The reason for this shift is that water is needed to hydrate the glycerol molecules and hence, less water is left to hydrate the head groups of the surfactant. Therefore, the volume of the head group decreases resulting in a decrease of the spontaneous curvature of the surfactant film and the phase boundaries shift to lower temperatures. Note, that because of the high viscosity and therefore slow kinetics the samples demanded equilibration times of more than half an hour. The higher the surfactant concentration the longer was the equilibration time. Furthermore, a clear distinction between lamellar and vesicular phase became difficult due to the air bubbles resulted from stirring.

4.1.4 H₂O/NaCl – C₁₂E₅

From *Strey et al.*¹⁵⁴ it is known that the L _{α} ⁺ phase can also be generated in the binary H₂O - C₁₂E₅ system by adding a lyotropic salt which makes the surfactant effectively more hydrophobic and thus shifts the phase boundaries to lower temperatures (Figure 10)¹⁵⁴. Comparing the phase behavior of the NaCl-free H₂O - C₁₂E₅ (Figure 34, left) with that of the H₂O - C₁₂E₄ system (Figure 31) one can see almost the same general phase behavior. However, the L _{α} ⁺ phase that occurs in the H₂O – C₁₂E₄ system can't be observed in the H₂O – C₁₂E₅ system. Due the larger surfactant head group the miscibility gap is shifted to higher temperatures, $T_c(\text{C}_{12}\text{E}_4) = 6.6^\circ\text{C}$ ¹⁵⁵ and $T_c(\text{C}_{12}\text{E}_5) = 32.0^\circ\text{C}$ ¹⁵⁵. Caused by the larger spontaneous curvature of the amphiphilic film also the hexagonal H₁ phase occurs in the H₂O – C₁₂E₅ system at higher surfactant concentrations ($\gamma > 0.30$).

The influence of the addition of NaCl to the binary H₂O - C₁₂E₅ system is shown in Figure 34, right where 18.5 wt% of water is replaced with NaCl ($\epsilon=0.185$). Thereby, the amount of NaCl was adjusted in such a way that the phase boundary L₁' + L₁'' to L _{α} is shifted on top of the same phase boundary in the H₂O - C₁₂E₄ system (see also Figure 5). As can be seen the addition of NaCl shifts the phase boundaries of H₂O/NaCl - C₁₂E₅ to lower temperatures. Again this shift is caused by the fact that water is needed to hydrate the salt molecules and hence, less water is left to hydrate the head groups of the surfactant which makes the

¹⁵⁴ R. Strey, W. Jahn, G. Porte, P. Bassereau, *Langmuir*, **6** (11), 1635 (1990).

¹⁵⁵ K. V. Schubert, R. Strey, M. Kahlweit, *J. Colloid Interf. Sci.*, **141** (1), 21 (1991).

surfactant effectively more hydrophobic. Beside this shift of the phase boundaries to lower temperatures and the generation of the L_{α}^+ phase it is obvious that the extension of the L_3 -phase on the temperature-scale is considerably decreased.

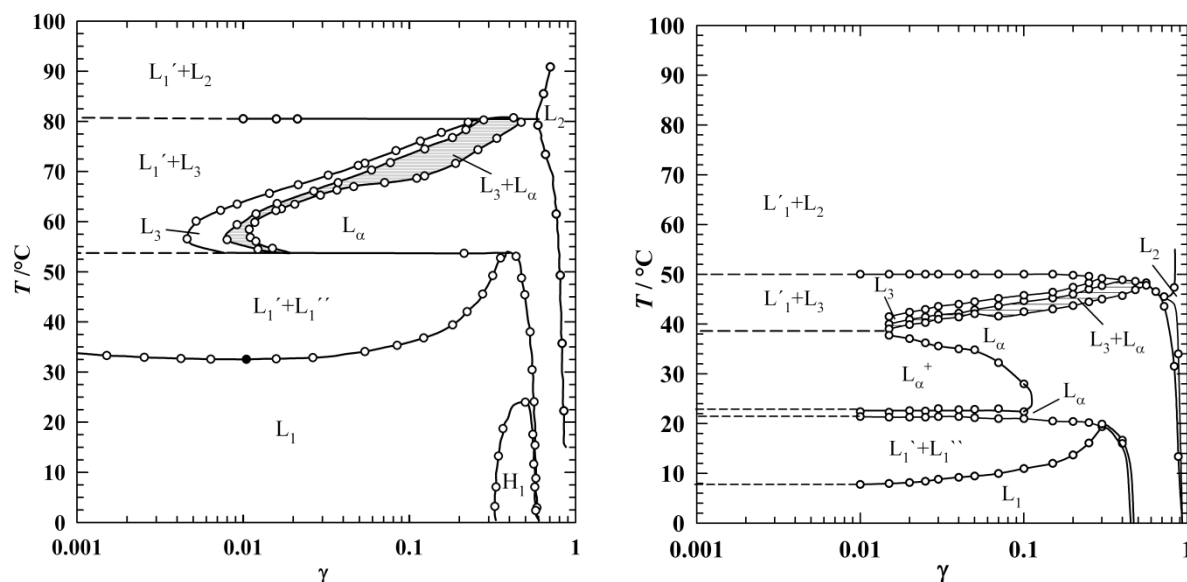


Figure 34: Left: Phase behavior of the binary water- non-ionic surfactant $H_2O - C_{12}E_5$ ^{35,156}. Note that the surfactant concentration γ is shown in weight percent wt%. Right: Phase behavior of the pseudo-binary $H_2O/NaCl - C_{12}E_5$ system ($\epsilon = 0.185$). The miscibility gap is lowered by approximately $24^\circ C$.

In Figure 35 the phase behaviour of the systems $H_2O/NaCl - C_{12}E_5$ and the $H_2O - C_{12}E_4$ are compiled in one graph to visualize the differences and similarities of both systems. As can be seen the phase behavior of the $H_2O/NaCl - C_{12}E_5$ -system qualitatively resembles the phase behavior of the $H_2O - C_{12}E_4$ system, *i.e.* the L_{α}^+ phase. The phase sequences which occur in both systems are identically. Having adjusted the mass fraction of salt in the $H_2O/NaCl$ mixture to $\epsilon=0.185$ the phase boundaries between L_1 and $L_1'+L_1''$ (lower miscibility gap) as well as the phase boundary between $L_1'+L_1''$ and L_{α}^+ (“three phase line”) are at approximately the same temperature. However, the extension of the L_{α}^+ phase in the $H_2O/NaCl - C_{12}E_5$ system on the temperature scale is considerably narrower than that of the $H_2O - C_{12}E_4$ system.

¹⁵⁶ R. Strey, W. Jahn, G. Porte, P. Bassereau, *Langmuir*, **6** (11), 1635 (1990).

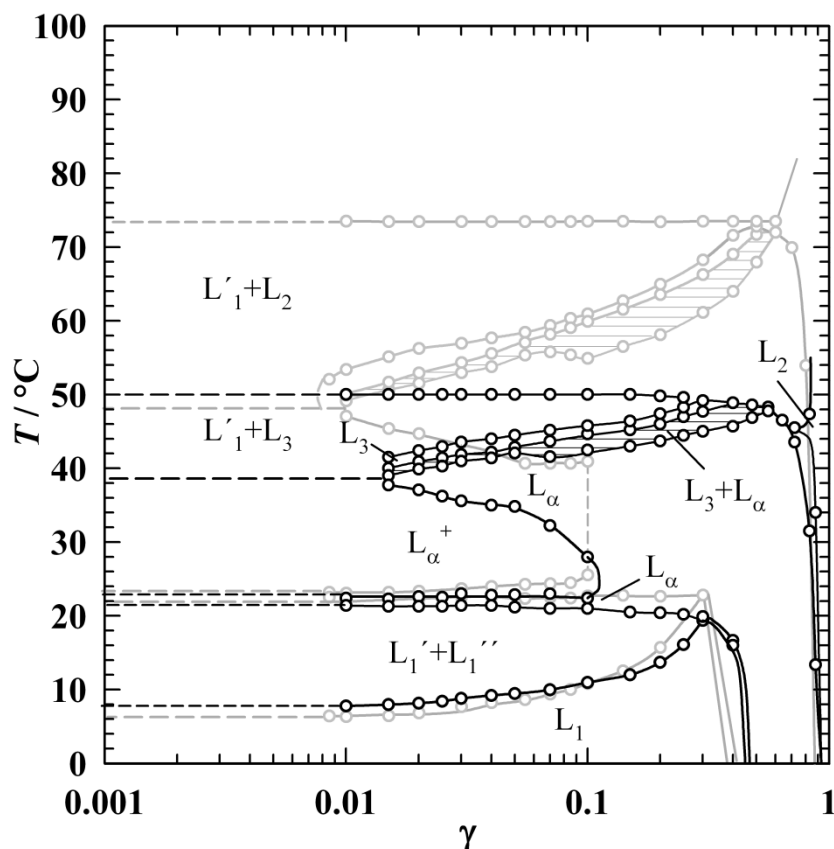


Figure 35: Phase behavior of H₂O - C₁₂E₄ (gray dots and lines) and H₂O/NaCl - C₁₂E₅ (ε = 0.185) (black dots and lines).

In the above the phase behavior of non-ionic surfactant C₁₂E₄ was revisited and the influence of the additives NaCl and glycerol on the H₂O - C₁₂E₅ and H₂O - C₁₂E₄ system have been studied. Interestingly, the H₂O/NaCl - C₁₂E₅ system resembles almost the phase behavior of the H₂O - C₁₂E₄ system, *i.e.* the L_α⁺ phase is generated. In the following chapters the structural nature of the vesicular phase L_α⁺ is studied by means of these three systems. As mentioned above, the methods used to study the samples are dynamic light scattering, small angle neutron scattering and nuclear magnetic resonance. For selected samples freeze fracture microscopy images were made to support the scattering techniques. Figure 36 illustrates the surfactant concentration range in which the methods have been applied.

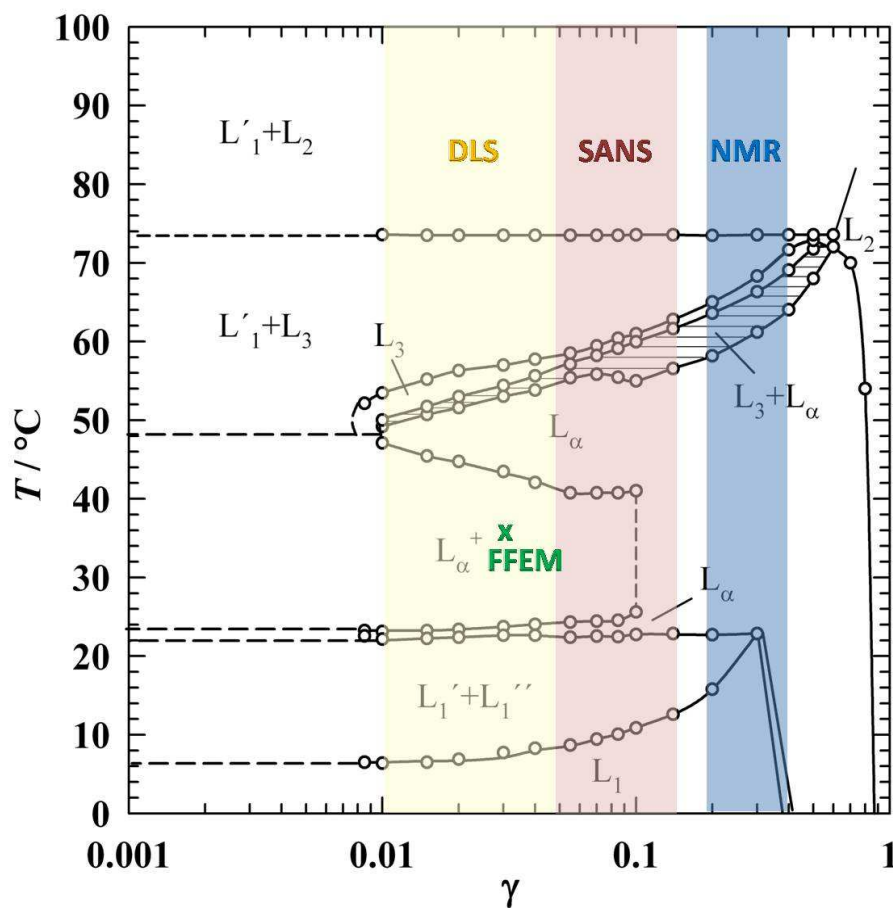


Figure 36: Phase behavior of the binary system $\text{H}_2\text{O} - \text{C}_{12}\text{E}_4$. The microstructure of the samples was studied by dynamic light scattering (yellow area), small angle neutron scattering (red area) and nuclear magnetic resonance (blue area). To support the findings, selected samples were studied by freeze fracture electron microscopy (green cross).

4.2 STRUCTURE DETERMINATION WITH DYNAMIC LIGHT SCATTERING

The main focus of this work was the study of the equilibrium structure of the L_{α}^+ phase and therefore temperature jumps (T -jumps) from the phases adjacent, (L_{α} phase (below L_{α}^+), (L_{α} phase (above L_{α}^+) L_1 and L_3 phase) were used to trigger the formation of the L_{α}^+ phase. Obtaining identical structures from these different temperature jumps would be a clear indication that the vesicular phase is a thermodynamically stable phase. At first, the dynamic light scattering (DLS) of samples of the system $H_2O-C_{12}E_4$ were performed to determine the size of the vesicles and their dependence on the preparation method, temperature and surfactant concentration ($0.01 \leq \gamma \leq 0.05$). However, one has to keep in mind that dynamic light scattering provides only information about the diffusion of the structures studied. Assuming spherical aggregates a hydrodynamic radius R_{hydr} can be calculated using the *Stokes-Einstein* equation (Eq. 25).

4.2.1 $H_2O - C_{12}E_4$: NEGATIVE T - JUMPS

The negative temperature jumps were performed in the following way: the samples were rapidly transferred from a water bath (high temperature) to the toluene bath of the DLS machine (low temperature, L_{α}^+ phase). Since the L_{α}^+ phase don't form spontaneously, the samples were stirred for 30 seconds after the T - jump and equilibrated (for 30 minutes) before they were measured. The scattering at each angle θ (angles from 30° to 150° in 10° steps) was detected three times to improve the statistics.

In the following the common features of the obtained DLS-results are discussed by means of an exemplary negative temperature jump performed at a surfactant mass fraction $\gamma = 0.02$ from $T=48^\circ C$ (L_{α}) to $T=35^\circ C$ (L_{α}^+). Figure 37 shows the obtained autocorrelation function (left) and the line width distribution (right, obtained by *Contin*) recorded at the scattering angle $\theta = 40^\circ$.

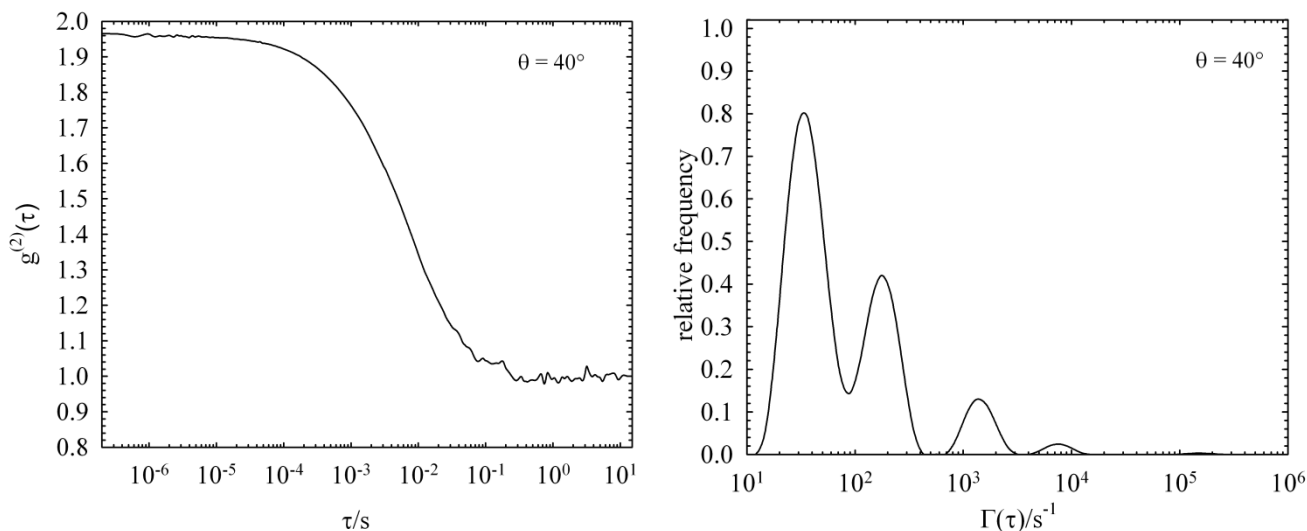


Figure 37: DLS-results ($\theta=40^\circ$) obtained for a sample of the system $H_2O - C_{12}E_4$ at $\gamma = 0.02$ after an exemplary temperature jump (from $T = 48^\circ C$ to $T = 35^\circ C$). Left: Autocorrelation function $g^{(2)}(\tau)$. Right: Corresponding line width distribution showing five maxima.

Analyzing the autocorrelation function recorded at a scattering angle of $\theta = 40^\circ$ (Figure 37, right) the line width distribution displays five maxima at the decay rates $\Gamma_{\max 1} = 36.8s^{-1}$, $\Gamma_{\max 2} = 176.0s^{-1}$, $\Gamma_{\max 3} = 1320s^{-1}$, $\Gamma_{\max 4} = 7940s^{-1}$ and $\Gamma_{\max 5} = 146000s^{-1}$. Assuming only translational diffusion processes of spherical objects and inserting the viscosity of water the corresponding hydrodynamic radii are obtained by using the *Stokes-Einstein*-equation: $1.08\mu m$, $226nm$, $31nm$, $5.0nm$ and $0.3nm$. Thereby the decay rates $\Gamma_{\max 4}$ ($R_{\text{hydr}4} = 5.0nm$) and particularly $\Gamma_{\max 5}$ ($R_{\text{hydr}5} = 0.3nm$) are presumably artifacts of the evaluation of the autocorrelation function by *Contin*. However, the concomitant existence of several diffusion processes is a first indication that the region denoted as L_{α}^+ comprises a cumulus of structural aggregates.

In particular if – as in this case – samples are studied which comprises a variety of structures it is indispensable to record and analyze the dynamic light scattering signal for different scattering angles. While larger particles scatter mainly towards small scattering angles, smaller particles scatter towards large scattering angles. Figure 38 shows the line width distributions of the L_{α}^+ -phase (for composition an preparation see Figure 37) for the scattering angles ($\theta=50^\circ$, 70° , 100° and 130°). As shown in Figure 38 several maxima are obtained (5 maxima for $\theta = 50^\circ$ and 4 maxima for $\theta = 70^\circ$) at small scattering angles, while for large scattering angles a very broad distribution of relaxation rates Γ is obtained by

analyzing the autocorrelation function. In between, at $\theta = 100^\circ$, one can observe that the maxima are smeared out.

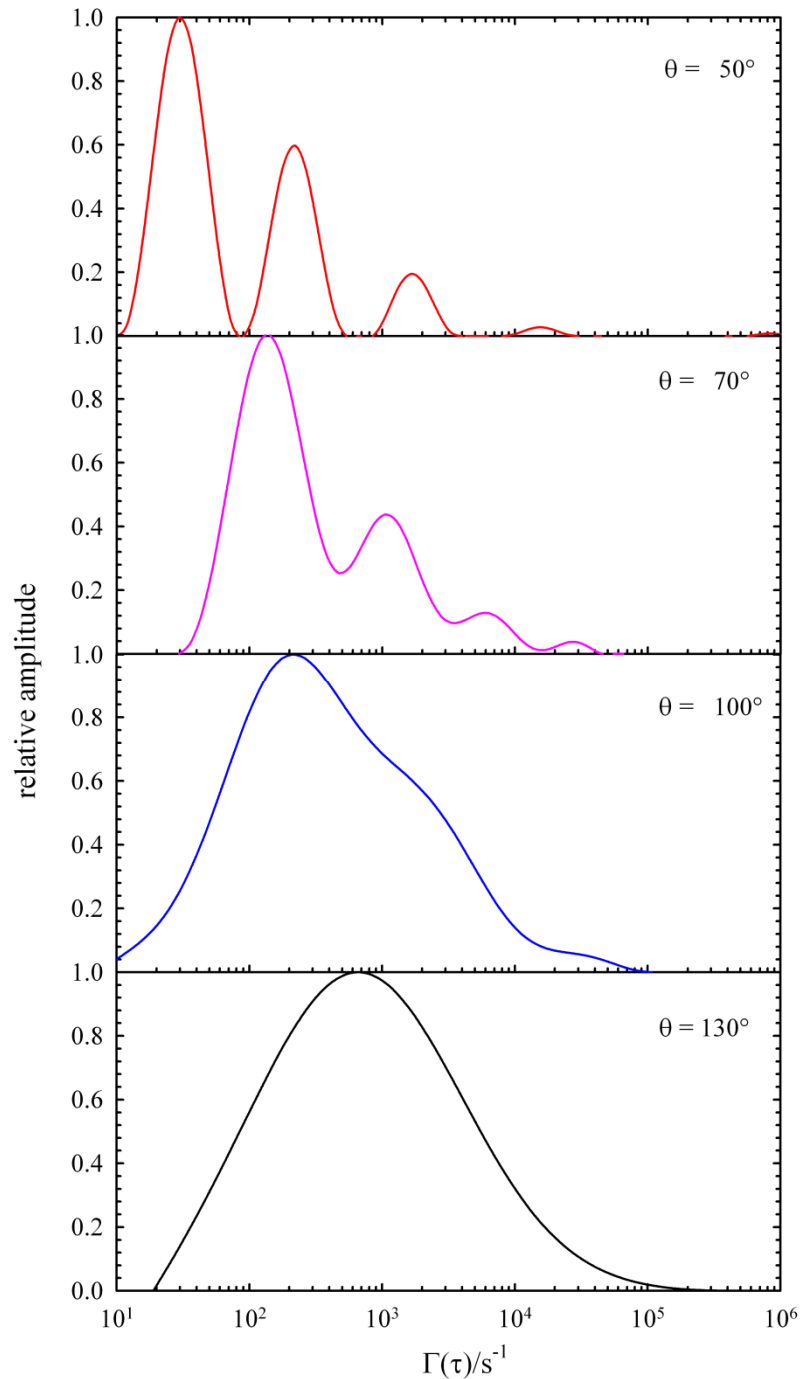


Figure 38: Relative amplitudes of the relaxation rate Γ for four scattering angles $\theta=50^\circ$, 70° , 100° and 130° , obtained for a sample of the system $H_2O - C_{12}E_4$ at $\gamma = 0.02$ after an exemplary temperature jump (from $T = 48^\circ C$ to $T = 35^\circ C$). At small scattering angles ($\theta=50^\circ$ and 70°) the line width distributions show 4-5 maxima; at large scattering angles ($\theta=100^\circ$ and 130°) a broad distribution is obtained.

These results demonstrate that the quantitative evaluation of DLS-data in the work at hand is difficult due to obvious abundance of structures. However, as an example the hydrodynamic radii of the different diffusion species were determined considering the q -dependence of the first three relaxation rates Γ_1 , Γ_2 and Γ_3 which can only be resolved at small scattering angles ($\theta = 40^\circ, 50^\circ, 60^\circ, 70^\circ$ and 80°). In Figure 39 the respective relaxation rates Γ_n are plotted versus the scattering wave vector squared q^2 . According to the *Landau - Placzek* equation (Eq. 23) the data should fall on a straight line crossing the origin. That this is really the case can be seen in Figure 39 yielding the diffusion coefficient D from the slope of the lines. The obtained diffusion coefficients are $D_1 = 2.11 \cdot 10^{-13} \text{m}^2/\text{s}$, $D_2 = 1.58 \cdot 10^{-12} \text{m}^2/\text{s}$, and $D_3 = 1.21 \cdot 10^{-11} \text{m}^2/\text{s}$. The hydrodynamic radii can be calculated using the *Stokes - Einstein* equation (Eq. 25) yielding $R_{\text{hydr}1} = 1.4 \mu\text{m}$, $R_{\text{hydr}2} = 184 \text{nm}$ and $R_{\text{hydr}3} = 24.0 \text{nm}$.

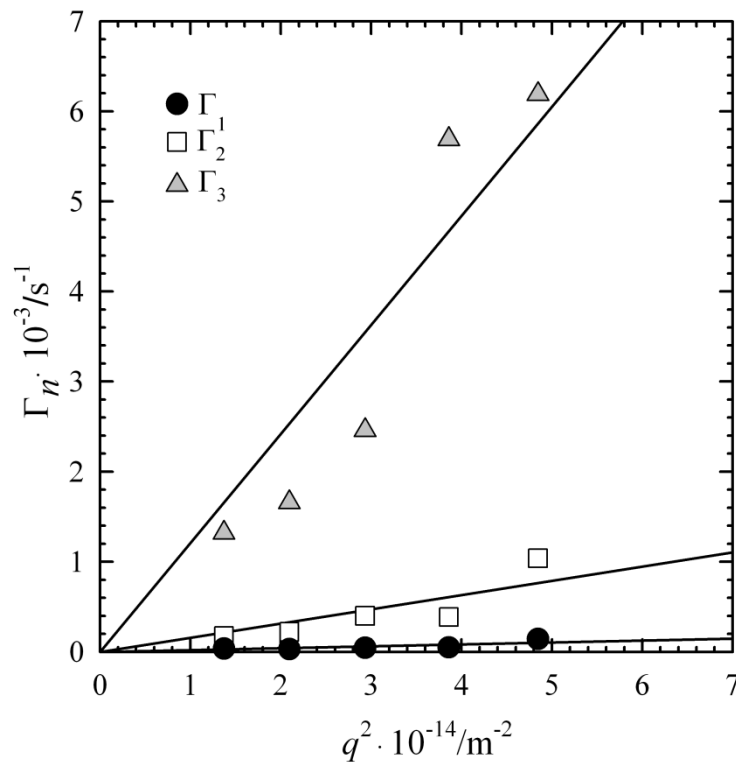


Figure 39: Relaxation rates Γ_n as a function of the quadratic scattering vector q^2 for one exemplary sample of the system $\text{H}_2\text{O} - \text{C}_{12}\text{E}_4$ at $\gamma = 0.02$ after a temperature jump (from $T = 48^\circ\text{C}$ to $T = 35^\circ\text{C}$). Analyzing the autocorrelation function at the scattering angles ($\theta = 40^\circ, 50^\circ, 60^\circ, 70^\circ$ and 80°) via *Contin* provides the values of the first three corresponding relaxation rates Γ_1, Γ_2 and Γ_3 . The diffusion coefficients $D_1(T), D_2(T)$ and $D_3(T)$ can be read off the slope straight lines.

L_{α} (48°C) TO L_{α}^{+} (25°C) AND L_{α} ($T = 48^{\circ}\text{C}$) TO L_{α}^{+} ($T = 35^{\circ}\text{C}$)

Due to the wealth of DLS-data a rather rudimentary analysis of the data is used in the following. The existence of different diffusing species is neglected considering at each scattering angle only the decay rate with the largest relative amplitude. In Figure 40 the in this way obtained hydrodynamic radius R_{hydr} is plotted versus the scattering angle θ .

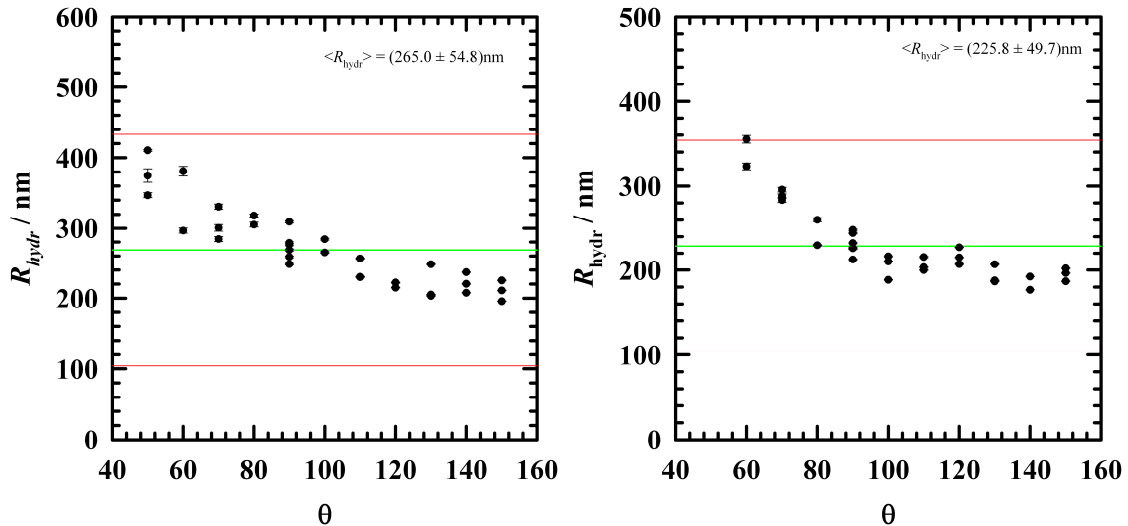


Figure 40: Hydrodynamic radii R_{hydr} as function of scattering angle θ L_{α}^{+} phase formed by temperature jumps from $T = 48^{\circ}\text{C}$ (L_{α}) to $T = 25^{\circ}\text{C}$ (L_{α}^{+}) (left) and from $T = 48^{\circ}\text{C}$ (L_{α}) to $T = 35^{\circ}\text{C}$ (L_{α}^{+}) (right), for an exemplary one exemplary sample of the system $\text{H}_2\text{O} - \text{C}_{12}\text{E}_4$ at $\gamma = 0.01$

In Figure 40 the DLS-results of two L_{α}^{+} samples of the system $\text{H}_2\text{O}-\text{C}_{12}\text{E}_4$ at $\gamma = 0.01$ prepared by two different ways are displayed. Figure 40 (left) shows the hydrodynamic radius of the L_{α}^{+} phase prepared by a temperature jump from the L_{α} phase to a temperature of $T = 25^{\circ}\text{C}$, while Figure 40 (right) shows R_{hydr} prepared by a T -jump from the L_{α} phase to $T = 35^{\circ}\text{C}$. Both figure show the same trend: the hydrodynamic radius R_{hydr} decreases systematically from large values at small scattering angles θ to smaller values at large θ . As discussed above the reason for this trend is that in these samples which comprises a variety of structures larger particles scatter mainly towards small scattering angles, while smaller particles scatter towards large scattering angles. Calculating the average value of the hydrodynamic radius for both temperatures $R_{\text{hydr}} = 226 \pm 50 \text{ nm}$ ($T = 25^{\circ}\text{C}$) and $R_{\text{hydr}} = 265 \pm 55 \text{ nm}$ ($T = 35^{\circ}\text{C}$) are obtained.

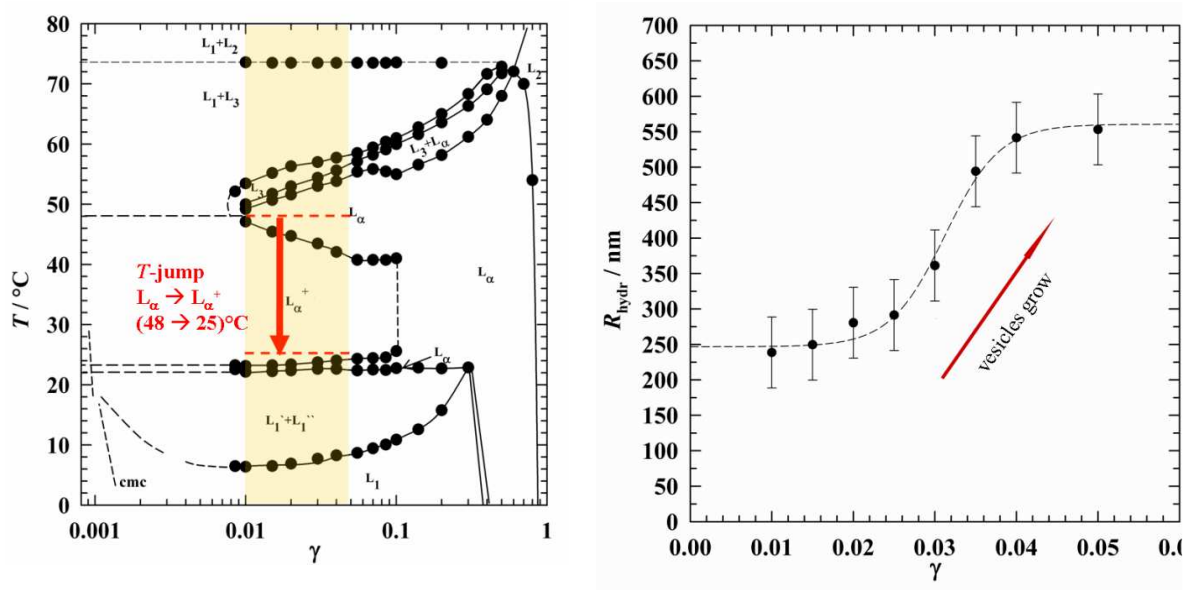


Figure 41: Left: Phase behavior of the system H₂O - C₁₂E₄: the red arrow indicates schematically the temperature jump from $T = 48^\circ\text{C}$ (L_α) to $T = 25^\circ\text{C}$ (L_α^+) which have been performed for several surfactant mass fractions in the range of $\gamma = 0.01 - 0.05$ (yellow area). Right: Variation of hydrodynamic radius R_{hydr} with surfactant mass fraction. Note, that the existence of different diffusing species is neglected by analyzing only the decay rate with the largest relative amplitude.

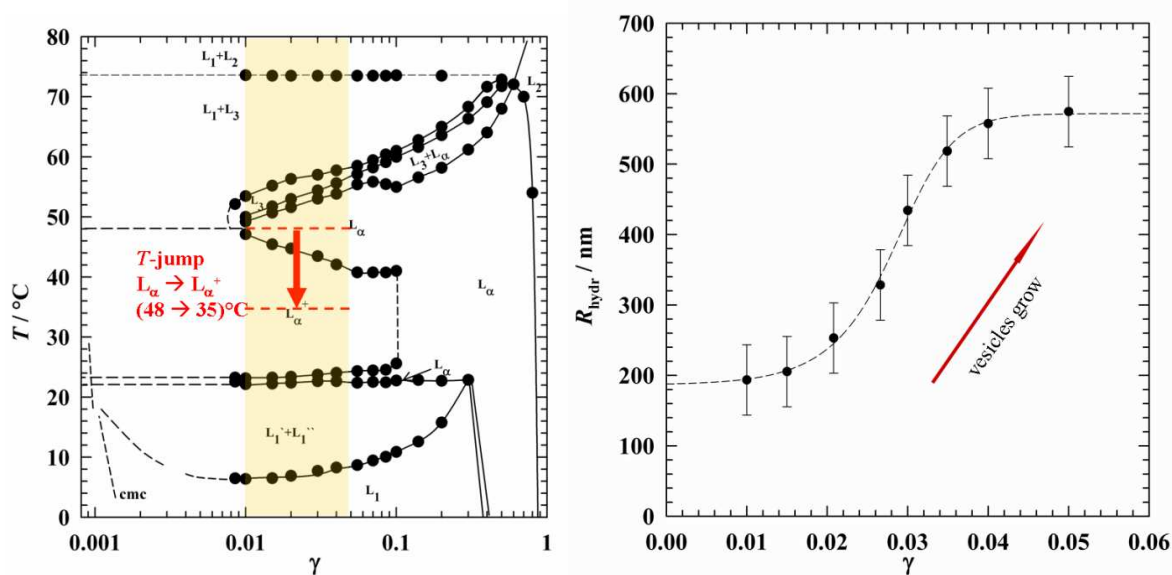


Figure 42: Left: Phase behavior of the system H₂O - C₁₂E₄: the red arrow indicates schematically the temperature jump from $T = 48^\circ\text{C}$ (L_α) to $T = 35^\circ\text{C}$ (L_α^+), which have been performed for several surfactant mass fractions in the range of $\gamma = 0.01 - 0.05$ (yellow area). Right: Variation of hydrodynamic radius R_{hydr} with surfactant mass fraction. Note, that the existence of different diffusing species is neglected by analyzing only the decay rate with the largest relative amplitude.

The effect of the depth of the T -jump on the hydrodynamic radius of L_{α}^{+} samples is also displayed in the above two figures. The right hand side of Figure 41 and Figure 42 shows the variation of the hydrodynamic radius (averaged over the different scattering angles) with the surfactant mass fraction γ for samples prepared via T -jumps (red arrow) from the lamellar phase (48°C) to the vesicular phase (25°C (Figure 41) and 35°C (Figure 42)). The left hand side of both figures shows the phase diagram of the studied water – $C_{12}E_4$ system, in which the temperature jumps are schematically illustrated by red arrows. As can be seen the averaged hydrodynamic radius grows with increasing surfactant mass fraction γ irrespective of the depth of the T -jump. Thereby, the hydrodynamic radii obtained for the L_{α}^{+} samples at $T = 35^{\circ}\text{C}$ are slightly smaller than the ones obtained L_{α}^{+} samples at $T = 25^{\circ}\text{C}$. Similar results are obtained by the group of Olsson⁸⁵ However, from the above it must be clear that the rather rudimentary analysis of the DLS-data used, *i.e.* considering only the decay rate with the largest relative amplitude, is questionable. Thus, we refrain from a further discussion of the obtained results.

L_{α} TO L_{α}^{+} ($T = 35^{\circ}\text{C}$) - DIFFERENT LOCATIONS WITHIN L_{α} PHASE

While until now we have been looking for negative temperature jumps from the middle of the lamellar phase L_{α} to two different depth of the vesicular phase L_{α}^{+} , now we wanted to see the effect on the vesicle size while changing the initial state (different depth within the lamellar region).

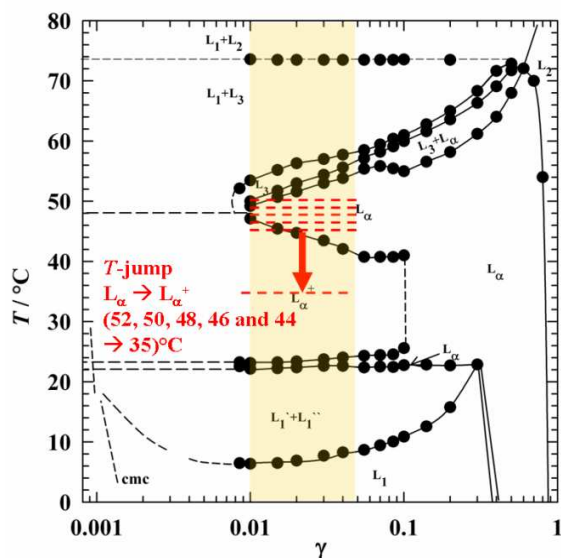


Figure 43: Phase behavior of the system $\text{H}_2\text{O} - \text{C}_{12}\text{E}_4$: the red arrow represents schematically the temperature jumps from different depth within the lamellar phase L_{α} to $T = 35^{\circ}\text{C}$ (L_{α}^{+}). The numbers indicate the different positions within L_{α} . ($T = 44, 46, 48, 50, 52^{\circ}\text{C}$) for one surfactant concentration $\gamma = 0.03$.

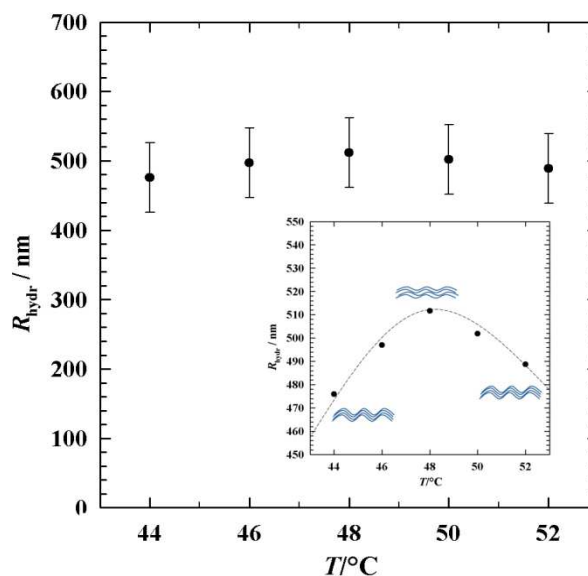


Figure 44: Distribution of hydrodynamic radii R_{hydr} for one surfactant concentration $\gamma = 0.03$ for temperature jumps from different depth within the lamellar phase to $T = 35^{\circ}\text{C}$ (L_{α}^{+}).

Figure 43 points out the temperature jumps from the different initial states within the lamellar phase (L_{α}) to one position within the vesicular phase (L_{α}^{+}) at $T = 35^{\circ}\text{C}$ for one surfactant concentration $\gamma = 0.03$. Figure 44 indicates a possible trend of hydrodynamic radii R_{hydr} for the temperature jumps shown in Figure 43. At first view vesicles formed from lamellar phase close to the phase transition lines are smaller than vesicles formed from lamellar phase that subsists in the very middle of the lamellar region. The difference is $\Delta R_{\text{hydr}} \pm 40\text{nm}$.

L_3 PHASE (42, 44, 46, 48, 50°C) TO L_{α}^+ PHASE (35°C)

Also the negative temperature jumps were performed from sponge phase L_3 that is situated above L_{α} separated by a tiny two phase ($L_{\alpha}+L_3$) channel for the investigated surfactant concentration range.

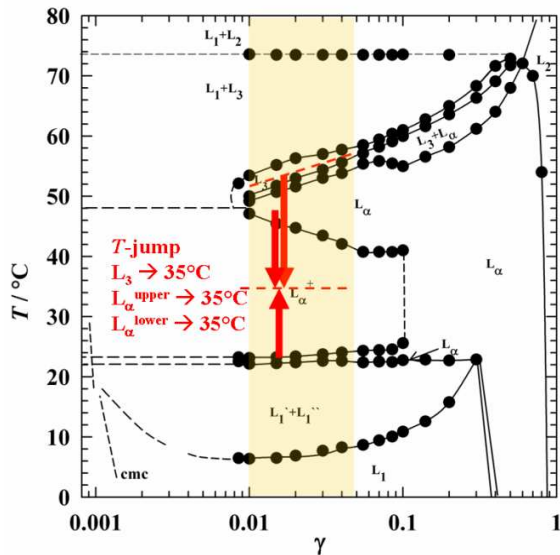


Figure 45: $T/(\gamma)$ - cut of the system $H_2O - C_{12}E_4$: the red arrow represents schematically the temperature jump from $T = 48^\circ C$ (upper L_{α}) to $T = 35^\circ C$ (L_{α}^+), $T = 21^\circ C$ (lower L_{α}) to $T = 35^\circ C$ (L_{α}^+) and $T = 42^\circ C - 50^\circ C$ (L_3) to $T = 35^\circ C$ (L_{α}^+).

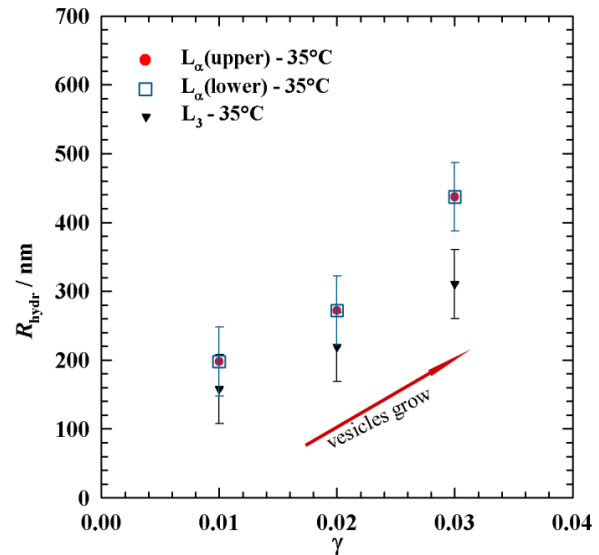


Figure 46: Distribution of hydrodynamic radii R_{hydr} for three concentrations, $\gamma = 0.01 - 0.03$ for temperature jumps from $T = 48^\circ C$ (upper L_{α}) to $T = 35^\circ C$ (L_{α}^+) (L_{α}^+ (red dot), $T = 21^\circ C$ (lower L_{α}) to $T = 35^\circ C$ (L_{α}^+) (blue square) and $T = 42^\circ C - 50^\circ C$ (L_3) to $T = 35^\circ C$ (L_{α}^+) (black triangle).

As can be seen Figure 46 the sizes of vesicles obtained from temperature jumps from L_{α} agree for both L_{α} regions (upper and lower). Whereas the vesicles obtained from jumps from L_3 phase have smaller size. Nevertheless the trend of increasing vesicles with increasing surfactant concentration γ is once more demonstrated.

SUMMARY

DLS measurements were performed to determine the structure sizes of the vesicles and their dependence on temperature and surfactant concentration for a concentration range of $\gamma = 0.01$ to $\gamma = 0.05$. Several temperature jumps were performed from different depth within L_{α} phase to different depth of L_{α}^+ phase, as well as temperature jumps from L_3

phase to L_{α}^+ . Regarding the autocorrelation functions ($g^{(2)}(\tau)/\tau$ - plots) and the resulting line width distributions (relative Amplitude of $\Gamma/\Gamma(\tau)$ - plot) for small scattering angles θ three relevant hydrodynamic radii R_{hydr} can be extracted, $1.08\mu\text{m}$, 226nm and 31nm . At higher scattering angles θ the maxima of the line width distributions are blurred out and one broad maximum is obtained, that indicates a wealth of structure sizes. Neglecting the assumed polydispersity and analyzing the diffusion coefficients as consequence of each relaxation rate Γ , the smallest vesicle radii are found to be $\sim 160\text{nm}$. Furthermore, following the approximation, it was established that the radii were increasing with increasing surfactant mass fraction for all kinds of T -jumps and for all different initial states although the distances between the bilayers in the lamellar phase are known to decrease with increasing surfactant mass fraction. The dimension of calculated vesicles of the different types of temperature jumps is the same. Moreover, DLS results show a high grade of polydispersity within all samples. Apparently, DLS is not able to give clear, sensible information concerning vesicle sizes. Looking at the phase diagram DLS is able to cover only a small concentration range. To look closer to vesicle evaluation with increasing concentration small angle neutron scattering was the method of choice. These results will be presented in the next chapter.

4.3 SMALL ANGLE NEUTRON SCATTERING

Small angle neutron scattering (SANS) is a very powerful tool to determine the structural characteristics of self-assembled water-surfactant systems. In the work at hand the nanostructure of the systems $D_2O - C_{12}E_4$ and $D_2O/\text{glycerol} - C_{12}E_4$ is studied by SANS. Because of the accessible q -range SANS experiments were used to study samples with surfactant concentrations of $\gamma > 0.05$. All measurements were carried out within two beam times at the spectrometer KWS-2 at the FRMII research reactor in Munich, Germany. In order to ensure the same conditions as in the lab, two water bathes were set next to the SANS instrument. The experiments at the KWS-2 were carried out at two different sample-detector distances $d_{sd} = 2\text{m}$ and 8m , using neutron wave lengths $\lambda = 4.5\text{\AA}$ and 12\AA covering a q -range of approximately $0.003\text{\AA}^{-1} - 0.2\text{\AA}^{-1}$. Distances of 4m to 20m between the collimation aperture and the sample were used to reduce the divergence of the incident neutrons and thus to increase resolution. Thereby the distance between the guide and the sample was chosen to be at least as large as the sample-detector distance. The sample was kept in *Hellma*-quartz QS glass cells of 1mm path length. Samples were thermostated in a cell holder during the measurements.

4.3.1 $D_2O - C_{12}E_4$

In order to study the structural nature of the vesicles formed within $D_2O - C_{12}E_4$ system two types of temperature jumps (T -jumps) were performed *i.e.* negative and positive T -jumps. For *negative temperature jumps* (L_3 to L_α to L_{α^+}) samples of bilayer volumes $\phi = 0.02, 0.05, 0.08$ and 0.11 were investigated. First scattering curves of the L_3 phase were recorded, then the ones of L_α phase. Finally the T -jumps were performed by transferring the samples from the water bath with the higher temperature (L_3 to L_α) to water bath with lower temperature (L_{α^+}). Knowing that the relaxation kinetics of these systems can be slow an equilibration time of 1 hour was chosen. Afterwards all L_{α^+} samples were treated in the following way. At first, the scattering curve was recorded for the untreated L_{α^+} sample. Then, the L_{α^+} sample (*i.e.* the entire cell holder) was shaken for 60 seconds. Having detected the scattering intensity of the shaken L_{α^+} phase, the sample was vortexed for 60 seconds and the intensity of the vortexed sample was measured. Finally, the intensity of this sample was recorded after 60 seconds of sonication. This order was chosen in order to increase the strength of the perturbation from shaking to vortexing and sonication. If the structures obtained following these different perturbation methods are in agreement, this would be a

strong indication that the vesicular phase is a thermodynamically stable state. Furthermore *positive temperature jumps* (L_1 to L_{α}^+) were performed on samples of bilayer volume fractions $\phi = 0.002, 0.02, 0.05, 0.08$ and 0.11 . Only one preparation method was chosen, the samples were shaken immediately after the T -jump. Thereby at first, the scattering curve of the initial L_1 phase was recorded, then that of the L_{α}^+ phase after 1 hour equilibration time.

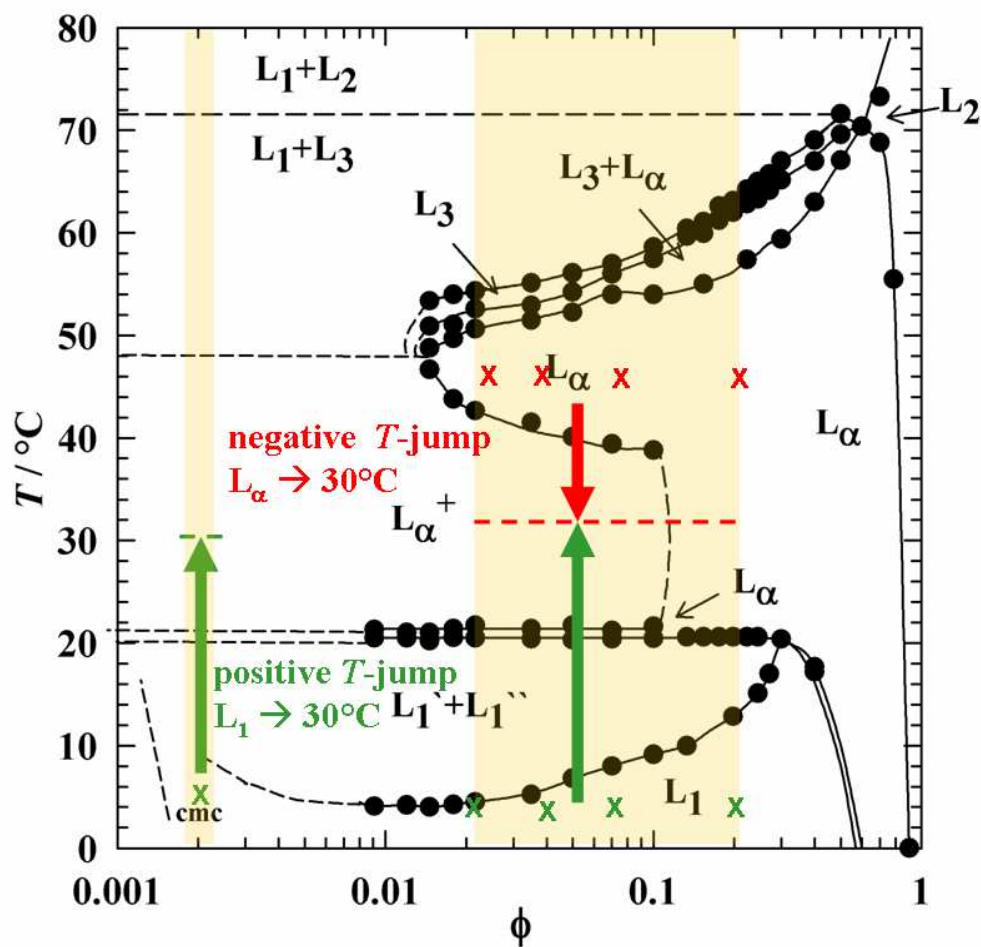


Figure 47: Phase diagram of the $D_2O - C_{12}E_4$ system. The composition of the samples studied before and after negative temperature jumps (red arrows) from $T = 46^\circ C$ (upper L_{α}) to $T = 30^\circ C$ (L_{α}^+) and positive temperature jumps (green arrows) from $T = 4^\circ C$ (L_1) to $T = 30^\circ C$ (L_{α}^+) are displayed.

4.3.1.1 NEGATIVE TEMPERATURE JUMP EXPERIMENTS:

EQUILIBRIUM STRUCTURE OF THE SPONGE PHASE L_3

A well defined lamellar phase L_{α} , which was the initial state for later T -jumps to the vesicular phase, was obtained by performing temperature jumps from the L_3 to the L_{α} phase. In order to characterize the initial structure of the L_3 -phase SANS-experiments were performed in bulk contrast. Figure 48 shows the scattering curve of the L_3 phase at the three different surfactant volume fractions $\phi = 0.02, 0.05$ and 0.11 . As can be seen the scattering intensity is almost constant at low q -values. After a weak maximum which can be observed at intermediate q -values the scattering intensity is dominated by a q^{-2} -dependence. Then, at high q -values the expected q^{-4} dependence is observed. Increasing the surfactant volume fraction the weak maximum shifts towards higher q values, *i.e.* to smaller length scales, which is in agreement with the observations made by *Strey and Porte*^{157,158} and others. Note, that this maximum could not be detected with the available experimental set-up.

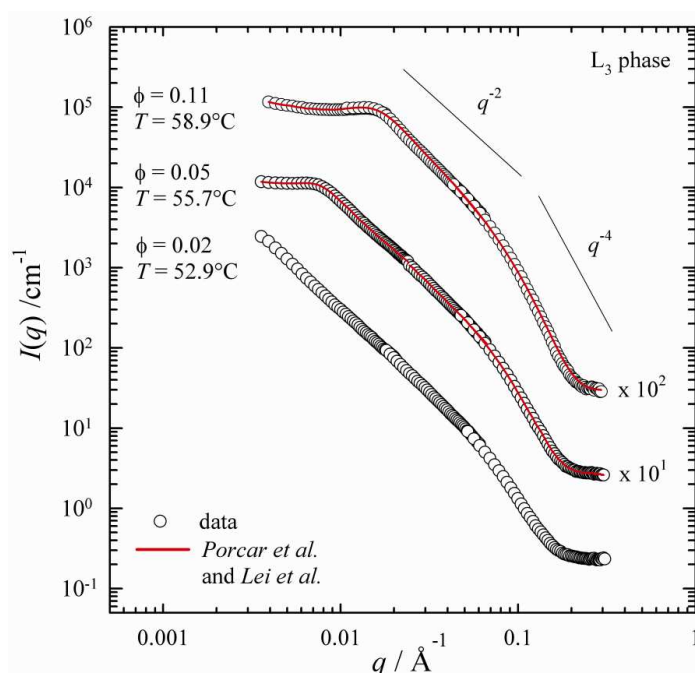


Figure 48: SANS-intensity I plotted versus the scattering vector q for the sponge phase L_3 in the $D_2O - C_{12}E_4$ system at a surfactant volume fraction $\phi = 0.02$ and a temperature $T = 52.9^\circ\text{C}$, $\phi = 0.05$ and a temperature $T = 55.7^\circ\text{C}$ and at $\phi = 0.11$ and a temperature $T = 58.9^\circ\text{C}$ in a double-log plot. The scattering curve at $\phi = 0.02$ corresponds to absolute intensities while the others are separated by a factor of ten. The data was analyzed using the description of *Porcar et al.* and *Lei et al.*¹⁵⁹.

¹⁵⁷ R. Strey, W. Jahn, M. Skouri, J. Marignan, G. Porte, U. Olsson, *Structure and Dynamics of strongly interacting Colloids and Supramolecular Aggregates in Solution*, Kluxer Academic Publishers, Netherlands, 351 (1992).

¹⁵⁸ G. Porte, *J. Phys. Cond. Matter*, 4, 8649 (1992).

As the q -value of the weak maximum is a measure for the average distance d between the midplanes of two neighboring bilayers the latter can be calculated according to $d = 2\pi/q_{\max}$. More quantitative values of d are obtained using the structure factor of *Lei et al.*¹⁵⁹, which may be written

$$S(q) = 1 + \frac{A \arctan[q\xi_{io}/2]}{q} + \frac{B}{1/\xi_3^2 + (q - q_3)^2} \quad [42]$$

with ξ_{io} being the "inside - outside" correlation length and ξ_3 the sponge correlation length. The first two terms of this expression are the structure factor derived by *Roux et al.*^{160,161} and describe the membrane correlations on a length scale much larger than the pore size in terms of "inside - outside" correlation length ξ_{io} . This expression has been successfully used to fit light scattering data from different systems over a broad range of very small q -values. The last term is a *Lorentzian* term, which characterizes the scattering from the sponge structure by a correlation length ξ_3 and the average pore size $\xi \equiv 2\pi/q_3$.

Starting from an averaged membrane form factor *Porcar et al.*¹⁶² have derived an analytical approximation for the form factor

$$P(q) \approx 4(\pi\sigma^2\Delta\rho)^2 \frac{(1 - \cos[qt_0] \exp[-q^2 t_0^2 / 32]) / q^2}{q^2 \sigma^2 + 2 \exp[-q^2 \sigma^2 / 6]} \quad [43]$$

with $(\Delta\rho)^2$ being the nominal scattering contrast factor, σ the gyration and t_0 is the scattering contrast thickness. The scattering intensity is given by

$$I(q) = NP(q)S(q) + I_{incoh} \quad [44]$$

¹⁵⁹ N. Lei, C. R. Safinya, D. Roux, K. S. Liang, *Phys. Rev. E* **56**, 608 (1997).

¹⁶⁰ D. Roux, M. E. Cates, U. Olsson, R. C. Ball, F. Nallet, A. M. Bellocq, *Europhys Lett.*, **11**, 229 (1990).

¹⁶¹ D. Roux, C. Coulon, *J. Phys. Chem.*, **96**, 4147 (1992).

¹⁶² W. A. Hamilton, L. Porcar, P. D. Butter, G. G. Warr, *J. Chem. Phys.*, **116** (2002).

With N being the effective number of density $N = \phi/\pi\sigma^2\delta$, where δ is the membrane thickness and I_{incoh} the incoherent background scattering.

As can be seen the experimental data are quantitatively described by using the description of *Porcar et al.* and *Lei et al.*¹⁵⁹ (red curve). Table 2 summarizes the obtained parameters, *i.e.* the sponge scattering vector q_3 , ξ_{io} the "inside - outside" correlation length, ξ_3 the sponge correlation length, the average pore size ξ , σ the gyration, t_0 is the scattering contrast thickness and the incoherent scattering intensity I_{incoh} . Note, that with increasing surfactant volume fraction ϕ the pore size ξ is decreasing.

Table 2: Sponge scattering vector q_3 , ξ_{io} the "inside - outside" correlation length, ξ_3 the sponge correlation length, the average pore size ξ , σ the gyration, t_0 is the scattering contrast thickness and the incoherent scattering intensity I_{incoh} for $\text{D}_2\text{O} - \text{C}_{12}\text{E}_4$ system.

ϕ	$q_3/\text{\AA}^{-1}$	$\xi_{\text{io}}/\text{\AA}$	$\xi_3/\text{\AA}$	$\xi/\text{\AA}$	$\sigma/\text{\AA}$	$t_0/\text{\AA}$	$I_{\text{incoh}}/\text{cm}^{-1}$
0.05	$6.4 \cdot 10^{-3}$	400	35	982	26	25	0.27
0.11	$1.46 \cdot 10^{-2}$	300	24.5	430	32	22	0.38

EQUILIBRIUM STRUCTURE OF THE LAMELLAR PHASE L_α

The lamellar phase L_α , which is the initial state for later T -jumps to vesicular phase, was obtained by a T -jump from the L_3 phase, which microstructure has been already characterized. Scattering experiments in bulk contrast were performed for four different surfactant volume fractions $\phi = 0.02, 0.05, 0.08$ and 0.11 . The scattering curves obtained are shown in Figure 49:

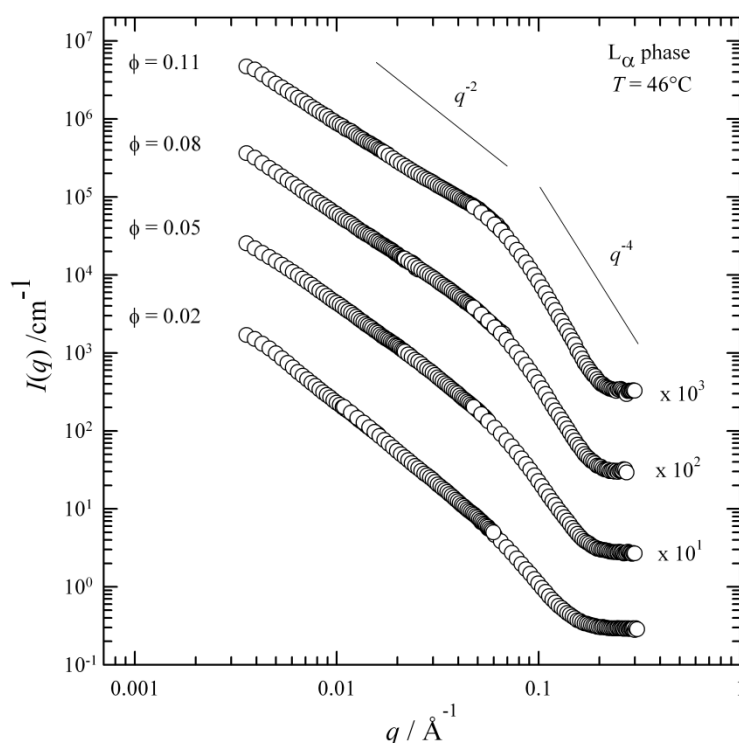


Figure 49: SANS-intensity I plotted versus scattering vector q for lamellar phase L_α in $D_2O - C_{12}E_4$ system at surfactant volume fractions $\phi = 0.02, 0.05, 0.08$ and 0.11 and a temperature $T = 46.0^\circ\text{C}$ in a double-log plot. At intermediate q -values the scattering is dominated by the leading q^{-2} dependence. The scattering curve at $\phi = 0.02$ corresponds to absolute intensities while the others are separated by a factor of ten.

As can be seen, *Bragg* peaks which is typical for lamellar ordered are not significantly present. This is possibly due to little order within the lamellar phases on the one hand and on the other hand caused by large membrane fluctuations, which are present at small surfactant volume fractions ϕ . The smaller the surfactant fraction the less significant the shoulder at mean q -values becomes.

EQUILIBRIUM STRUCTURE OF THE VESICULAR PHASE L_{α}^+ AS RESULT OF NEGATIVE T -JUMP

The temperature jump experiments were generally carried out after obtaining scattering curves of the initial phases (sponge or lamellar). A visual examination of the samples was then carried out to confirm the attainment of the desired one phase region. For diluted samples ($\phi = 0.02$ and 0.05) the equilibrium was attained fast and the equilibration of these samples occurred fast enough to overcome the phase separation stage. For the more concentrated samples ($\phi = 0.08$ and 0.11) this was not the case. Because of a wider two-phase channel (L_3+L_{α}) and faster kinetics due to higher surfactant concentration, the samples phase separated within seconds. Nevertheless, measurements were carried out on the phase separated samples. After scattering curves of equilibrium L_3 and L_{α} phases have been recorded, temperature jumps in water bath to L_{α}^+ phase ($T = 30^{\circ}\text{C}$) were performed. Three types of treatments of vesicular phase were performed on order to investigate size dependence of vesicles formed: first the unperturbed sample was recorded, then vortexed and finally sonicated. The chronological order was chosen from bigger to smaller size distribution of vesicles. Figure 50 shows the neutron scattering curves obtained from these experiments in the above mentioned order. Since the scattering curves do not demonstrate a *Bragg* peak or another characteristic feature, it is not possible to evaluate structural sizes quantitatively. What can be observed is a shoulder at mean q -values that becomes more recessed, as for lamellar phase. On the other hand the distribution of curves presented here has been reported already to show typical polydisperse behavior of vesicles¹⁶³. Generally, we expect $I(q)$ to show a dominant q^{-D} dependence, whereas D is the dimensionality of aggregates being $D = 2$ for bilayers. The scattering patterns of all samples of the L_{α}^+ phase do not show specific features and therefore they do not provide direct evidence for vesicles.

At intermediate q -values we find the leading q^{-2} dependence characteristic for the local bilayer. But at lower q -values there is a progressive crossover towards a weaker dependence which depends in a non-straightforward manner on the system and the concentration of the sample.

¹⁶³ P. N. Pusey, in *Neutrons, X-rays and Light: Scattering Methods Applied to Soft Condensed matter*, edited by P. Lindner and T. Zemb, Elsevier, Amsterdam, p. 312 (2002).

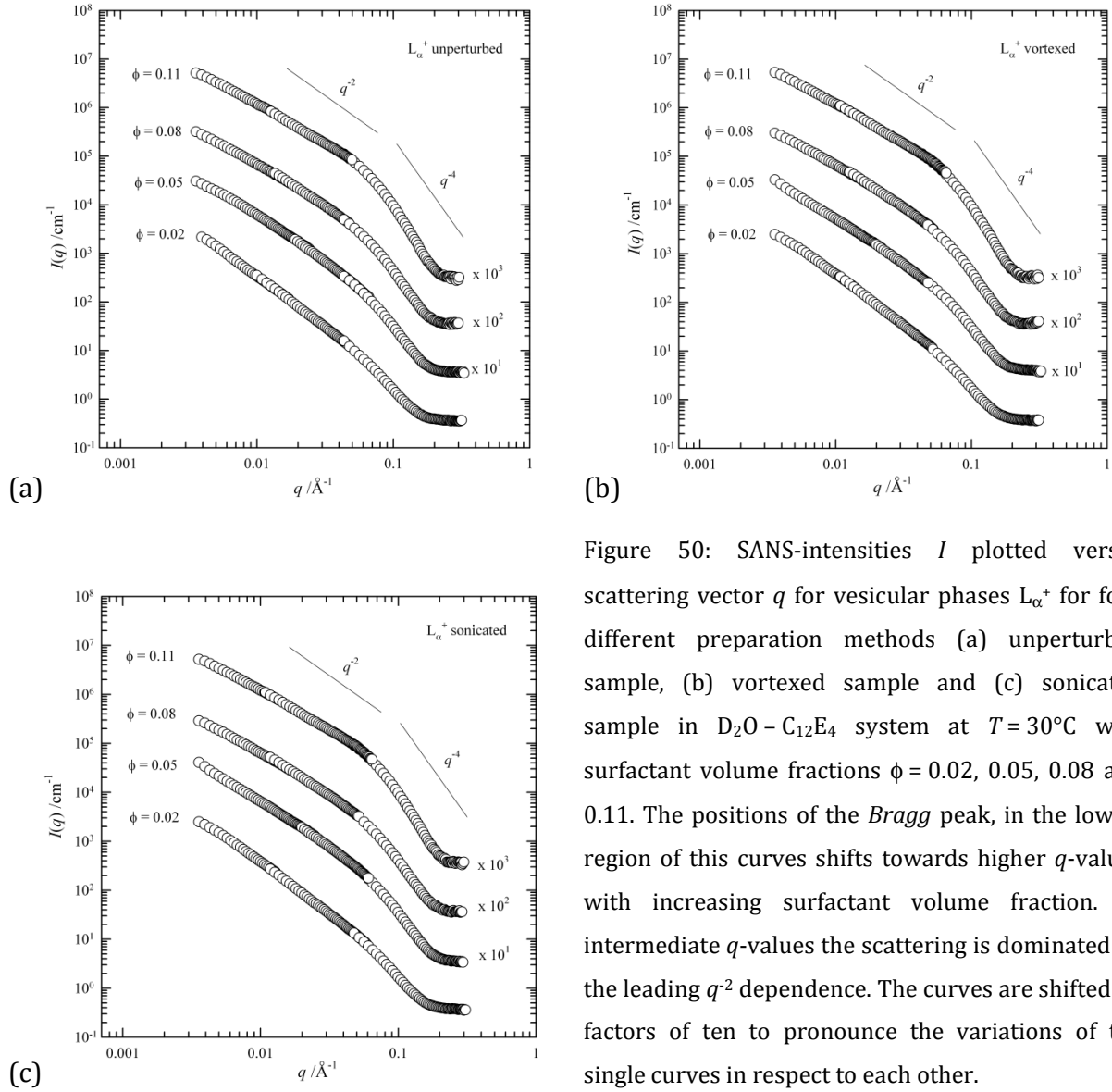


Figure 50: SANS-intensities I plotted versus scattering vector q for vesicular phases L_{α}^{+} for four different preparation methods (a) unperturbed sample, (b) vortexed sample and (c) sonicated sample in $D_2O - C_{12}E_4$ system at $T = 30^{\circ}C$ with surfactant volume fractions $\phi = 0.02, 0.05, 0.08$ and 0.11 . The positions of the *Bragg* peak, in the low q -region of this curves shifts towards higher q -values with increasing surfactant volume fraction. At intermediate q -values the scattering is dominated by the leading q^{-2} dependence. The curves are shifted by factors of ten to pronounce the variations of the single curves in respect to each other.

The main reason for the non specific character of the scattering curves is the size polydispersity. Neglecting interactions, for a monodisperse dispersion of vesicles of internal radius R_i and external radius R_e (so $R_e - R_i = \delta$), we would expect for the scattering intensity:

$$I(q) = \phi V(\Delta\rho)^2 \left(3 \frac{\sin qR_e - qR_e \cos qR_e - \sin qR_i + qR_i \cos qR_i}{q^3(R_e^3 - R_i^3)} \right)^2. \quad [45]$$

Eq. 45 indeed shows a series of maxima and minima when $q^2 I(q)$ is plotted versus q , characteristic of the radii: R_i and R_e . But for the very polydisperse situation typical for the L_{α}^{+}

phase, these maxima and minima are blurred out and nothing specific remains to be exploited in the scattering. "Static scattering" alone cannot characterize unambiguously phases of polydisperse vesicles.

4.3.1.2 POSITIVE TEMPERATURE JUMP EXPERIMENTS:

EQUILIBRIUM STRUCTURE OF THE MICELLAR PHASE L_1

The micellar phase L_1 , which is found in the phase diagram at low temperatures is the initial state for positive T -jumps to vesicular phase. Scattering experiments in bulk contrast were performed for the L_1 phase at $T = 4^\circ\text{C}$ within $\text{D}_2\text{O} - \text{C}_{12}\text{E}_4$ system with five different surfactant volume fractions $\phi = 0.002, 0.02, 0.05, 0.08$ and 0.11 . Figure 51 shows the neutron scattering curves obtained from these experiments. The individual curves are multiplied by factors of ten to shift them in respect to each other for transparency. What can be observed is a shift in forward scattering with increasing concentration. At the lowest surfactant volume fraction $\phi = 0.002$ (black dots) a q^{-1} dependence is observed, the scattering curve has a typical shape for cylindrical micelles. But for higher concentrations this dependence is not obvious, because of inter-aggregate interaction effects⁹⁶.

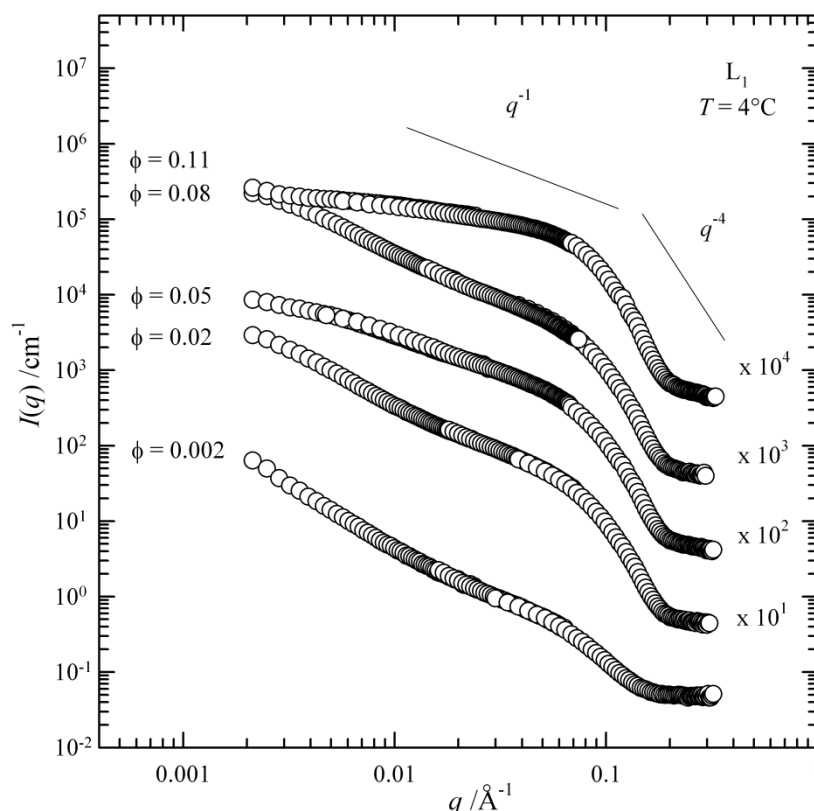


Figure 51: SANS-intensities I plotted versus scattering vector q for micellar phase L_1 in $\text{D}_2\text{O} - \text{C}_{12}\text{E}_4$ system with surfactant volume fractions $\phi = 0.002, 0.02, 0.05, 0.08$ and 0.11 at temperature $T = 4^\circ\text{C}$. At intermediate q -values the scattering is dominated by the leading q^{-1} dependence for $\phi = 0.02, 0.05, 0.08$. The curves are shifted by factors of ten to pronounce the variations of the single curves in respect to each other.

For the positive temperature jumps it is important to know the initial state within L_1 . As shown in Figure 52 within the L_1 micelles can form different kind of aggregates. At very low temperatures and surfactant mass fractions globular micelles can be found. With increasing surfactant mass fraction γ and with increasing temperature T larger aggregates form, like cylinders or even networks. It is also important to notice, that below the critical point the so called critical fluctuations are present, which can influence measurements.

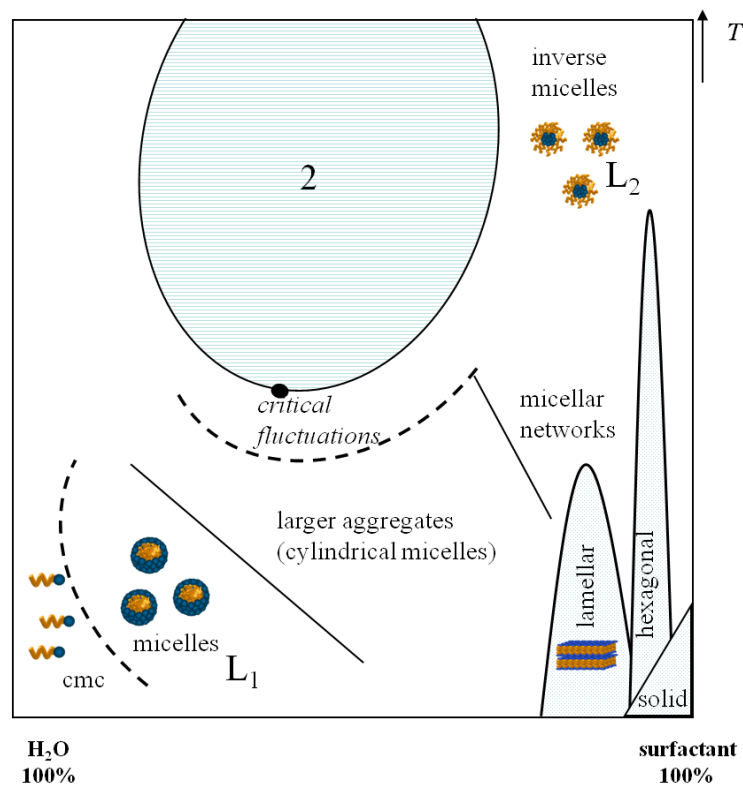
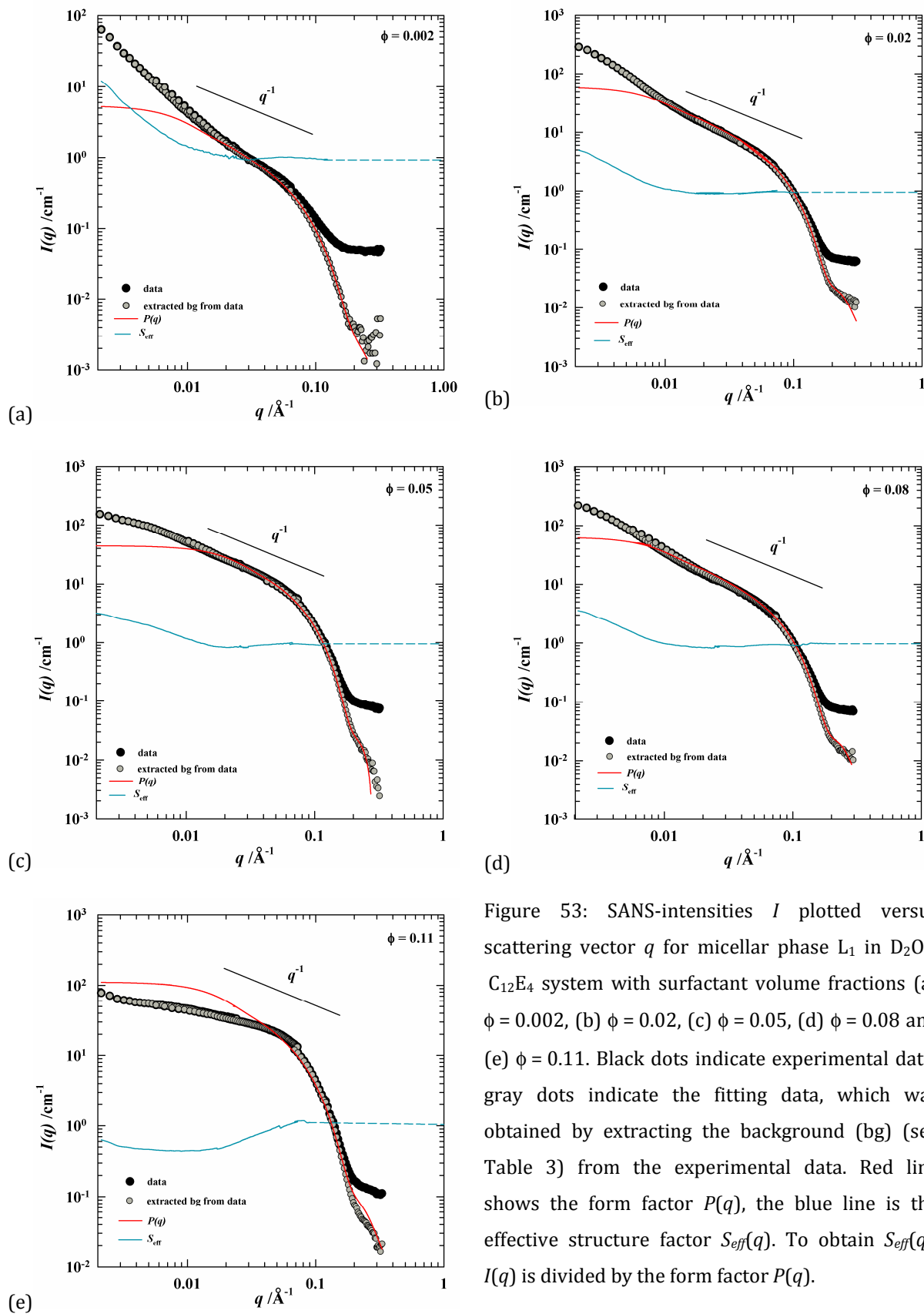


Figure 52: Schematic phase diagram of a binary non ionic surfactant - water system focusing the regime below the critical point, the L_1 regime, redrawn from *Strey et al.*⁸³.

For the present work we are not interested in correct fitting, but on the overall equilibrium structure of this phase, in order to know about the initial state for the temperature jumps (L_1 to L_{α^+}). Figure 53 shows SANS-intensities I plotted versus scattering vector q for micellar phase L_1 in $D_2O - C_{12}E_4$ system with surfactant volume fractions (a) $\phi = 0.002$, (b) $\phi = 0.02$, (c) $\phi = 0.05$, (d) $\phi = 0.08$ and (e) $\phi = 0.11$.



We used the model of cylinders with polydisperse cross section

$$I(q) = n\Delta\rho^2 S(q)L^2 P_{rod}(q) \int_0^{\infty} A^2 P_{cross}(q, R) W(R, R_0, \sigma) dR + bg. \quad [46]$$

to describe the scattering curves, with n being the number of density of droplets (calculated by dividing the total area of the internal interface $\phi_{c,i}a_s/v_s$ by the interfacial area $4\pi(R_0^2 + \sigma^2)$ per droplet), $S(q)$ the structure factor (Eq. [55]), A , $W(R, R_0, \sigma)$ the distribution function, which yields an analytical solution of the integral, R the cylinder radius and σ the polydispersity, bg the incoherent background. The axial contribution along the rods of length L is given by

$$P_{rod}(q) = \frac{2Si(qL)}{qL} - 4 \frac{\sin^2(qL/2)}{q^2 L^2} \quad [47]$$

and

$$P_{cross}(q) = \left(\frac{J_1(qR)}{qR} \right)^2 \quad [48]$$

is the cross section contribution for a polydisperse spherical cross section of area A , with J_1 being the *Bessel* function first order¹⁶⁴.

The form factor $P(q)$ for cylindrical micelles was calculated and added to the graphs (red lines), for all five different surfactant volume fractions $\phi = 0.002, 0.02, 0.05, 0.08$ and 0.11 (Figure 53). As can be seen the fit describes the curve at intermediate q -values quantitatively, while at low q -values deviations to the data are big. The effective structure factor $S_{eff}(q)$ was obtained by dividing $I(q)$ by the form factor $P(q)$ (blue lines). It is plotted in

¹⁶⁴ T. Foster, Dissertation, Köln (2006).

the same graphs in Figure 53 to make the effect within the low and high q -regime clear. At low surfactant volume fractions ($\phi = 0.002$) this effect is small, but for the biggest surfactant volume fractions ($\phi = 0.11$) this effect is big. For cylindrical micelles the scattering data should continue the q^{-1} gradient, but due to the $S_{eff}(q)$ the curves are pressed down. With increasing q -values, the magnitude of such fluctuations increases since local structural rearrangements and density fluctuations are more likely to occur. This leads to an increase of structure factor with increasing q -values. Accordingly, the effective structure factor $S_{eff}(q)$ is much lower for immediate q -values than the high q value of $S_{eff}(q) \approx 1$. The effective structure factor $S_{eff}(q)$ increases monotonically with increasing q -values to reach his limit value at high q -values (instead of oscillations). This behavior might be explained by a polydispersity in the average of cylindrical structures, or by shape polydispersity due to fluctuations of the surfactant membrane. These fluctuations are relevant for phase transitions in such a binary surfactant - water system. So far, the fit parameters are summarized in Table 3:

Table 3: Variable parameters, the background bg , of the form factors $P(q)$ for the five different surfactant volume fractions $\phi = 0.002, 0.02, 0.05, 0.08$ and 0.11 .

ϕ	bg	σ	L [Å]	R_0 [Å]
0.002	- 0.04585	5.0	500	17.0
0.02	- 0.0500	4.1	550	18.8
0.05	- 0.0718	4.0	200	18.8
0.08 (corr: 0.025)	- 0.0575	4.0	500	18.8
0.11	- 0.0955	4.5	250	18.0

Close to upper miscibility gap *i.e.* $\phi = 0.002, 0.02, 0.05$ and 0.08 we observe a strong increase of the scattering intensity at low q -values caused by critical fluctuations which are known to come into play near critical phase boundaries. Therefore the product of the modified *Ornstein-Zernike* structure factor was fitted to the effective structure factor^{165,166}

¹⁶⁵ L.S. Ornstein and F. Zernike. Accidental deviations of density and opalescence at the critical point of a simple substance. *Proc. Koninklijke Akademie Van Wetenschappen Te Amsterdam*, **17**:793-806, 1914.

¹⁶⁶ M. Kotlarchyk, S. H. Chen, J. S. Huang. *Phys. Rev. A*, **28**(1), 1983.

$$S(q) = 1 + \frac{I_0}{1 + q^2 \xi^2}. \quad [49]$$

with ξ is the correlation length. This is fitted for the two surfactant concentrations $\phi = 0.05$ and $\phi = 0.08$ and shown in Figure 54.

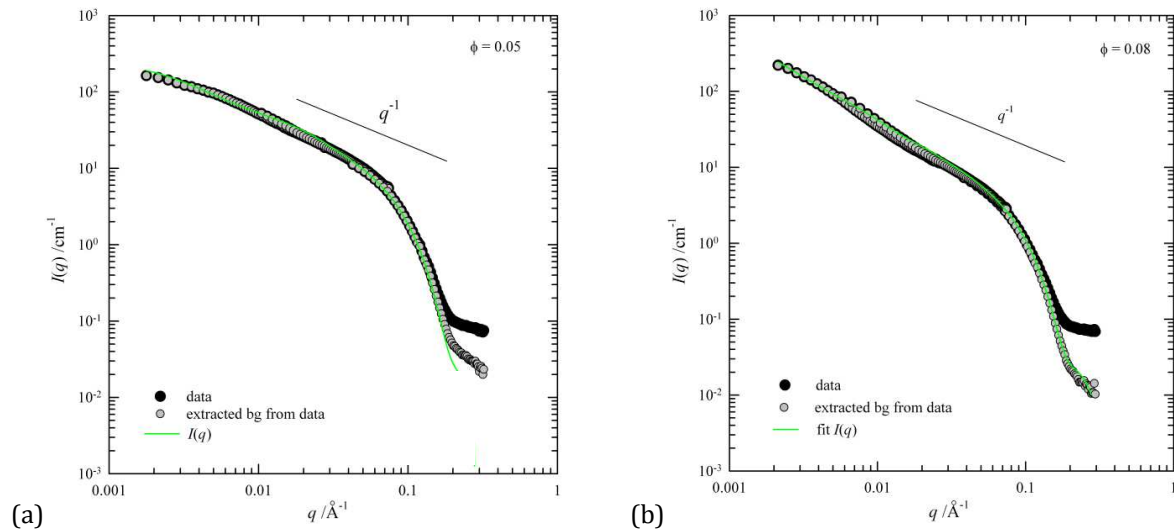


Figure 54: SANS-intensities I plotted versus scattering vector q for micellar phase L_1 in $D_2O - C_{12}E_4$ system with surfactant volume fractions (a) $\phi = 0.05$ and (b) $\phi = 0.08$. Black dots indicate experimental data; gray dots indicate the fitting data, which was obtained by extracting the background (bg) (see Table 3) from the experimental data. Green line shows the the fitted intensity $I(q)$ that was obtained with the cylinder form factor and the *Ornstein-Zernike* structure factor.

The fits for the two samples describe the data quantitatively. The fit parameters are summarized in Table 4 and as can be seen the correlation length is increasing with increasing surfactant mass fraction. For the lower and the higher surfactant concentrations, $\phi = 0.002, 0.02$ and 0.11 , these fits were not adequate and therefore they are not shown here.

Table 4: Fit parameters I_0 and the correlation length ξ for the two different surfactant volume fractions $\phi = 0.05$ and $\phi = 0.08$.

ϕ	I_0	ξ
0.05	4.5	350
0.08	9.1	680

EQUILIBRIUM STRUCTURE OF THE VESICULAR PHASE L_{α}^{+} AS RESULT OF POSITIVE T -JUMP

The temperature jump experiments were generally carried out after obtaining scattering curves of the initial phases (micellar). A visual examination of the samples was then carried out to confirm the attainment of the desired one phase region. For diluted samples ($\phi = 0.002, 0.02$ and 0.05) the equilibrium was attained fast and occurred fast enough to not significantly interfere with the phase transition kinetics. For the more concentrated samples ($\phi = 0.08$ and 0.11) this was not the case. Because of a wider two-phase channel ($L_1' + L_1''$) the samples phase separated within seconds. Nevertheless, measurements were carried out on the phase separated samples. After scattering curves of equilibrium L_1 phase was recorded, positive temperature jumps in water bath to L_{α}^{+} phase ($T = 30^{\circ}\text{C}$) were performed. Figure 55 shows scattering curves for the five surfactant volume fractions $\phi = 0.002, 0.02, 0.05, 0.08$ and 0.11 . The graphs include the scattering curves of L_{α}^{+} phases.

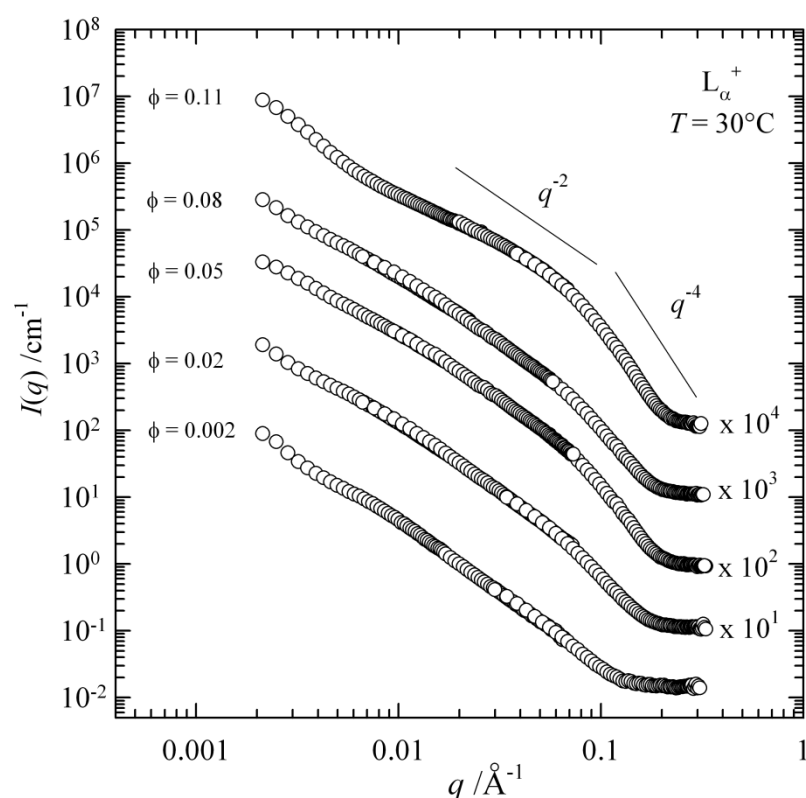


Figure 55: SANS-intensities I plotted versus scattering vector q for vesicular phases L_{α}^{+} in $\text{D}_2\text{O} - \text{C}_{12}\text{E}_4$ system with surfactant volume fractions $\phi = 0.002, 0.02, 0.05, 0.08$ and 0.11 . The positions of the *Bragg* peak, in the low q -region of this curves shifts towards higher q -values with increasing surfactant volume fraction. At intermediate q -values the scattering is dominated by the leading q^{-2} dependence. The curves are shifted by a factor of ten to pronounce the variations of the single curves in respect to each other.

As it was already shown for negative T -jumps in the previous paragraph, the scattering curves of L_{α}^+ phase in Figure 55 do not provide clear evidence for vesicles, but due to q^{-2} dependence in the intermediate q -regime bilayer structure can be taken for granted. The quantitative evaluation is difficult. What can be extracted from the graphs is that a potential shoulder of the single scattering curves is shifted to higher q -values with increasing surfactant volume fraction ϕ , so the possible inter-lamellar distances of the possible multilamellar vesicles decrease. At low q -values the scattering curves show rise to high intensities. A possible explanation could be the presence of bigger structures.

4.3.2 D₂O/GLYCEROL – C₁₂E₄

Phases of investigation in D₂O/glycerol – C₁₂E₄ system were same as for D₂O/glycerol – C₁₂E₄ system (L₃, L_α and L_α⁺). L_α⁺ phase was not introduced by a T -jump since the L_α⁺ phase is stable for a very wide temperature interval $T = 0 - 28^\circ\text{C}$. L₃, L_α and L_α⁺ phases samples of bilayer volumes $\phi = 0.02, 0.05$ and 0.08 were investigated. First scattering curves of the equilibrium L₃ phase were recorded, then the equilibrium L_α phase and finally of L_α⁺ phases. As an appropriate equilibration time for all three phases L₃, L_α and L_α⁺ 1 hour was chosen. D₂O/glycerol - C₁₂E₄ was investigated to benefit from the high viscosity and slow kinetics triggered by the presence of glycerol. Left graph in Figure 56 gives an overview of change of phase boundaries of D₂O - C₁₂E₄ by partial displacement of water by glycerol. At $\psi_{gly} = 0.50$ L_α⁺ phase ranges to zero degrees Celsius. Therefore it was chosen as adequate glycerol amount and in a next step the phase diagram was measured for the concentrations of interest (Figure 56, right).

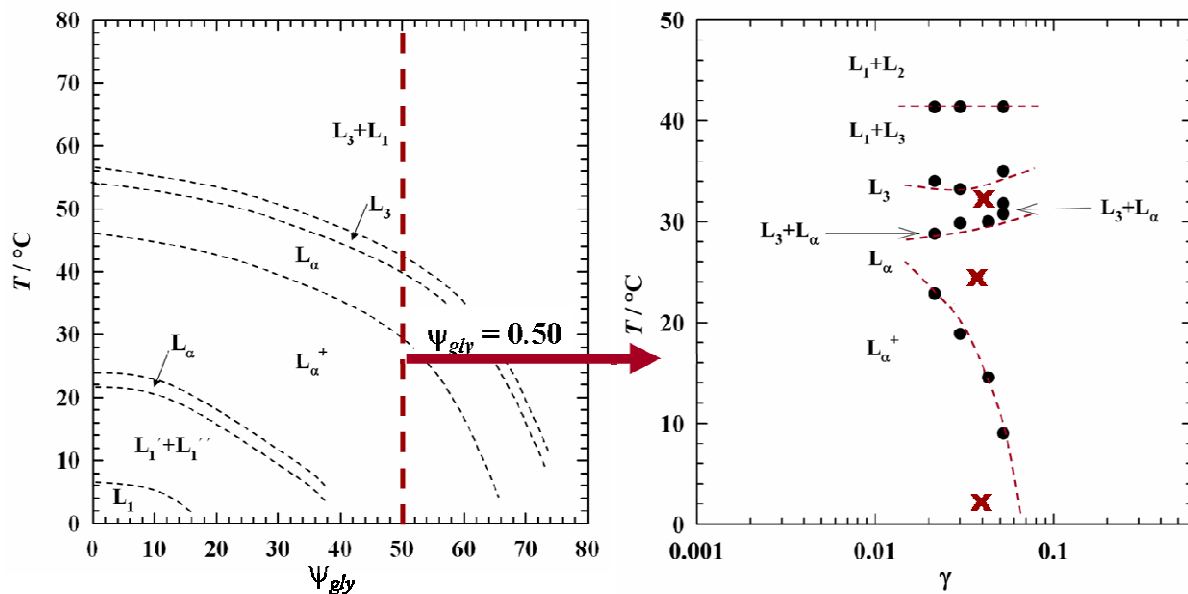


Figure 56: Left: Phase diagram of D₂O/glycerol – C₁₂E₄ at constant surfactant mass fraction γ with increasing glycerol amount ψ_{gly} . Temperature T is plotted versus glycerol mass fraction ψ_{gly} . Dashed perpendicular line indicates $\psi_{gly} = 0.50$. Right: Temperature T is plotted versus surfactant mass fraction γ for D₂O/glycerol – C₁₂E₄ system with $\psi_{gly} = 0.50$. Red crosses indicate schematically the positions of measured samples at a constant surfactant mass fraction γ , but three different temperatures $T = 4^\circ\text{C}$ (L_α⁺), 20°C (L_α) and 28°C (L₃).

EQUILIBRIUM STRUCTURES OF SPONGE L_3 , LAMELLAR L_α AND VESICULAR L_α^+ PHASE

The results obtained from small angle neutron scattering for D_2O /glycerol - $C_{12}E_4$ system are shown in Figure 57 for three surfactant volume fractions $\phi = 0.02, 0.05$ and 0.08 .

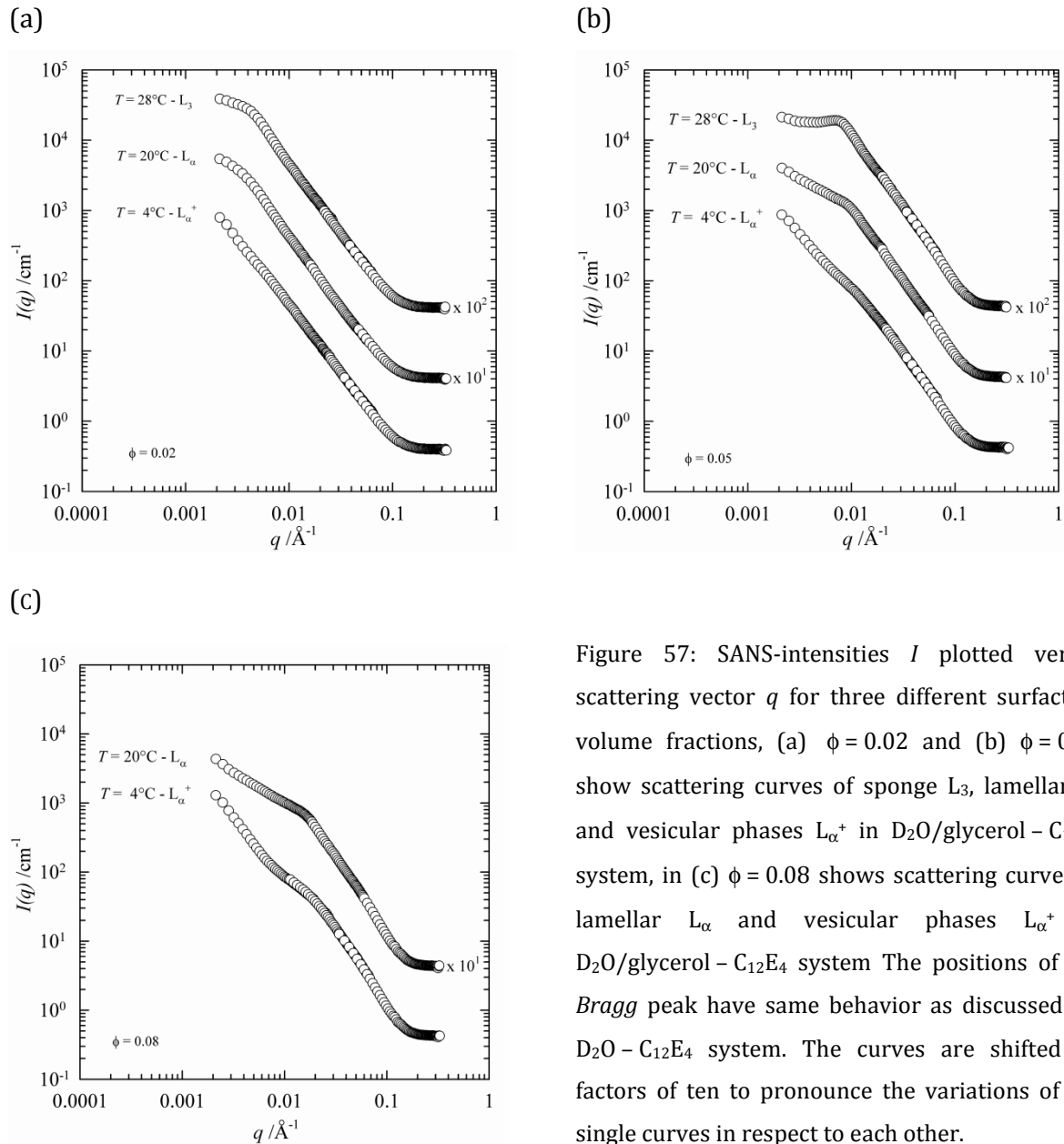


Figure 57: SANS-intensities I plotted versus scattering vector q for three different surfactant volume fractions, (a) $\phi = 0.02$ and (b) $\phi = 0.05$ show scattering curves of sponge L_3 , lamellar L_α and vesicular phases L_α^+ in D_2O /glycerol - $C_{12}E_4$ system, in (c) $\phi = 0.08$ shows scattering curves of lamellar L_α and vesicular phases L_α^+ in D_2O /glycerol - $C_{12}E_4$ system. The positions of the *Bragg* peak have same behavior as discussed for $D_2O - C_{12}E_4$ system. The curves are shifted by factors of ten to pronounce the variations of the single curves in respect to each other.

As for $D_2O - C_{12}E_4$ system the scattering patterns of all samples of the L_α^+ phase do not show adequate and specific features and therefore they do not provide direct evidence for vesicles. At intermediate q -values we find the leading q^{-2} dependence characteristic for the local bilayer¹⁶³. But at lower q -values there is a progressive crossover towards a weaker

dependence which depends in a non-straightforward manner on the system and the concentration of the sample and signs size polydispersity.

Fitting the lamellar peaks for D_2O /glycerol - $C_{12}E_4$ system with the help of the *Nallet et al.*¹⁶⁷ fit, one obtains a spacing of the water domains. The spacing is calculated via $d = 2\pi/q_{\max}$, which leads to a spacing of the amphiphilic surfactant layers of $d/2$ of each layer.

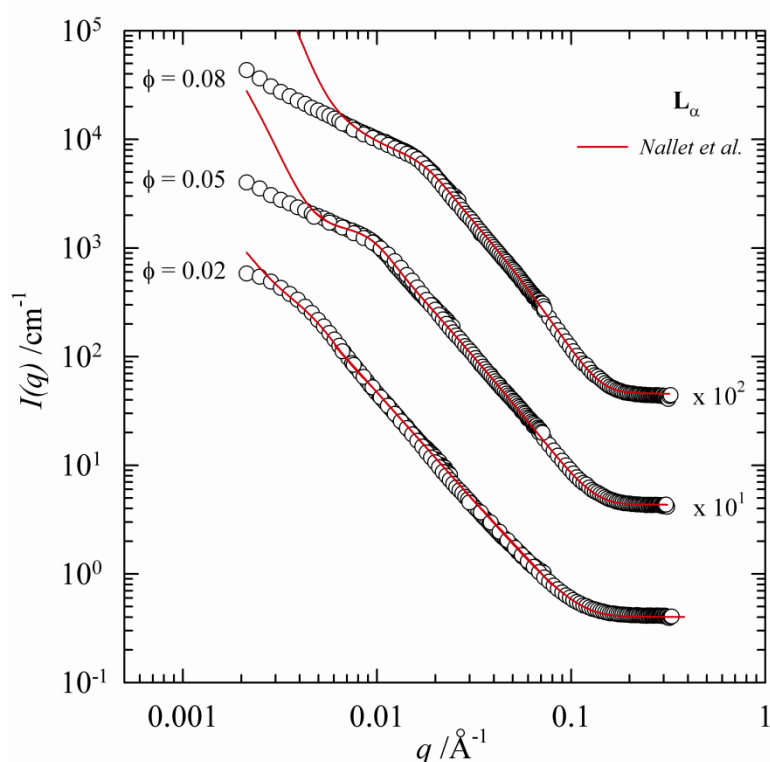


Figure 58: SANS-intensities I plotted versus scattering vector q for lamellar phase L_α in D_2O /glycerol - $C_{12}E_4$ system with surfactant volume fractions $\phi = 0.02, 0.05$ and 0.08 . The positions of the *Bragg* peak, in the low q -region of this curves shifts towards higher q -values with increasing surfactant volume fraction. At high q -values the scattering is dominated by the leading q^{-2} dependence. The curves are shifted by factors of ten to pronounce the variations of the single curves in respect to each other. The red lines show fits according with *Nallet et al.*¹⁶⁷.

One can observe that the typical characteristically lamellar *Bragg* peaks are rarely present. This is possibly due to little order within the lamellar phases on the one hand and on the other hand caused by large membrane fluctuations, which are present at small surfactant volume fractions ϕ . The smaller the surfactant fraction the less significant the peak at mean q -values becomes. The shoulders of the scattering curves are fitted using the *Nallet et al.*

model¹⁶⁷. With the help of a model combining geometry of the bilayers and layer displacement fluctuations, the scattering spectrum of a lyotropic lamellar phase is described quantitatively. As geometrical model a finite-size crystal of a lyotropic lamellar phase is described as the regular stacking – period d – of n identical layers of the thickness δ . However, the purely geometric model fails to describe the features of the scattering spectrum that are related to thermal fluctuations. These features are reflected in the broad shape of the *Bragg* peak and the occurrence of an anisotropic small angle scattering. The *Caillé*¹⁶⁸ model takes into account properly the thermodynamics of a lyotropic lamellar phase and describes rigorously these two features. *Nallet et al.*¹⁶⁷ combined the relevant features of the previous two models, *i.e.* taking into account consistently both the geometry – the finite thickness of the membrane – and the thermodynamics – the layer displacement fluctuations. Using *Caillé* model, the form factor $P(q)$ is given by

$$P(q) = \frac{2\Delta\rho^2}{q^2} \left[1 - \cos(q\delta)e^{-q^2\sigma^2/2} \right] \quad [50]$$

with $\Delta\rho$ being the contrast between the hydrophobic and hydrophilic part. σ is the geometric thickness of the layer. The geometrical thickness for *n*-decyltetraoxyethylene (C₁₂E₄), having 12 carbon atoms, was chosen $\delta = 12\text{\AA}$. σ is fixed at $\delta/4$. Approximating the effect of final resolution, this yields the following expression for the resolution-limited structure factor $S(q)$:

$$S(q) = 1 + 2 \sum_1^{N-1} \left(1 - \frac{n}{N} \right) \cos \left(\frac{qdn}{1 + 2\Delta q^2 d^2 \alpha(n)} \right) \cdot \exp \left(\frac{-2q^2 d^2 \alpha(n) + \Delta q^2 d^2 n^2}{2(1 + \Delta q^2 d^2 \alpha(n))} \right) \cdot \left(\frac{1}{\sqrt{1 + 2\Delta q^2 d^2 \alpha(n)}} \right). \quad [51]$$

$\alpha(n)$ denotes the correlation function

¹⁶⁷ F. Nallet, R. Laversanne, D. Roux, *J. Phys. II*, **3**, 487 (1993).

¹⁶⁸ A. Caillé, *Hebdo. Acad. Sci. Paris B* **274**, 891 (1972).

$$\alpha(n) = \frac{\eta}{2\pi^2} [\ln(\pi n) + 0.5772] \quad \text{for } n \gg 1 \quad [52]$$

with n being the number of undulating bilayers. Δq^2 is the resolution function. The resolution function is taken from *Glinka et al.*¹⁶⁹ and transformed into the shape as shown in *Suganuma et al.*¹⁷⁰. Whereas the form factor $P(q)$ is a slowly varying function the structure factor $S(q)$ is sharply peaked and has much stronger variations. Fitting now the lamellar peak with the help of the *Nallet* model one obtains a spacing d_{fit} of the water domains. The spacing is calculated via $d_{\text{fit}} = 2\pi/q_{\text{max}}$, which leads to a spacing of the amphiphilic surfactant layers of $d/2$ of each layer. The fitting values are shown in Table 5. For the lowest surfactant volume fraction $\phi = 0.02$ the *Bragg* peak is positioned at low q -values, that were measured with neutron wave length of 12\AA , for this regime the fit of *Nallet* is not suitable. Therefore the spacing of the water domains cannot be determined accurately using the *Nallet* model for $\phi = 0.02$.

Table 5: Spacing of the water domains d_{fit} and q_{max} for the four surfactant mass fractions $\phi = 0.02, 0.05$ and 0.08 for $\text{D}_2\text{O}/\text{glycerol} - \text{C}_{12}\text{E}_4$ system ($\psi = 0.50$).

ϕ	d_{fit}/nm
0.02	1400
0.05	610
0.08	285

For $\phi = 0.05$ and For $\phi = 0.08$ the spacing of the water domains d_{fit} is decreasing with increasing surfactant mass fraction. Due to the increase of surfactant molecules in solution more interface is needed; this is reflected by the d_{fit} -value.

¹⁶⁹ C. J. Glinka, J. M. Rowe, and J. G. LaRock, *J. Appl. Cryst.* **19**, 427 (1986).

¹⁷⁰ Y. Suganuma, M. Imai, and K. Nakaya, *J. Appl. Cryst.* **40**, 303 (2007).

4.4 IMAGING OF LAMELLAR-, SPONGE- AND VESICLE PHASE

Freeze fracture electron microscopy (FFEM) experiments were done for $\text{H}_2\text{O} - \text{C}_{12}\text{E}_4$ and $\text{H}_2\text{O}/\text{glycerol} - \text{C}_{12}\text{E}_4$ systems. In $\text{H}_2\text{O} - \text{C}_{12}\text{E}_4$ system positive (from L_1 to L_{α^+} phase) and negative (from L_{α} to L_{α^+} phase) temperature jumps were performed for an exemplary surfactant concentration of $\gamma = 0.03$, in $\text{H}_2\text{O}/\text{glycerol} - \text{C}_{12}\text{E}_4$ system the steady state L_3 , L_{α} and L_{α^+} phases were recorded. To begin with results obtained from FFEM for $\text{H}_2\text{O} - \text{C}_{12}\text{E}_4$ system will be presented in the following chapter.

Sample solutions were prepared in special glass tubes (see Appendix). Negative temperature jumps were performed in the water bath, from lamellar phase L_{α} to vesicular phase L_{α^+} .

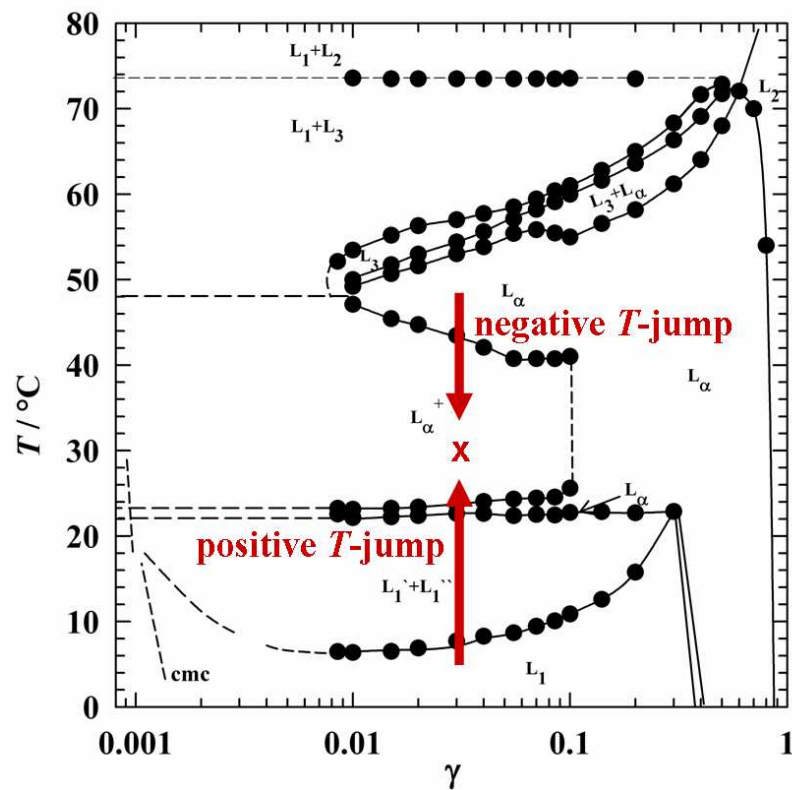


Figure 59: Phase diagram of $\text{H}_2\text{O} - \text{C}_{12}\text{E}_4$ system. Negative temperature jumps (red arrows) from $T = 48^\circ\text{C}$ (upper L_{α}) to $T = 30^\circ\text{C}$ (L_{α^+}) and positive temperature jumps from $T = 5^\circ\text{C}$ (L_1) to $T = 30^\circ\text{C}$ (L_{α^+}). FFEM pictures were taken for surfactant mass fraction $\gamma = 0.03$ after both T -jumps at same temperature $T = 30^\circ\text{C}$ (red cross).

Figure 59 allows a picture view of the performed T -jumps and investigated samples (indicated with red cross).

4.4.1 H₂O – C₁₂E₄: NEGATIVE T – JUMPS

The main focus was the study of the equilibrium structure of the L_{α}^+ phase and therefore temperature jumps (T -jump) from the phases adjacent, (L_{α} phase (below L_{α}^+), (L_{α} phase (above L_{α}^+) and L_3 phase) were used as a method to trigger the formation of the L_{α}^+ phase. This technique allows us to study the type and size of structures, especially formed in surfactant/water systems. FFEM was performed in this work to complement and support results obtained from DLS and SANS. Thus, the first step was to make images of the L_{α}^+ phase after a T -jump from L_{α} phase.

The results obtained from FFEM for H₂O - C₁₂E₄ after negative T -jump were unexpected. Noticeable, but not unexpected is that different structures within same grid were obtained. The most striking images from negative T -jumps are presented in Figure 60- Figure 62.

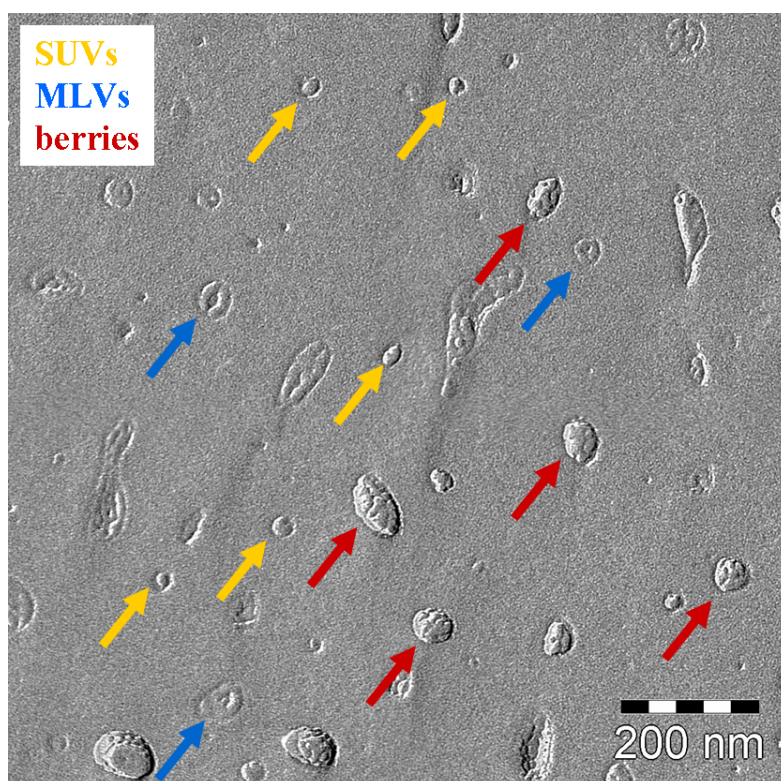


Figure 60: FFEM image of H₂O - C₁₂E₄ system after negative T -jump within the L_{α}^+ phase at $T = 30^{\circ}\text{C}$ for $\gamma = 0.03$.

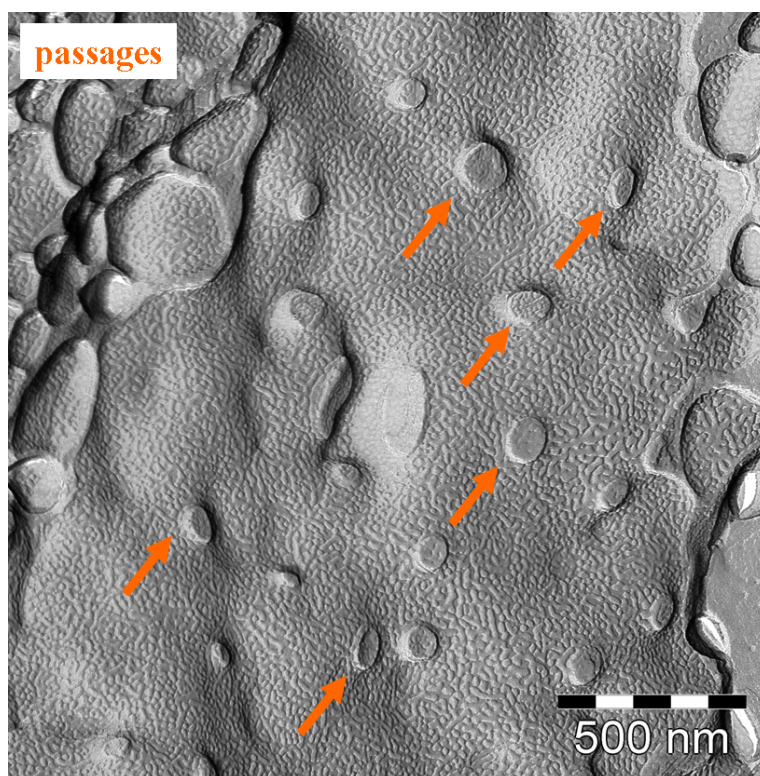


Figure 61: FFEM image of $\text{H}_2\text{O} - \text{C}_{12}\text{E}_4$ system after negative T - jump at $T = 30^\circ\text{C}$, $\gamma = 0.03$.

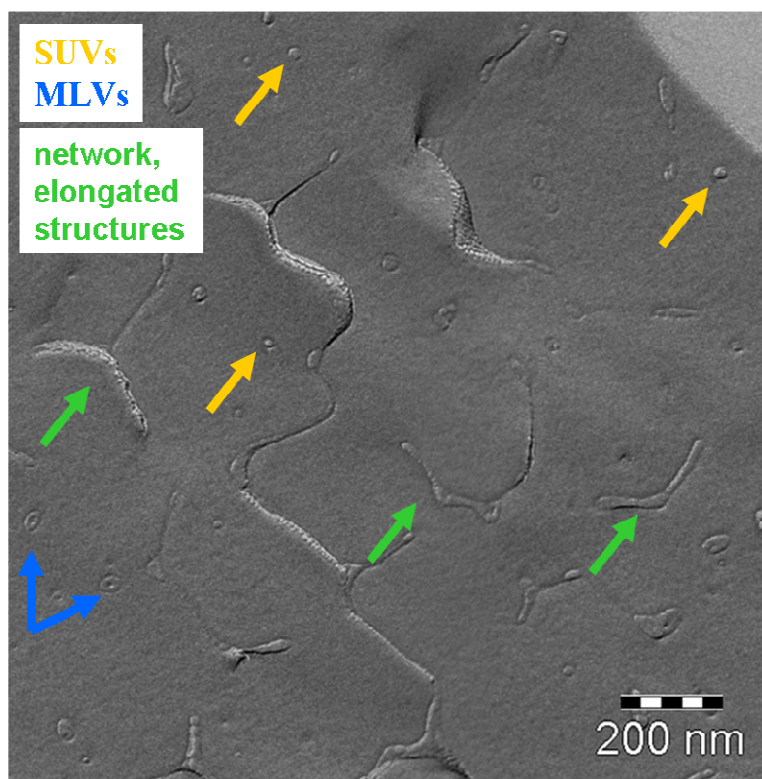


Figure 62: FFEM image of $\text{H}_2\text{O} - \text{C}_{12}\text{E}_4$ system after negative T - jump at $T = 30^\circ\text{C}$, $\gamma = 0.03$.

Figure 60 shows a fraction. Due to small surfactant concentration a lot of water surrounds the structures. Three types of structures are visible here: single lamellar vesicles (SUVs; yellow arrows), multi lamellar vesicles (MLVs; blue arrows) and also some structures that have an undulating surface and remind on raspberries (red arrows). That's why they are called here: "berries". These berries have a diameter of 60 to 80nm, whereas the SUVs measure 20 - 30nm and the MLVs 40 to 50nm. The corrugated surface of the berries will be discussed later in this chapter.

In Figure 61 another image is shown taken from another position of the same grid. One can see a waved surface dominating the image. In between one can notice some disk-like indentations, which represent interbilayer passages. One has to assume, that the fraction took place between two bilayer sheets, which are connected through passages. These passages are here indicated with red arrow bars. They have similar diameters of approximately 100nm.

Figure 62 shows an image also taken from same grid, showing once more SUVs and MLVs, but also some elongated structures (green arrows) that seem to come from kind of a network structure.

4.4.2 H₂O - C₁₂E₄: POSITIVE T - JUMPS ($L_1 \rightarrow L_{\alpha^+}$)

A thermodynamically stable phase is independent on way or procedure that led to its formation (path-independent). That is to say if structures within the L_{α^+} were thermodynamically stable then we should observe same structure, no matter if performing negative T - jump from L_{α} phase or positive T - jump from L_1 phase. Therefore positive T - jumps (from L_1 at 5°C to L_{α^+} at 30°C) were performed within the H₂O - C₁₂E₄ system and same surfactant concentration ($\gamma = 0.03$) as for the opposite T - jumps in order to determine the structures with FFEM and to see whether the results for both type of T - jumps agree.

The results obtained from FFEM for H₂O - C₁₂E₄ after positive T - jump show same structures as for negative T - jumps. Although, different structures were observed within same grid the majority of recorded images agree for both types of T - jumps. The most striking images from positive T - jumps are presented in Figure 63 - Figure 65.

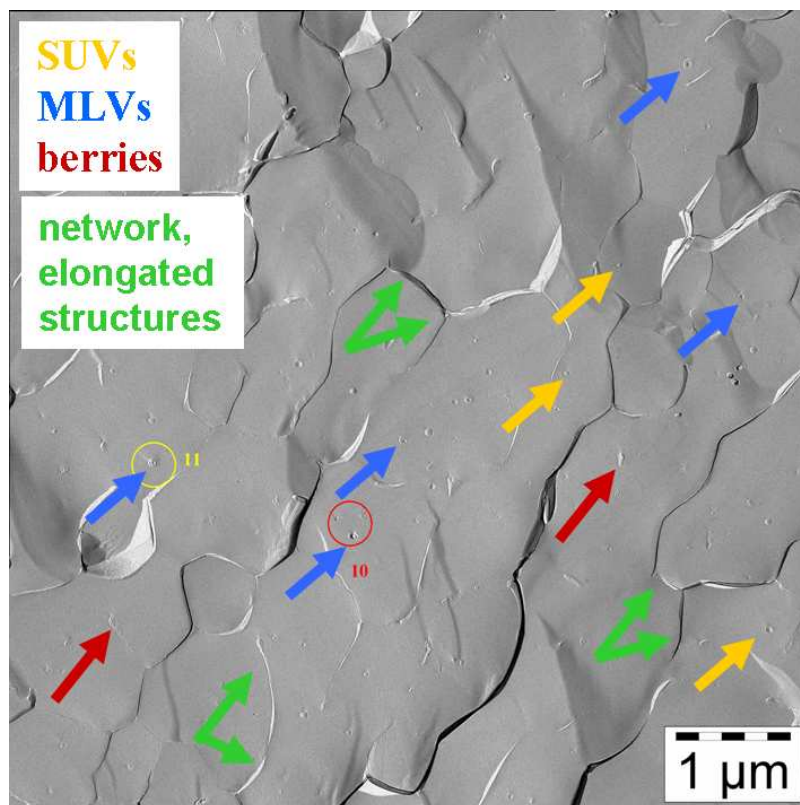


Figure 63: FFEM image of H₂O - C₁₂E₄ system after positive T - jump at $T = 30^\circ\text{C}$ (L_{α^+} phase), $\gamma = 0.03$.

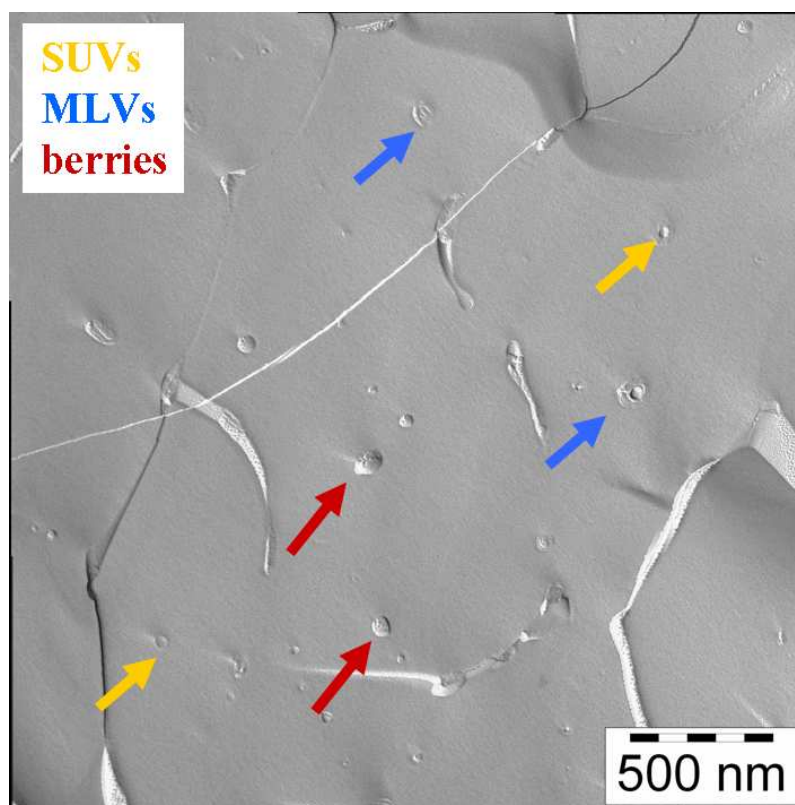


Figure 64: FFEM image of H₂O - C₁₂E₄ system after positive T - jump at $T = 30^\circ\text{C}$ (L_α^+ phase), $\gamma = 0.03$.

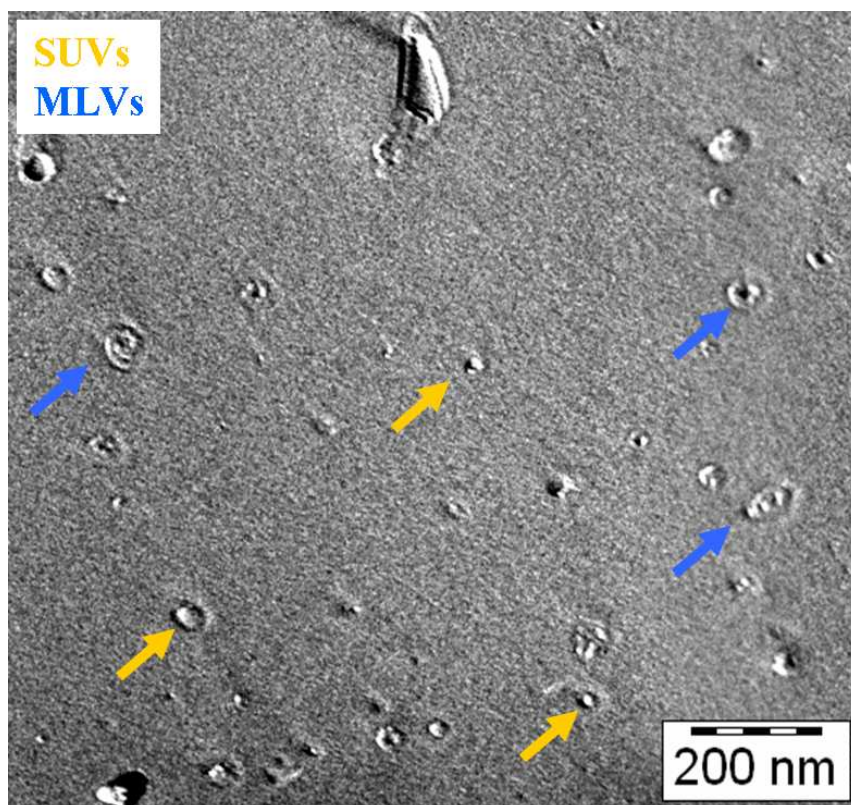


Figure 65: FFEM image of H₂O - C₁₂E₄ system after positive T - jump at $T = 30^\circ\text{C}$ (L_α^+ phase), $\gamma = 0.03$.

Figure 63 shows three types of structures visible: single lamellar vesicles (SUVs; yellow arrows), multi lamellar vesicles (MLVs; blue arrows) and also some structures that have an undulating surface and remind on raspberries (red arrows). They are all surrounded by a lot of water (the whole grey area). These structures are distributed in within the sample solution being almost equidistant. Another structure that appears as kind of super-lattice is network-like elongated aggregates. The berries have a diameter of 60 to 80nm, whereas the SUVs measure 20 – 30nm and the MLVs 40 to 50nm. The structure sizes here are in good agreement to the ones from negative T – jumps. Figure 64 shows another image taken from a different position of the same grid. Furthermore, the scale is 500nm so the structures mentioned already above can be observed better. Figure 65 is zoomed even better showing once more SUVs and MLVs.

4.4.3 H₂O/GLYCEROL – C₁₂E₄

L_{α}^+ ($T = 4^{\circ}\text{C}$), L_{α} ($T = 20^{\circ}\text{C}$) and L_3 ($T = 32^{\circ}\text{C}$) in H₂O/glycerol – C₁₂E₄ system ($\gamma = 0.08$) were freeze fractured and observed. The breaking difference to H₂O – C₁₂E₄ system is high viscosity and much slower kinetics but also the fact that miscibility gap of water/glycerol is at temperatures below 0°C . During the freezing process we do not undergo the two phase region, and therefore a phase separation into $L_1' + L_1''$ is avoided.

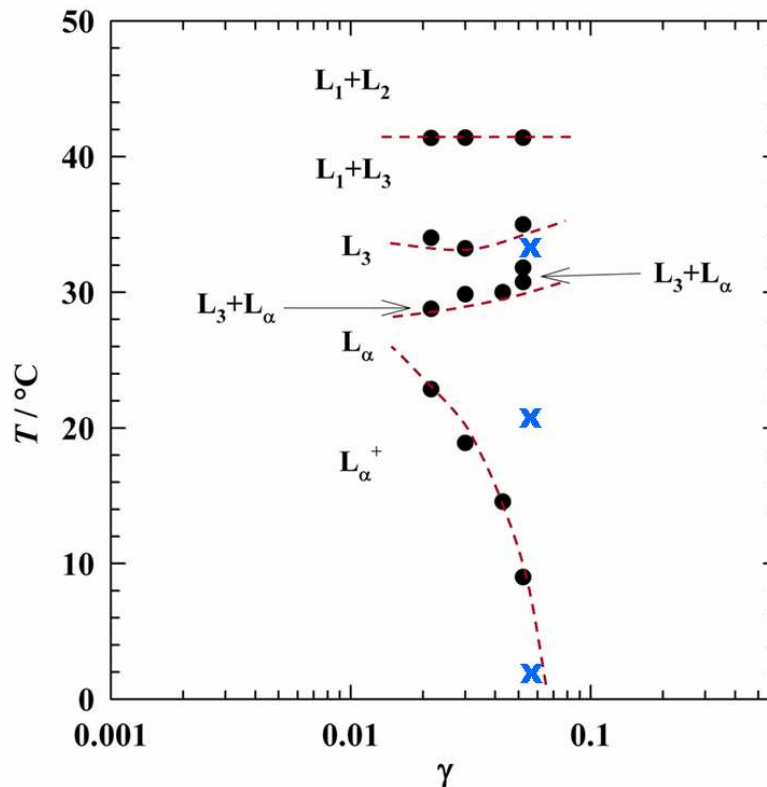


Figure 66: Phase diagram of the pseudo-binary water/glycerol – non-ionic surfactant system H₂O/glycerol – C₁₂E₄ for the five concentrations $\gamma = 0.02 - 0.06$. Blue crosses indicate the positions where the FFEM images are taken.

Figure 66 shows a partial phase diagram of H₂O/glycerol – C₁₂E₄ system, whereas the samples measured with FFEM and presented in the following are marked with blue crosses. The surfactant concentration was chosen in order to reproduce sample of Strey and Jahn and to ensure that the freezing process we use here corresponds to the results that were produced already with an older sample preparation method from 1996.

SPONGE PHASE L_3

In H_2O /glycerol - $C_{12}E_4$ system steady state samples were observed. Contrary to temperature jumps, samples were prepared in the special tubes, brought to desired temperature (here: $T = 32^\circ C$), than equilibrated for 30 min. This equilibration time is known to be sufficient, since the kinetics of L_3 at $\gamma = 0.08$ are known to be fast.

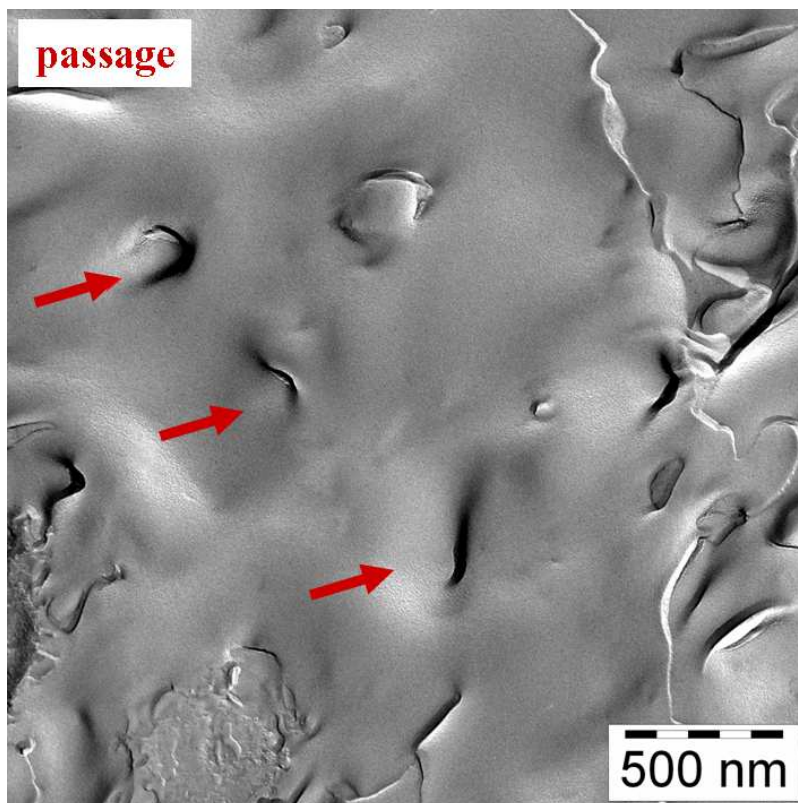


Figure 67: FFEM image of H_2O /glycerol - $C_{12}E_4$ system, $\psi = 0.50$, within the L_3 phase at $T = 32^\circ C$ for $\gamma = 0.08$.

In Figure 67 L_3 phase from H_2O /glycerol - $C_{12}E_4$ system is presented showing passages (stressed with red arrows). These passages are known to connect two bilayer sheets. The fraction is along these two bilayer sheets, whose surface is very smooth but still waves can be interpreted. The passages have elongated form exhibiting a size range of 200 – 300nm. In general the shapes of passages differ from those observed previously in the absence of glycerol.

LAMELLAR PHASE L_{α}

Figure 68 - Figure 70 present FFEM images from lamellar phase L_{α} within $H_2O/glycerol - C_{12}E_4$ system at $T = 25^{\circ}C$. Temperature was tuned to the desired value, while sample was stirred. After making sure that the sample shows birefringence it was equilibrated. The lamellar sample is very viscous. Due to slow kinetics and bubbling, equilibration time was one hour.

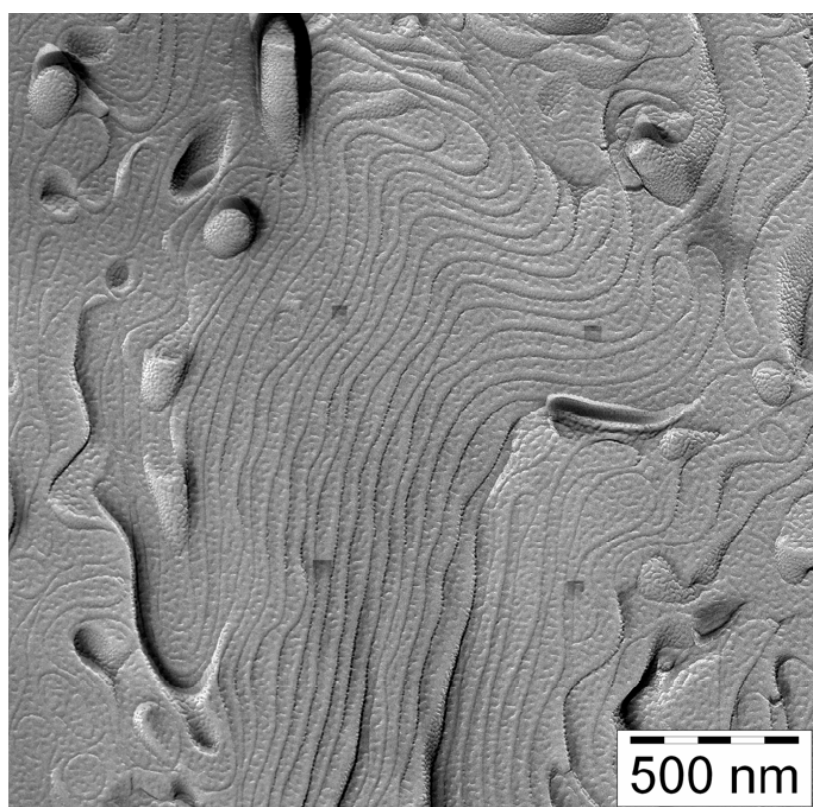


Figure 68: FFEM image of $H_2O/glycerol - C_{12}E_4$ system, $\psi = 0.50$, within the L_{α} phase at $T = 25^{\circ}C$ for $\gamma = 0.08$.

In Figure 68 an image of lamellar phase is shown, illustrating nearly equidistant lamellae. This lamellar structure is undulating, forming droplets at the end of the sheets. The area between the sheets is textured (see also Figure 61). Some spherical forms can also be found, which maybe a result of sample stirring. Figure 69 and Figure 70 present the lamellar phase from another part of the grid showing bilayer closed to a sphere - a typical multi lamellar vesicle (MLV) consisting of 10 - 30 layers. In Figure 69 these layers are not connected but fit together like a cogwheel (red arrow). Blue arrows indicate the centre of such a sphere. Interlamellae distances are approximately 40 nm.

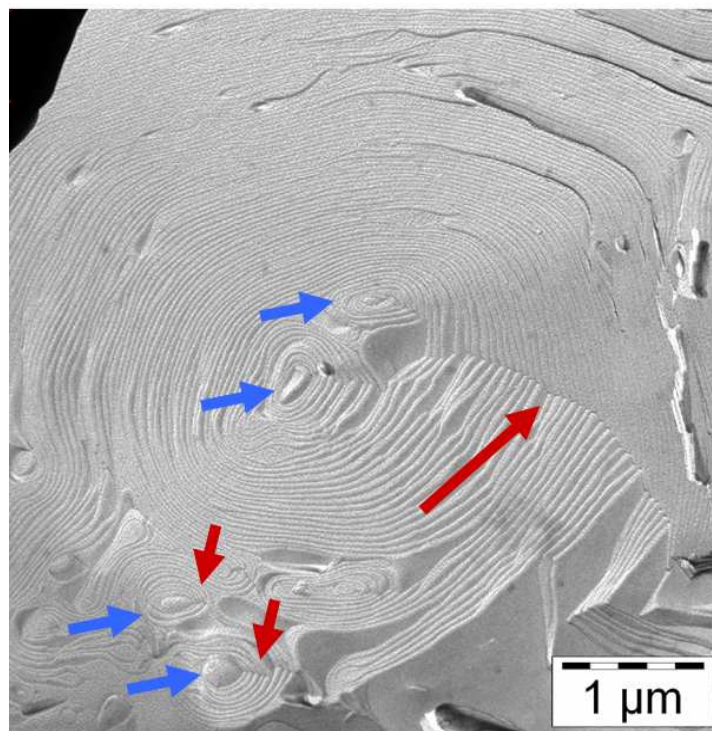


Figure 69: FFEM image of H₂O/glycerol - C₁₂E₄ system within the L α phase at $T = 25^\circ\text{C}$ for $\gamma = 0.08$.

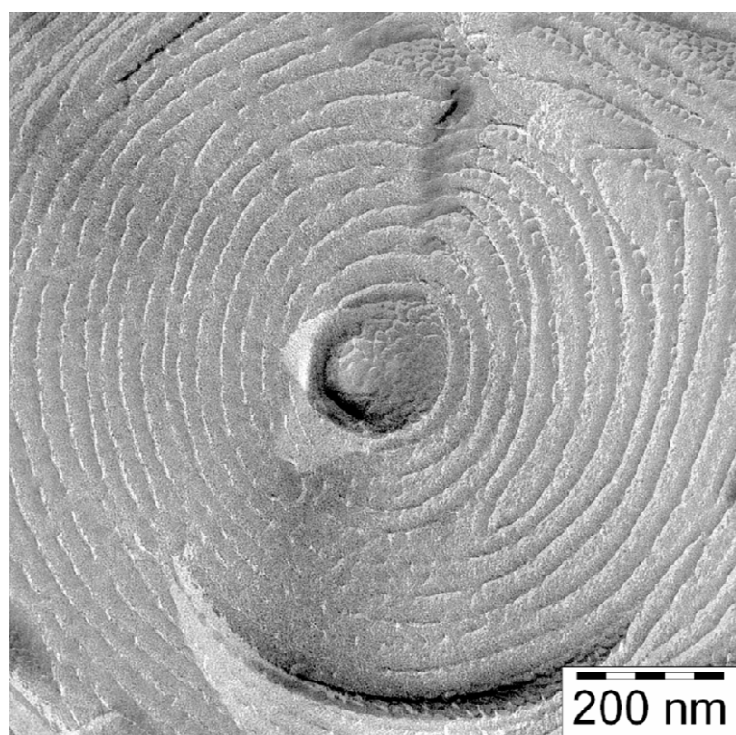


Figure 70: FFEM image of H₂O/glycerol - C₁₂E₄ system within the L α phase at $T = 25^\circ\text{C}$ for $\gamma = 0.08$.

VESICULAR PHASE L_{α}^{+}

In this subsection FFEM images from vesicular phase L_{α}^{+} within H_2O /glycerol - $C_{12}E_4$ system at $T = 8^{\circ}C$ are presented. Temperature was regulated with a cryostat to the desired value, while the sample was stirred. After making sure that the sample shows streaming birefringence it was equilibrated. As the lamellar sample, the vesicular phase is also viscous. Because of slow kinetics, low temperature and bubbling equilibration time was chosen to be over night (12 hours).

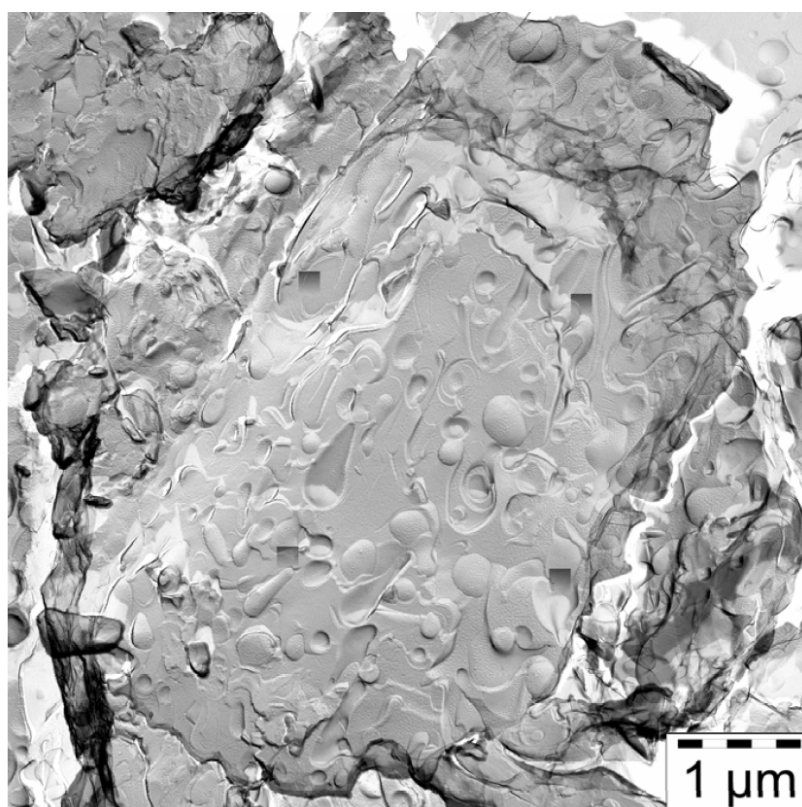


Figure 71: FFEM image of H_2O /glycerol - $C_{12}E_4$ system, $\psi = 0.50$, within the L_{α}^{+} phase at $T = 8^{\circ}C$ for $\gamma = 0.08$.

Figure 71 presents polydisperse vesicles of 200 – 500nm size in diameter surrounded by water and other vesicles. The image looks dynamic, which could indicate that the thermodynamic equilibrium is not reached yet. This image is a result that we have expected and predicted to see. In Figure 71 a summary of most predicative images recorded within L_{α}^{+} phase is shown. Images (a), (b) and (d) have a magnification of $1\mu m$, whereas (c) exhibits 500nm zoomed view. In image (a) bilayer sheets can nicely be recognized. The fraction shows a view on the different layers, but also on the surface of some layers.

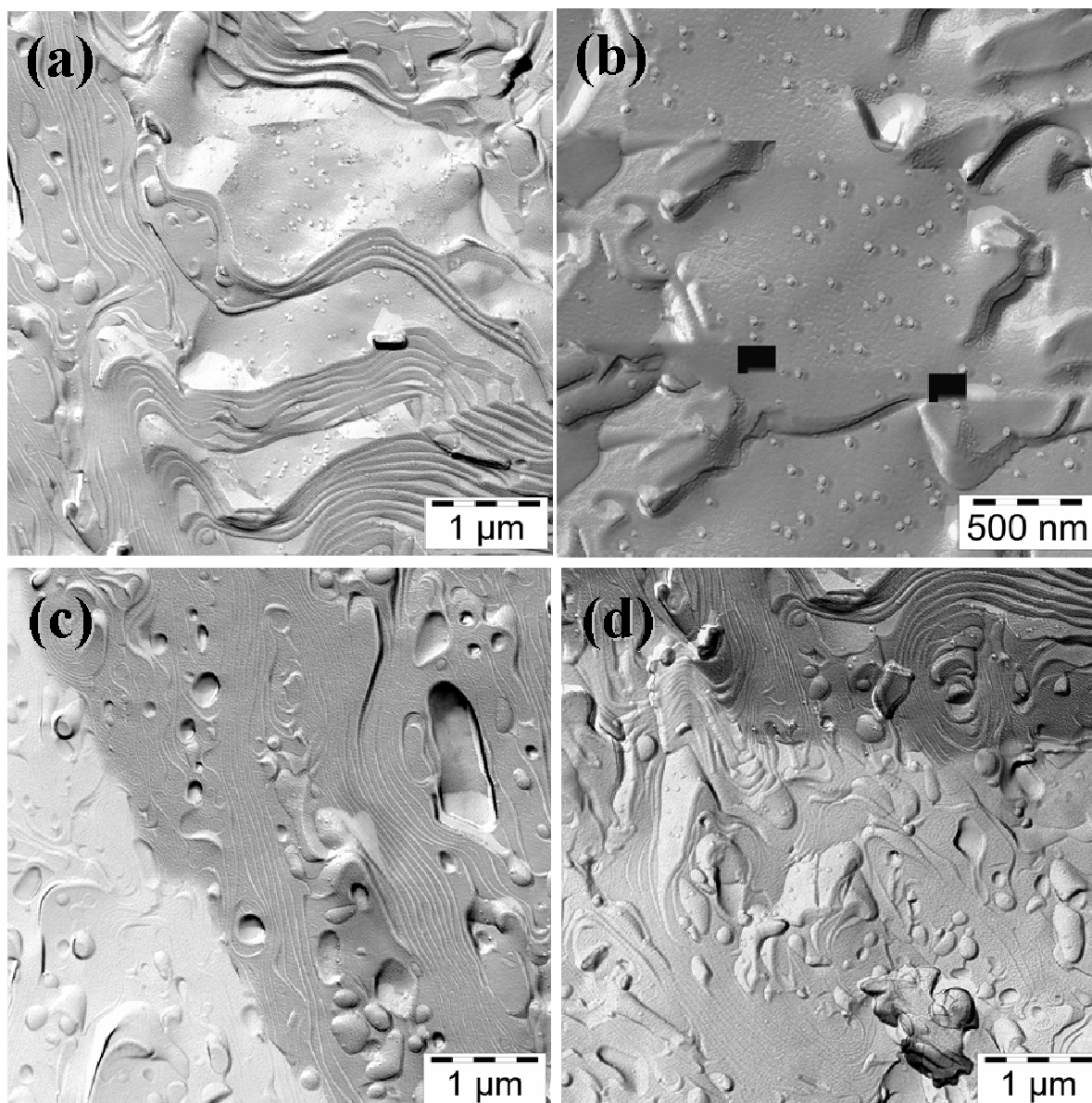


Figure 72: FFEM images of H₂O/glycerol - C₁₂E₄ system within the L_α⁺ phase at $T = 8^\circ\text{C}$ for $\gamma = 0.08$ showing the predominant structures found (a - d).

Most interesting discovery here are the monodisperse vesicles that are bedded on the interfacial surface of the lamellar layers. These small vesicles can be observed better in image (b). Their size is about 40nm. In images (c) and (d) coexistence between lamellar and vesicular phase is illustrated. Depending on fraction vesicles are either ripped out of the water or they appear as bumps. In the upper right corner of image (d) the lamellae are curving and are shown from the front. The lamellar distances are Equidistant having values of 40 nm, corresponding to the surfactant mass fraction of the sample and vesicles in image (b).

SUMMARY

FFEM have been determined to support the scattering techniques. Positive temperature jumps (L_1 to L_{α}^+) as well as negative temperature jumps (L_{α} to L_{α}^+) in $H_2O - C_{12}E_4$ system were performed (surfactant mass fraction $\gamma = 0.03$). To state a clear initial state for the positive temperature jump L_1 ($T = 5^\circ C$) was observed and network structure is persistent. L_{α}^+ phase ($T = 35^\circ C$) displays due to the network structure a number of monodisperse and single shell vesicles of 100nm mean size. L_{α}^+ phase ($T = 35^\circ C$) formed from L_{α} phase shows similar structures. Surprisingly and highly interesting are berry like structures of different sizes and shapes. A zoo of structures is presented, that clearly shows a non-equilibrium state in spite of equilibration time of $t = 30$ minutes. In addition L_{α}^+ ($T = 4^\circ C$), L_{α} ($T = 20^\circ C$) and L_3 ($T = 28^\circ C$) in $H_2O/glycerol - C_{12}E_4$ system ($\gamma = 0.06$) were freeze fractured and observed. The breaking difference due to high viscosity and much slower kinetics of this system is the fact that miscibility gap of water/glycerol is at temperatures below $0^\circ C$. During the freezing process we do not undergo the two phase region, and therefore a phase separation into $L_1' + L_1''$ is avoided. The results are as expected meaningful for this thesis, because they present why the prior scattering techniques have been difficult to evaluate. L_{α}^+ shows multilamellar vesicles, closed lamellae of 10 and more layers. But also in between the sheets one can find small monodisperse and unilamellar vesicles of 40 – 50nm diameter. L_{α} FFEM pictures show clearly the lamellar structure as the dominating structure. The direction of the lamellae can vary, but they are clearly equidistant. Both phases present also another very interesting feature. The undulations of the amphiphilic film are visible. L_3 sample shows still lamellar structures, but this might be because of the freezing process one passes the lamellar region. But more interesting are the droplet shaped passages that are formed between the layers.

4.5 NUCLEAR MAGNETIC RESONANCE EXPERIMENTS

In the following chapter results of NMR experiments on $^2\text{H}_2\text{O} - \text{C}_{12}\text{E}_4$ binary system will be presented. They were carried out on a Bruker DMX100 NMR – spectrometer operating at 15.371 MHz in a 2.3 T magnetic field, situated at Lund University in the Department of Physical Chemistry (under supervision of Prof. Dr. Ulf Olsson). The instrument is controlled using XWIN NMR version 1.1 software. The samples were prepared in 17mL glass tubes, then transferred into 5mm NMR tubes, which were used for the subsequent investigations. Spectra were obtained by Fourier transformation of the signal following a single pulse. Typically, 16 - 32 scans were accumulated for each spectrum, and a recycle delay of 1 s was used. The temperature of the sample was controlled using an air-flow system that was calibrated prior to the experiments and has an accuracy of $\Delta T \pm 0.5^\circ\text{C}$ for temperatures from $T = 15 - 35^\circ\text{C}$ and of $\Delta T \pm 1^\circ\text{C}$ for temperatures from $T = 35 - 60^\circ\text{C}$.

Vesicular L_{α}^+ and lamellar L_{α} phase formed in the $^2\text{H}_2\text{O} - \text{C}_{12}\text{E}_4$ system within the surfactant concentration range of $\gamma = 0.20 - 0.40$ were investigated with nuclear magnetic resonance (NMR) technique. Three types of experiments were performed: (i) temperature jumps (T -jumps) from L_{α} to L_{α}^+ phase within concentration range of $\gamma = 0.20 - 0.25$, (ii) investigation of “three-phase-line” (between $L_1' + L_1''$ and L_{α}^+) and (iii) temperature scan of L_{α} phase within concentration range of $\gamma = 0.30 - 0.40$.

4.5.1 T - JUMPS

The aim was performing T - jumps from L_{α} ($T = 45^\circ\text{C}$) to L_{α}^+ phase ($T = 30^\circ\text{C}$) in order to characterize vesicles formed in the $^2\text{H}_2\text{O} - \text{C}_{12}\text{E}_4$ system at higher concentrations, *i.e.* $\gamma = 0.20 - 0.25$, then DLS, SANS and FFEM. For the initial state, within the L_{α} phase, we expect to see a clear doublet. As simple doublet is only observed if the lamellar phase has been well aligned, for example, by applying a magnetic field. A disordered lamellar phase consisting of many domains of extended flat layers whose orientations are isotropically distributed in space give rise to the characteristic line shape of a polycrystalline sample also known as powder or powder *Pake* pattern. After the T -jump, within the L_{α}^+ phase we expect the powder pattern to turn into a broad single peak, that is characteristic for (multilamellar-) vesicles. When the two morphologies, lamellae and vesicles, coexist, the spectrum consists of a superposition of a central singlet, operating from the vesicles, and a doublet arising from the lamellar phase. The two concentrations investigated for the T -jump experiment were $\gamma = 0.20$ and $\gamma = 0.25$. The L_{α} phase at $T = 45^\circ\text{C}$ was first equilibrated

in a water bath that was situated next to the NMR magnet, and then brought in to the magnet. After 15 minutes of further equilibration inside the magnet the spectrum was recorded. Then T -jump was performed outside the magnet in the into the water bath, which was meanwhile cooled to $T = 30^\circ\text{C}$. Again, sample (5mm NMR tube) was equilibrated, before recording the spectrum. Figure 73 ($\gamma = 0.20$ and $\gamma = 0.25$) show first the results of T -jump experiments. In Figure 73 a broad singlet is observed for both states. The red line, which indicates the singlet for L_{α^+} phase ($\Delta\nu_{1/2} = 70\text{Hz}$), has a width at half height of 10Hz broader than the blue line, indicating L_{α} phase ($\Delta\nu_{1/2} = 60\text{Hz}$). Additionally, at a relative intensity of $I \sim 0.18$, some shoulders are visible, which most likely indicate some quadrupolar splitting and are therefore a signature also of a certain degree of anisotropy within the sample. We observe a coexistence of both phases, with the values for quadrupolar splitting $\Delta\nu_Q = 210\text{Hz}$ for L_{α^+} phase and $\Delta\nu_Q = 190\text{Hz}$ for L_{α} phase.

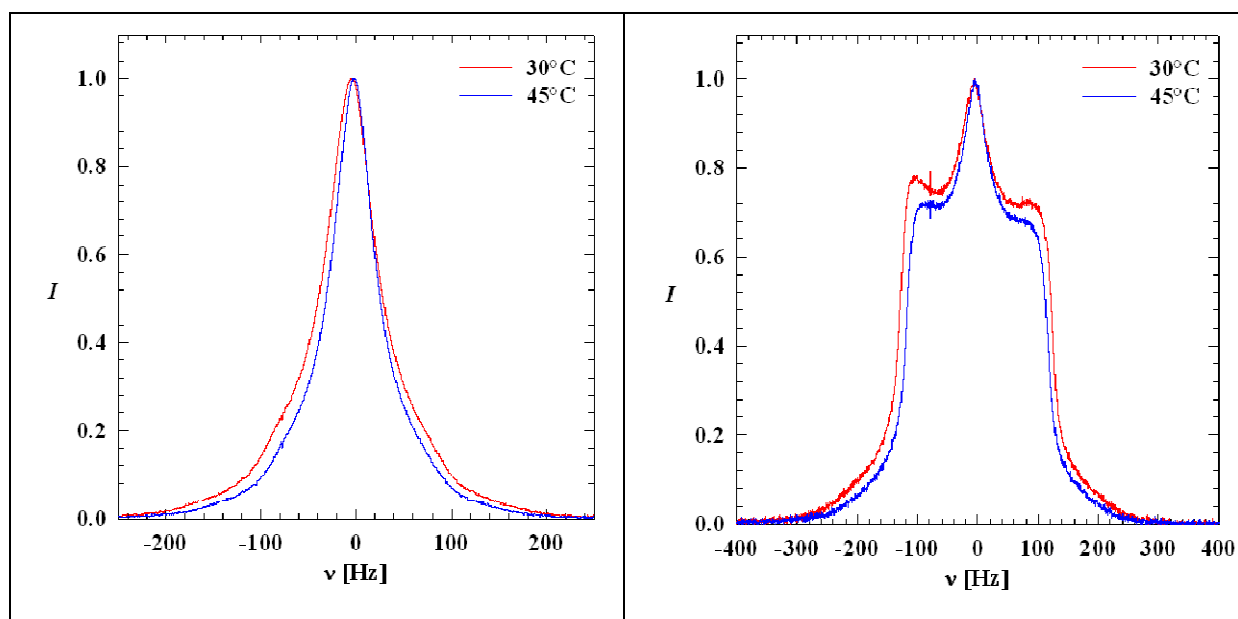


Figure 73: (left) NMR spectra for L_{α} (blue line) and L_{α^+} (red line) phase within $^2\text{H}_2\text{O} - \text{C}_{12}\text{E}_4$ system and surfactant mass fraction $\gamma = 0.20$. (right) NMR spectra for L_{α} (blue line) and L_{α^+} (red line) phase within $^2\text{H}_2\text{O} - \text{C}_{12}\text{E}_4$ system and surfactant mass fraction $\gamma = 0.25$.

L_{α}^{+} REGIME AND THE “PROBLEM” OF THERMODYNAMIC EQUILIBRIUM

Because the first results were surprising since no doublet within L_{α} region was observed the $\gamma = 0.20$ sample was investigated more in detail. In the following graphs, one can see how the structure changes with time. First the sample tube was measured at time $t_0 = 0$ min, $t_1 = 60$ min up to $t_n = 4$ days at $T = 25^{\circ}\text{C}$ (Figure 74 (a-c)).

The evolution from the graphs shows that the degree of anisotropy of the L_{α} phase is increasing with time.

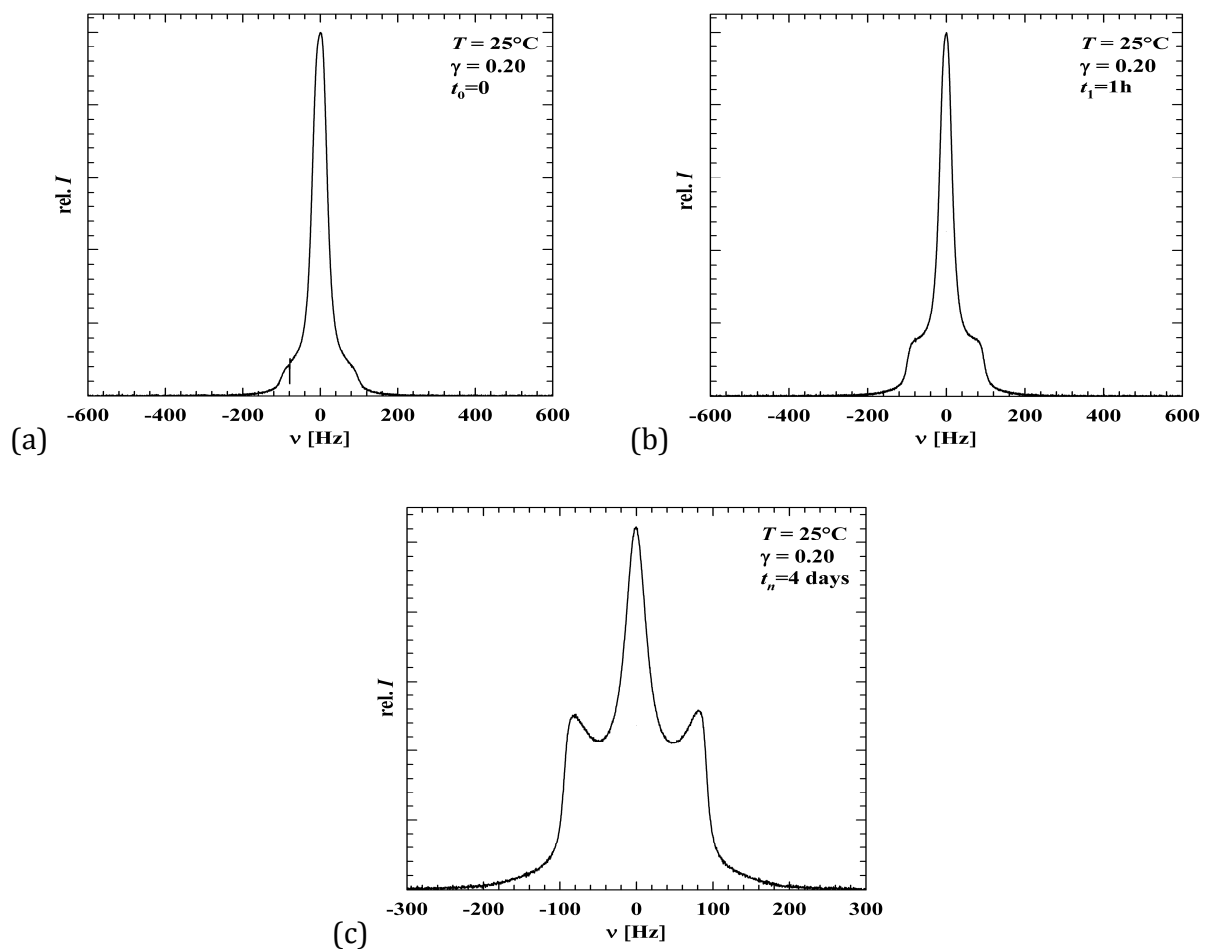


Figure 74: NMR spectrum for L_{α}^{+} within $^2\text{H}_2\text{O} - \text{C}_{12}\text{E}_4$ system and surfactant mass fraction $\gamma = 0.20$ at $T = 25^{\circ}\text{C}$ taken (a) immediately after the T -jump ($t_0 = 0$ min) from lamellar phase, (b) 1 hour after the T -jump ($t_1 = 1\text{h}$) from lamellar phase and (c) 4 days after the T -jump ($t_n = 4\text{days}$) from lamellar phase.

This time evolution of anisotropy clearly indicates a non-equilibrium system, there is one more fact: the spectra differ with different preparations and treatment of the samples.

In Figure 75 NMR spectra for three differently treated sample of the same surfactant concentration $\gamma = 0.20$ are shown.

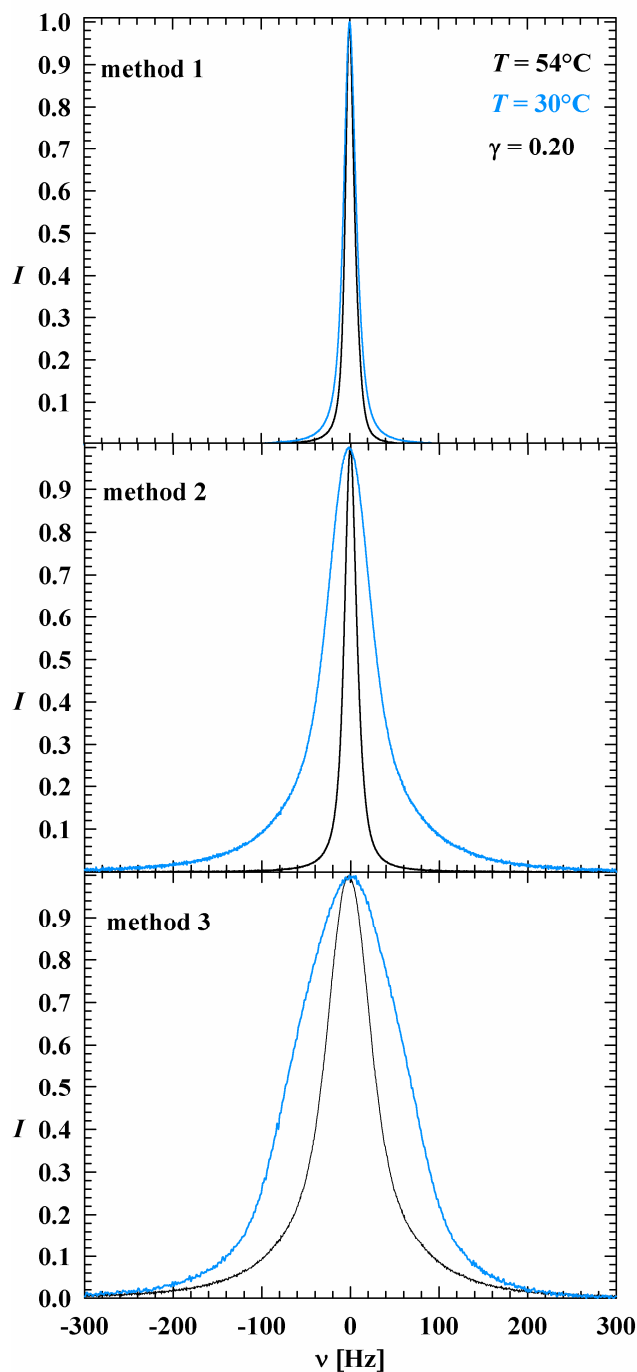


Figure 75: NMR spectra for L_α ($T = 54^\circ\text{C}$) and L_{α^+} ($T = 30^\circ\text{C}$) within $^2\text{H}_2\text{O} - \text{C}_{12}\text{E}_4$ system three differently treated samples of the same surfactant concentration $\gamma = 0.20$.

In method 1 the sample solution, containing 20% surfactant, was prepared in a 17ml tube, heated to $T = 54^\circ\text{C}$ (L_α) in a water bath, transferred into a 5mm NMR tube within the water bath, transferred into the magnet and equilibrated for 30min. Then the spectrum within the lamellar phase L_α was recorded. In method 2 the sample solution was again prepared in a 17ml tube, heated to $T = 63^\circ\text{C}$ (L_3) in a water bath. Then temperature jump was performed to $T = 54^\circ\text{C}$ (L_α), transferred into a 5mm NMR tube within the water bath, transferred into the magnet and then equilibrated for further 30min. Then the spectrum within the lamellar phase L_α was recorded. In method 3 the sample solution was again prepared in a 17ml tube, heated to $T = 63^\circ\text{C}$ (L_3) in a water bath, transferred into a 5mm NMR tube within the water bath, then temperature jump was performed to $T = 54^\circ\text{C}$ (L_α), transferred into the magnet and equilibrated for 30min. Then the spectrum within the lamellar phase L_α was recorded. The T - jump from L_α to L_α^+ followed the same procedure for all three prepared initial states. The results are shown in Figure 75.

The more energy is put into the system with lamellar phase (shear, mix, vortex...), the narrower are the *Lorenzians*. None, of the treatment methods led to a split of the singlet into a doublet. This of course can also be due to the fact that the NMR machine was not so sensitive to low quadrupolar splitting signals and thus induced a signal averaging. The L_α singlet is narrower than the L_α^+ singlet for all preparation methods. In Figure 76 the temperature T is plotted against the values of the width at half heights of the singlets. The arrows indicate the change between L_α and L_α^+ .

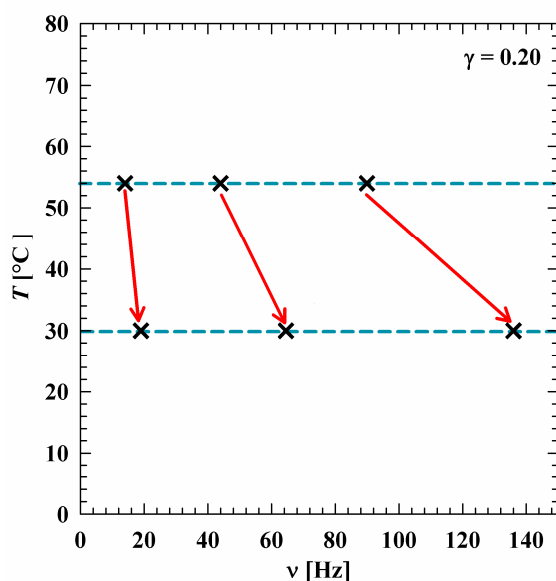


Figure 76: Temperature T [°C] plotted versus the values of the width at half heights $v_{1/2}$ [Hz] for three differently treated samples of same surfactant mass fraction $\gamma = 0.20$.

L_{α} REGIME AND THE “PROBLEM” OF DEFINING AN INITIAL STATE

The aim was to investigate vesicles induced by temperature jumps from lamellar phase, which occurs at higher temperature than vesicular phase. Recording a clear doublet that indicates more or less aligned lamellae was not observed even though several methods, which were used previously with good results were employed. Among this methods of aligning the lamellae within L_{α} phase are: T - jump from L_3 phase, shearing with low shear rate, also vortexing and centrifuging. Additionally, we also used the method developed by Strey and Olsson, which implies using a tube containing many glass layers having distance of 0.5mm between them (Figure 77). If the sample solution is slowly pipetted into this tube, the bilayer sheets assume the form and are finally aligned.

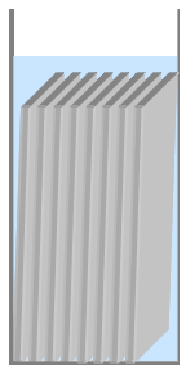


Figure 77: Sketch of the tube that has many glass layers with a distance of 0.5mm inside, developed by Strey and Olsson.

In the end, even though optical observation indicates, that anisotropic structure exists, NMR results show a broad isotropic peak, which indicates onion like vesicles. For higher dilution ($\gamma < 0.10$) one may find planar bilayers (aligned lamellae), but within the concentration range capable by NMR technique, this is not the case. Due to higher viscosity of L_{α} and smaller distances between the bilayers they could also prefer to close up and build multilamellar vesicles (MLVs).

4.5.2 “3-PHASE-LINE”

The aim was to observe the phase transition, especially to investigate the so called “three-phase-line”, which is the phase transition between the three phases L_{α}^{+} and $L_1'+L_1''$. In order to achieve that, we planned a temperature scan across this transition ($L_{\alpha}^{+} \rightarrow L_1'+L_1''$). Apart from structure investigations within the phases of interest (*i.e.* L_{α} , L_{α}^{+} , L_3), we also focused on determining the precise location of the “three-phase-line” to better understand the system’s kinetics. Figure 78 shows the schematic phase diagram of the system of investigation $H_2O - C_{12}E_4$, pointing out the phase transition between L_{α}^{+} and the two-phase region $L_1'+L_1''$ (red arrow).

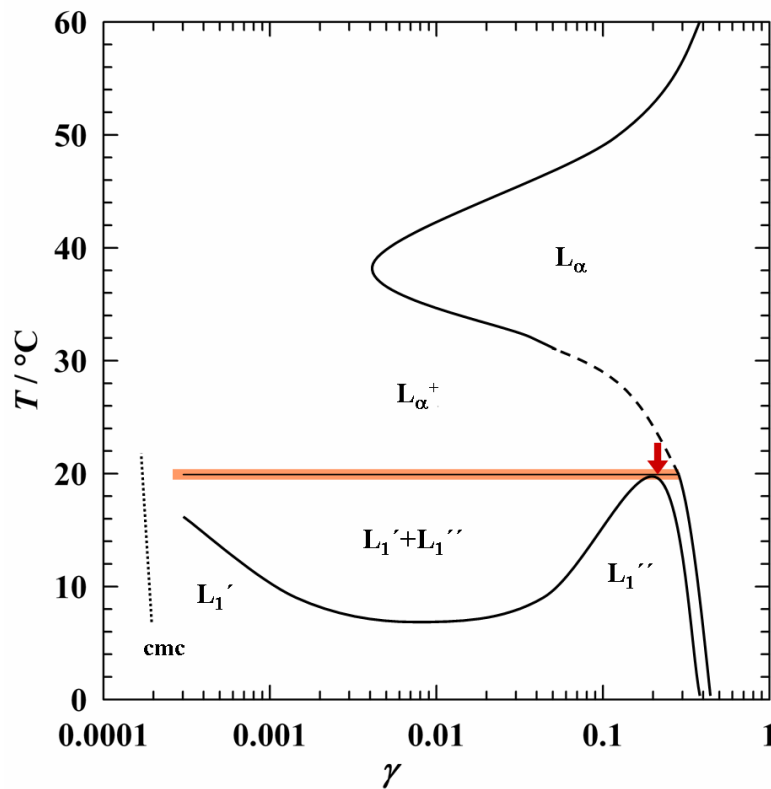


Figure 78: Schematic phase diagram of $H_2O - C_{12}E_4$ system, pointing out the phase transition between L_{α}^{+} and the two-phase region $L_1'+L_1''$ (red arrow).

Therefore temperature was decreased slowly from $T = 25^\circ\text{C}$ to $T = 20^\circ\text{C}$ with a step of $\Delta T = 0.5^\circ\text{C}$ a spectrum was taken. Results for five different surfactant concentrations $\gamma = 0.20, 0.25, 0.30, 0.35$ and 0.40 are shown in Figure 79 – Figure 81.

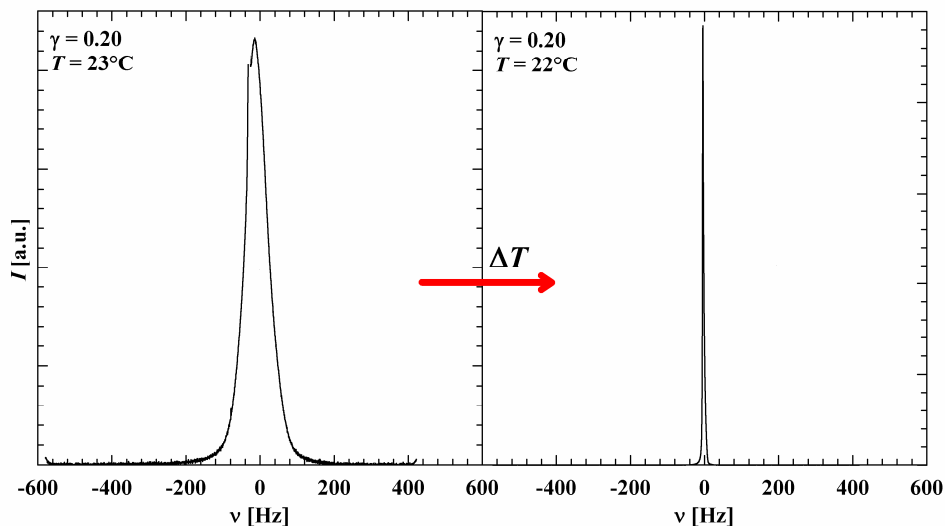


Figure 79: NMR spectra for $^2\text{H}_2\text{O} - \text{C}_{12}\text{E}_4$ system, $\gamma = 0.20$. Left: $T = 23^\circ\text{C}$. Right: $T = 22^\circ\text{C}$.

Our prediction was proved right since the transition in question was marked by a dramatic change in the NMR *Lorenzian*. For the L_{α}^+ phase a sharp single peak was observed.

In Figure 79 at $T = 25^\circ\text{C}$ a clear change from a broad singlet to a narrow singlet is observed.

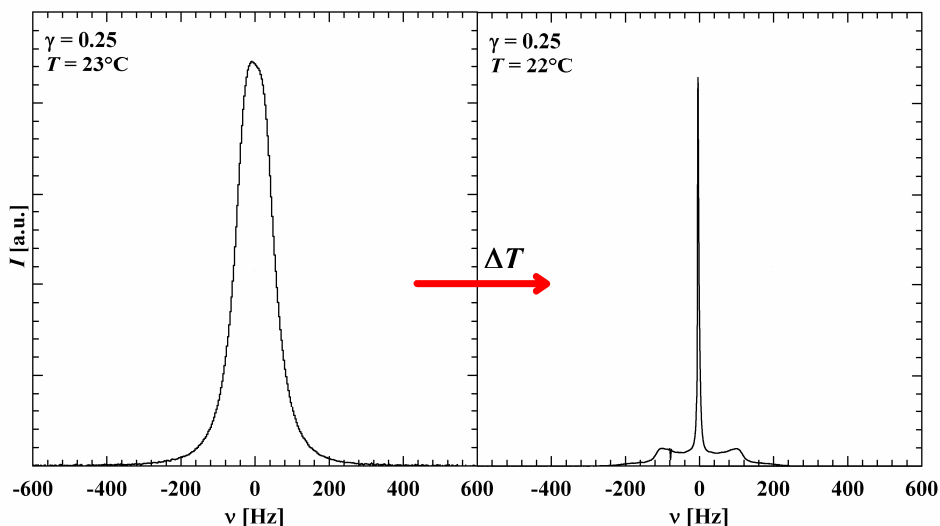


Figure 80: NMR spectra for $^2\text{H}_2\text{O} - \text{C}_{12}\text{E}_4$ system, $\gamma = 0.25$. Left: $T = 23^\circ\text{C}$. Right: $T = 22^\circ\text{C}$.

Whereas the broad singlet ($\nu_{1/2} = 65\text{Hz}$) indicates the vesicles, the sharp and tiny singlet ($\nu_{1/2} = 3\text{Hz}$) indicates micellar phase.

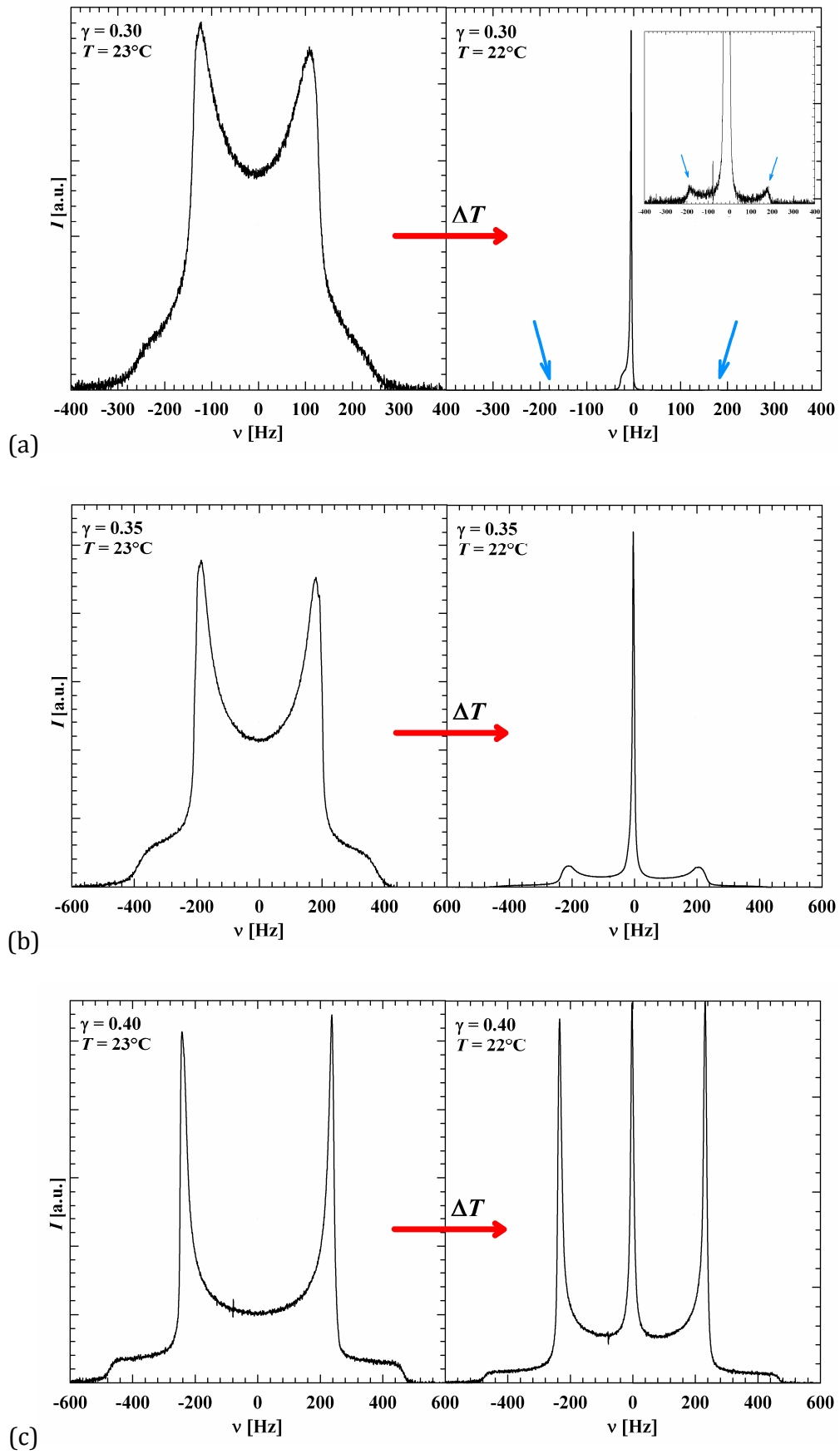


Figure 81: NMR spectra for $^2\text{H}_2\text{O} - \text{C}_{12}\text{E}_4$ system, $\gamma = 0.40$. Left: $T = 23^\circ\text{C}$. Right: $T = 22^\circ\text{C}$.

Figure 80 shows a singlet ($\nu_{1/2} = 200\text{Hz}$) indicating vesicles, changing into a triplet that indicates two coexisting phases, an isotropic and anisotropic phase (lamellar and micellar phase) Figure 81 on the left the spectra were taken at $T = 23^\circ\text{C}$ for three surfactant concentrations $\gamma = 0.30$ (a), $\gamma = 0.35$ (b) and $\gamma = 0.40$ (c), showing quadrupolar splitting (clear *Pake* powder pattern) within the lamellar phase. On the right the spectra are shown recorded at $T = 22^\circ\text{C}$. The three spectra have in common that a single peak occurs in the centre, coexisting with the quadrupolar splitting of the lamellar doublet. The higher the surfactant concentration the higher is the splitting. For $\gamma = 0.30$ this quadrupolar splitting is hard to see, just by scaling up the graph one can observe the splitting.

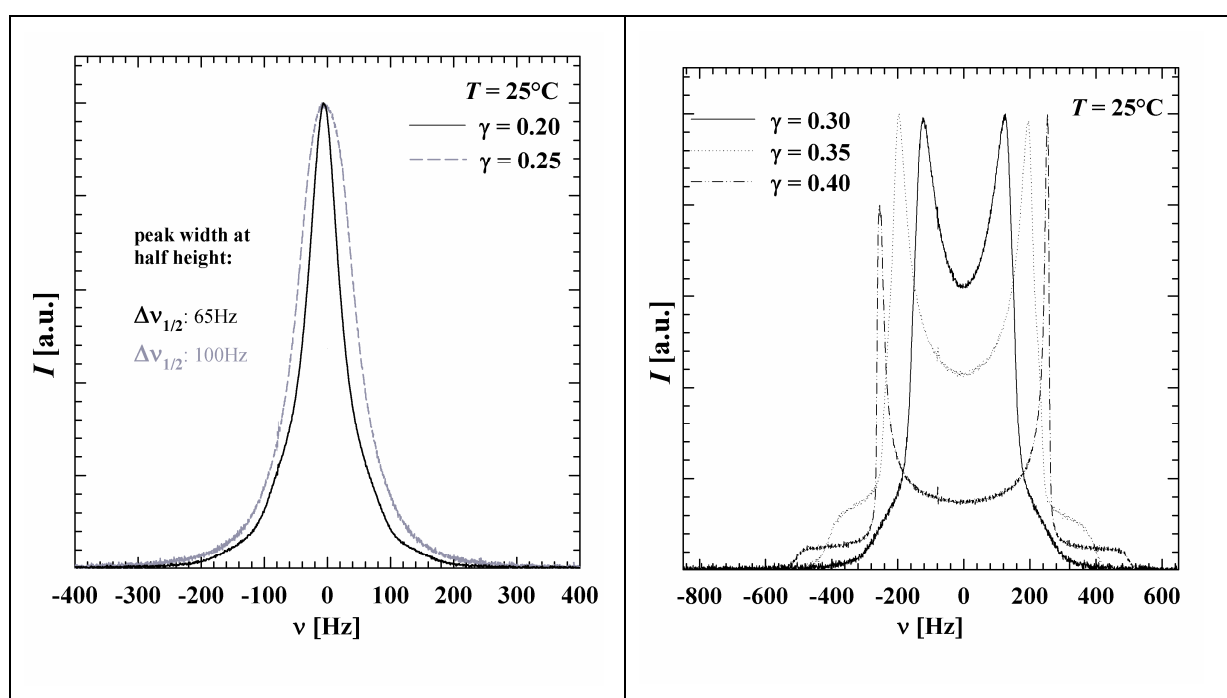


Figure 82: NMR spectrum for L_α at $T = 25^\circ\text{C}$ for two surfactant concentrations $\gamma = 0.20$ and 0.25 (left) and NMR spectrum for L_α at $T = 25^\circ\text{C}$ for three surfactant concentrations $\gamma = 0.30, 0.35$ and 0.40 (right).

The value of the quadrupolar splitting is a reflection of the surfactant concentration. However the splitting at $T = 20^\circ\text{C}$ have same values for all concentrations. Since the phase transition is discontinuous, passing through a state of two coexisting structures, it is possible to separate the spectra into different components. In general, the area under NMR spectrum is proportional to the concentration of molecules in a particular state. By fitting the spectra with a weighed sum of the spectra of each component, one can determine the

amount of each component. The spectrum of the MLV component can be described as a Lorentzian function¹⁷¹:

$$I(\nu) = \frac{I_{\max}}{1 + (2(\nu - \nu_0) / \Delta\nu_{1/2})^2} \quad [53]$$

where ν is the frequency, ν_0 is the peak centre, I_{\max} is the peak maximum and $\Delta\nu_{1/2}$ is the peak width at half height. The line shape of the doublet arising from the lamellar phase, on the other hand, can be represented as sum of two Lorentzian functions.

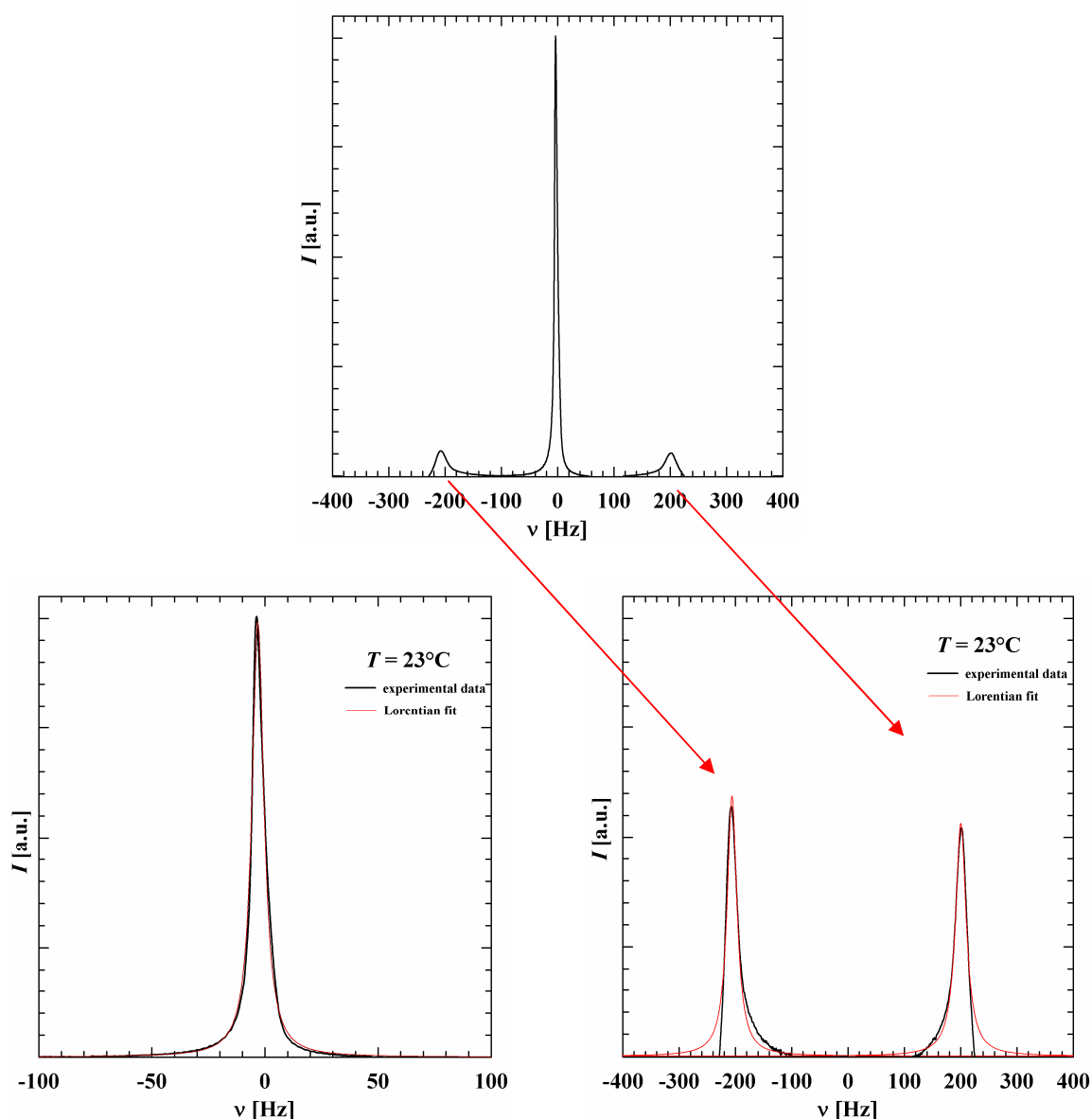


Figure 83: Upper graph shows the NMR spectrum for the exemplary sample $\gamma = 0.35$ at $T = 23^\circ\text{C}$. Lower graphs show the splitted singlet (left) and the doublet (right) and their corresponding fits with Lorentzian function (red lines).

¹⁷¹ A. Abragam, *Principles of Nuclear Magnetism*; Clarendon: Oxford (1961).

4.5.3 T – SCAN

Making use of the fact that the system under investigation is temperature sensitive, we performed NMR measurements (T – scans) while gradually heating (or cooling) the sample. The experiments were performed at five different concentrations $\gamma = 0.20, 0.25, 0.30, 0.35$ and 0.40 . Until now this system has only been investigated under shear, where it is known that at low temperatures (25 to 40°C) the steady state under shear flow is multilamellar vesicles (MLV)^{172,173}, whereas at higher temperatures the structure transforms into planar lamellar state.

As already mentioned the ²H-NMR the quadrupolar splitting of the ²H₂O molecules, $\Delta\nu$ gives information about the nature of the lyotropic liquid crystalline phases formed. For non-ionic surfactant systems *Rendall et al.*¹⁷⁴ established that the main contribution to the quadrupolar splitting comes from the ²H₂O molecules perturbed (sometimes also referred to as “bound”) to the first or second EO group attached to the alkyl chain. Thus the quadrupolar splitting for non-ionic surfactant systems is expressed as:

$$\Delta\nu = \frac{3}{4} E_{Q,b} p_b f_b S_b \quad [54]$$

where, f_b is the fraction of perturbed water molecules, p_b is the number of perturbed water molecules, S_b is the orientational order parameter of perturbed water molecules, whilst $E_{Q,b}$ is a constant representing the splitting associated with single perturbed water molecule. S_b is intimately related with the interfacial curvature of the surfactant aggregates.

In water - non ionic surfactant systems has been shown that within lamellar phases, at lower temperature bilayer rich in random water filled defects can occur^{175,176,177,178}. The NMR experiment allows us to detect bilayer defects, in the following referred to as defects, and the question we address here is whether there is a correlation between the presence of perforations and the lamellar phase stability. Recent detailed structural studies have resulted in a number of reports on bilayer perforations and lamellar-mesh phases, starting with the pioneering work of *Holmes et al.* In several non-ionic surfactant water lamellar

¹⁷² S. Müller, C. Börschig, W. Gronshi, C. Schmidt, *Langmuir*, **15**, 7558 (1999).

¹⁷³ T. D. Le, U. Olsson, K. Mortensen, *Phys. Chem. Chem. Phys.*, **3**, 1310 – 1316 (2001).

¹⁷⁴ K. Rendall, G. J. T. Tiddy, *J. Chem. Soc. Farad. Transact. 1*, **80**, 3339 – 3357 (1984).

¹⁷⁵ S. S. Funari, M. C. Holmes, G. J. T. Tiddy, *J. Phys. Chem.* **98**, 3015 (1994).

¹⁷⁶ S. S. Funari, M. C. Holmes, G. J. T. Tiddy, *J. Phys. Chem.* **96**, 11039 (1992).

¹⁷⁷ C. Fairhurst, M. C. Holmes, M. Leaver, *Langmuir* **13**, 4964 (1997).

¹⁷⁸ J. Burgoyne, M. C. Holmes, G. J. T. Tiddy, *J. Phys. Chem.* **99**, 6054 (1995).

phases, as in the water- $C_{12}E_5$ and water- $C_{16}E_6$ systems, the bilayers appear to be highly perforated at lower temperatures while being essentially perforation-free at higher temperatures. Signatures of perforations provided by 2H -NMR experiments^{179,180,181,182}. In NMR experiments the pattern for bilayer defects is the low quadrupolar splitting value with temperature as a result of a lower value of the order parameter due to random water filled defects within lamellae.

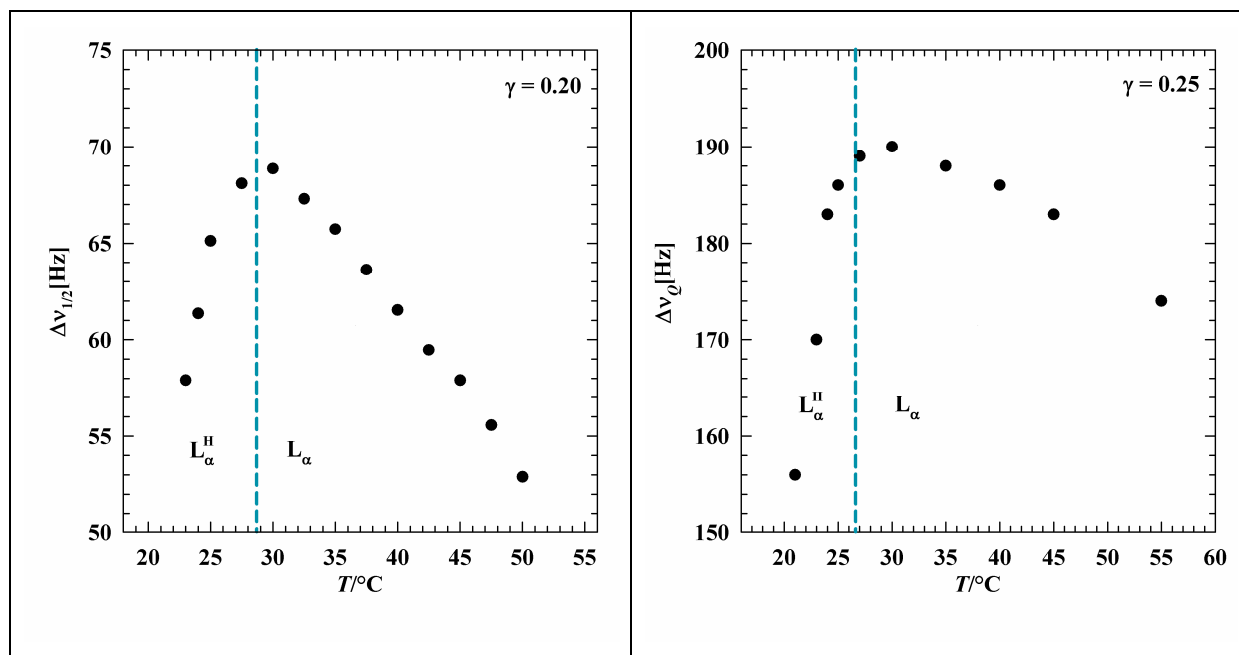


Figure 84: Distribution of values taken from width at half height $\Delta v_{1/2}$, versus temperature T for $^2H_2O - C_{12}E_4$ system, $\gamma = 0.20$ (left) and $\gamma = 0.25$ (right).

Same trend was observed for higher concentrations of $\gamma = 0.30$, $\gamma = 0.35$ and 0.40 .

¹⁷⁹ M. Baciú, U. Olsson, M. Leaver, M. C. Holmes, J. Phys. Chem. 110, 16 (2006).

¹⁸⁰ M. Imai, A. Saeki, T. Teramoto, A. Kawaguchi, K. Nakaya, T. Kato, K. Ito, J. Chem. Phys. 115, 10525 (2001).

¹⁸¹ M. Imai, A. Saeki, M. Kikuchi, K. Nakaya, A. Saeki, T.J. Teramoto, Chem. Phys. 122, 214906 (2005).

¹⁸² M. Imai, A. Kawaguchi, A. Saeki, K. Nakaya, T. Kato, K. Ito, Y. Amemiya, Phys. Rev. E 62, 6874 (2000).

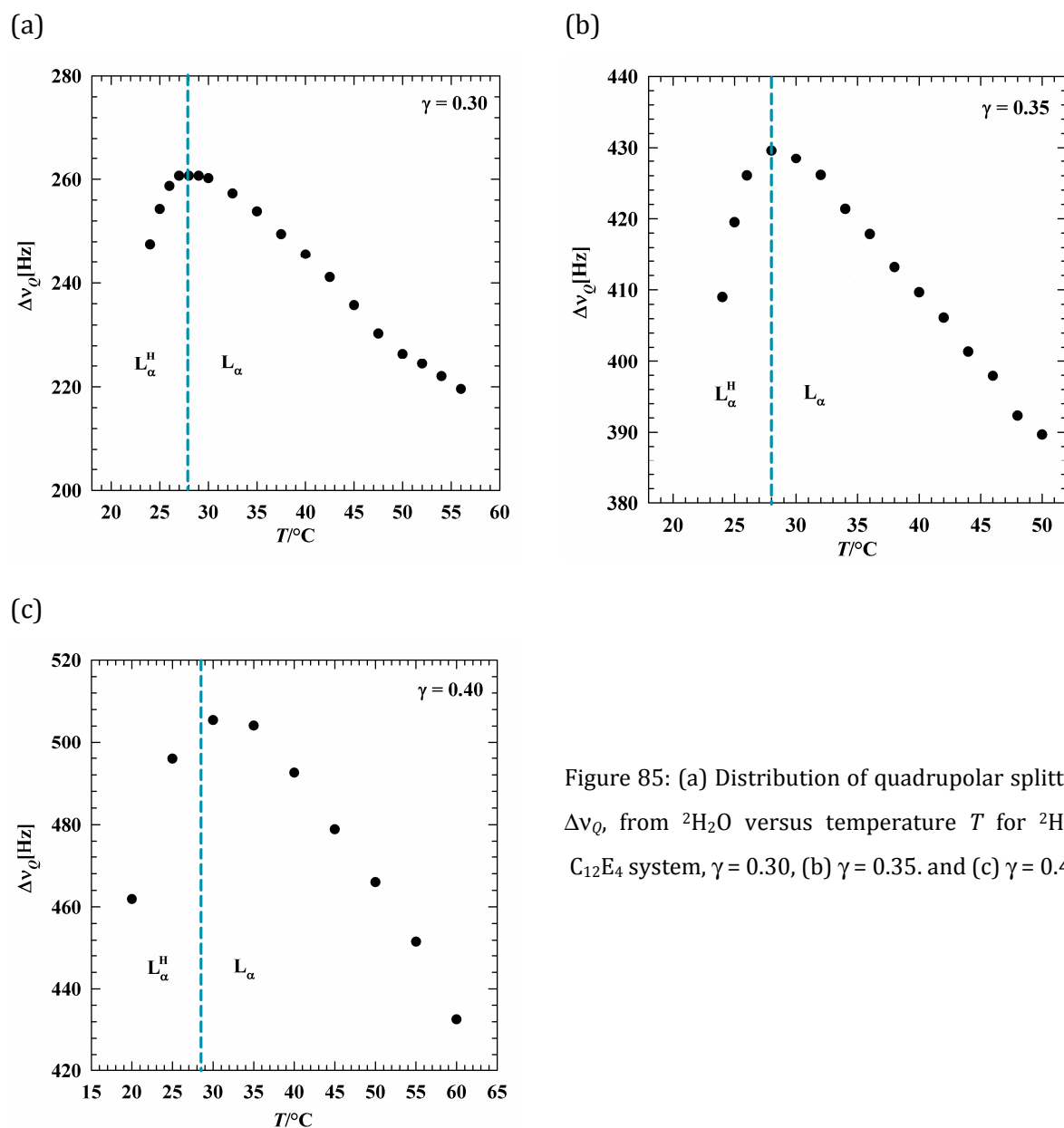


Figure 85: (a) Distribution of quadrupolar splittings $\Delta\nu_Q$, from ${}^2\text{H}_2\text{O}$ versus temperature T for ${}^2\text{H}_2\text{O} - \text{C}_{12}\text{E}_4$ system, $\gamma = 0.30$, (b) $\gamma = 0.35$. and (c) $\gamma = 0.40$.

Interestingly, a random mesh structure also occurs in the present water- C_{12}E_4 lamellar phase; however, perforations appear first below ca. 25°C. In Figure 85 we present how the recorded ${}^2\text{H}$ quadrupolar splitting, $\Delta\nu_Q$ evolves with temperature for the samples of surfactant concentrations $\gamma = 0.30$, 0.35 and 0.40. Cooling from 60°C, $\Delta\nu_Q$ first increases, as is normally found in surfactant liquid crystalline phases, due to an increased local ordering of water molecules hydrating the surfactant layer. Near 25°C, however, $\Delta\nu_Q$ shows a maximum and a further decrease of the temperature results in a strong decrease of $\Delta\nu_Q$. Such a decrease has been found previously¹³⁴ to correlate with the formation of a mesh

structure. In a two-state discrete exchange model, $\Delta\nu_Q$ depends on (i) the fraction of water molecules, p_b , that are perturbed by the bilayer-water interfaces, (ii) how the interface is curved in space, because the local orientational ordering in the perturbed “hydration layer”, characterized, *e.g.*, by a “reference” quadrupolar splitting, $\Delta\nu_Q^0$. Molecular diffusion along a curved surface results in an averaging of the quadrupolar interaction. The partial averaging due to diffusion over the locally curved interface in a perforation can be characterized by the order parameter, S_c , bound by $0 \leq S_c \leq 1$, where $S_c = 1$ corresponds to the absence of perforations and $S_c = 0$ to a completely isotropic distribution of orientations sampled by the lateral interfacial diffusion. With these assumptions

$$\Delta\nu_Q(T) = p_b(T)\Delta\nu_Q^0(T)S_c(T) \quad [55]$$

can be written, where all parameters are temperature-dependent. The parameters are, however, expected to vary consistently with temperature. p_b and $\Delta\nu_Q^0$ - quadrupolar splitting estimated for defect free L_1 phase - are expected to decrease with increasing temperature. The non- consistent variation of $\Delta\nu_Q$ then implies that S_c increases with increasing temperature but levels off above a certain temperature, here 25-30°C. At higher temperatures, where $S_c \approx 1$, $\Delta\nu_Q$ decreases approximately linearly with increasing temperature. We stress, nevertheless, that the non- consistent temperature variation of $\Delta\nu_Q$ can be explained by two terms: one which decays weakly with temperature, which we in fact expect due to local thermal motions, and one increasing function which levels off at higher temperatures.

SUMMARY

^2H - NMR measurements were performed to follow the L_α to L_α^+ transition in $^2\text{H}_2\text{O}$ - C_{12}E_4 system. The use of ^2H - NMR spectroscopy proves to be particularly advantageous, since different, characteristic ^2H - NMR patterns of the two phases allow a rigorous examination (*e.g.* singlet for the isotropic L_α^+ phase and a doublet for the anisotropic L_α phase) of the L_α to L_α^+ transition. Due to small resolution of the machine the concentration range was limited ($\gamma > 0.30$). For sample concentration $\gamma = 30$, $\gamma = 35$ and $\gamma = 40$ the quadrupolar splitting of $^2\text{H}_2\text{O}$ molecules $\Delta\nu$ was measured temperature dependent ($T = 20^\circ\text{C}$

to $T = 60^\circ\text{C}$) and gives information about the nature of lyotropic liquid crystalline phases formed. With increasing temperature the distribution of quadrupolar splitting $\Delta\nu$ shows a maximum that differs with concentration, shifting to higher values the higher the concentration is. Samples with $\gamma < 0.30$ gave broad singlet in lamellar as well as in vesicular regions. It could not be distinguished between onion structure and lamellar alignment of the bilayers. Nevertheless, not $\Delta\nu$ but $\Delta\nu_{1/2}$ was detected for sample s $\gamma = 20$ and $\gamma = 25$, which show same behavior as quadrupolar splitting of prior higher samples with higher surfactant mass fractions.

5 DISCUSSION

Understanding the structure of L_{α}^+ phase in $H_2O - C_{12}E_4$ system was the main goal of this work. Therefore scattering techniques, such as dynamic light scattering (DLS) and small angle neutron scattering (SANS) were used and supported by freeze fracture electron microscopy (FFEM) images. In the sections 4.2 and 4.3 the results of the scattering experiments have been presented and also analyzed by describing the scattering data with adequate scattering functions. FFEM images of the vesicular phase L_{α}^+ , but also of the sponge L_3 and lamellar phase are presented in section 4.4. In the following the results obtained by the scattering techniques DLS and SANS and the imaging technique FFEM will be compared for exemplary samples. Furthermore NMR results will be consulted.

TEMPERATURE JUMPS

The process of vesicles formation induced by a temperature jump is schematically illustrated in Figure 86. Bilayer sheets of a bilayer thickness δ_{bil} and distance D are shown on the left hand side of Figure 86. Taking into account thermal fluctuations undulating bilayers are shown in Figure 86, centre. Performing a temperature jump, *i.e.* changing the curvature of the amphiphilic film will promote fusion and fission processes which together with additional shearing of the sample lead to the formation of vesicles (right hand side of Figure 86).

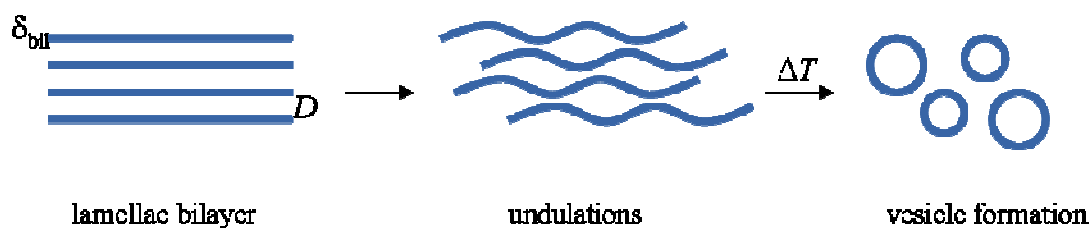


Figure 86: Schematic drawing of possible way of vesicle formation from L_α phase induced by a temperature jump.

Following these thoughts, the smallest diameter of unilamellar vesicles formed should be closely related to the bilayer repeat distance of the lamellar phase. Taking into account thermally induced undulations the repeat distance D of the bilayers can be calculated by¹⁸³

$$D \approx \frac{\delta_{\text{bil}}}{\phi_{\text{C}_{12}\text{E}_4}} \left(1 - \frac{k_{\text{B}}T}{4\pi\kappa} \ln \phi_{\text{C}_{12}\text{E}_4} \right), \quad [56]$$

with δ_{bil} being the bilayer thickness, $\phi_{\text{C}_{12}\text{E}_4}$ the surfactant volume fraction, k_{B} the *Boltzmann* constant, T the temperature and κ the bending rigidity. Hereby the bilayer thickness

$$\delta_{\text{bil}} = 2\delta_{\text{mono}}, \quad [57]$$

and

$$\delta_{\text{mono}} = \frac{v_{\text{C}_{12}\text{E}_4}}{a_{\text{C}_{12}\text{E}_4}}, \quad [58]$$

with δ_{mono} being the thickness of a monolayer of the non-ionic surfactant C_{12}E_4 , $v_{\text{C}_{12}\text{E}_4}$ the volume per C_{12}E_4 -molecule ($v_{\text{C}_{12}\text{E}_4} = 634 \text{ \AA}^3$)¹⁸⁴ and $a_{\text{C}_{12}\text{E}_4}$ the area per C_{12}E_4 -molecule ($a_{\text{C}_{12}\text{E}_4} = 53.8 \text{ \AA}^2$)¹⁸⁴. From Eq. 57 it follows that $\delta_{\text{bil}} = 2.36 \text{ nm}$. From Eq. 56 it can be easily seen that increasing the surfactant volume fraction $\phi_{\text{C}_{12}\text{E}_4}$ leads to smaller values of bilayer repeat distance D .

¹⁸³ R. Strey, R. Schomäcker, *J. Chem. Soc. Faraday Trans.* **86**, 2253 – 2261 (1990).

¹⁸⁴ T. Sottmann, PhD thesis, University of Goettingen (1997).

DLS vs. FFEM

DLS was one method used to study the structural nature of the L_{α}^+ phase. However, DLS provides in general only an autocorrelation function. Furthermore, it turned out that the quantitative evaluation of the DLS-data obtained in the work at hand is difficult due to abundance of diffusing particle sizes present in the L_{α}^+ phase. Thus, a quantitative interpretation of the scattering data requires knowledge of the shape of microstructures present. Only the interplay of both, the DLS data and the FFEM images allow a complete analysis of the structure of L_{α}^+ phase

In Figure 87 (above left) the relaxation rates Γ_n as a function of the quadratic scattering vector q^2 for one exemplary sample of the system $H_2O - C_{12}E_4$ at $\gamma = 0.02$ is shown. In the $\Gamma/(q^2)$ -plot three lines are obtained (Γ_1 , Γ_2 and Γ_3) for the scattering angles $\theta = 40^\circ$ - 80° . According to *Landau-Placzek* equation (Eq. 23) the diffusion coefficients result from the slope of the lines, which when applying *Stokes-Einstein* equation (Eq. 25) give three different hydrodynamic radii R_{hydr} in the range of $R_{hydr1} = 30\text{nm}$, $R_{hydr2} = 100\text{nm}$ and $R_{hydr3} = 1\mu\text{m}$. Comparing both, the hydrodynamic radii obtained from the DLS measurements and the structures visible in the FFEM micrographs (Figure 87, right) at least a qualitative agreement is observed. In the upper FFEM micrograph berry-like structures with a size of 100nm are observed as well as smaller vesicles of 40nm diameter. The lower FFEM micrograph shows network-like structures which length scale compares almost quantitatively with the hydrodynamic radius $R_{hydr3} = 1\mu\text{m}$ obtained analyzing the autocorrelation function. These results show clearly, that even when vesicles were the dominant feature of the L_{α}^+ phase, they were far from being uniform in size and degree of lamellar, *i.e.* uni- or multilamellar vesicles were equally present. Thus, a thermodynamic stability of the L_{α}^+ phase is not supported by this work.

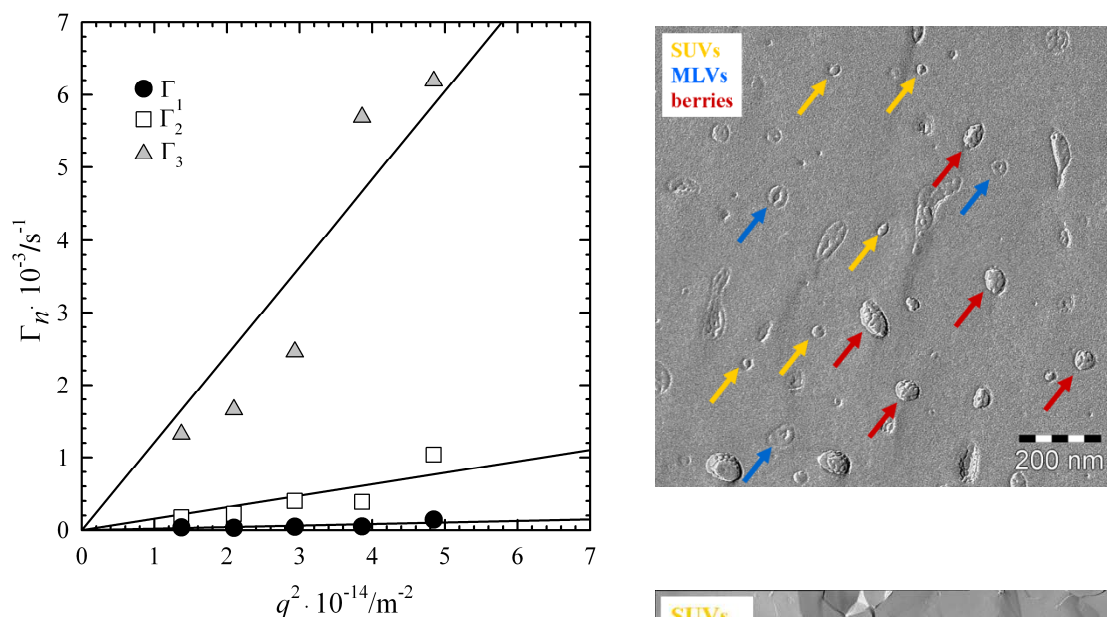


Figure 87: Above: Relaxation rates Γ_n as a function of the quadratic scattering vector q^2 for one exemplary sample of the system $\text{H}_2\text{O} - \text{C}_{12}\text{E}_4$ at $\gamma = 0.02$ after a temperature jump (from $T = 48^\circ\text{C}$ (L_α) to $T = 35^\circ\text{C}$ (L_α^+)). Analyzing the autocorrelation function at the scattering angles ($\theta = 40^\circ, 50^\circ, 60^\circ, 70^\circ$ and 80°) via *Contin* provides the values of the first three corresponding relaxation rates Γ_1 , Γ_2 and Γ_3 . Right: FFEM images of $\text{H}_2\text{O} - \text{C}_{12}\text{E}_4$ system after negative T -jump within the L_α^+ phase at $T = 30^\circ\text{C}$ for $\gamma = 0.03$.

SANS vs. FFEM

As DLS provides only the diffusion coefficients of the different species present in the L_α^+ phase also small angle neutron scattering (SANS) has been used to study the structure of the $\text{D}_2\text{O} - \text{C}_{12}\text{E}_4$ system. The experiments were performed for surfactant mass fractions of $\gamma = 0.02$ to $\gamma = 0.11$. Due to the fact that the $\text{H}_2\text{O}/\text{glycerol} - \text{C}_{12}\text{E}_4$ system is ideal for freeze fracture electron microscopy (FFEM) both SANS and FFEM experiments have been performed on samples of this system. In Figure 88 (left) the scattering curve of the L_α^+ phase of the sample $\text{D}_2\text{O}/\text{glycerol} - \text{C}_{12}\text{E}_4$ at $\phi = 0.08$ and $T = 4^\circ\text{C}$ is shown. As can be seen the scattering curve of the L_α^+ -phase shows a slight dent at intermediate q -values. Moreover, the leading q^{-2} dependence at intermediate q -values indicates the presence of bilayers. However, without any further information about the different coexisting structures a quantitative evaluation of the scattering curve was not possible. Having taken FFEM images for the same

sample (Figure 88, right) complementary information is obtained about the shape of the structures. As can be seen besides lamellar sheets, and large multi-lamellar vesicles also a large number of small vesicles can be observed in the pictures.

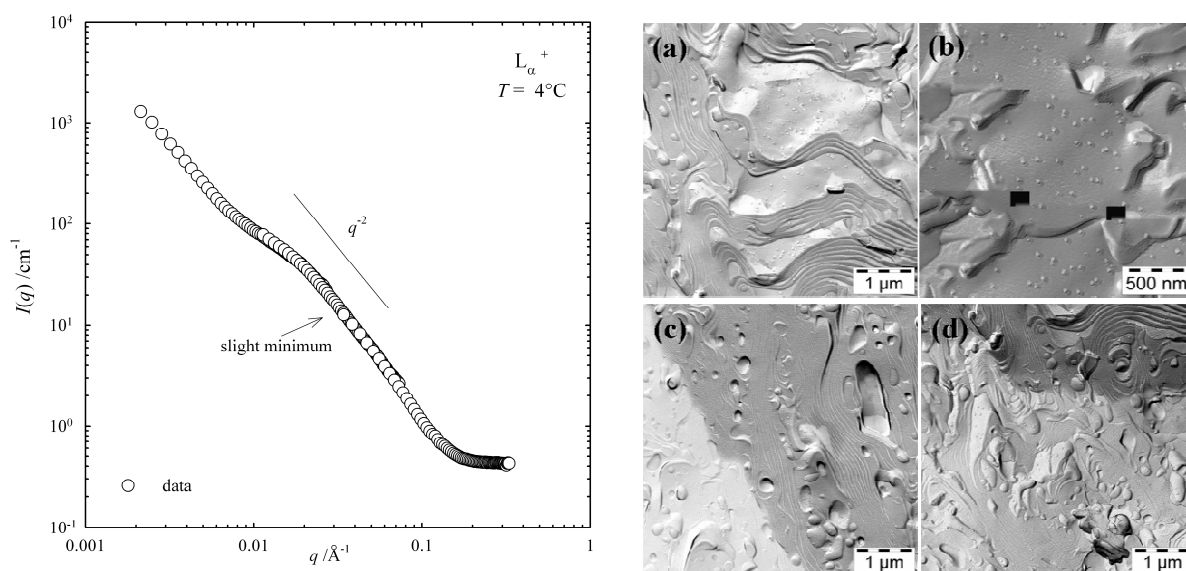


Figure 88: Left: The intensity I plotted versus the scattering vector q for the sample $D_2O/glycerol - C_{12}E_4$ with $\phi = 0.08$ at $T = 4^\circ C$. Right: FFEM micrographs for the sample $H_2O/glycerol - C_{12}E_4$ with $\gamma = 0.08$ at $T = 4^\circ C$ showing 4 different sections.

Magnifying the small vesicles displayed in Figure 88, right (b) (see Figure 89 (left)) allows for evaluating the average size of the small vesicles. The obtained distribution is shown in Figure 89 (right). Evaluating a total number of 107 vesicles a weighted mean diameter of $(39.0 \pm 5.2) nm$ was obtained.

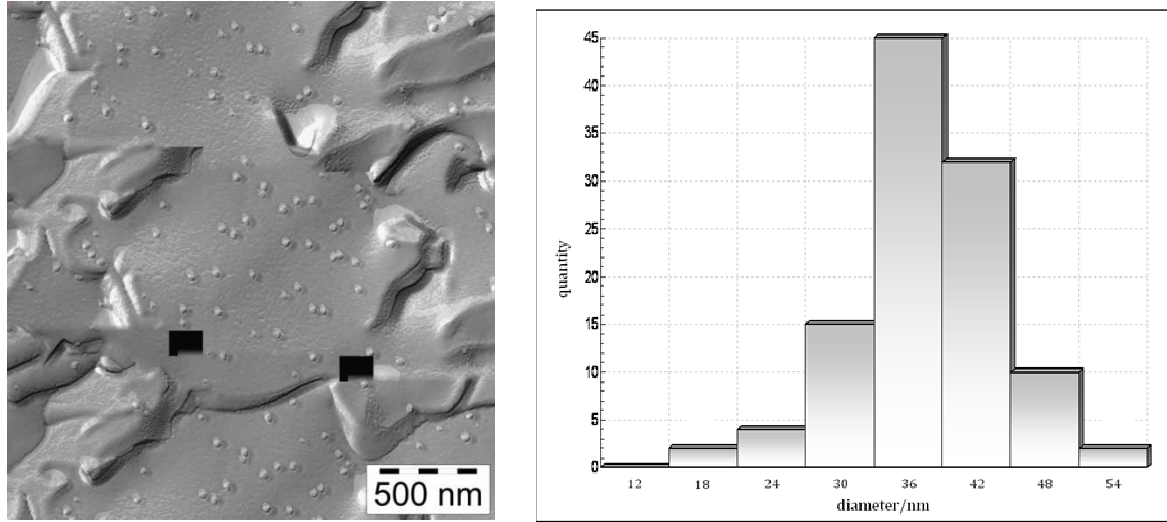


Figure 89: FFEM image of $H_2O/glycerol - C_{12}E_4$ system after negative T -jump at $T = 4^\circ C$ (L_α^+ phase), surfactant mass fraction $\gamma = 0.08$ showing monodisperse vesicles with a weighted mean diameter of $(39.0 \pm 5.2) nm$.

Thus, assuming that the predominant structures of the L_α^+ phase are small uni-lamellar vesicles and lamellar sheets the obtained SANS curve might be described by a combination of the respective structure factors. Thereby structure factor of *Nallet et al.*¹⁴⁸ is used to describe the scattering of lamellar sheets, while the contribution of the uni-lamellar vesicles is taken into account by assuming a polydisperse *Gaussian* distribution of spheres with a radius r and a diffuse interface of the thickness t . This contribution is given by¹⁸⁶:

$$I(q) = \frac{36\pi}{3} \phi r^3 \frac{(\Delta\rho)^2}{(qr)^6} \cdot (f_1 + f_2 + f_3 + f_4) + bg \quad [59]$$

$$f_1 = \frac{1}{2} [1 - \cos(2qr) \exp(-2\sigma^2 q^2)],$$

$$f_2 = -q[r \sin(2qr) + 2q\sigma^2 \cos(2qr)] \exp(-2\sigma^2 q^2),$$

$$f_3 = \frac{1}{2} q^2 [-4qr\sigma^2 \sin(2qr) \exp(-2\sigma^2 q^2) + r^2 + \sigma^2], \quad [60]$$

$$f_4 = \frac{1}{2} q^2 [r^2 \cos(2qr) \exp(-2\sigma^2 q^2) + \sigma^2 \cos(2qr) \cdot (1 - 4\sigma^2 q^2) \exp(-2\sigma^2 q^2)].$$

ϕ is the volume fraction of the scattering solution and $\Delta\rho$ is the difference in scattering length density, bg displays the incoherent background. The model contains three fit parameters: the radius r , a diffuse interface of the thickness t and the standard deviation σ

of the polydispersity distribution. These parameters are obtained from fitting the form factor to the experimental data in the intermediate and high q -regime.

Figure 90 shows again the scattering curve of the L_{α}^{+} phase for the system D_2O /glycerol - $C_{12}E_4$ at $\phi = 0.08$ and $T = 4^{\circ}C$. Combining both fits, *i.e.* the *Gaussian* shell fit (green line) for the unilamellar vesicles and the *Nallet* structure factor for the lamellar sheets (blue line) an almost quantitative description of the experimental data points is obtained (red curve). However, the systematic deviation at small values of q can be ascribed to an overestimation of membrane fluctuation within the model of *Nallet*.

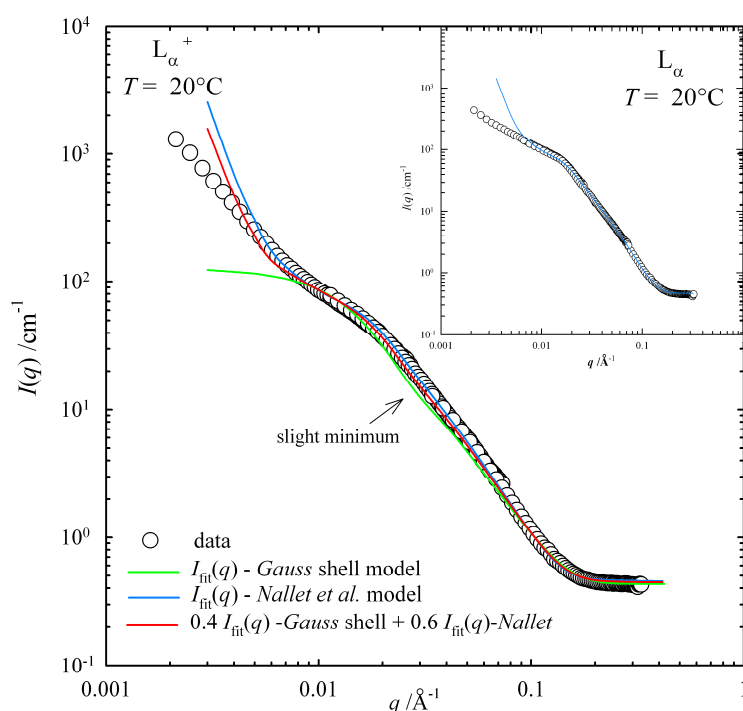


Figure 90: Scattering intensity I plotted versus the scattering vector q for the sample D_2O /glycerol - $C_{12}E_4$ with $\phi = 0.08$ at $T = 4^{\circ}C$. Combining the scattering contributions stemming from lamellar sheets and monodisperse small vesicles (green and blue curve) an almost quantitative description of the experimental data points is obtained at least for the intermediate and high q -range (red curve).

THERMODYNAMIC STABILITY OF VESICLES IN NMR

The DLS, SANS and FFEM results have demonstrated that within the L_{α}^+ phase a “zoo” of structures is present. Another method used in the work at hand to yield additional information concerning the structure and the thermodynamic stability of the L_{α}^+ phase was nuclear magnetic resonance (NMR).

In Figure 91 the NMR spectra for three differently treated $^2\text{H}_2\text{O}-\text{C}_{12}\text{E}_4$ samples containing a surfactant concentration of $\gamma = 0.20$ are shown. In method 1 the sample was prepared in a big tube, heated to $T = 54^\circ\text{C}$ (L_{α}), transferred into the thinner NMR tube. In method 2 the sample solution was again prepared in the big tube, heated to $T = 63^\circ\text{C}$ (L_3), then temperature jump was performed to $T = 54^\circ\text{C}$ (L_{α}) and transferred into the thinner NMR tube. In method 3 the sample solution was again prepared in the big tube, heated to $T = 63^\circ\text{C}$ (L_3), transferred into the thinner NMR tube, then temperature jump was performed to $T = 54^\circ\text{C}$ (L_{α}). Comparing the spectra of the L_{α} phases (black lines) of all three methods, one can see that the signals obtained from method 1 and 2 are sharper than method 3. A reason of this observation might be that the lamellar phases in the first two methods are oriented due to shearing. On the contrary in method 3 the signal is broader as a result of the temperature jump from sponge phase to the lamellar phase. To prepare the vesicular phase ($T = 30^\circ\text{C}$) negative temperature jumps to from the differently prepared lamellar phases ($T = 54^\circ\text{C}$) were performed. As can be seen, the L_{α}^+ singlet (blue lines) is broader than the L_{α} singlet for all preparation methods. As for the L_{α} phase, the signals of the L_{α}^+ phase become wider from method 1 to method 3.

To sum up, the more energy (*e.g.* shearing) is put into the system to prepare the lamellar phase, the narrower are the signals of both, the L_{α} and the resulting L_{α}^+ phase. The quintessence of the experiment shown in Figure 91 is that L_{α}^+ is once more shown to be a not thermodynamically stable phase, since its structure strongly depends on the way of preparation. Thermodynamic equilibrium would require same structures independent of the way of preparation.

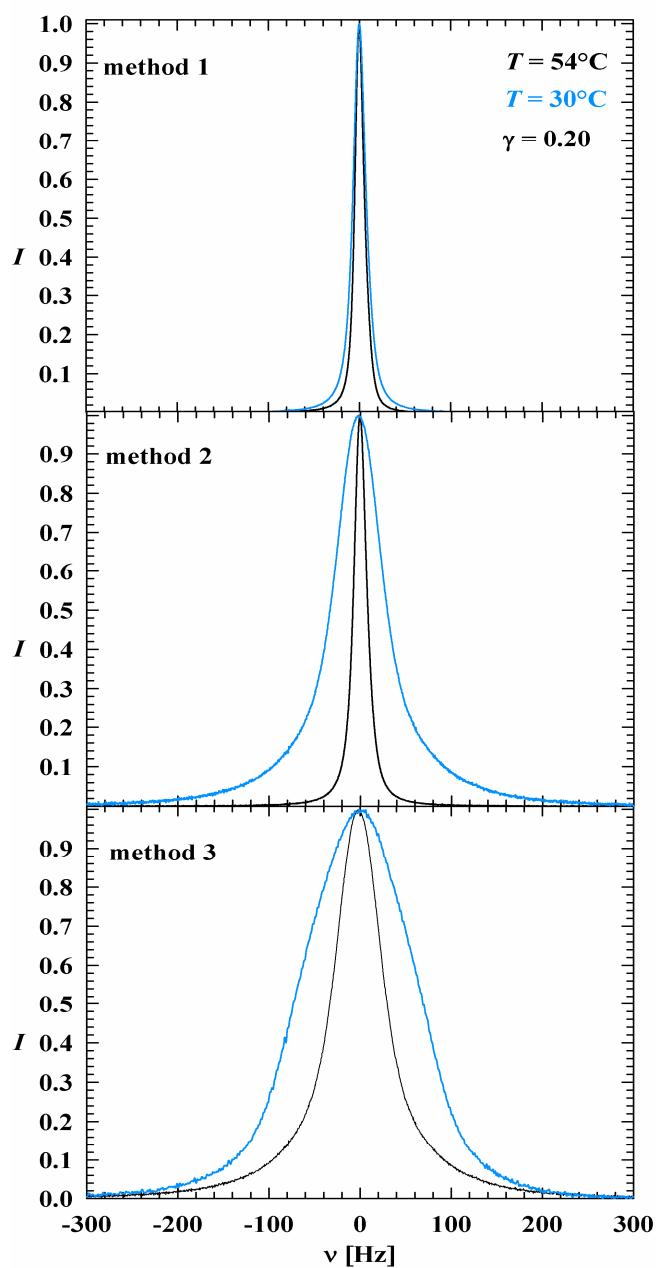


Figure 91: NMR spectra for L_{α} ($T = 54^\circ\text{C}$) and L_{α}^+ ($T = 30^\circ\text{C}$) within $^2\text{H}_2\text{O} - \text{C}_{12}\text{E}_4$ system three differently treated samples of the same surfactant concentration $\gamma = 0.20$.

VESICLE STABILITY – A THEORETICAL APPROACH

The experiments above show that within the L_{α}^+ region of the water – $C_{12}E_4$ system vesicles both multi- and uni-lamellar seem to coexist with the lamellar structure. Thus, this work provides strong indication that the L_{α}^+ phase is not a thermodynamically stable phase. Also in literature vesicles made out of surfactants are mostly considered to be metastable structures¹⁸⁵. However, there are also several reports in the literature claiming that thermodynamically stable vesicles have been found^{186,187,188,189}.

In order to discuss the thermodynamic stability of the L_{α}^+ phase the bending energy of the vesicle can be considered:

$$E = (2\kappa + \bar{\kappa})[(H_{eff} + H_{out})^2 + (H_{eff} + H_{in})^2], \quad [61]$$

in which H_{out} is the spontaneous curvature of the outer monolayer, H_{in} is the spontaneous curvature of the inner monolayer and H_{eff} is taken to be the effective curvature. The two monolayers of a spherical vesicle, as schematically shown in Figure 92, have curvatures with opposite signs, $c_e = -c_i$, and of nearly equal magnitude (if the radius is much larger than δ_{bi}). However, the total sum is slightly negative.

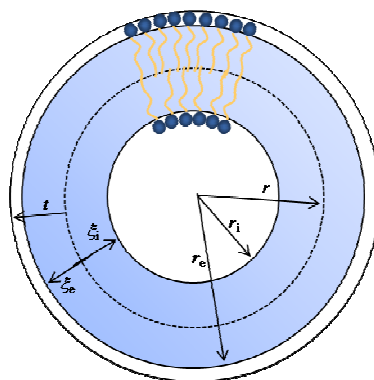


Figure 92: Model of a spherical unilamellar bilayer vesicle.

¹⁸⁵ U. Olsson, K. Nakamura, H. Kunieda, R. Strey, *Langmuir* **12**, 3045 (1996).

¹⁸⁶ E. F. Marques, A. Khan, M. d. G. Miguel, B. Lindman, *J. Phys.Chem.* **97**, 4729 (1993).

¹⁸⁷ R. Joannic, L. Auvray, D. D. Lasic, *Phys. Rev. Lett.* **78**,3402 (1997).

¹⁸⁸ I. Schleifer, O. V. Gerasimov, D. H. Thompson, *Proc. Natl. Acad.Sci. U.S.A.*, **95**, 1032 (1998).

¹⁸⁹ A. Khan, E. F. Marques, *Curr. Opin. Colloid Interface Sci.* **4**, 402 (2000).

For large vesicles all curvatures are almost zero and similar, *i.e.* $H_{\text{eff}} = H_{\text{in}} \approx H_{\text{out}}$. Therefore the bending energy of lamellar sheets and vesicles are almost equal. Neglecting entropic contributions which may favor the formation of vesicles, both lamellar structures as well as vesicles will most probably coexist in water – surfactant systems. However, by increasing the bending rigidity considerably using lipids the bending energy difference of the lamellar and vesicular phases increases. Therewith the formation of thermodynamically stable vesicles is favored.

6 SUMMARY & CONCLUSION

Vesicles occur in biological systems and medical applications. Also they are important for the effect of spatial compartmentalization in biologically relevant reactions. One promising route to understand the physical and chemical properties of these complex biological systems is the study of vesicles formed in simple systems. Thus, I became interested in understanding the vesicular phase, in particular in binary water - non-ionic surfactant systems. The existence of the vesicle phase (L_{α}^+) in the water - non-ionic surfactant $C_{12}E_4$ system is known since many years³⁴. However, preparing samples by temperature jumps from the lamellar phase L_{α} to the L_{α}^+ phase one finds that without stirring the phase stays anisotropic. Only after a small input of energy via slight stirring of the sample the anisotropy vanishes, *i.e.* the vesicle phase is formed. This observation raises the question whether this vesicle phase is thermodynamically stable. As a tool of probing the stability of the vesicular phase temperature jump experiments (ΔT), negative as well as positive from the adjacent single phases above and below the L_{α}^+ phase, respectively, were performed. If the structures obtained following complementary opposite temperature jumps are in agreement, this would be a strong indication that the vesicular phase is a thermodynamically stable state.

Starting point of this work was the study of the phase behavior of the binary system $H_2O - C_{12}E_4$. It could be confirmed that the L_{α}^+ phase extends over a wide surfactant mass fraction range of $\gamma = 0.01 - 0.275$ (Figure 32). Furthermore, the L_{α}^+ phase is located between

two branches of lamellar phase, one at high and one at low temperature. These separate branches connect, though, at higher surfactant mass fraction γ . In preparation for characterization of the microstructure by dynamic light scattering (DLS), small angle neutron scattering (SANS), freeze fracture electron microscopy (FFEM), nuclear magnetic resonance (^2H - NMR) also the phase behavior of the $\text{D}_2\text{O} - \text{C}_{12}\text{E}_4$ system was measured. As anticipated from other studies by replacing H_2O with D_2O the whole phase behavior is shifted to lower temperatures by $\Delta T \sim 2^\circ\text{C}$ (Figure 33). Also the phase behavior of the $\text{H}_2\text{O}/\text{NaCl} - \text{C}_{12}\text{E}_5$ system, with a salt content of $\varepsilon = 0.185$, was measured. By adding salt I achieved that the phase behavior of the $\text{H}_2\text{O} - \text{C}_{12}\text{E}_5$ system resembles almost that of the phase behavior of the $\text{H}_2\text{O} - \text{C}_{12}\text{E}_4$ system (Figure 37). Finally the $\text{H}_2\text{O}/\text{glycerol} - \text{C}_{12}\text{E}_4$ system was measured for two reasons. Firstly the kinetics are slower due to the high viscosity and secondly with a glycerol amount of $\psi = 0.50$ the L_{α}^+ phase is stable at very low temperatures (Figure 34), so the $\text{H}_2\text{O}/\text{glycerol} - \text{C}_{12}\text{E}_4$ system is ideal for freeze fracture electron microscopy (FFEM)¹²⁷.

The first technique used to study the microstructure of the L_{α}^+ phase was DLS. L_{α}^+ samples were prepared by negative temperature jumps both from the lamellar (L_{α}) and the sponge (L_3) phase. Plotting the obtained diffusion coefficients as a function of q^2 it turned out that the samples consist, independent of the preparation method used, of at least two diffusing species (Figure 40). Assuming spherical objects the *Stokes-Einstein*-equation is used inserting the viscosity of water to determine their hydrodynamic radii. The radii obtained were of the order of 30, 100 and 1000nm, respectively and therewith one order of magnitude larger than the bilayer repeat distances of the initial lamellar and sponge phases. However, one has to keep in mind that both the use of *Stokes-Einstein*-equation and the viscosity of water are questionable. Varying the surfactant concentration from $\gamma = 0.01$ to $\gamma = 0.05$ the hydrodynamic radius (averaged over the different scattering angles) is found to increase from 160nm to 500nm (Figure 43 and Figure 44). Thereby the same trend is observed for both preparation methods. However, the increase of the hydrodynamic radius with increasing γ is reverse to the variation of repeat distance of the bilayers in the initial lamellar and sponge phases. Furthermore, the trend found disagrees with the observation made by *Strey*³⁶ that the samples become increasingly bluish with decreasing surfactant concentration. The results obtained by DLS indicate that several, *i.e.* at least two different structures exist within the existence region of the L_{α}^+ phase.

In order to obtain information on the occurring structural length scales within the L_{α}^+ -phase SANS measurements have been performed for surfactant mass fractions of

$\gamma = 0.02$ to $\gamma = 0.11$. Positive temperature jumps (L_1 to L_{α}^+) as well as negative temperature jumps (L_{α} to L_{α}^+) were performed on samples of the $D_2O - C_{12}E_4$ system. In each case the scattering curves of the L_3 , L_{α} and L_1 phases were recorded in order to define the structure of the initial states. Using the structure factors of *Lei et al* for the L_3 Phase (Figure 50) and *Nallet et al.* (Figure 51) for the L_{α} phase as well as the form factor of cylinders in the L_1 case (Figure 55 and Figure 56) all scattering curves could be analyzed. The shape of the SANS curves of L_{α}^+ phase obtained both by positive and negative temperature jumps resemble the shape the L_{α} curves. However, it is interesting to notice that the shoulder of the L_{α}^+ scattering curve appears at higher q -values compared to the one of the L_{α} phase. Furthermore, the higher intensity at low values of the scattering vector indicates the existence of larger structures (Figure 52 and Figure 57). In a second series of experiments negative temperature jumps (L_{α} to L_{α}^+) were also performed on samples of the D_2O /glycerol - $C_{12}E_4$ system. Again also the scattering curves of the initial states were recorded and described by the respective structure factors (Figure 60). The scattering curves of the L_{α}^+ phase obtained in the glycerol containing system shows compared to glycerol-free system a slight dent at intermediate q -values (Figure 59). However without further information concerning the shape of structures a reasonable description of the data was not feasible.

To support the findings from DLS and SANS, selected samples were studied by freeze fracture electron microscopy (FFEM). Positive temperature jumps (L_1 to L_{α}^+) as well as negative temperature jumps (L_{α} to L_{α}^+) in $H_2O - C_{12}E_4$ system were performed at the surfactant mass fraction $\gamma = 0.03$. In both cases a wealth of structures is seen that indicates a non-equilibrium state. In case of the positive temperature jump the L_{α}^+ phase displays many unilamellar vesicles with a size between 30, 100 and 1000nm and some berry-like structures (Figure 64 and Figure 65). Similar structures are found in the image of the L_{α}^+ phase obtained by a negative temperature jump from the L_{α} phase. However, compared to the positive T -jump more berries are found (Figure 62). In addition the H_2O /glycerol - $C_{12}E_4$ system has been chosen to picture samples of the L_{α}^+ ($T = 4^{\circ}C$), L_{α} ($T = 20^{\circ}C$) and L_3 phase ($T = 28^{\circ}C$). The FFEM pictures (Figure 69) of the L_3 phase show droplet shaped passages while the dominating feature which can be found in the pictures of the L_{α} phase is the lamellar structure (Figure 70). Large multilamellar vesicles (Figure 42), lamellar structures, but also many small monodisperse and unilamellar vesicles of a size of 40nm can be observed in the FFEM-picture of the L_{α}^+ phase (Figure 74). Thus, a support of thermodynamic equilibrium of the L_{α}^+ phase from FFEM images cannot be deduced.

However, with the help of the structural information obtained from FFEM, one exemplary SANS curve of the L_{α}^+ phase could be described quantitatively (Figure 89).

^2H - NMR measurements were performed to gain a better insight into the L_{α} to L_{α}^+ transition in $^2\text{H}_2\text{O} - \text{C}_{12}\text{E}_4$ system. The use of ^2H - NMR spectroscopy proves to be particularly advantageous, since the different ^2H - NMR patterns of the two phases allow a rigorous examination (*e.g.* singlet for the isotropic L_{α}^+ phase and a doublet for the anisotropic L_{α} phase) of the L_{α} to L_{α}^+ transition. However, due to the low resolution of the NMR equipment the concentration range was limited ($\gamma > 0.20$). Three types of experiments were performed. (i) Temperature jumps (T -jumps) from L_{α} to L_{α}^+ phase within concentration range of $\gamma = 0.20 - 0.25$ which were expected to give information about the phase transition line between the two phases L_{α} and L_{α}^+ (Figure 75 - Figure 77). (ii) Investigation of "three-phase-line" (between $L_1' + L_1''$ and L_{α}^+) focusing the determination of the precise location of the "three-phase-line" to better understand kinetics on the one hand and on the other hand gain more information about thermodynamic stability of L_{α}^+ phase (Figure 81 - Figure 83). (iii) Temperature scan of L_{α} phase within concentration range of $\gamma = 0.30 - 0.40$. For sample concentrations $\gamma = 0.30$, $\gamma = 0.35$ and $\gamma = 0.40$ the quadrupolar splitting of $^2\text{H}_2\text{O}$ molecules $\Delta\nu$ was measured temperature dependent ($T = 20^\circ\text{C}$ to $T = 60^\circ\text{C}$) and provides information on the nature of lyotropic liquid crystalline phases formed. With increasing temperature the distribution of quadrupolar splitting $\Delta\nu$ shows a maximum that differs with concentration, shifting to higher values the higher the concentration is (Figure 86 and Figure 87). Samples with $\gamma < 0.30$ gave broad singlet in lamellar as well as in vesicular regions. Interestingly, a random mesh structure also occurs in the present water- C_{12}E_4 lamellar phase; however, perforations appear first below ca. 25°C .

In conclusion this work contributed to a better understanding of the vesicular phase L_{α}^+ formed in the non-ionic surfactant C_{12}E_4 - water system. It appears that the region denoted as L_{α}^+ should not be conceived as a separate phase, but rather represents a cumulus of structural aggregates within which vesicular objects are present, but always together with lamellar structures. Even when vesicles were the dominant feature, they were far from being consistent in size and degree of lamellar, *i.e.* uni- or multilamellar vesicles were equally present. Thus, a thermodynamic stability of the L_{α}^+ phase is not supported by this work.

7 APPENDIX

DYNAMIC LIGHT SCATTERING - EXPERIMENTAL SETUP AND PROCEDURE

For the experiments, monochromatic and coherent laser light is sent through the sample placed in a toluene bath for index matching.

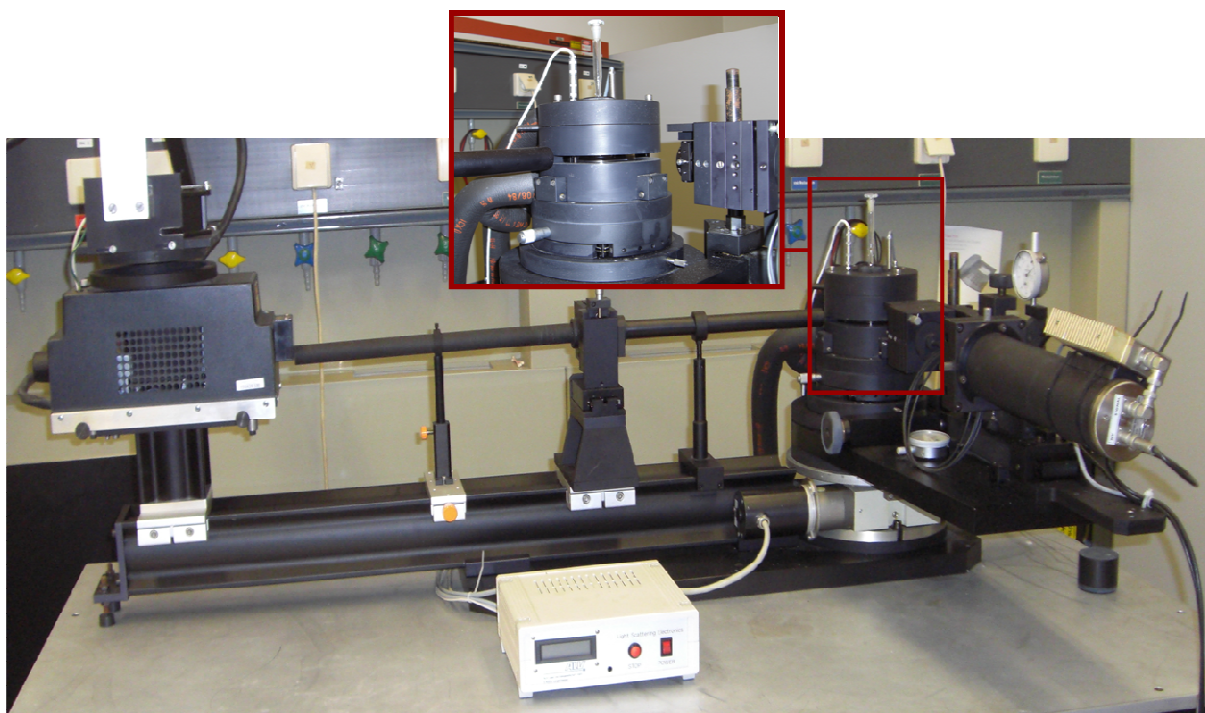


Figure 93: Dynamic Light Scattering (DLS) setup.

For dynamic light scattering measurements special cylindrical glass cuvettes (Schott borosilicate glass, Schott GmbH) with a closure head are used. The inner diameter is 7 mm, the outer diameter 10mm. For experiments 1mL solution is sufficient. Available spectrometers/instruments were from ALV – 5000e Multiple Tau® - digital correlators (ALV – Laser Vertreibsgesellschaft mbH). As light source an argon-ion-laser (Spectra Physics, model 161B, 15mW) and a helium-neon-laser (NEC model GIG5741, 35mW) with wavelength of $\lambda = 488\text{nm}$ and $\lambda = 632.8\text{nm}$ respectively were disposed. The measurements were done in 10° steps within an angle range from 30° to 150° and detected by a photomultiplier (Thorn EMI Electron Tubes, GB) installed on a goniometer arm which is free rotatable between the above mentioned scattering angles.

FREEZE FRACTURE ELECTRON MICROSCOPY - SAMPLE PREPARATION

In the following section the sample preparation will be described more in detail. For the detailed description mainly the dissertation of S. Burauer, who worked on freeze fracture microscopy very much in detail, was used.

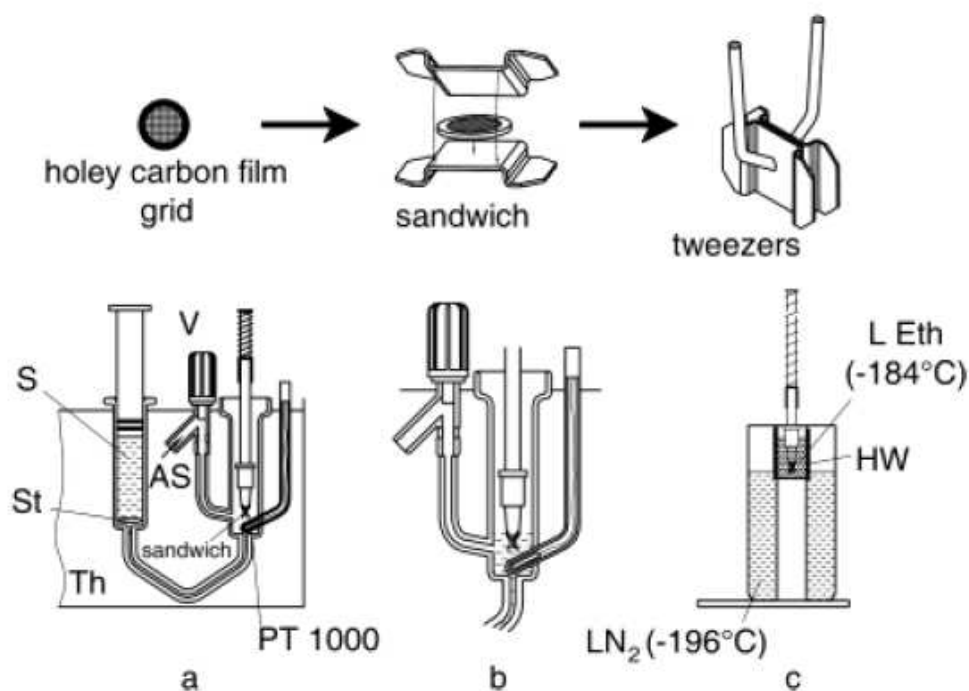


Figure 94: Schematic drawing of the procedure according to which the specimens of the FFDI technique are prepared. Top: sandwich building. Bottom: (a) glass tube with the solution S, stirrer St, air stream AS, and valve V in a water bath Th; (b) sandwich in contact with the solution; and (c) sandwich in L Eth, which is placed in a copper vessel with a heating wire (HW) and cooled in a Dewar with liquid nitrogen (L N₂)¹⁹⁰.

¹⁹⁰ L. Belkoura,* C. Stubenrauch, and R. Strey, *Langmuir*, **20**, 4391-4399 (2004).

The procedure of preparing the specimen for FFDI is as follows: Two copper plates of 0.1mm thickness (BU 012056-T, Bal-Tec, Lichtenstein) were first coated with a carbon layer (10-40nm) by evaporating a carbon thread in a sputter coater (SCD 005, Bal-Tec, Lichtenstein) at 0.1mbar. Depending on the solution to be investigated, hydrophilic or hydrophobic surfaces are needed for the preparation. Thus, to modify the surfaces, the coated copper plates and a copper grid with a holey carbon film (Quantifoil QS 7/2, Jena, Germany) are then exposed in the sputter coater to a glow discharge in an argon atmosphere for 60s at 0.1mbar and 10mA. In Figure 94, schematic drawings of the most important preparation steps are shown. First, the copper plates and the copper grid are assembled to form a sandwich, which is held by tweezers. Second, the sandwich is inserted in the new developed tube, which is equipped with a temperature sensor (Pt 1000). With a stream of dried air (AS), the sandwich is brought to thermal equilibrium, monitored by the temperature sensor Pt 1000. After thermal equilibrium is reached, the air stream is closed (valve V) and the solution (S) is brought into contact with the sandwich (b). The solution penetrates into the sandwich, which is then rapidly transferred into the cryogen (LEth) with the aid of a plunging device. Because ethane solidifies at the liquid nitrogen is activated to keep it at its liquid state. Shortly before the transfer, the heating is switched off and the sandwich is plunged into the cryogen just before LEth starts to solidify. For specimen preparations at room temperature, a cryobox (GA G34-215, Zeiss, Oberkochen, Germany) equipped with a spring-propelled plunging rod was used. After the transfer into liquid nitrogen, the sample is fractured under liquid nitrogen and the grid is mounted in a cryo-holder and viewed in the TEM. The sandwich is dipped into the solution, rapidly frozen, and fractured as schematically drawn in Figure 3. After the fracture under liquid nitrogen one grid is used for DI (FFDI) and the second grid, its complementary counterpart, is shadowed with Ta/W and coated with a carbon layer (FFEM)¹⁹¹. The copper plates undergo the same coating and glow discharge procedure as mentioned above before they are assembled to a sandwich. The bare grid used is a hexagonal-mesh tabbed copper TEM grid (*Ted Pella, Inc.*, 8HGC360) 3 mm in diameter. To fix the bare grid on the copper plate, its tab was bent on the copper plate and glued on the back side with a small amount of glue (*Pattex WA97, Henkel, Germany*) as described in Vinson et al¹⁹².

In Figure 95 the whole unit is shown in detail.

¹⁹¹ Burauer, S.; Belkoura, L.; Stubenrauch, C.; Strey, R. *ColloidsSurf.*, **228** (1-3), 159 (2003).

¹⁹² P. K. Vinson, J. G. Sheehan, W. G. Miller, L. E. Scriven, H. T. Davis, *J. Phys. Chem.* **95**, 2546 (1991).

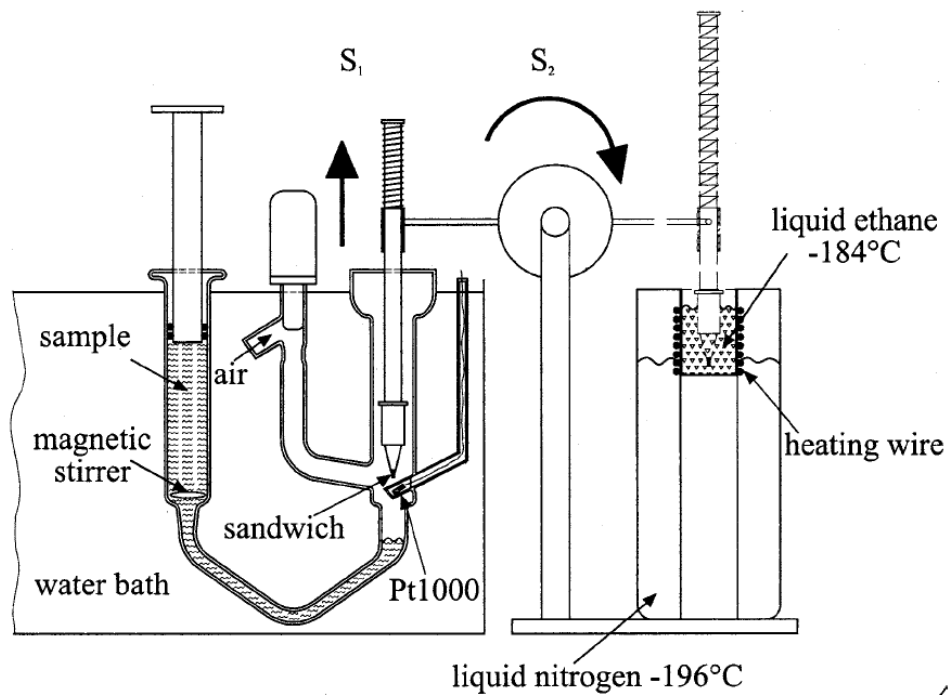
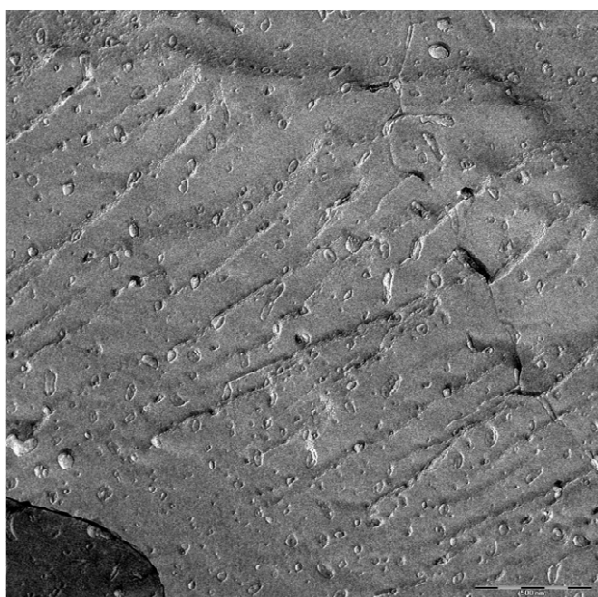
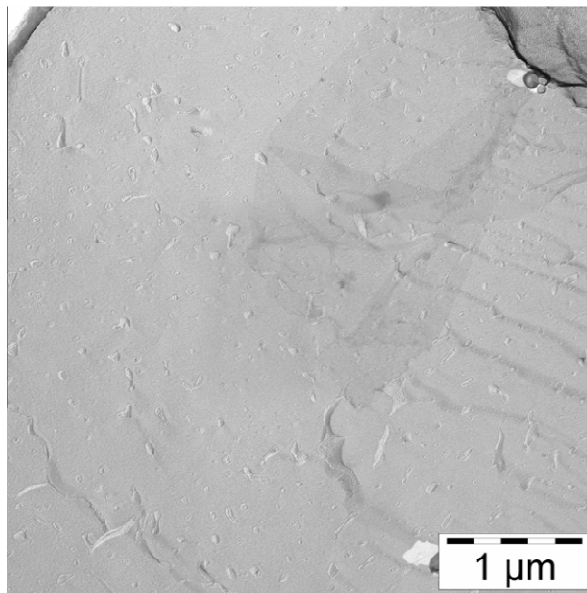
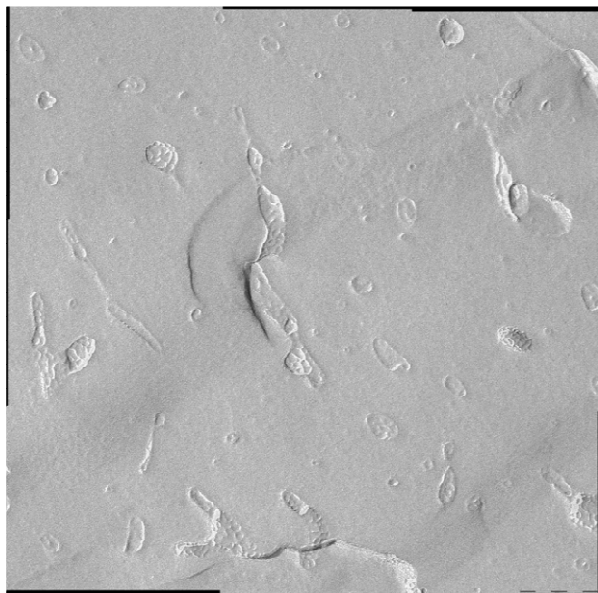


Figure 95: Unit to control the preparation temperature within accuracy of ± 0.02 K prior to freezing. The sandwich and the tweezers by which it is held are placed in the unit such that they are both passed by an air stream, which has the same temperature as the solution. When the temperature difference between the air and the liquid sample is below 0.02 K, the air flow is stopped and the syringe is used to bring the solution and the sandwich into contact. To freeze the sample it is transferred into liquid ethane with a plunging device executing two spring motions, namely an upward (S1), followed by a half circular motion (S2).

After the grid is prepared the replicas are imaged with an electron microscope. Several pictures can be taken from different positions (approximately 800 possible positions) on each grid.

*FFEM: ADDITIONAL IMAGES*NEGATIVE T - JUMPS ($\text{H}_2\text{O} - \text{C}_{12}\text{E}_4$)

In the following some additional FFEM pictures are presented taken from negative temperature jumps within $\text{H}_2\text{O} - \text{C}_{12}\text{E}_4$ system.



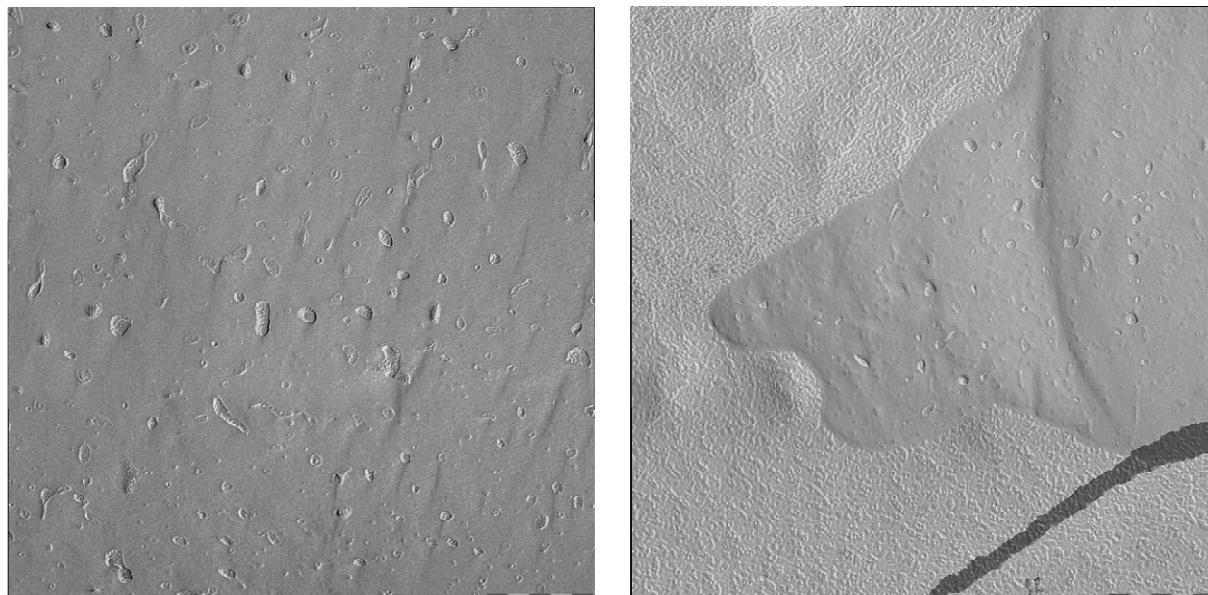


Figure 96: FFEM images of $\text{H}_2\text{O} - \text{C}_{12}\text{E}_4$ system, taken after negative T - jump for an exemplary surfactant mass fraction of $\gamma = 0.03$.

Figure 96 shows vesicles associated in “berry” – type structures of more or less similar size and some other vesicle structures that could be interpreted as uni- and multilamellar vesicles.

POSITIVE T - JUMPS ($\text{H}_2\text{O} - \text{C}_{12}\text{E}_4$)

In this sequence some additional FFEM pictures are presented taken from positive temperature jumps within $\text{H}_2\text{O} - \text{C}_{12}\text{E}_4$ system.

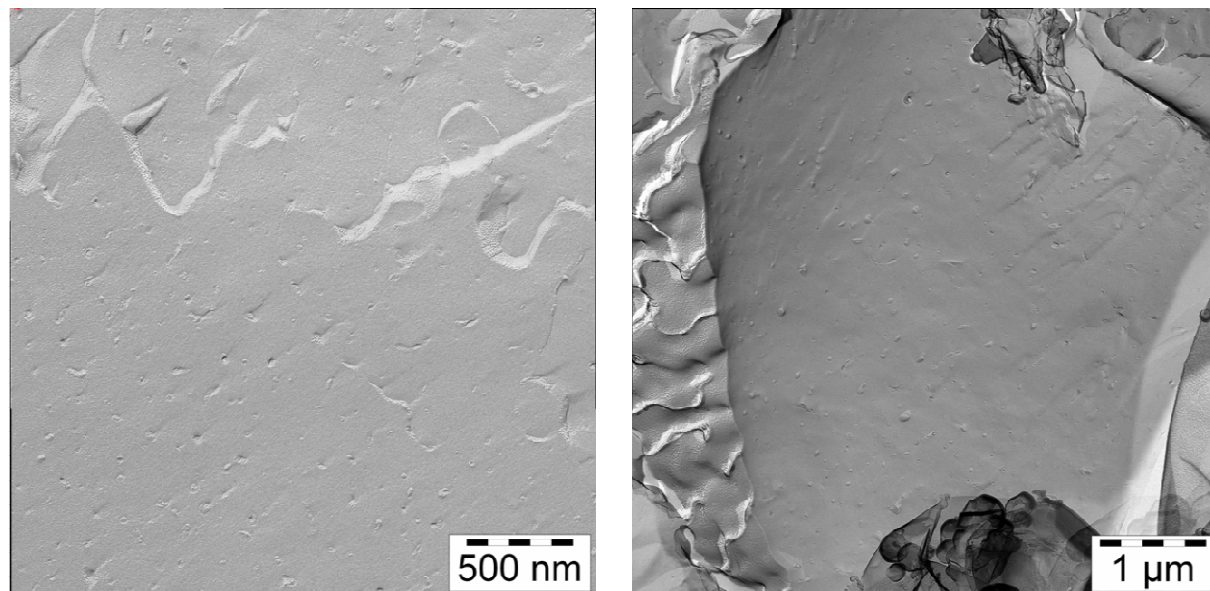


Figure 97: FFEM images of $\text{H}_2\text{O} - \text{C}_{12}\text{E}_4$ system, taken after positive T - jump for a surfactant mass fraction of $\gamma = 0.03$.

 $\text{H}_2\text{O}/\text{GLYCEROL} - \text{C}_{12}\text{E}_4$ (L_3)

Additional FFEM pictures from sponge phase L_3 within $\text{H}_2\text{O}/\text{glycerol} - \text{C}_{12}\text{E}_4$ system.

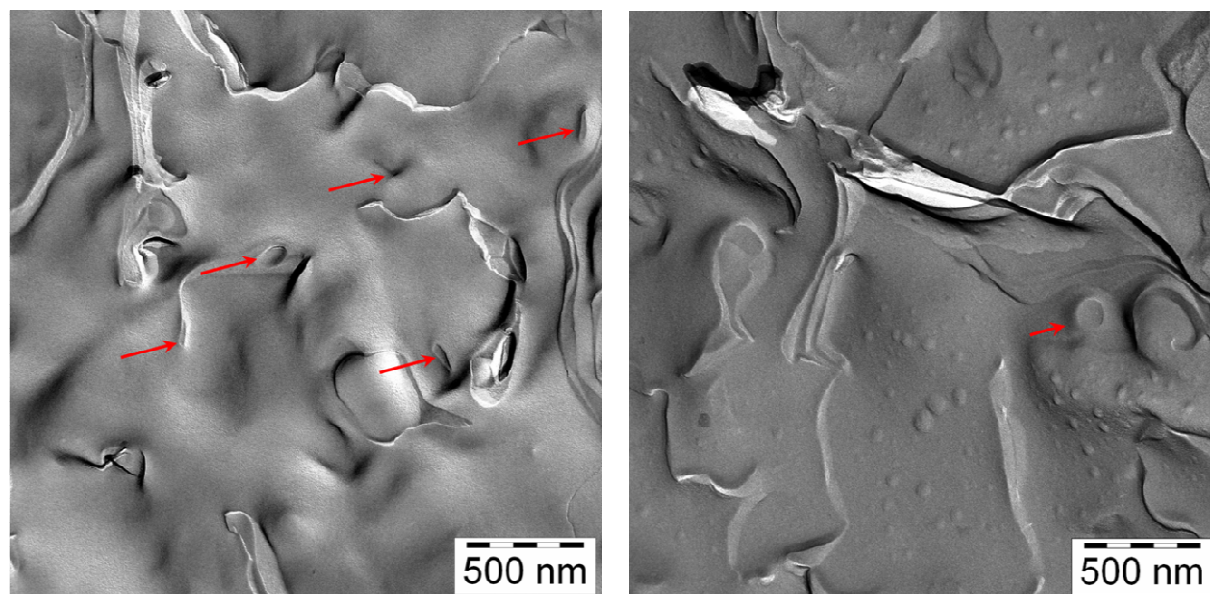


Figure 98: FFEM images of $\text{H}_2\text{O}/\text{glycerol} - \text{C}_{12}\text{E}_4$ system, taken for equilibrium sponge phase L_3 at a temperature $T = 32^\circ\text{C}$ with a surfactant mass fraction of $\gamma = 0.03$.

$\text{H}_2\text{O}/\text{GLYCEROL} - \text{C}_{12}\text{E}_4 (\text{L}_{\alpha}^+)$

Additional FFEM pictures from vesicular phase L_{α}^+ within $\text{H}_2\text{O}/\text{glycerol} - \text{C}_{12}\text{E}_4$ system.

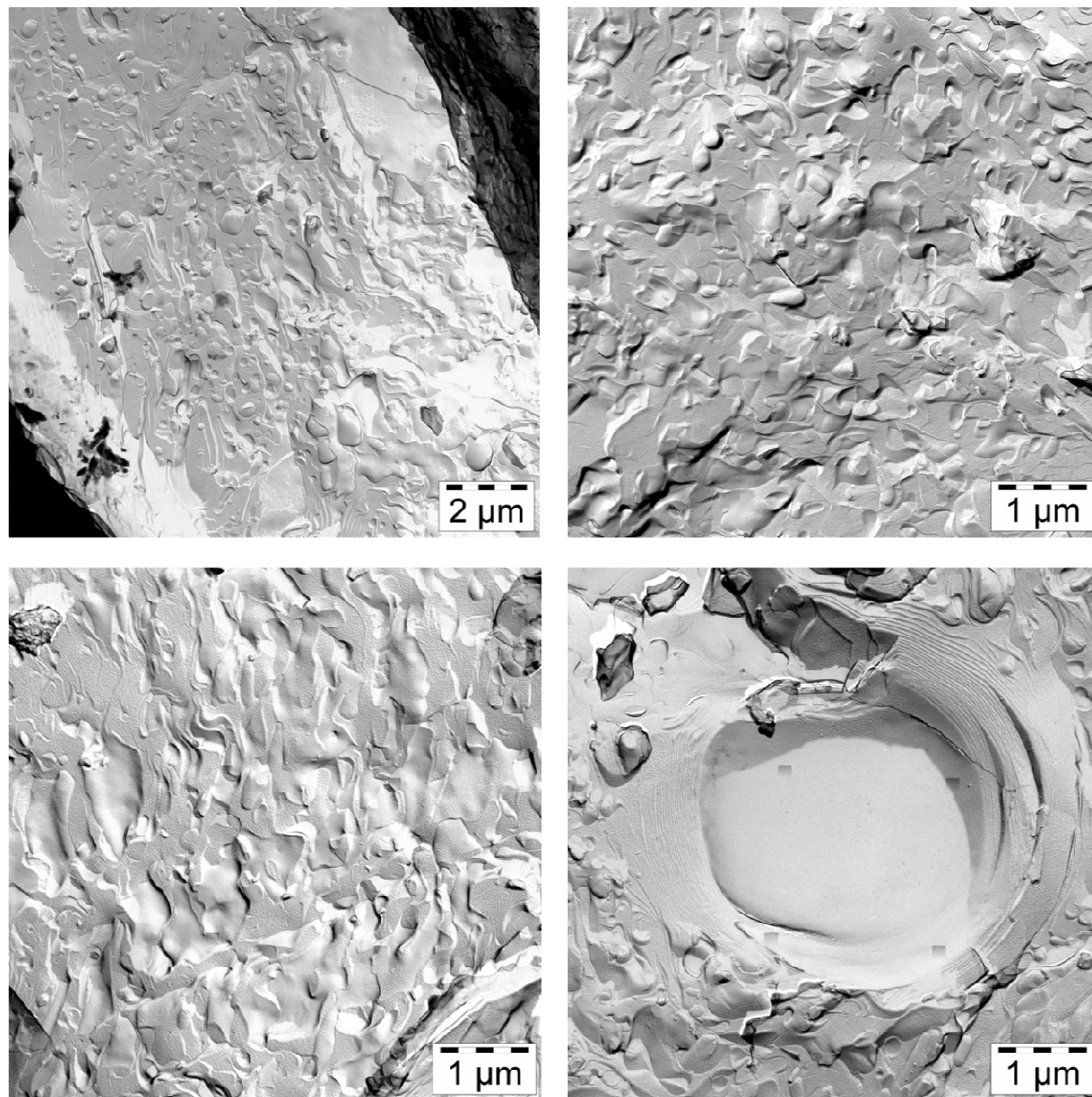


Figure 99: FFEM images of $\text{H}_2\text{O}/\text{glycerol} - \text{C}_{12}\text{E}_4$ system, taken for equilibrium vesicular phase L_{α}^+ at a temperature $T = 4^\circ\text{C}$ with a surfactant mass fraction of $\gamma = 0.03$.

$\text{H}_2\text{O}/\text{GLYCEROL} - \text{C}_{12}\text{E}_4 (L_\alpha)$

Additional FFEM pictures from vesicular phase L_α within $\text{H}_2\text{O}/\text{glycerol} - \text{C}_{12}\text{E}_4$ system.

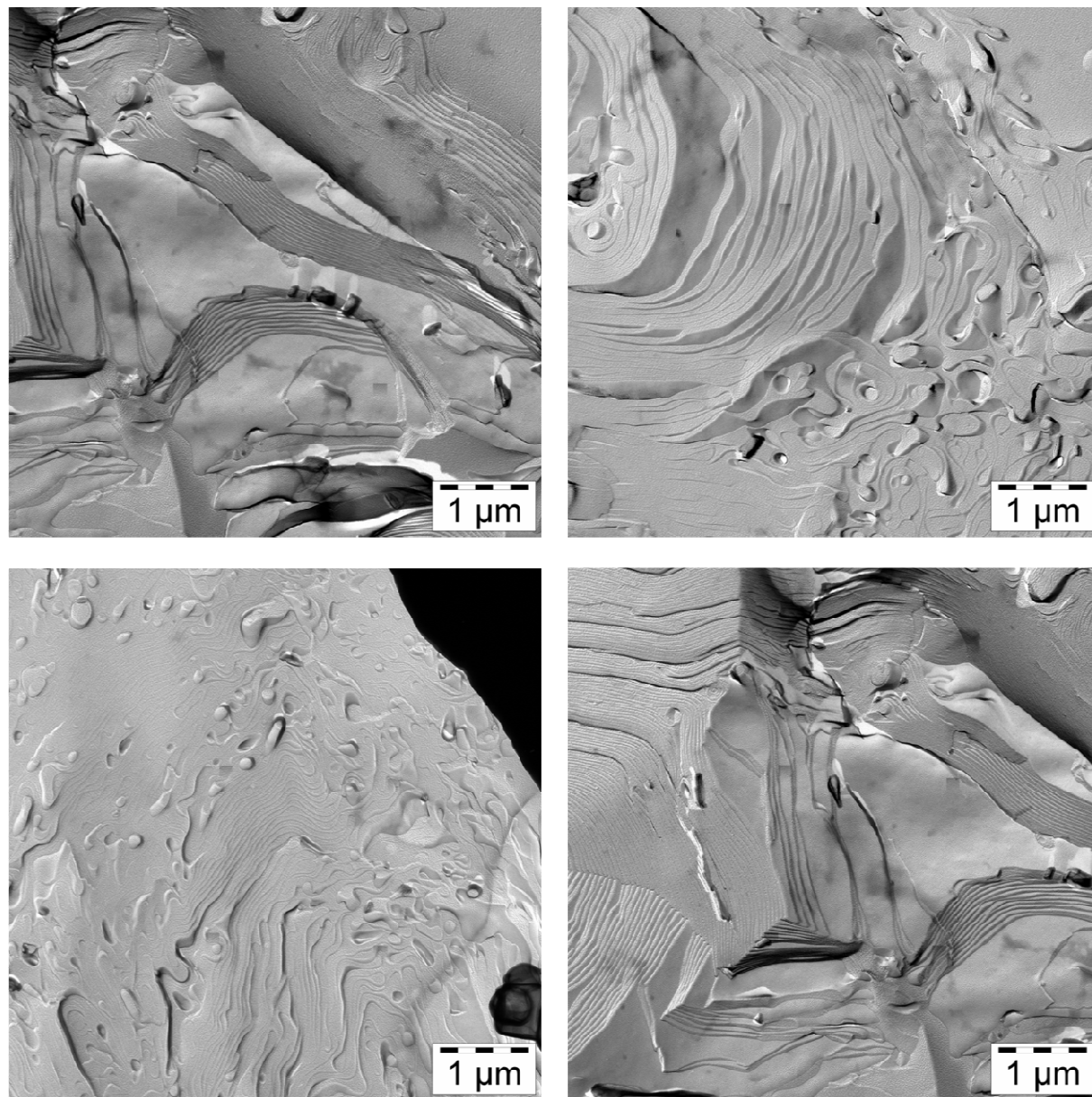


Figure 100: FFEM images of $\text{H}_2\text{O}/\text{glycerol} - \text{C}_{12}\text{E}_4$ system, taken for equilibrium lamellar phase L_α at a temperature $T = 20^\circ\text{C}$ with a surfactant mass fraction of $\gamma = 0.03$.

NUCLEAR MAGNETIC RESONANCE - EXPERIMENTAL SETUP AND PROCEDURE

NMR APPARATUS

^2H NMR experiments were carried out in Bruker DMX 100 NMR (Figure 101: Bruker DMX 200) spectrometer operating at 15.371 MHz in a 2.3 T magnetic field. The samples were filled in 4 cm long glass tubes of 5mm diameter, which were sealed with Teflon plug and epoxy glue. The tubes were inserted into a home-built goniometer probe such that the tube axis was perpendicular to the static magnetic field.

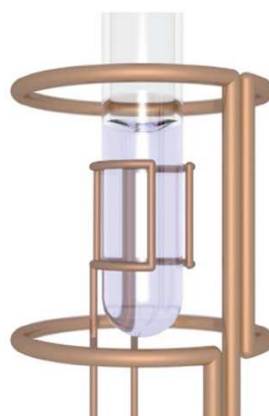


Figure 101: Sample in a rf (radio frequency) coil in a magnet.

The quadrupolar splitting values in the lamellar and vesicular phase were recorded using the quadrupolar-echo sequence. The temperature of the sample was achieved and maintained using an airflow system, to an accuracy of $\pm 1^\circ\text{C}$.

The heart of the spectrometer is the computer. It controls all of the components of the spectrometer. The RF components under control of the computer are the RF frequency source and pulse programmer. The source produces a sine wave of the desired frequency. The pulse programmer sets the width, and in some cases the shape, of the RF pulses. The RF amplifier increases the pulses power from milli Watts to tens or hundreds of Watts. The computer also controls the gradient pulse programmer which sets the shape and amplitude of gradient fields. The gradient amplifier increases the power of the gradient pulses to a level sufficient to drive the gradient coils. The operator of the spectrometer gives input to the computer through a console terminal with a mouse and keyboard.

THE MAGNET

The NMR magnet is one of the most expensive components of the nuclear magnetic resonance spectrometer system. Most magnets are of the superconducting type. Figure 102 shows a picture of superconducting magnet from an NMR spectrometer. A superconducting magnet has an electromagnet made of superconducting wire. Superconducting wire has a resistance approximately equal to zero when it is cooled to a temperature close to absolute zero (-273.15°C or 0 K) by immersing it in liquid helium. Once current is caused to flow in the coil it will continue to flow for as long as the coil is kept at liquid helium temperatures. The length of superconducting wire in the magnet is typically several miles. This wire is wound into a multi-turn solenoid or coil. The coil of wire is kept at a temperature of 4.2K by immersing it in liquid helium. The coil and liquid helium are kept in a large dewar. This dewar is typically surrounded by a liquid nitrogen (77.4K) dewar, which acts as a thermal buffer between the room temperature air (293K) and the liquid helium.



Figure 102: NMR 200 as it is in the lab of fekm1 in Lund University, Sweden.

THE RF COILS

RF coils create the B_1 field which rotates the net magnetization in a pulse sequence. They also detect the transverse magnetization as it precesses in the XY plane. Most RF coils on NMR spectrometers are of the saddle coil design (Figure 101) and act as the transmitter of the B field and receiver of rf energy from the sample. RF coils used in NMR spectrometers need to be tuned for the specific sample being studied. An RF coil has a bandwidth or specific range of frequencies at which it resonates. The B field of an RF coil must be perpendicular to the B_0 magnetic field. Another requirement of an RF coil in an NMR spectrometer is that the B field needs to be homogeneous over the volume of your sample. If it is not, one will be rotating spins by a distribution of rotation angles and you will obtain strange spectra.

THE PROBE

The sample probe is the name given to that part of the spectrometer which accepts the sample, sends RF energy into the sample, and detects the signal emanating from the sample. It contains the RF coil, sample spinner, temperature controlling circuitry, and gradient coils.

SHIMMING

The purpose of shimming a magnet is to make the magnetic field more homogeneous and to obtain better spectral resolution. Shimming can be performed manually or by computer control. Broad lines, asymmetric lines, and a loss of resolution are indications that a magnet needs to be shimmed. The shape of an NMR line is a good indication of which shim is misadjusted. In general, asymmetric line shapes result from mis-adjusted even-powered Z shims. This can be seen by looking at the shape of a Z^2 shim field. As one goes further away from the center of the sample in the $+Z$ or $-Z$ direction, the field increases, giving more components of the spectral line at higher fields. The higher the power of the Z inhomogeneity, the further away the asymmetry is from the center of the line. Symmetrically broadened lines are from mis-adjusted odd-powered Z shims. Consider the shape of the Z^3 shim field. The top of the sample ($+Z$) is at a higher field, resulting in higher field spectral components, while the bottom ($-Z$) is at a lower field, giving more lower field spectral components. Transverse shims (X,Y) will cause large first order or second order spinning sidebands when the sample is spun. The shape of these inhomogeneities cause the sample, when it is spun, to experience a periodic variation in the magnetic field. Those shims

(XY or X^2-Y^2) causing a spinning sample to experience two variations per cycle will create second order spinning sidebands.

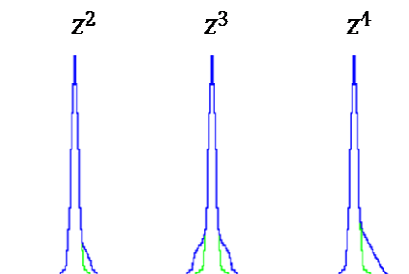


Figure 103: Series of spectra depict the appearance of the exemplary spectral line in the presence of various inhomogeneities.

SAMPLE PREPARATION AND MEASUREMENT

NMR samples are prepared by dissolving an analyte in a deuterium lock solvent. Some of these solvents will readily absorb moisture from the atmosphere and give water signal in the spectrum. It is therefore advisable to keep bottles of these solvents tightly capped when not in use. Most routine high resolution NMR samples are prepared and run in 5 mm glass NMR tubes. The NMR tubes are always filled to the same height with lock solvent. This will minimize the amount of magnetic field shimming required.

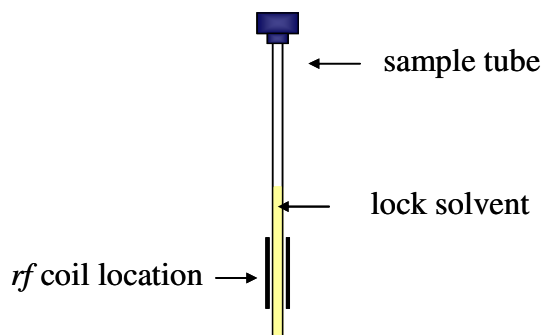


Figure 104: NMR tube filled with solvent such that it fills the rf coil.

The concentration of a sample should be great enough to give a good signal-to-noise ratio in the spectrum, yet minimize exchange effects found at high concentrations. The exact concentration of the sample in the lock solvent will depend on the sensitivity of the spectrometer.

8 TABLES

MATERIALS

Bi-distilled water was used in all experiments with H₂O. D₂O (²H₂O) was purchased from *Cambridge Isotope Laboratories, Inc.* Sodium chloride (NaCl) had a p.a.-quality and was obtained from *Merck* (Darmstadt, Germany), as Glycerol as well. The surfactants C₁₂E₄ and C₁₂E₅ (*n*-dodecyltetraoxyethylene, quoted 98 %, $T_c = 6.6^\circ\text{C}$; *n*-dodecylpentaoxyethylene quoted 98 %, $T_c = 32.0^\circ\text{C}$) were obtained from *Nikko Chemicals co., ltd.* (Tokyo, Japan).

Table 6: Macroscopic densities ρ and molar masses M of components employed.

		ρ [g/cm ³]	M [g/mol]
Water	H ₂ O	0.998	18.015
Deuterium	D ₂ O	1.105	20.029
<i>n</i> -Dodecyltetraoxyethylene	C ₁₂ E ₄	0.950	362.550
<i>n</i> -Dodecylpentaoxyethylene	C ₁₂ E ₅	0.967	406.600
Sodiumchloride	NaCl	---	58.442
Glycerol	C ₃ H ₅ (OH) ₃	1.260	92.094

The cloud point temperatures T_c , at the critical composition of the binary H₂O – surfactant systems were checked to verify the purity and to minor possible degradation of the surfactants.

SAMPLE PREPARATION

The surfactant mass fraction γ is calculated by

$$\gamma = \frac{m_{\text{surfactant}}}{m_{\text{surfactant}} + m_{\text{water}}} \quad [62]$$

with m [g] being the mass of the particular component. The surfactant mass fraction γ is calculated by

$$\phi = \frac{V_{\text{surfactant}}}{V_{\text{surfactant}} + V_{\text{water}}} \quad [63]$$

with V [ml] being the volume of the particular component. Since it is technically easier to deal with masses, knowing the density ρ of the components n the surfactant volume fractions ϕ can be turned into the mass fractions γ :

$$V_n = \frac{m_n}{\rho_n} \quad [64]$$

Stock solutions for H₂O/NaCl and H₂O/glycerol were used: In Eq. [20] the salt mass fraction and in Eq. [21] the glycerol mass fraction is given.

Table 7: Masses of components weighed for the two stock solutions used in this work: H₂O/NaCl and H₂O/glycerol.

	m_{total} [g]	m_{NaCl} [g]	m_{glycerol} [g]
H ₂ O/NaCl	10.000	1.850	8.150
H ₂ O/glycerol	10.000	5.000	5.000

PHASE DIAGRAMS

In the following phase transition temperatures T ($^{\circ}\text{C}$) for phase transitions that occur in the corresponding phase diagrams are given. The phase diagrams presented in this work are

- 1) $\text{H}_2\text{O} - \text{C}_{12}\text{E}_4$,
- 2) $\text{H}_2\text{O}/\text{NaCl} - \text{C}_{12}\text{E}_5$ ($\varepsilon = 0.185$),
- 3) $\text{D}_2\text{O} - \text{C}_{12}\text{E}_4$ and
- 4) $\text{H}_2\text{O}/\text{glycerol} - \text{C}_{12}\text{E}_4$ ($\psi = 0.50$).

Table 8: Phase transition temperatures T [°C] of the $\text{H}_2\text{O} - \text{C}_{12}\text{E}_4$ system.

γ	T [°C]										
	$L_1/L_1'+L_1''$	$L_1'+L_1''/L_\alpha$	L_α/L_α^+	L_α^+/L_α	$L_\alpha/L_\alpha+L_3$	$L_\alpha+L_3/L_3$	L_3/L_1+L_3	L_1+L_3/L_1+L_2	L_α/L_2		
0.0085	6.48	22.57	23.25	48.56	49.60	---	---	---	---		
0.010	6.38	22.15	23.13	47.11	49.2	50.00	52.13	73.58	---		
0.015	6.50	22.24	23.25	45.44	50.70	51.73	53.45	73.56	---		
0.020	6.89	22.39	23.39	44.74	51.59	51.98	55.16	73.46	---		
0.030	7.72	22.63	23.73	43.47	53.02	54.40	56.30	73.52	---		
0.040	8.27	22.53	24.04	42.07	53.83	55.62	57.00	73.56	---		
0.055	8.68	22.39	24.32	40.75	55.40	57.11	57.73	73.52	---		
0.070	9.44	22.53	24.42	40.75	55.84	58.22	58.50	73.56	---		
0.085	10.07	22.46	24.55	40.74	55.45	59.11	59.43	73.48	---		
0.100	10.87	22.75	25.60	41.00	54.98	59.97	60.39	73.56	---		
0.140	12.59	22.85	---	---	56.57	61.61	60.98	73.52	---		
0.200	15.77	22.70	---	---	58.18	63.60	62.78	73.48	---		
0.300	22.87	---	---	---	61.20	66.33	65.01	---	---		
0.400	---	---	---	---	64.04	69.09	---	---	---		
0.500	---	---	---	---	68.00	71.75	---	---	---		

Table 9: Phase transition temperatures T [°C] of the $D_2O - C_{12}E_4$ system.

γ	T [°C]													
	$L_1/L_1'+L_1'$	$L_1'+L_1''/L_\alpha$	L_α/L_α^+	L_α^+/L_α	$L_\alpha/L_\alpha+L_3$	$L_\alpha+L_3/L_3$	L_3/L_1+L_3	L_1+L_3/L_1+L_2	$L_1/L_1''+L_\alpha$	$L_1''+L_\alpha/L_\alpha$	L_α/L	L_2/L_1+L_2		
0.009	4.08	20.50	21.30	46.10	---	51.09	51.95	---	---	---	---	---		
0.012	4.19	20.50	21.00	45.20	---	50.00	52.80	---	---	---	---	---		
0.015	4.00	20.21	21.00	46.69	48.78	50.90	53.3700	---	---	---	---	---		
0.018	4.26	20.57	21.40	43.80	49.71	51.07	54.00	---	---	---	---	---		
0.022	4.50	20.52	21.72	42.66	50.65	52.61	54.31	---	---	---	---	---		
0.035	5.24	20.41	21.40	41.51	51.47	52.95	55.13	---	---	---	---	---		
0.050	6.80	20.33	21.71	40.12	52.25	54.24	56.11	---	---	---	---	---		
0.070	8.00	20.40	21.20	39.40	54.00	56.00	57.00	---	---	---	---	---		
0.100	9.14	20.45	21.60	38.80	54.00	57.51	58.61	---	---	---	---	---		
0.133	10.00	20.60	---	---	---	59.65	60.41	---	---	---	---	---		
0.154	---	20.60	---	---	55.00	59.98	61.06	---	---	---	---	---		
0.176	---	20.60	---	---	---	61.20	62.60	---	---	---	---	---		

Table 11: Phase transition temperatures T [°C] of the $\text{H}_2\text{O}/\text{NaCl} - \text{C}_{12}\text{E}_5$ system, $\varepsilon = 0.185$.

γ	T [°C]													
	$L_1/L_1'+L_1''$	$L_1'+L_1''/L_\alpha$	L_α/L_α^+	L_α^+/L_α	$L_\alpha/L_\alpha+L_3$	$L_\alpha^+/L_\alpha+L_3$	$L_\alpha+L_3/L_3$	L_3/L_1+L_3	L_1+L_3/L_1+L_2	$L_1/L_1'+L_1''$	$L_1''+L_\alpha/L_\alpha$	L_α/L	L_2/L_1+L_2	
0.010	7.77	21.39	22.60	22.60	37.72	39.00	40.00	41.50	50.00	---	---	---	---	
0.015	7.95	21.29	22.60	22.60	37.72	39.00	40.00	41.50	50.00	---	---	---	---	
0.020	8.15	21.29	22.60	22.60	37.07	39.88	40.90	42.38	50.00	---	---	---	---	
0.025	8.40	21.30	22.60	22.60	36.20	40.30	41.40	42.95	50.00	---	---	---	---	
0.030	8.79	21.40	22.60	22.60	35.58	40.97	41.86	43.56	50.00	---	---	---	---	
0.040	9.20	21.40	22.60	22.60	35.10	41.40	42.20	44.00	50.00	---	---	---	---	
0.050	9.45	21.18	22.60	22.60	34.61	42.07	42.86	44.48	50.00	---	---	---	---	
0.070	9.96	20.99	22.60	22.60	32.33	41.57	43.66	45.16	50.00	---	---	---	---	
0.100	10.95	20.99	20.99	27.96	42.47	42.47	44.65	45.77	50.00	---	---	---	---	
0.150	12.00	20.50	20.50	43.00	43.00	43.00	45.20	46.40	50.00	---	---	---	---	
0.200	13.70	20.40	20.40	43.70	43.70	43.70	46.00	47.40	49.80	---	---	---	---	
0.250	16.09	20.19	20.19	44.45	44.45	44.45	46.98	48.28	49.60	---	---	---	---	

Table 13: Phase transition temperatures T [°C] of the H₂O/glycerol - C₁₂E₅ system, $\phi_{gly} = 0.50$.

γ	L_{α^+}/L_{α}	$L_{\alpha}/L_{\alpha^+L_3}$	$L_{\alpha^+L_3}/L_3$	L_3/L_1+L_3	L_1+L_3/L_1+L_2
T [°C]					
0.022	22.85	---	28.77	34.02	41.37
0.300	18.89	---	29.85	33.23	41.40
0.430	14.56	---	30.00	---	---
0.052	9.00	30.75	31.81	35.00	41.40

DLS DATA POINTS

In this sequence values of hydrodynamic radii R_{hydr} of the vesicles for all presented experiments are given.

Table 14: Hydrodynamic radii R_{hydr} for eight surfactant mass fractions, $\gamma = 0.01 - \gamma = 0.05$ for temperature jumps from $T = 48^\circ\text{C}$ (L_α) to $T = 35^\circ\text{C}$ (L_{α^+}) and $T = 48^\circ\text{C}$ (L_α) to $T = 25^\circ\text{C}$ (L_{α^+}).

γ	R_{hydr} [nm]	
	L_α ($T = 48^\circ\text{C}$)	L_α ($T = 48^\circ\text{C}$)
	L_{α^+} ($T = 25^\circ\text{C}$)	L_{α^+} ($T = 35^\circ\text{C}$)
0.01	230	180
0.015	250	210
0.02	290	260
0.025	300	330
0.03	---	440
0.035	360	530
0.04	490	560
0.05	510	575

Table 15: Hydrodynamic radii R_{hydr} for one surfactant mass fraction $\gamma = 0.03$ for temperature jumps from different depth within the lamellar phase L_α to $T = 35^\circ\text{C}$ (L_{α^+}).

γ	R_{hydr} [nm]				
	L_α		L_{α^+}	L_{α^+}	
	$T = 45^\circ\text{C}$ $T = 35^\circ\text{C}$	$T = 47^\circ\text{C}$ $T = 35^\circ\text{C}$	$T = 49^\circ\text{C}$ $T = 35^\circ\text{C}$	$T = 51^\circ\text{C}$ $T = 35^\circ\text{C}$	$T = 53^\circ\text{C}$ $T = 35^\circ\text{C}$
0.03	476	497	512	502	489

Table 16: Hydrodynamic radii R_{hydr} for three mass fractions, $\gamma = 0.01 - 0.03$ for temperature jumps from $T = 48^\circ\text{C}$ (upper L_α) to $T = 35^\circ\text{C}$ (L_{α^+}), $T = 21^\circ\text{C}$ (lower L_α) to $T = 35^\circ\text{C}$ (L_{α^+}) and $T = 42^\circ\text{C} - 50^\circ\text{C}$ (L_3) to $T = 35^\circ\text{C}$ (L_{α^+}).

R_{hydr} [nm]							
γ	$T = 42-50^\circ\text{C}$		$T = 35^\circ\text{C}$	$T = 48^\circ\text{C}$	$T = 35^\circ\text{C}$	$T = 21^\circ\text{C}$	$T = 35^\circ\text{C}$
	L_3	L_{α^+}		$L_{\alpha}(\text{upper})$	L_{α^+}	$L_{\alpha}(\text{lower})$	L_{α^+}
0.01		158.1			193.3		197.8
0.02		219.1			273.6		273.6
0.03		310.5			437.0		434.3

SANS

Table 17: Calibration before the SANS experiments with λ being the wavelength of the neutron beam, coll the collimation, app the apertures, EC the empty cell and ECH the empty cell holder, BC+BG the boron carbide background.

$\lambda/\text{\AA}$	coll	det	app	EC+ECH	EC+ECH+Plexi	BC+BG
4.5	8	1.9	8x8	15min	25min	15min
4.5	8	4	8x8	15min	50min	15min
4.5	8	8	8x8	15min	15min	15min
12	8	8	8x8	15min	15min	15min

Table 18: $\text{H}_2\text{O} - \text{C}_{12}\text{E}_4$ - negative T -jumps for sponge phase L_3 , lamellar phase L_α and vesicular phase L_α^+ with ϕ being the surfactant volume fraction, T the temperature, coll the collimation, app the apertures and λ the wavelength of the neutron beam.

L_3 - phase	ϕ	$T/^\circ\text{C}$	coll	det	app	$\lambda/\text{\AA}$
IS1_2	0.02	52.87	8	8	15x15	4.5
IS1_2	0.02	52.87	8	1.9	15x15	4.5
IS1_2	0.02	52.87	8	7.98	15x15	12
IS1_5	0.05	55.68	8	8	15x15	4.5
IS1_5	0.05	55.68	8	1.9	15x15	4.5
IS1_5	0.05	55.68	8	7.98	15x15	12
IS1_8	0.08	57.87	8	8	7x7	4.5
IS1_8	0.08	57.87	8	1.9	7x7	4.5
IS1_8	0.08	57.87	8	7.98	15x15	12
IS1_11	0.11	58.86	8	8	15x15	4.5
IS1_11	0.11	58.86	8	1.9	7x7	4.5
IS1_11	0.11	58.86	8	7.98	7x7	12

L_α	ϕ	$T/^\circ\text{C}$	coll	det	app	$\lambda/\text{\AA}$
IS1_2	0.02	45.99	8	8	15x15	4.5
IS1_2	0.02	45.99	8	1.9	15x15	4.5
IS1_2	0.02	45.99	8	7.98	15x15	12
IS1_5	0.05	45.99	8	8	15x15	4.5
IS1_5	0.05	45.99	8	1.9	15x15	4.5
IS1_5	0.05	45.99	8	7.98	15x15	12
IS1_8	0.08	45.99	8	8	7x7	4.5

IS1_8	0.08	45.99	8	1.9	7x7	4.5
IS1_8	0.08	45.99	8	7.98	15x15	12
IS1_11	0.11	45.99	8	8	15x15	4.5
IS1_11	0.11	45.99	8	1.9	7x7	4.5
IS1_11	0.11	45.99	8	7.98	7x7	12

L_{α^+} unperturbed	ϕ	$T/^{\circ}\text{C}$	coll	det	app	$\lambda/\text{\AA}$
IS1_2	0.02	29.86	8	8	15x15	4.5
IS1_2	0.02	29.86	8	1.9	15x15	4.5
IS1_2	0.02	29.86	8	7.98	15x15	12
IS1_5	0.05	29.86	8	8	15x15	4.5
IS1_5	0.05	29.86	8	1.9	15x15	4.5
IS1_5	0.05	29.86	8	7.98	15x15	12
IS1_8	0.08	29.86	8	8	7x7	4.5
IS1_8	0.08	29.86	8	1.9	7x7	4.5
IS1_8	0.08	29.86	8	7.98	15x15	12
IS1_11	0.11	29.86	8	8	15x15	4.5
IS1_11	0.11	29.86	8	1.9	7x7	4.5
IS1_11	0.11	29.86	8	7.98	7x7	12

L_{α^+} vortexed	ϕ	$T/^{\circ}\text{C}$	coll	det	app	$\lambda/\text{\AA}$
IS1_2	0.02	29.86	8	8	15x15	4.5
IS1_2	0.02	29.86	8	1.9	15x15	4.5
IS1_2	0.02	29.86	8	7.98	15x15	12
IS1_5	0.05	29.86	8	8	15x15	4.5
IS1_5	0.05	29.86	8	1.9	15x15	4.5
IS1_5	0.05	29.86	8	7.98	15x15	12
IS1_8	0.08	29.86	8	8	7x7	4.5
IS1_8	0.08	29.86	8	1.9	7x7	4.5
IS1_8	0.08	29.86	8	7.98	15x15	12
IS1_11	0.11	29.86	8	8	15x15	4.5
IS1_11	0.11	29.86	8	1.9	7x7	4.5
IS1_11	0.11	29.86	8	7.98	7x7	12

L_{α^+} sonicated	ϕ	$T/^\circ\text{C}$	coll	det	app	$\lambda/\text{\AA}$
IS1_2	0.02	29.86	8	8	15x15	4.5
IS1_2	0.02	29.86	8	1.9	15x15	4.5
IS1_2	0.02	29.86	8	7.98	15x15	12
IS1_5	0.05	29.86	8	8	15x15	4.5
IS1_5	0.05	29.86	8	1.9	15x15	4.5
IS1_5	0.05	29.86	8	7.98	15x15	12
IS1_8	0.08	29.86	8	8	7x7	4.5
IS1_8	0.08	29.86	8	1.9	7x7	4.5
IS1_8	0.08	29.86	8	7.98	15x15	12
IS1_11	0.11	29.86	8	8	15x15	4.5
IS1_11	0.11	29.86	8	1.9	7x7	4.5
IS1_11	0.11	29.86	8	7.98	7x7	12

Table 19: $\text{H}_2\text{O} - \text{C}_{12}\text{E}_4$ – positive T -jumps for micellar phase L_1 and vesicular phase L_{α^+} with ϕ being the surfactant volume fraction, T the temperature, coll the collimation, app the apertures and λ the wavelength of the neutron beam.

L_1	ϕ	$T/^\circ\text{C}$	coll	det	app	$\lambda/\text{\AA}$
IS1_0.2	0.002	4.0	8	8	30x30	4.5
IS1_0.2	0.002	4.0	8	1.9	30x30	4.5
IS1_0.2	0.002	4.0	8	7.98	30x30	12
IS1_2	0.02	4.0	8	8	30x30	4.5
IS1_2	0.02	4.0	8	1.9	30x30	4.5
IS1_2	0.02	4.0	8	7.98	30x30	12
IS1_5	0.05	4.0	8	8	30x30	4.5
IS1_5	0.05	4.0	8	1.9	30x30	4.5
IS1_5	0.05	4.0	8	7.98	30x30	12
IS1_8	0.08	4.0	8	8	30x30	4.5
IS1_8	0.08	4.0	8	1.9	30x30	4.5
IS1_8	0.08	4.0	8	7.98	30x30	12
IS1_11	0.11	4.0	8	8	30x30	4.5
IS1_11	0.11	4.0	8	1.9	30x30	4.5
IS1_11	0.11	4.0	8	7.98	30x30	12

L_{α^+}	ϕ	$T/^\circ\text{C}$	coll	det	app	$\lambda/\text{\AA}$
IS1_0.2	0.002	29.86	8	8	30x30	4.5
IS1_0.2	0.002	29.86	8	1.9	30x30	4.5
IS1_0.2	0.002	29.86	8	7.98	30x30	12
IS1_2	0.02	29.86	8	8	30x30	4.5
IS1_2	0.02	29.86	8	1.9	30x30	4.5
IS1_2	0.02	29.86	8	7.98	30x30	12
IS1_5	0.05	29.86	8	8	30x30	4.5
IS1_5	0.05	29.86	8	1.9	30x30	4.5
IS1_5	0.05	29.86	8	7.98	30x30	12
IS1_8	0.08	29.86	8	8	30x30	4.5
IS1_8	0.08	29.86	8	1.9	30x30	4.5
IS1_8	0.08	29.86	8	7.98	30x30	12
IS1_11	0.11	29.86	8	8	30x30	4.5
IS1_11	0.11	29.86	8	1.9	30x30	4.5
IS1_11	0.11	29.86	8	7.98	30x30	12

Table 20: H₂O/glycerol – C₁₂E₄ for for sponge phase L₃, lamellar phase L _{α} and vesicular phase L _{α^+} with ϕ being the surfactant volume fraction, T the temperature, coll the collimation, app the apertures and λ the wavelength of the neutron beam.

L ₃ - phase	ϕ	$T/^\circ\text{C}$	coll	det	app	$\lambda/\text{\AA}$
IS1_2	0.02	52.87	8	8	30x30	4.5
IS1_2	0.02	52.87	8	1.9	30x30	4.5
IS1_2	0.02	52.87	8	7.98	30x30	12
IS1_5	0.05	55.68	8	8	30x30	4.5
IS1_5	0.05	55.68	8	1.9	30x30	4.5
IS1_5	0.05	55.68	8	7.98	30x30	12
IS1_8	0.08	57.87	8	8	30x30	4.5
IS1_8	0.08	57.87	8	1.9	30x30	4.5
IS1_8	0.08	57.87	8	7.98	30x30	12

L _{α}	ϕ	$T/^\circ\text{C}$	coll	det	app	$\lambda/\text{\AA}$
IS1_2	0.02	20	8	8	30x30	4.5
IS1_2	0.02	20	8	1.9	30x30	4.5
IS1_2	0.02	20	8	7.98	30x30	12

IS1_5	0.05	20	8	8	30x30	4.5
IS1_5	0.05	20	8	1.9	30x30	4.5
IS1_5	0.05	20	8	7.98	30x30	12
IS1_8	0.08	20	8	8	30x30	4.5
IS1_8	0.08	20	8	1.9	30x30	4.5
IS1_8	0.08	20	8	7.98	30x30	12

L_{α^+}	ϕ	$T/^\circ\text{C}$	coll	det	app	$\lambda/\text{\AA}$
IS1_2	0.02	4	8	8	30x30	4.5
IS1_2	0.02	4	8	1.9	30x30	4.5
IS1_2	0.02	4	8	7.98	30x30	12
IS1_5	0.05	4	8	8	30x30	4.5
IS1_5	0.05	4	8	1.9	30x30	4.5
IS1_5	0.05	4	8	7.98	30x30	12
IS1_8	0.08	4	8	8	30x30	4.5
IS1_8	0.08	4	8	1.9	30x30	4.5
IS1_8	0.08	4	8	7.98	30x30	12
IS1_11	0.11	4	8	8	30x30	4.5
IS1_11	0.11	4	8	1.9	30x30	4.5
IS1_11	0.11	4	8	7.98	30x30	12

NMR SAMPLES

Table 21: Width at half heights $\nu_{1/2}$ [Hz] for three differently treated samples of same surfactant mass fraction $\gamma = 0.20$ at temperatures $T = 54^\circ\text{C}$ (L_{α}) and $T = 30^\circ\text{C}$ (L_{α^+}).

$\gamma = 0.20, \nu_{1/2}$ [Hz]		
	$T = 54^\circ\text{C}$ (L_{α})	$T = 30^\circ\text{C}$ (L_{α^+})
method 1	19.2	14.1
method 2	64.1	44.0
method 3	136.6	90.4

Table 22: Widths at half height $\nu_{1/2}$ for each surfactant mass fraction respectively.

$\gamma = 0.20$		$\gamma = 0.25$	
T [°C]	$\nu_{1/2}$ [Hz]	T [°C]	$\nu_{1/2}$ [Hz]
23.0	57.91	20.5	156.0
24.0	61.35	23.0	174.0
25.0	65.13	24.0	189.0
27.5	68.10	25.0	197.0
30.0	68.86	30.0	204.0
32.5	67.30	35.0	197.0
35.0	65.73	40.0	186.0
37.5	64.17	45.0	183.0
40.0	61.04		
42.5	59.47		
45.0	57.91		
47.5	55.56		
50.0	53.99		

Table 23: Widths at half height ν_Q for each surfactant mass fraction respectively.

$\gamma = 0.30$		$\gamma = 0.40$		
T [°C]	$\nu_{1/2}$ [Hz]	T [°C]	$\nu_{1/2}$ [Hz]	
	50.0	226.4150		
	52.0	224.4800		
	54.0	222.0350		
	56.0	219.5900		
24.0	247.4660		20.0	461.85
25.0	254.2910		25.0	495.90
26.0	258.7150		30.0	505.45
27.0	260.6490		35.0	504.09
28.0	260.6710		40.0	492.51
29.0	260.6710		45.0	478.88
30.0	260.1820		50.0	465.94
32.5	257.2480		55.0	451.63
35.0	253.8240		60.0	432.56
37.5	249.4230			
40.0	245.5100			
42.5	241.1080			
45.0	235.7290			
47.5	230.3490			

SYMBOLS AND ABBREVIATIONS

Latin characters

A	area element
a_0	effective area per head group
B	magnetic field
c	temperature coefficient of curvature
c_1 and c_2	principal curvatures
c_0	spontaneous curvature of the film
$c_{0,mono}$	spontaneous curvature of the monolayer
$c_{0,bil}$	spontaneous curvature of the bilayer
DLS	dynamic light scattering
D	bilayer repeat distance
D	diffusion coefficient
d_{sd}	sample-detector distance
efg	electric field gradients
ΔE	energy
e	elementary charge

$E_{Q,b}$	constant representing the splitting associated with single perturbed water molecule
E	bending energy
f_b	is the fraction of perturbed water molecules
FFEM	freeze fracture electron microscopy
$g^{(2)}(t)$	intensity-intensity-autocorrelation function
h	<i>Planck's constant</i>
\hbar	<i>Dirac constant</i>
H_0	mean curvature
H_{bil}	mean curvature of the bilayer
H_{mono}	mean curvature of the monolayer
H_0	Zeeman Hamiltonian
H_Q	quadrupole Hamiltonian
H ₂ O	water
² H ₂ O/ D ₂ O	deuterium oxide ("heavy" water)
I	spin quantum number
I	spin angular momentum
I_{max}	peak maximum

$I(q)$	absolute intensity
I_{SANS}	scattering intensity
K	Gaussian curvature
k_{B}	<i>Boltzmann</i> constant
L_1'	dilute micellar phase
L_1''	concentrated micellar phase
L_2	inverse micellar phase
L_3	sponge phase
L_{α}	lamellar phase
L_{α}^+	vesicular phase
l	length of the hydrocarbon chains
m	mass
m_1	spin quantum number
MLV	multi lamellar vesicle
M_{W}	molecular weight
N_{A}	Avogadro constant
NMR	nuclear magnetic resonance
N_{S}	surfactant packing parameter

n_λ	refractive index
$P(q)$	form factor
p_b	number of “bound” (perturbed) water molecules
PD	polydispersity index
q	absolute value of the scattering vector
Δq^2	resolution function
R_1 and R_2	radii for the two perpendicular directions
r_1 and r_2	principle curvature radii
R_{hydr}	hydrodynamic radius
R_i and R_e	internal and external radii of a vesicle
rf	radio frequency
SANS	small angle neutron scattering
S_b	orientational order parameter of perturbed water molecules
SUV	single lamellar vesicles
$S(q)$	structure factor
T	temperature
T_K	<i>Krafft</i> temperature

T_0 or \bar{T}	phase inversion temperature
T_u	upper temperature of the three phase body
T_l	lower temperature of the three phase body
Ta/W	tantalum/tungsten
v	volume of the hydrophobic part of the surfactant molecule
V	sample volume
v_{\max}	maximal speed of neutrons
w_b	numbers of moles of bound water per molecule surfactant
w_f	numbers of moles of free water per molecule surfactant

Greek characters

$\alpha(n)$	correlation function
β	temperature independent system specific coefficient
χ	nuclear quadrupole coupling constant
δ_{bil}	bilayer thickness
ε	mass fraction of salt in water-phase
ϕ	volume fraction of surfactant in the binary systems
$\phi(v)dv$	neutron flux per area and second
γ	surfactant mass fraction
γ	gyromagnetic ratio
$\eta(\tau)$	viscosity of the solvent as function of temperature T
η^{20}_{water}	viscosity of water
$\eta^{20}_{\text{glycerol}}$	viscosity of glycerol
Γ	maximum of line widths (DLS)
κ	elastic bending modulus
κ_{mono}	elastic bending modulus of a monolayer
$\bar{\kappa}$	saddle splay modulus
λ	wavelength
μ	magnetic moment
ν	electromagnetic radiation of frequency
ν_0 and ν_L	<i>Larmor frequency</i>

$\Delta v_{1/2}$	peak width at half height
Δv_Q	quadrupolar splittings
ρ	density
ρ	scattering length density
σ_R	standard deviation
θ	scattering angle
ξ	structural length
ψ	mass fraction of glycerol in the water-phase

Ich versichere, dass ich die von mir vorgelegte Dissertation selbstständig angefertigt, die benutzten Quellen und Hilfsmittel vollständig angegeben und die Stellen der Arbeit – einschließlich Tabellen, Karten und Abbildungen –, die anderen Werken im Wortlaut oder dem Sinn nach entnommen sind, in jedem Einzelfall als Entlehnung kenntlich gemacht habe; dass die Dissertation noch keiner anderen Fakultät oder Universität zur Prüfung vorgelegen hat; dass sie – abgesehen von unten angegebenen Teilpublikationen – noch nicht veröffentlicht worden ist sowie, dass ich eine solche Veröffentlichung vor Abschluss des Promotionsverfahrens nicht vornehmen werde. Die Bestimmungen der Promotionsordnung sind mir bekannt. Die von mir vorgelegte Dissertation ist von Prof. Dr. Reinhard Strey betreut worden.

Köln, den 08. Dezember 2009

Ivana Fehr

Lebenslauf

PERSÖNLICHE DATEN

Ivana Fehr, geb. Savić

Geboren am 27. Februar 1981 in Belgrad, Serbien

Deutsche Staatsangehörigkeit

Verheiratet

Sohn, Lennox Fehr, geb. 10. Mai 2009

BERUFLICHER WERDEGANG

10/2004 – 06/2006

Tätigkeit als studentische Hilfskraft an der Universität zu Köln am Institut für Physikalische Chemie, Arbeitsgruppe Prof. Dr. Reinhard Strey

09/2006 – 09/2009

Wissenschaftliche Mitarbeiterin an der Universität zu Köln am Institut für Physikalische Chemie, Arbeitsgruppe Prof. Dr. Reinhard Strey

STUDIUM

10/2001 – 06/2006

Studium der Chemie an der Universität zu Köln

11/2003

Vordiplom

06/2006

Hauptdiplom; Hauptfach: Physikalische Chemie

Diplomarbeit unter Anleitung von Prof. Dr. Reinhard Strey; Titel der Diplomarbeit: „*H₂O – Bioöl – Bioamphiphil*“

11/2006 – 11/2009

Mitglied der Graduiertenschule: “Helmholtz Research School on Biophysics and Soft Matter”

02/2008 – 06/2008

Forschungsaufenthalt bei Prof. Dr. Ulf Olsson an der Lund Universität, Lund, Schweden

10/2006 – 11/2009

Promotion in Physikalischer Chemie an der Universität zu Köln unter Anleitung von Prof. Dr. Reinhard Strey; Titel der Dissertation: „*Vesicles in Simple Binary Water – non-ionic Surfactant Systems*“

SCHULAUSSBILDUNG

1987 – 1990

Grundschule in Belgrad

1990 – 1991

Grundschule in Köln

1991– 1995

Gymnasium „*Georg-Büchner-Gymnasium*“, Köln

1995 – 2001

Gymnasium „*Elisabeth von Thüringen Gymnasium*“, Köln

Abschluss: Allgemeine Hochschulreife

